2015

Single Molecule Electrophoresis and Optical Detection Using Thermoplastic Nanofluidic Devices: An Experimental and Simulation Study

Kumuditha Madushanka Weerakoon Ratnayake
Louisiana State University and Agricultural and Mechanical College, kratna1@lsu.edu

SINGLE MOLECULE ELECTROPHORESIS AND OPTICAL DETECTION USING THERMOPLASTIC NANOFLUIDIC DEVICES: AN EXPERIMENTAL AND SIMULATION STUDY

A Dissertation

Submitted to the Graduate Faculty of the
Louisiana State University and
Agricultural and Mechanical College
in partial fulfillment of the
requirements for the degree of
Doctor of Philosophy

in

The Department of Chemistry

by
Kumuditha Madushanka Weerakoon Ratnayake
B.S., University of Colombo – Sri Lanka, 2008
December 2015

To my dearest parents, loving wife and my brother

for their endless love, support and encouragement.

In Honor of:

Jayathilake Weerakoon Ratnayake

In Memory of:

Daya Wimalagunaratne

ACKNOWLEDGMENTS

First and foremost, I would like to sincerely thank my advisor, Professor Steven Allan Soper for his guidance and continuous support throughout my doctoral carrier and especially for his confidence in me and his persistent assistance, insightful decisions which has made this work successful. I would truly appreciate giving me the opportunity to pursue various projects without any objection. I would also like to thank the members of my dissertation committee, Prof. Dorel Moldovan, Prof. George Stanley, Prof. Bin Chen, and Prof. Xue-Bin Liang for their valuable time, contribution, and support towards the realization of my degree.

My special thanks goes to past and current member of the Soper research group Dr. Maggie Witek, Dr. Matt Hupert, Dr. Rattikkan Chantiwas, Dr. Samuel Njoroge, Dr. Udara Dharmasiri, Dr. Swathi Pullagurla, Dr. Franklin Uba, Dr. Nyote Calixte, Dr. Joyce Kamande, Dr. Katrina Battle, Dr. Michael Vicente, and colleagues Matt Jackson, Colleen O'Neil, Robert Schotzinger, for their supportive involvement including all the new members. Colleagues that I worked with in collaboration projects, Dr. Bhupender Thakur, Dr. Brian Novak, Dr. Kai Xia for their support and contributions. Best wishes to everyone in all your future endeavors.

A special heartfelt thanks goes to my family for their endless love and encouragement during this long journey. I am so grateful to have you all around me. My greatest thanks goes to my loving mother, Daya Wimalgunarathna; you were my inspiration. I'm certainly glad to make your dream come true, even though you're not with us today. I certainly know you are proud of myself for who I am today. Also, my loving farther Jayathilaka Weerakoon Ratnayake; my role model from my childhood. You are the most supportive person in my life always encouraging me at my difficult situations. You were there whenever I fall to offer your hand to rise stronger. You believed in my capabilities and determined me to gradually reach my goal. I would kindly

like to thank to my loving stepmother, Tilisia Senanayake for being with us throughout especially in our most difficult time in our lives. The love and care you have given me have kept you in my mother's position. I would like to thank my one and only loving brother, Indeewara Ratnayake for being supportive by taking care of my parent while I'm pursing my studies abroad. You are the best brother I could ever have. Additionally, my loving aunt and uncle, Kema Ratnayake and Ajith Karunaratne were always there whenever I needed a helping hand and always encouraged me to be who I am today.

To all my friends, thank you all for your understanding and encouragement in many ways. I cannot list all the names here but you are always in my heart, and will be there. Finally, my heartiest gratitude and greatest thanks goes to my lovely wife for her effort in bearing with me, by my side in every situation. I would not be able to succeed in finishing up everything on time without your love and care. None of this would possible without your endless support and encouragement. I love you all from the bottom of my heart and thank you very much for everything! May triple gem bless you!

TABLE OF CONTENTS

LIST OF TABLES

LIST OF FIGURES

ABBREVIATIONS AND ACRONYMS

AC	Alternating Current
B	Bandwidth (Hz)
C_{eq}	Equivalent Concentration
Ci	Bulk ionic Concentration of solution (mol/dm^3)
Cyt c	Cytochrome c
DC	Direct Current
DL	Diffuse Layer
DNA	Deoxyribonucleic acid
D_u	Dukhin number
E	Electric Field strength (V/cm)
EDL	Electric Double Layer
EDTA	Ethylene Diamine Tetra Aceticacid
EOF	Electroosmotic flow
eV	electron Volt ($1\ eV = 1.6026 \times 10^{-19}$ J)
F	Faraday's Constant (96,485 C/mol)
F_d	Drag Force (N)
F_e	Electrical force (newton/N)
f_H	Henry's constant
FIB	Focused Ion Beam
FITC	Fluorescein Isothicyanate
G	Conductance (Ω^{-1}or siemens)
g	Acceleration due to gravity ($9.8ms^{-2}$)

G_B	Conductivity of Buffer
I	Ionic strength of electrolytes
$I_{cond,\ bulk}$	Conduction Current from Bulk solution conductivity (A)
$I_{cond,\ surf}$	Conduction Current from Surface conductivity (A)
I_t	Tunneling Current
k_B	Boltzmann constant (1.38×10^{-23} JK^{-1})
l_p	Persistence length (nm)
L_{cont}	Contour length
m	Mass of electron ($9.10938188 \times 10^{-31}$ kg)
NA (mol^{-1})	Avogadro's number of molecules /ions (6.02214×10^{23})
PDMS	Poly (dimethylsiloxane)
Q	Volume Flow rate (liter per min)
R ($JK^{-1}mol^{-1}$)	Molar Gas constant
RMS	Root-Mean-Square
SL	Stern Layer
T	Kelvin Temperature (Kelvin or K)
TBE	Tris(hydroxymethyl)aminomethane-borate-EDTA
u_i	Effective Ionic Mobility (m^2/sV)
u_i^{∞}	Absolute Ionic mobility
V (volts)	Applied Voltage
v_{eof} ($cm\ s^{-1}$)	Electrophoretic velocity
v_{ep}	Electrophoretic velocity
z_i	Ionic Charge

ΔG	Change in conductivity
Δp (atm)	Pressure drop
ΔV (volts)	Voltage drop
ε_0	Electrical permittivity of vacuum
ε_e	Electrical Permittivity of a medium
ε_r	Relative dielectric constant
ε_w	Dielectric permittivity of solvent (usually water)
ζ (mV)	Zeta Potential
η	Dynamic Viscosity of solution
κ	Electrical Conductivity (siemens per centimeter or S/cm)
κ_b	Bulk electrolyte conductivity ($\Omega^{-1}m^{-1}$)
κ_d	Debye-Hӧckel parameter
κ_s	Surface conductivity ($\Omega^{-1}m^{-1}$)
λ_d	Debye Length
μ_{eof}	Electroosmotic flow mobility ($cm^2\ V^{-1}s^{-1}$)
μ_{ep}	Electrophoretic mobility ($cm^2\ V^{-1}s^{-1}$)
ν_{eof} (cms^{-1})	Electroosmotic Flow Velocity
ρ (Ω cm)	Resistivity at a temperature T
σ (gcm^{-3})	Density
h	Planck's Constant

ABSTRACT

Nanofludic devices provide a great platform for single molecular analysis. The unique phenomena in nanoscale gained such interest in investigating the single molecular behavior in nanochannels. Sizes less than 200 nm in one or two-dimensional structures have lead to fascinating observations not accessible in microscale. When a single molecule translocate through a nanotube it interacts with channel walls by adsorption/ desorption, van der Waals interactions and hydrophilic interactions providing a mechanism for separation without any extra additives. Moreover, double layer thickness governed by the background electrolyte plays a vital role. We report single molecular electrophoresis phenomena in nanochannels and nanoslits based on experiment and simulation studies. This will provide the guidance for sequencing DNA by clipped single monomer nucleotides based on their unique time-of-flight (ToF) signatures when electrokinetically driven through a nanotube.

The nanofluidic devices were fabricated in thermoplastic devices using mixed micro-scale and nanoscale methodologies. We also report a novel bonding methodology at low temperature using thermoplastic devices with high glass transition substrate sealed to a low glass transition cover plate. This approach prevents distorted nanochannels specially when fabricating nanochannels less than 50 nm to facilitate DNA stretching studies.

Genomic mapping of single molecules has gained attention significantly during the last decade. Genomic mapping of DNA molecules facilitated region-specific drug development. We study the development of a nanofluidic-based sensor to monitor chemotherapy responses in cancer patients by stretching their genomic DNA in nanochannels and identifying the specific damage sites.

CHAPTER 1. TRANSPORT PROPERTIES OF SINGLE MOLECULES IN NANOCHANNELS

1.1 Introduction

Recently, DNA sequencing has shown promising advances in research and technology developments. In the early 1970's there were revolutionary developments in this area. For example, Maxam-Gilbert method[1] was introduced two years after the groundbreaking publication by Sanger and Coulson,[2] which was named the "plus-minus" method. Although these methods were popular during that time, several drawbacks have been reported due mostly to the extensive amount of labor associated with acquiring sequencing data. As an example, different genetic variations can be used as effective biomarkers for various diseases such as known point mutations, gene expression, copy number variation, which can be used in diagnostic applications. However, the uses of these DNA sequencing techniques are limited due to their high cost of implementation and lack of advance instruments and the need for professional expertise.[3] Hence, researchers have discovered faster and cheaper methods for DNA sequencing.

Most of the biological processes such as transcription and translation occurs in micro- to nanometer scales. Innovative Lab-on-a-Chip methods have become popular because of its simplicity and its low-cost implementation.[4] Many fields of research have been revolutionary drivers for the development of this technology. Lab-on-a-Chip methods have become a solid platform to sequence the complete genomes of individuals.

Microfluidics can be defined as the science and technology that process and manipulate nano- to picoliters of fluids in the micro-dimension scale (10 μm-sub millimeter range).[5] It has created a perfect linkage between Biology, Chemistry and Engineering to develop methods to analyze biological targets in a simple way.[6-9] Over the past few decades, microchip-CE has become more popular compared to conventional CE for the analysis of biomolecules. Ability to

assay hundreds of samples at a fast rate, achieving ultrahigh throughput with rapid analysis and parallel analysis arrays, consumption of very low sample volume (picoliters), integrated fluidic platforms for sample preparation and analysis functions makes it an captivating technology.[10] With those attractive operations available, microchip-CE has been implemented for numerous biomedical and bioclinical applications.[11-16] Even though microfluidic systems are capable of analyzing smaller biomolecules, fast development of research has showed that more powerful and efficient methods are necessary to analyze much smaller volumes than microfluidics. This lead to a fascinating new field called "nanofluidics" which is in the dimensional range of 1-100 nm.[17] Interestingly, nanochannel based devices can offer great flexibility in terms of shape and size with increased robustness and surface properties, which can be tuned based on the required function which is not readily achievable in micro-scale.[18,19] They have also been applied in the separation,[20,21] manipulation and detection[22] of single molecules and control of molecular transport and wall interactions.[23,24]

The discovery of nanopores for DNA sequencing was an enormous step in human genome technology. Invention of devices with nanopores has shown some promising results perceptively by reading a single strand of DNA or a strand RNA without the use an external molecular label such as fluorescent dyes.[25-31] Electrical signature based nucleotide recognition came into play in this field and has been used to analyze nucleotides without labeling the strands with a fluorescent dye. Nanopores are commonly constructed from an organelle of a bacterium called *Staphylococcus aureus*, which makes a proteinaceous membrane channel called α-hemolysin. The use of α-hemolysin as a nanopore has been reported extensively.[25-29] When an electric field is applied across this nanopore it will drive only a single strand through the nanopore because of its fixed pore size. As each molecule resides inside the pore it will generate an electrical signal,

which is measured as a blockade of ionic current. However, these biological nanopores have several limitations such as stability and fixed pore size. Because of the limitations of natural nanopores, the use of solid-state/synthetic nanopores has been reported.[32-34] Synthetic nanopores monitor the tunneling current or blockade current with transverse electrodes using decorated nanopores. [35-38]

The technique used by both of the above mentioned nanopores are being used to identify single nucleotides or peptides using the blockade current amplitude when they travel through the nanopore. Further development of this technique has been reported. Davis *et al.*[39] and Wu *et al.*[40] have reported the use of a highly processive exonuclease enzyme to clip the nucleotides from DNA sequentially so that the original order of the nucleotides can be maintained. Fitting the α-hemolysin (α-HL) nanopores with a cyclodextrin molecule[40] and bonding it with exonuclease enzymes[41] are further advancements of nanopores. Considering the poor accuracy and efficiency[42] of these blockade current measuring methods, it has necessitated the need for a new method with advanced base identification approaches and pore sequencing strategies. Hence, in response to address these limitations of nanopores, nano-channel based devices are being investigated.

Whether considering nanopores or nanochannels, understanding the behavior of liquid flow in nano-domains is vital as well as other fields such as drug delivery, catalytic reactions, separation and analysis of biomolecules.[43] Some of the studies that scientists have studied include the motion of single molecules through nano-sized channels.[44-45] In addition, several methods of fabricating nano-channels on glass, silica or fused silica substrate have been reported. [19, 46-48]

In order to get a better understanding of the behavior of single entities in nano-domains, the support of Molecular Dynamics Simulations (MDS)[49-50] is significant. Molecular dynamics simulations can be defined as a method that provides details about the motion of particles using the interaction of atoms and molecules over a known period of time.[43] Basically, it is based on Newton's second law to model the interaction of particles with each other. MDS of the fluids in nano-domains can be categorized into various categories, but to narrow the complexity we will focus only on pressure driven flows[51] and electro kinetic flows.[24, 52-55] Because of the limitations in pressure driven flow, mainly due to the need of a large pressure gradient which is hard to achieve experimentally, alternate methods such as electrically driven flow MDS have been considered as well.[43]

Transportation of biomolecules through nano-channels has been well discussed in literature.[56] Computational studies about DNA in nano-channels have been reported extensively.[57-61] However, studies about single entity transport in nano-scale environments have yet to be reported. Hence, we conducted MD simulations on LONI and HPC clusters using the LAMMPS code[62] for all four deoxyribonucleotide monophosphates (dNMPs) in aqueous medium.

Generally, there are force fields available in the literature for most of the biomolecules.[63-66] The ability to predict correct conclusions about a system is greatly influenced by choosing the correct force field. In that case, force field development will be a key factor in designing more realistic simulations. Force fields can be classified as "all-atom",[64, 67-68] which considers all of the atoms including hydrogen, "united atoms"[69-70] with considers methyl or methylene groups and hydrogen atoms acting as a single interaction center. The "course grained"[71] approach

considers one residue as a single interaction center. Comparisons of different kinds of force fields enhance the better choice of parameters for the molecular dynamics simulation.

Many studies about developing and comparing force fields for DNA molecules have been reported in the literature.[72-73] AMBER[64, 74-75] and GROMACS[68] are two widely used packages to develop force fields for biomolecules and to analyze biological systems using molecular dynamic simulations.

1.2 Parameters Effecting the Electrophoresis in Nanofluidics

Several important parameters that affect the nanoscale electrophoresis phenomena can be identified. The following section will discuss those parameters and their functionality in nano-geometries.

1.2.1 Electroosmotic Flow (EOF)

Electro-osmotic flow (EOF) studies have been reported as early as in 18th century. Reuss discovered that flow in capillary could be induced by clay particles in water under an external electric field.[76] Wiedmann reported fundamental theories of electrokinetics from his studies after couple of decades to support the findings by Reuss.[77] Evolving from that point, EOF theories playing a vital role in electrokinetic separation science. Scientists such as Helmholtz (1879)[78], Smoluchowickz (1903)[79] derived double layer theory, which occurs under electrokinetic transport phenomena.[80]

Under the influence of an external electric field, a charged capillary or micro/nano-confined tube filled with a solution of ions produces a bulk flow. The bulk that consists of positive and negative (or counter ions and co-ions) starts to flow towards the electrodes. A bulk flow moving in the direction of anode to cathode is considered as a positive EOF while the opposite is considered as negative EOF (see Figure 1.1).

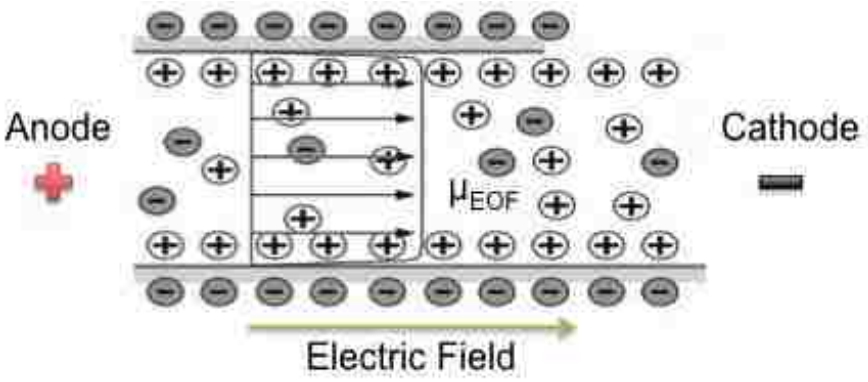

Figure 1.1 Electrokinetic flow dynamics of a buffer in a nanochannel with negatively charged walls. Electric field direction is from anode to cathode. (Reproduced from Uehera *et al.*)

This phenomenon is a result of the charge of the channel walls. For example, if the channel wall is negatively charged, positive ions will attract more towards the wall producing a double layer. The excess counter ions in the bulk close to the channel walls start moving towards the cathode by an occurrence called viscous drag. This gives rise to a positive EOF towards the cathode in a surrounding with negatively charged walls. EOF is solely dependent on applied electric field, channel wall material and the bulk solutions in contact with the channel wall.[81] The flow profile of an electrically driven flow differs when compared to that of a pressure driven flow. Figure 1.2 illustrates the imaging of flow profile identified for a pressure driven and hydrodynamically driven fluorescent dye. Under a thin EDL system, hydrodynamic flow profile holds a "parabolic" shape (also called as laminar flow profile) while it is a "plug-like" profile for electrokinetically driven flow. However, based on the plug-like profile the separation efficiency can increase enormously. This has been reported in numerous studies. [82-84]

EOF is related to the charge on the channel wall as well as viscosity and dielectric constant of the buffer. EOF mobility μ_{EOF} is given by;

$$\mu_{EOF} = -\frac{\varepsilon\zeta}{\eta} \tag{1.1}$$

where η is viscosity and ζ is the zeta potential of the charges wall. Thus, EOF is highly governed by the pH of the buffer since charges of the surface groups (which is ζ) are dependent on the solution pH.[85-86]

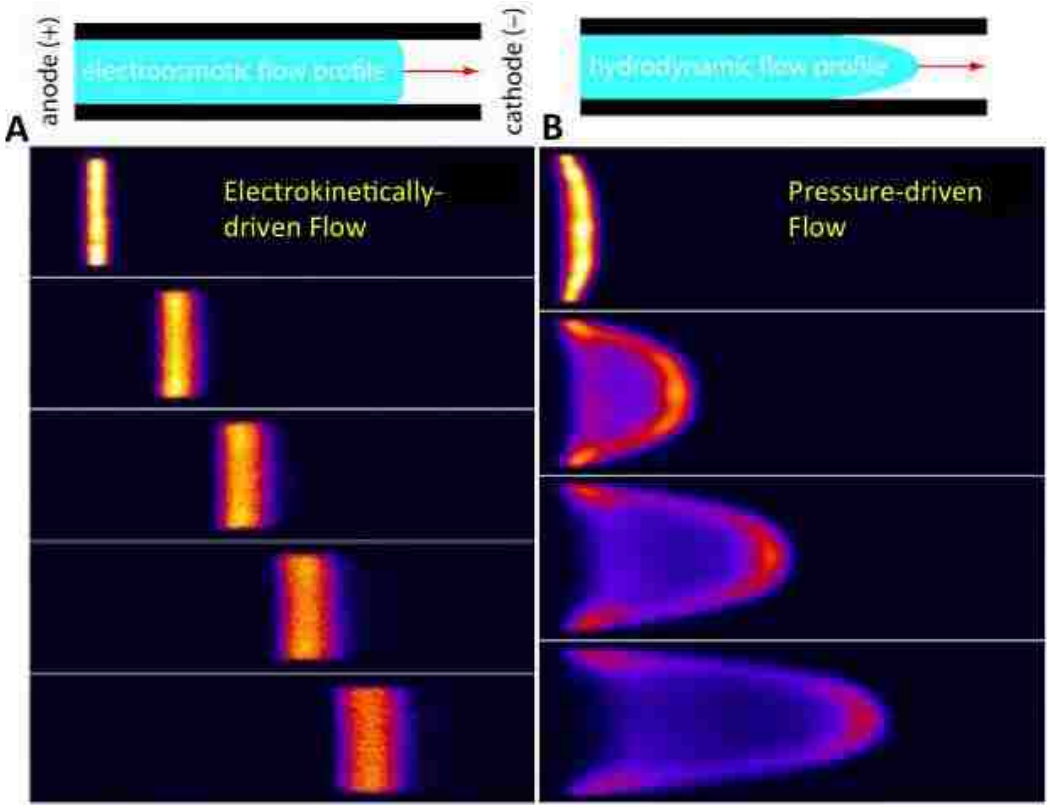

Figure 1.2 Images showing the fundamental difference in the dynamics of sample dispersion between electroosmotically-driven and pressure-driven flows. This visualization was performed using a molecular tagging technique (caged fluorescence visualization described later on in the chapter) and shows the reduced sample dispersion for (A) electroosmotic flow (in a capillary with a rectangular cross section 200 micron wide and 9 micron deep) as compared to (B) pressure-driven flow (rectangular cross-section 250 micron wide and 70 micron deep). (Reproduced from http://microfluidics.stanford.edu/Projects/Archive/caged.htm)

Also, electrophoretic velocity, $v_{EOF,}$ is given by multiplying μ_{EOF} with the electric field strength. Therefore,

$$v_{EOF} = -\frac{\varepsilon\zeta}{\eta}E \tag{1.2}$$

EOF velocity is linearly proportional to the applied electric field strength through the column. Therefore, changing the applied voltage would change the velocity of the flow of ions.

1.2.2 Electric Double Layer (EDL)

When applying an electric field through a micro/ nano sized channel filled with bulk solution, it induces surface charge on the surface of the channel. This surface charge occurs from the interaction of the surface groups with the buffer solution and the ion exchange reactions such as protonation and deprotonation. Because of the induced charges on the wall surface, counter ions in the solution attract very close to the wall to neutral the induced charge density on the wall. The compact layer is strongly bound to the channel surface and it is usually called as the Stern layer. Excess counter ions diffuse further away from the channel walls to assemble as diffuse layer.[87] Electric double layer (EDL) can be defined as the unification of Stern and diffuse layers. Investigations about EDL runs in to history as early as 18th century with the findings of Helmholtz[88] (1853), Gouy[89] (1910), Chapman[90] (1913) and Stern[91] (1924). Stern managed to combine the diffuse layer introduced in Gouy-Chapman model with the Helmholtz model introducing an internal Stern layer.[92] Gouy-Chapman-Stern (GSC) model describes the counter ions in the Stern layer and diffuse layer and EDL is comprised of these two layers. Outer edge of the Stern layer is introduced as the outer Helmholtz plane (OHP). Figure 1.3 shows a pictorial representation of Stern and diffuse layers as well as the potential drop through the two layers. Stern layer of counter ions does not move usually thus contributing to conductivity of the plane.[86]

EDL is one of the most important parameters in nanoscale electrophoresis. EDL is also called Debye layer since EDL thickness can be related to Debye length (λ_D) as follows.[92-93] For a monovalent electrolyte,

$$\lambda_D = \left(\frac{\varepsilon_0 \varepsilon_r k_B T}{2N_A e^2 I}\right)^{1/2} \quad (1.3)$$

where ε_0, permittivity of free space, ε_r, dielectric constant of the solution, k_B, Boltzmann constant, T, temperature of the electrolyte, N_A, Avogadro number and e, elementary charge.[94] For a symmetrical electrolyte (1:1 ionic ratio), it can be defined as,

$$\lambda_D = \left(\frac{\varepsilon_0 \varepsilon_r RT}{2F^2 c}\right)^{1/2} \quad (1.4)$$

where R, gas constant, F, Faraday constant and c is the ionic concentration of the electrolyte.

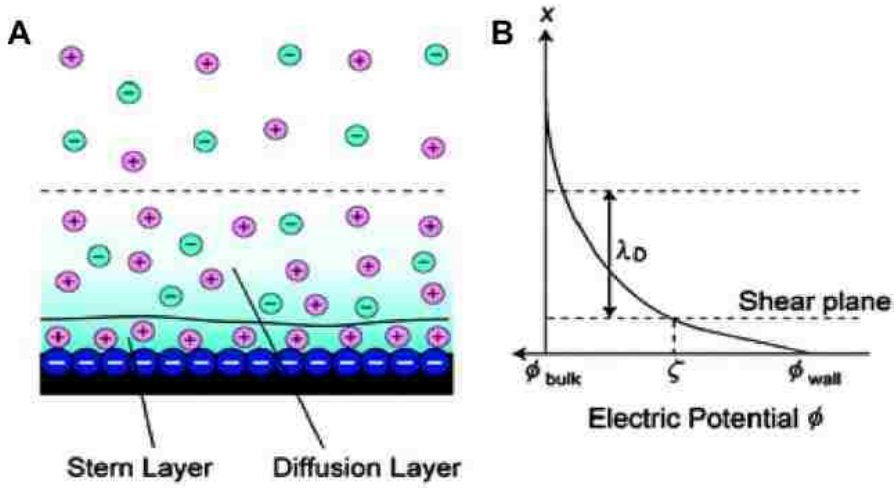

Figure 1.3 Schematic of an electrical double layer and electric potential profile normal to the negatively charged wall (right) (Reproduced from Daiguji, H. *Chem. Soc. Rev.* 2010)

It is interesting to study how the electric potential represented by EDL changes with the size of the channel. To study how the channel height affects the EDL system, the ratio of λ_D to channel height, h, can be investigated. It has been reported that when reducing the channel sizes to nanoscale, Debye length to channel height ratio (λ_D/h) is one crucial parameter. In capillary electrophoresis (CE), λ_D/h is not critical since the Debye length is in the range of few nanometers and the channel height is significantly large, thus λ_D/h value is negligible. Even in channels in micro size to more than 100 nm sizes, λ_D/h values are much smaller. In the case, the channel

heights are in the same order as the Debye length λ_D/h values are closer 1, thus double layer overlapping is noted. (Figure 1.4) Numerous studies exist in literature where they have investigated the affects of double layer overlapping in nanoscale phenomena.[94-95]

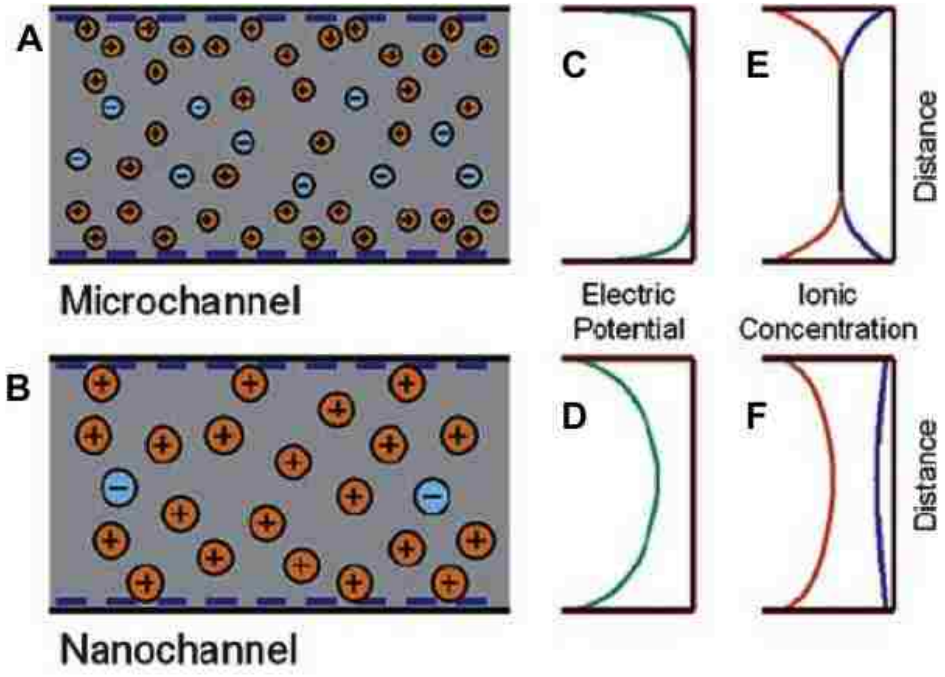

Figure 1.4 Surface charge effects in microchannels and nanochannels. (A) In a microchannel, the Debye length is typically much smaller than the channel dimensions and most of the solution in the channel is neutral. (B) In a nanochannel, the solution is charged when the Debye length is larger than the channel dimensions. (C) The electric potential in the microchannel decays rapidly to its bulk value in a distance of the order of the Debye length. (D) The electric potential even at the center of the nanochannel is influenced by the surface charge and is not equal to the bulk potential. (E) The concentration of cations (orange) and anions (blue) in the microchannel is equal to the bulk concentration. (F) In a nanochannel, the counterion concentration (orange) is much higher than the co-ion concentration (blue) (Reproduced from Napoli *et al. Lab Chip*, 2010)

1.2.3 Zeta Potential and Surface Charge

Zeta potential, ζ is another crucial parameter when considering the electrophoresis in nanoscale. Typically, ζ is defined as the potential at the shear plane (Figure 1.3) when moving from the channel surface. ζ is not directly measure most of the situation though it depends on

many factors such as pH of the solution, temperature, counterion valency and size of the counterions.[86] The relation is given below,

$$Sinh\left(\frac{-e\zeta}{2k_BT}\right) = q''\frac{\lambda_D e}{2\varepsilon k_BT} \quad (1.5)$$

where k_B, Boltzmann constant, T, temperature of the electrolyte, λ_D, Debye length and e, elementary charge.[96]

1.3 Single Entities in Nanochannels

The parameters dominated in nano geometries are investigated by behavior of model molecules in nano confinement. It is important to identify the unique properties of the model molecules to use in nanochannels devices produced by top-down approach or bottom-up approach to understand the nanoscale phenomena.[97] There are several molecules that can be explored in this case. Nanoparticles, DNA molecules (double stranded or single stranded), proteins, peptides (short and relatively- long) are some of the single molecules that can be used as models. Here we discuss the properties of the most important model molecules that have been studied extensively in literature.

1.3.1 Nanoparticles

Particles in nanometer size with a charge have gained the attention to use as a model for rigid single molecular systems in a nano-confinement. Polystyrene beads, metal nanoparticles, quantum dots are some of the particle of interest. Different capping agents will infuse a charge on the nanoparticles surface. The charges particle can be driven electrokinetically through a nanochannel. For example polystyrene nano bead surface can be functionalize with carboxylic group which produce a negative charge surface; silver nanoparticles can be capped with citrate group or PVP group to produce negative or positive charge on the surface. Single molecular nanoparticles are also used as optical biosensors called SMNOBS are used in biological

applications. Xu group has studied extensively about using silver nanoparticles about the usability to image single cell molecule cell imaging.[98-102]

1.3.2 DNA

DNA molecules are the most studied single molecules in nanochannels. The following section will discuss the basic biological and physical characteristics of the dsDNA.

1.3.2.1 Structure of DNA

Deoxyribonucleic acid, which is called DNA in its shorten form is the unique molecule that carries most of the biological information from any species root to the next generation. Even though there were preliminary studies occurred in 18th century, the reveal of DNA structure by James Watson and Francis Crick in 1953 was the revolutionary discovery.[103] DNA is composed of subunits called nucleotides containing a nitrogen base, phosphate groups (1 to 3 units), and a sugar group (2-deoxy ribose). Nucleotide bases are of 4 types named adenine (A), thymine (T), guanine (G) and cytosine (C). DNA has a double helical structure composed with these nucleotides repeating to generate unique order called genetic code. Figure 1.5 illustrates that the distance between two nucleotides are 0.34 nm and a diameter around 2 nm.

Reisner and coworkers extensive studies about DNA confinement, dynamics and conformational characteristics inside a nanochannel have guided researchers to fabricate nanochannels with proper geometry.[104-106] When a DNA molecule stretched to its full length in double helical structure, the length it occupies is called the contour length, L_c, of the DNA. Persistence length, L_p, can be defined as the mean square radius of DNA molecule that it becomes rigid.[107-109] If a DNA molecule confines in a space less than L_p, it becomes rigid while at other environments it acts as a flexible molecule. The effective width (w_{eff}) and wall-DNA depletion width (δ) are two other important parameters.[106] (see Figure 1.6)

Manning *et.al.*[109] reported a persistence length of ~50 nm and a width of 2 nm of dsDNA in 0.1 M aqueous NaCl solution. DNA has negative charges along its backbone and it is in a coiled conformation when it is in bulk solution. Thus, it acts as a self-avoidance polymer.

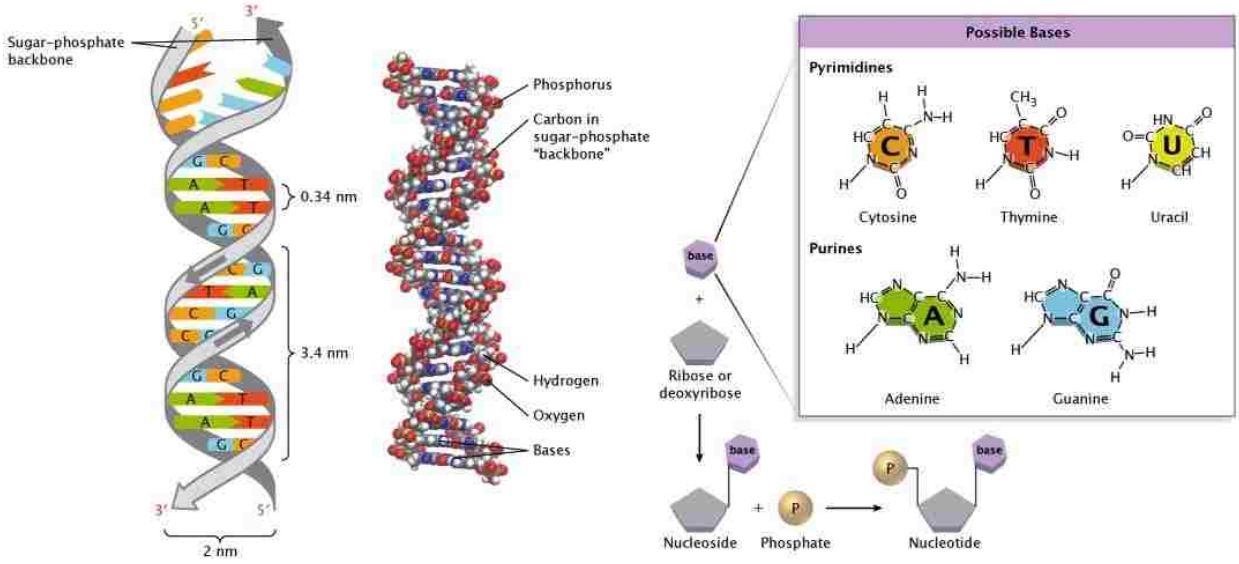

Figure 1.5 The 3-dimensional double helix structure of DNA, correctly elucidated by James Watson and Francis Crick. Complementary bases are held together as a pair by hydrogen bonds. A single nucleotide is made up of three components: a nitrogen-containing base, a five-carbon sugar, and a phosphate group. The nitrogenous base is either a purine or a pyrimidine. The five-carbon sugar is either a ribose (in RNA) or a deoxyribose (in DNA) molecule.[110] (Reproduced from Pray L. *Nature Education* 2008)

In 1953, Flory[111] first studied the self-avoidance of polymers followed by Schaefer *et al.*[112] studies from about the semi-flexible case. The rms radius of gyration, R_g, is represented as,

$$R_g = \left(L_p w_{eff}\right)^{1/5} {L_c}^{3/5} \tag{1.6}$$

The above equation was derived by Flory-Pincus for a self-avoiding polymer.[113] For ideal case if it is a non-self-avoiding polymer R_g is given by,

$$R_g \approx \left(L_p L_c\right)^{1/2} \tag{1.7}$$

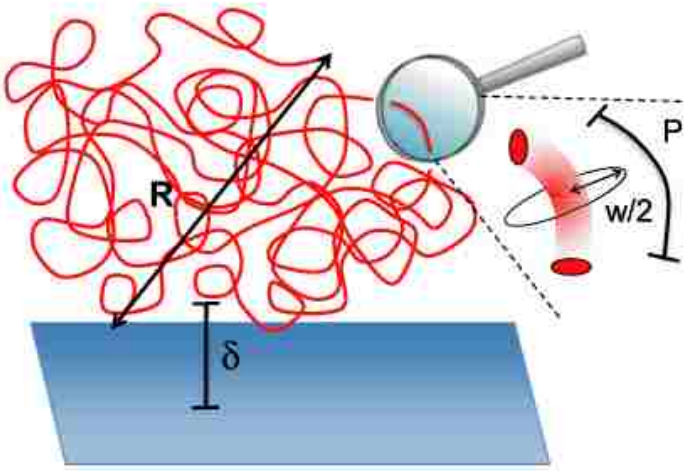

Figure 1.6 Cartoon defining the end-to-end length (R), persistence length (P), effective width (w) and wall–DNA depletion width (δ) (Reproduced from Reisner *et. al. Rep. Prog. Phys.* 2012)

1.3.2.2 Confinement of DNA in Nanochannels

The behavior of DNA inside nanochannels has led to fascinating studies about DNA in nano-confined environments. Studies concerning the stretching of DNA have been reported from as early in the beginning of 20th century. Its nature of stretching to its full contour length when it is confined in an environment has led to crucial studies in the medical field such as identifying genomic specific information. Confining DNA in nanochannel will lead it to stretch to a considerable fraction of its full contour length.[105] Reisner *et. al.*[105] reported that labeling the DNA backbone with a fluorescent dye such as YOYO-1 would increase up to 20% in contour and persistent lengths.

There are different regions in terms of nanochannel size where DNA will take its unique form (see Figure 1.7). When DNA is in a confined space much larger than its R_g, it will be in a coiled state and the structure can take different configurations. For larger volume of space there is less interaction with the channel walls thus mostly it resides in its coiled form as a one whole blob called "Pincus blob".[111]

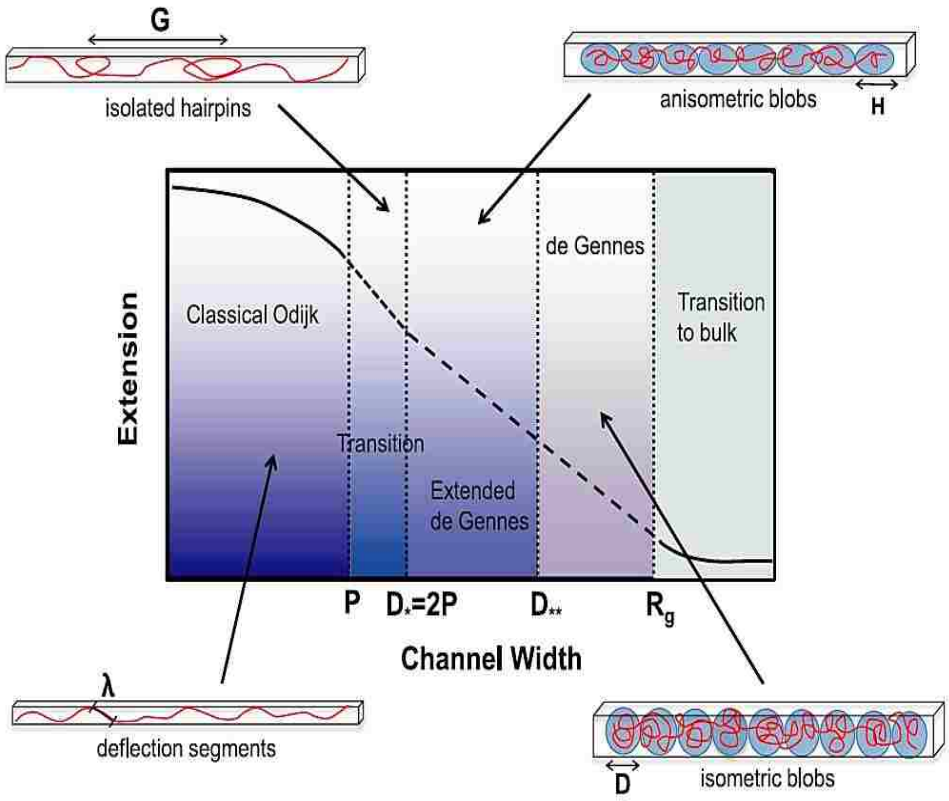

Figure 1.7 An overview of the physical regimes in nanochannel confinement. In the de Gennes regime, the conformation consists of a string of isometric Flory blobs. At D = D**, there is a transition to the extended de Gennes regime, characterized by elongated blobs that are at the cross-over between ideal and Flory behavior. At D = D*= 2P, the polymer enters a 'transition' regime, characterized by isolated hairpin backbends with a global persistence length G. ForD < P, hairpins are frozen out and the polymer can only store contour through a series of successive deflections with the wall, characterized by the deflection length λ (the 'classical Odijk' regime). (Reproduced from Reisner *et. al. Rep. Prog. Phys.* 2012)

In a confined nanochannel where the dimensions are larger than that of the persistence length, it represents its form in isomeric blobs where it has repulsion between each blob resulting the molecule to stretch in the nanochannel.[106] This region is called deGennes region. The smaller nanochannel dimensions up to $D = 2L_p$ is called extended deGennes similar region called anisometric blobs. The region between $L_p < D < 2\ L_p$ is the transition state where the DNA takes the form of isolated hairpin. The most significant region demonstrates as where the DNA can be

stretched in to its full contour length. Odijk regime phenomena occur when nanochannels dimensions are less than DNA's persistence length.[114-115]

The extension length of DNA, R_{ex}, can be calculated by,[104]

$$R_{ex} \cong L_c \left(\frac{w_{eff} L_p}{D_{av}^2}\right)^{1/3} \tag{1.8}$$

where $D_{av} = \sqrt{D \times h}$ and L_c is contour length and w_{eff} is the effective width (see Figure 1.8).

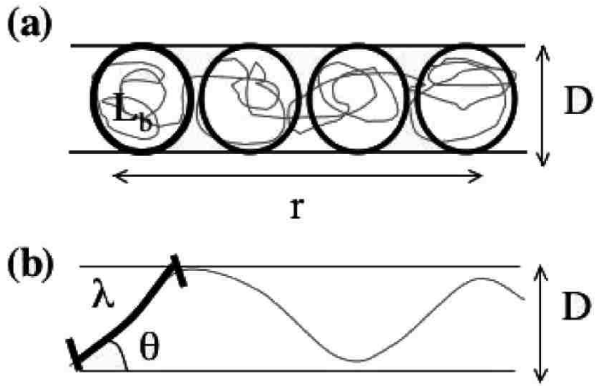

Figure 1.8 (a) A confined polymer in the de Gennes regime: D >>P. The molecule can be subdivided equally into a series of blobs with contour length Lb; the stretch arises from the mutual repulsion of the blobs. (b) A confined polymer in the Odijk regime: D <<P. (Reproduced from Reisner *et. al.* 2007)

The extension length at the Odijk regime, R_{Odijk}, can be calculated by,[106]

$$R_{Odijk} = L_c \cos\theta = L_c \left[1 - A\left(\frac{D_{av}}{L_p}\right)^{2/3}\right] \tag{1.9}$$

where $A = 0.361$. When the DNA molecule is in Odijk regime the stretching takes place as a result of confinement that will prevent looping and coiling up the DNA. At this situation, unfavorable back folding of DNA won't occur as a result from deflection by channel walls. Corresponding length is called as 'Odijk deflection length', λ_p, which can be expressed by $\lambda_p = (L_p D_{av})^{1/3}$.

1.4 Electrophoresis in Nanochannels

Nanoscale electrophoresis is a rapidly growing area over the last couple of decades. Nanochannel-based devices used for nanoscale electrophoresis can offer great flexibility in terms of shape and size with increased robustness and surface properties, which can be tuned based on the sized-related phenomena, which is not readily achievable in micro-scale. It will also enhance the ability to analyze, separate, manipulate and detect biomolecules with improved sensitivity, efficiency, and high throughput with an ease of use.

1.4.1 Nanoscale Electrophoresis Phenomena

Scaling down from micro to a dimension of less than 200 nm (at least one dimension), it introduces unique and interesting phenomena to nanoscale electrophoresis. At this length of scale there are several interesting parameters that comes in to play. Thus, conventional theories that were applicable to electrokinetic flow through microchannel such as Poisson–Boltzmann equation and Helmholtz–Smoluchowski slip velocity approach are not directly applicable to a similar situation in nanochannels.[116] Interfacial forces that lead to EDL overlap, consequences arising from high surface to volume ratio and surface roughness as well as transport properties in nanoscale are some of the phenomena that can be identified. [116-120]

Debye length or EDL is one of the mostly studied phenomena thus the most important phenomena in nano-electrophoresis. When the charges on the walls are induced by the bulk, the induced potential attracts opposite charged ions from the bulk producing high concentration of counter ions near the walls while repelling co-ions. This can be explained by the Boltzmann equation.[119]

$$c(y) = c_{bulk}.e^{(-ze\psi(y)/kT)} \tag{1.10}$$

where c is the concentration, z is the ionic charge, e is the unit charge, kT is the thermal energy, y is the coordinate perpendicular to wall and Ψ is the electrical potential compared to the bulk. (Figure 1.4) It was hypothesized even though the concentration in the middle of the channel is closer to the bulk it, there is an excess in the counter ions and lack of co-ions concentrations near the wall which is deviating from bulk concentration.[121-122] Because of this reason the EDL generates non-uniform motion of the bulk/neutral as well as non-uniform transverse electric fields.[117, 120, 123] It will result in generating Poiseuille-like flow on the nanochannels as a result analytes spend significant amount of time migrating through the EDL. At a point of time, it will generate equilibrium between the transverse electro-migration and the diffusion leading to a transverse concentration gradient inside the nanochannel.[117] Additionally, transport through the EDL becomes more selective depending on the valence of the counter ions. For example, two solutions with same ionic strength with divalent counter ions may have higher ionic concentration in nanochannel compared to that of monovalent counter ions given that there is no significant ionic adsorption to channel walls. If ionic adsorption occurs, it will immobilize some of the counter ions resulting in decrease in ζ potential which may reduce the EOF lower than the monovalent electrolyte.[123]

As a consequence of having a prevailing EDL, ion-enrichment and ion-depletion zones are possible most commonly near the intersection of microchannel and nanochannels.[117, 124] It was hypothesized that there is an increased ion flux inside the nanochannel due to amplified transport within the EDL which can lead to ion flux imbalance leaving such zones. Above phenomena is also called as concentration polarization. Usually it is observed near the inlet and outlet of the nanochannels. Polarization forces can cause anisotropic diffusivity as well as the rate it interacts with the channel walls.[117] When the ionic strength is relatively low, higher effective EDL

thickness will shield the ions from entering the nanochannel. The repelled ions will accumulate at the entrance or boundary of the EDL.

Transporting macromolecules in nanochannel leads to another interesting phenomena. These charged analytes such as DNA, proteins or nanoparticles have a surrounding electric double layer. Apart from having a double layer on the channel, having that on the molecule causing it to be more complex.

Figure 1.9 shows the spherical protein molecule with a diameter d in a nanochannel with height h. The surface potential on surface wall is different from that of the molecule. The

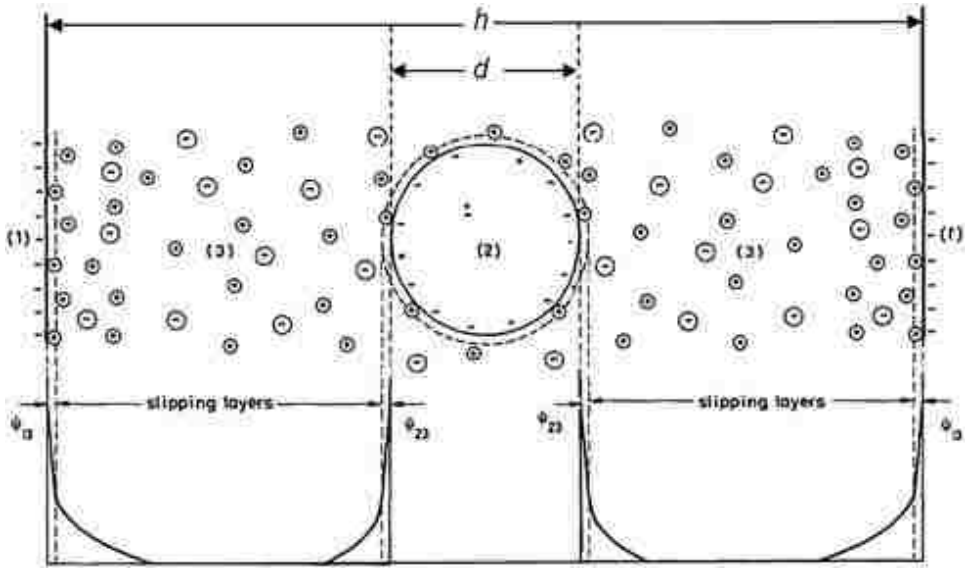

Figure 1.9 (Macro) molecular dimensions become important when on the scale of the nanofluidic confinement. The figure shows a globular protein of diameter d in a nanochannel of height h. The charge distributions are schematically indicated at the channel surface (1) and around the protein molecule (2), with their corresponding gradient in the electrostatic potential, c. The medium is indicated with subscript (3). (Reprinted from Napoli *et. al.*)

molecules surface potential depends on the bulk pH allowing it to be in protonated or deprotonated equilibrium as well as with the surface groups and it is different from the potential of the channel walls. Even though, for a DNA or protein molecule the surface charge changes

along the molecule because of the different charged surface groups for a charges particles capped with charged groups is hypothesized to be uniform.[119, 125-126]

Adsorption/ desorption of macromolecules is also plays an important role in macromolecular transport. This occurrence arises because of the interfacial forces such as electrostatic, van der Waals and hydration forces between the channel wall and the molecular surface.[119] Adsorption/desorption kinetics is dominant at shorter column lengths when Damkohler number (D_a) is small. k_{ads} is the rate constant for 1st order adsorption kinetics. D_a is given by,

$$D_a = k_{ads} h/D \tag{1.11}$$

For a 40 nm deep nanochannel the adsorption rate is 10^{-4} s, which is unusually low.[117] Also steric interaction influences the diffusion of the molecule effecting its location in the channel at a particular time and its orientation. The layer of counter ions on macromolecule can influence its mobility, steric interactions and diffusivity of the molecule inside a nanochannel mostly at high EDL situations.[117] Considering macromolecules inside a nanochannel, there are other important interfacial forces that can be identified. Forces such as van der Waals forces (including dipolar interactions) and Lewis acid-base forces including hydrogen bond force are some important forces that effect the 3D spatial arrangement and conformations of macromolecules. There is a strong repulsion force exist due to the overlap of the electron cloud of the wall and macromolecule called Born repulsion (also called as steric repulsion) which increase with the decreasing intermolecular distance, d. As Lennard-Jones model predicts this repulsion increases with d^{-12} and prevents molecules entering the nanoconfined areas.[119] For example, DNA molecule holds a folded coil configuration in the bulk solution. Usually a DNA molecules consist of a cross sectional diameter of 2 nm and 0.34 nm overall length per base pair. This gives a contour length of 340 nm for a 1 kbp DNA molecule. On contrary, the persistence length of a

DNA molecule is roughly 55 nm. To enter to a nanoconfined environment it should overcome the entropic barrier associated with it. Thus, a DNA molecule is forced to stretch in a nanochannel shorter than its persistence length, it extends linearly overcoming the steric repulsion. Though, for shorter DNAs (contour length shorter than its persistence length), because of its rod-like nature, it has to overcome additional rotational entropic barrier to enter the nano confinement.[127]

Dielectrophoresis is another noteworthy phenomena that occurs in nanoelectrophoresis. The electrophoretic force, f_{ep} on a particle under an electric field is given by,

$$f_{ep} = zFE \tag{1.12}$$

where z is the effective charge, F is Faraday's constant, and E is electric field. Electrophoresis force on a particle is a result of electrophoresis that is dependent on ratio of the charge of the particle and its hydrodynamic radius.[128] In contrast, dielectrophoresis (DEP) is the electric field gradient present on a polarizable particle and the dielectrophoresis force, f_{ep}, is given by,

$$f_{ep} = 2\pi\varepsilon_m r^3 K\nabla E^2 \tag{1.13}$$

where ε_m is the permittivity of the medium, r is the particle radius, E is the field strength applied, K is the Clausius-Mosotti factor. K is dependent on the conductivity and the permittivity of the medium and particle as well as frequency of applied electric field.[129] At the interface of microchannel and nanochannel, when the particle is in a medium less polarize than itself, the particle feels the dielectrophoretic force towards the high electric field gradient called positive DEP and when the medium is more polarizable than the particle it is repelled from high field gradients which is called negative DEP.[130] Kovarik and Jacobson[130] have shown that the DNA and proteins tends to trap at the entrance as a cause of dielectrophoretic trapping (evident from previous literature) by a COMSOL simulation model (Figure 1.10) representing a field drop

across a nanopore. At the tip it is 130 nm deep and the base is 1 μm, which has field drop of 4 V providing a maximum field strength of 1.3×10^4 V/cm and a maximum field gradient squared of 4.2×10^{13} V^2/cm^3.[130] Electrophoretic and dielectrophoretic forces can be tuned by optimizing the amplitude and frequency of the applied electric field thus can enhance the selectivity of the molecules entering the nanochannel.[119]

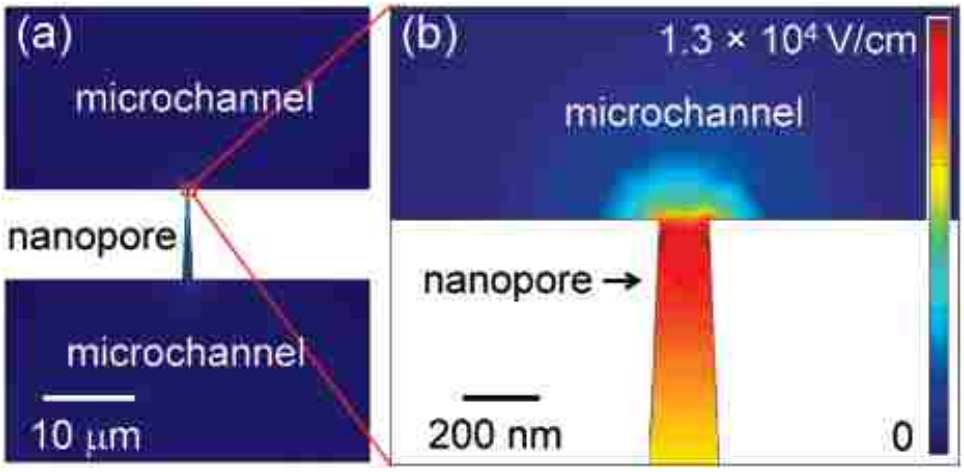

Figure 1.10 (a) COMSOL simulation of the electric field distribution at a nanopore. The nanopore was 130 nm in diameter at the tip, 1 μm in diameter at the base, and 10 μm long. A 20 μm thick layer of buffer was modeled on both sides of the pore, and the applied potential was 4 V. (b) Enlarged view of the nanopore tip where the electric field strength and the gradient of the field squared have their maximum values of 1.3 × 104 V/cm and 4.2 × 1013 V2/cm3, respectively. (Reprinted from Kovarik *et. al. Anal. Chem.* 2008)

Even though high surface-to-volume (S/V) ratio in nano-electrophoresis has its own advantages, there are several drawbacks that can be identified. Downscaling the dimensions affects the surface properties of the walls. When the nanochannel is filling because of the capillary action, the proton in the surface groups will release proton reducing the pH of the solvent front.[119, 131] As Squires *et al* points out there is a the EOF magnitude is possibly changing because of this protonation equilibrium occurs in nanochannel.[132] Also, high S/V ratio affects the adsorption/ desorption kinetics since diffusion transport becomes efficient as D_a decreases plus there is a effective mass lost inside the nanochannels.[117]

1.4.2 Efforts in Nanochannel Electrophoresis

Separations performed in nano-geometries have gained the interest especially in the past decade. Studies about electrokinetic transport of charged analytes in nanofluidic channels has revealed interesting information about separation of charged analytes in nanochannels. Preliminary efforts in nano confined devices laid the platform to investigate the unique behavior of single molecules separation studies in nanochannels.

Hibara and co-workers[133] investigated the time-resolved fluorescence measurements of rhodamine 6G (R6G), sulforhodamine 101 (SR101) and rhodamine B (RB) in 330 nm, 850 nm and 250 μm channels. They have found the decay of R6G and SR101 is higher in nanochannels while it was slower for RB. Lower dielectric constants and higher viscosities were forecasted in nano-sized channels. Plecis *et al.*[134] discussed about the exclusion-enrichment effect (EEE) which explains the affect of counterion enrichment and co-ion exclusion using a dianion, acation and a neutral probe using fluorescein salt, rhodamine 6G and rhodamine B in 50 nm nanoslit fabricated in Pyrex devices.

Garcia *et. al.*[135] studied the separation of two color dyes; Alexa 488 (green) and rhodamine B (red) in a nanochannel arrays (sizes ranging from 35 nm 200 nm) under electric field strengths of 0 to 2000 Vm^{-1} (Figure 1.11). They observed the negatively charged dye (Alexa 488) had a higher mobility towards the negative electrode compared to neutral dye (rhodamine B). The observation was controversial to what is expected in electrokinetic theory, which predicts a lower mobility of negative species than the neutral caused by the electrophoresis towards the positive electrode. At lower channel sizes possible overlap of the electric double layer affects the electroosmotic flow profile deviating from its expected “plug-like” profile.

Possible mechanism for the achieved separation was identified due to two possibilities. First, repelling of the negatively charged dyes from the negatively charged walls forcing it to travel closer to the center of the nanochannel where high EOF is observed. Second, the higher relative adsorption of the neutral dyes to the channel walls can cause slower mobilities of the neutral dyes. Pennathur and Santiago[95] compared the separation of two charged species in micro and

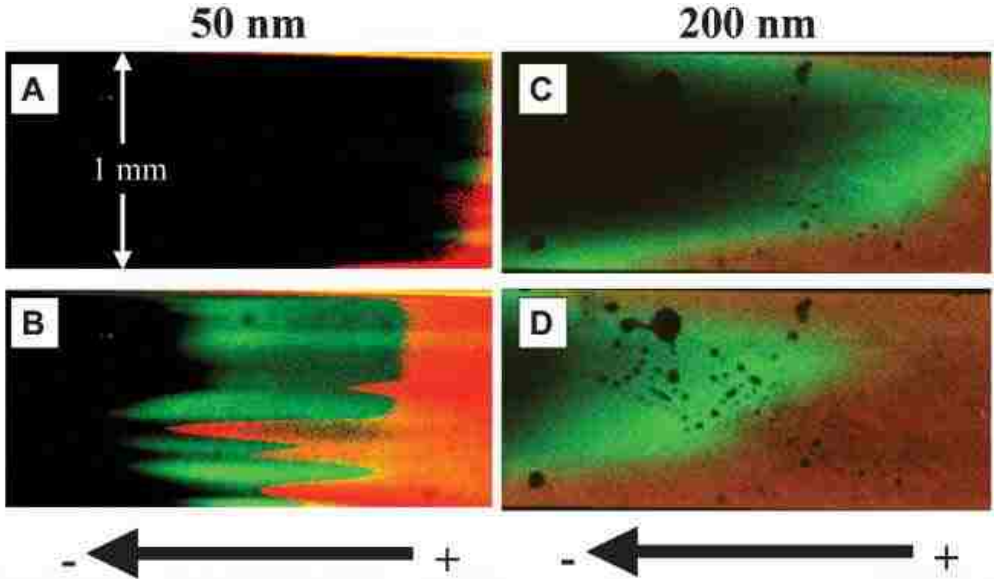

Figure 1.11 Sample two-color fluorescence micrographs (green = Alexa 488, red = rhodamine B) showing separation of dyes in nanochannel arrays containing channels ~50 nm wide at (A) time t = 0 and (B) t = 30 s, and ~200 nm wide channels at (C) time t = 0 and (D) t = 25.2 s. (Reprinted from Gracia *et. al. Lab Chip* 2005)

nano geometries using 2-μm and 40 nm deep channels. They adjusted the background buffer electrolyte concentration such that both micro and nanochannels have the same thin EDL condition generating same electrophoretic velocities for the same species. The separation of fluorescein (z_s = -2) and bodipy (z_s = -1) revealed that the separation distance between two species is lower in nanochannels (Figure 1.12) as a result of transverse electromigration phenomenon.

This phenomena was also expected from their theoretical predictions.[94] More negative dye with valence z_s = -2, was electromigrated away from negative charged channel walls

experiencing higher velocities compare to less negative dye with valence z_s = -1. Also, when the λ_D/h was increased, there was a decrease in area-averaged velocity. Under non-overlapping EDL conditions, the electrophoretic transport of species depends on the ion valency and mobility, ζ and λ_D as a result of transverse electromigration in the nanochannels as well as the stream-wise mobility.

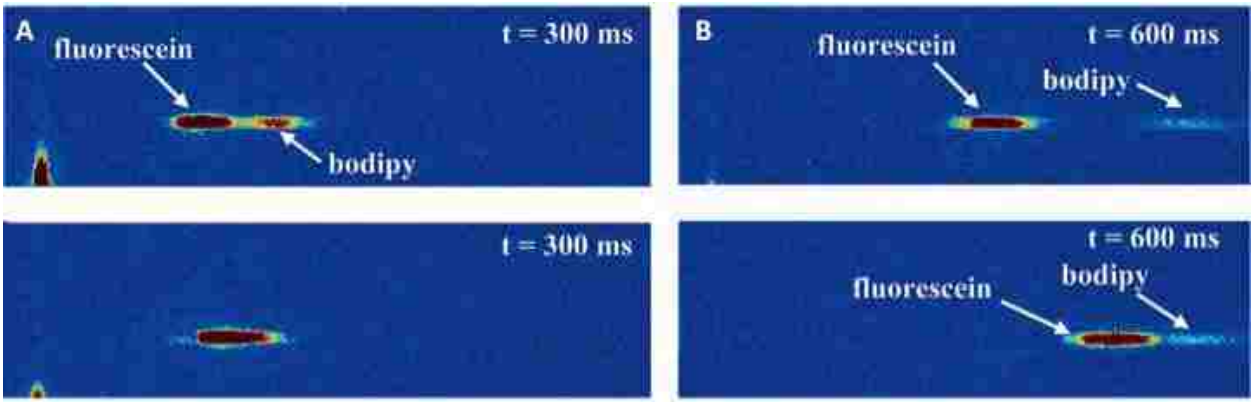

Figure 1.12 Sequence of epifluorescence images showing separations of 20 μM carboxyl fluorescein (z_s = - 2) and 40 μM bodipy (z_s = - 1) in devices with channel depths of 40 nm and 2 μM. The conditions result in an area-averaged liquid velocity of 25 μm/s. The bottom image of each pair is for a channel 1 μm wide and 40 nm deep filled with 1.5 mM sodium tetraborate buffer, resulting in an area-averaged liquid velocity of 24 μm/s. Scalar images are taken (A) t = 300 ms, and (B) t = 600 ms. In (B), the separation distance between the two analytes is lower for the nanochannel. This observation qualitatively supports the theory that transverse electromigration plays a key role in determining the net streamwise transport of a charged solute (Reprinted from Pennathur *et. al. Anal. Chem.* 2005)

1.4.3 Single Particle Electrophoresis in Nano-Geometries

To understand the nanoelectrophoresis phenomena it is crucial to design a simpler system before investigating the real biomolecules because its complex nature of interaction with walls and system. Particles in nanometer sizes that carry a charge can be used as model molecules to investigate the basic interaction behaviors and identify certain patterns while traveling through the nano domains. Studies of Xuan and coworkers about electrokinetic transport of charged particles in micro domain helped to build the nanoelectrophoresis phenomena.[136-138] They studied

the wall effects when polystyrene beads translocate through a converging-diverging microchannel. Study reveals that large particles are retarded near the channel walls when compared to the small particles as a effect of viscous forces. Supporting the above work, a mathematical model was derived by Qian *et al.*[139] explaining the spatial dependency of a particle electrophoresing through a converging-diverging microchannel to enhance the separation.

Several studies about particle behavior in nano-domains exist in the literature. Particle studies about separation in nano-domains,[140] diffusion of single particles,[140-143] single particle tracking[142, 144] provides guidance understand the nanoscale phenomena and proceed with single molecular nanoelectrophoresis. Furthermore, theoretical studies contributed enormously to understand the underlying theory and explain some unique phenomena occur in particle electrophoresis in nano-domain.[145-147] Kaji *et. al.*[141] tracked the trajectories of single nanoparticles with 50 nm diameters using single particle tracking methodology in a nanopillar chip. Authors managed to measure the simple diffusion, directed diffusion and other diffusions. It was concluded that nanopillars are able to prevent the hydrodynamic flow from nanochannels and it is lower in that region results in low diffusion of the particles. Hoang and coworkers studied the mobility of 25 nm single quantum dot in a 20 μm wide 150 nm deep nanoslits.[142] Authors realized that diffusion coefficients revealed using single particle imaging experiments are three times smaller than the calculated values using classical Brownian motion theory and they claim those results may be due to double layer overlap inside the nanochannels.

Pennathur and coworkers studied particle electrophoresis in nano-domaion using carboxylated polystyrene beads. Napoli *et al.*[140] reported the electrophoresis and separation of 50 nm and 100 nm polystyrene particles in 20 μm, 1 μm and 250 nm channels. The effects of pH change, ionic strength of the background electrolyte and the channel height. Authors suggest that

there are two contrary factors affecting a spherical particle electrophoresing through a nanochannel. They are viscous retardation effect and increased electric field near channel walls. When the boundary of particle and wall decreases as in the case of nanochannels, the velocity of the particles expected to decrease. This factor is limited until the electric field effects are dominant inside the channel. At high buffer concentrations particles are closer to the channel walls, which increase the particle velocity but at lower concentrations it leads to repelling particle away from the wall to travel closer to the center of the channel. It will increase the viscous drag effect that is in the opposite direction thus decreasing its velocity. They observed an increase of mobility in nanochannel as well as at low ionic strength of the buffer. Authors hypothesize that the increase concentration of the particles (negative charged) at the center of the channel result in increase concentration thus decrease of viscous retardation effects. As authors suggest, variation of pH may lead to opposing behavior in particle mobility when reducing the size of nanochannel from micro to nano. They suggest the pH and the ionic concentration of the background electrolyte should be carefully optimized and tuned to increase the separation efficiency and performance since it may have the ability to downgrade it. Also the diffusivity of the particle band at different channel positions has been investigated to calculate the range of zeta potential of the particles. Following up the work from Napoli, Wynne *et al.*[144] reported characterization of carboxylate polystyrene beads of size 42 nm in 100 nm nanochannels frustrated total internal reflection fluorescence microscopy. They found out that particle velocities are decreased when translocating through the nanochannels as a result of increase viscous drag effects near the confined nanochannels. Authors also observed that the increase buffer ionic concentration did not decrease the particle velocity as a result of electric double layer overlap and shear induced rotation of the particles. Additionally, they noted that the

physical phenomena such as entropic particle exclusion and/or concentration polarization prevented higher number of particles entering the nanochannels even for thin EDL systems.

1.4.4 Single Molecule Electrophoresis in Nano-Geometries

Nanochannel electrophoresis has been used for numerous vital research areas such as separation,[20, 148-150] manipulation,[22, 151-152] and detection[22-23] of single molecules. Robustness, surface modification ability, flexibility in controlling the shape and size boosts the usability and applications of nanochannel based devices. Being at the same size-scale (nm scale), nanochannels and biomolecules (such as DNA and proteins) lead to intriguing observations. This section will mainly focus on nanochannel-based studies carried out for single molecular electrophoresis using nanochannels.

To investigate the electrophoretic behavior of a specific single molecule (biomolecule/ biopolymer) inside the nanochannel requires it to be charged and flexible to change its configuration to fit the size and shape of nano confinement. Most biomolecules has a net change enabling the opportunities to analyze by electrophoresis. Considering the previous reports DNA has been studied extensively in nano-confinement due to its charged state (negative), size distributions, ability to stretch linearly in different stretching percentages (depending on the size of nano confinement), ability to confine in nano-geometries and confirmation stability.

Han and Craigheads studies reveal the possibility of separating different size DNA molecules (~40 kbps to ~160 kbps) using entropic trapping in 75-100 nm thin regions.[20, 151] The thin nano regions were connections for deeper microchannels. They claimed that the observed different mobilities for T2 DNA (164 kbps) and T7 DNA (37.9 kbps) are due to different energy barriers to escape from the entropy trap (Figure 1.13). Larger radius of gyration of longer DNA molecules result in higher probability to escape from the entropic trap due to high surface area

interactions. They witnessed higher at higher field strengths the separation was not possible due to reduce of the entropic trapping effect. The resolution (R_s) of the separation was defined as $R_s = (\Delta V/V)\sqrt{(N/16)}$ where $(\Delta V/V)$ gives the fractional band velocity.

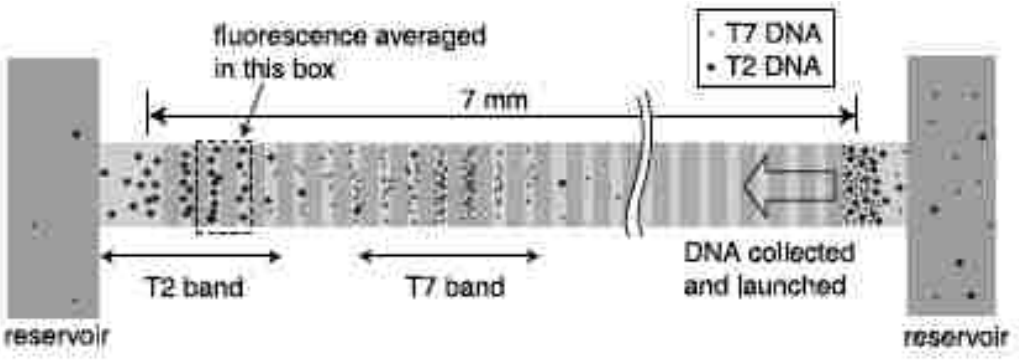

Figure 1.13 Schematic diagram for launching and data analysis. The arrival of DNA molecules was monitored at the other end of the channel. A rectangular region of interest was defined, and the fluorescence signal from this area was summed. (Reprinted from Han *et. al. Science* 2000)

Separation resolution increases at lower field where $(\Delta V/V)$ increases thus increasing the entropic trapping effect. Though, it may lead to band broadening (N larger) at these conditions. They further reported the separation of 5-200 kbps of DNA within 30 min concluding that resolution of the separation depends on the applied electric when using entropic traps and relaxation of DNA cannot be achieved under high field strengths.[153]

Following up the work from Han and Craighead, Pennathur and coworker reported separation of oligo-nucleotides using nanometer-sized channels.[150] The separation of a mixture of fluorescently labeled dsDNA oligonucleotides in the sizes of 10, 25, 50 and 100 bps, fluorescein, and fluorescein-12-UTP (UTP) was performed in fused silica nanoslits of depths 40, 100 and 1560 nm. Separation was performed in 1- 100 mM sodium borate buffer and the best separation was achieves in 10 mM buffer concentration in 100 nm channels (Figure 1.14).

Separation resolutions were acceptable in concentrations less than 10 mM too. More dominant EOF mobility overcomes the electrophoretic mobilities of the oligos resulting in net

travel towards the cathode. Authors observed the elution order was dependent upon the length of the oligo (l) and the EDL thickness (λ_D). λ_D/h and l/h parameters were varied to explore the optimal conditions for the separation. At 10 mM ($\lambda_D/h \approx 3\%$) the elution order was Fluorescein (FL), UTP, and 10, 25, 50 and 100 bp oligonucleotides as a result of their mobility order; $\mu_{FL} < \mu_{UTP} < \mu_{10bp} < \mu_{25bp} < \mu_{50bp} < \mu_{100bp}$. Authors observed the same order for 5 mM 5 mM ($\lambda_D/h \approx 4\%$) case too. Even though the elution order was the same, a reduction of resolution was observed for 20 mM and 100 mM case. However, it is expected that the resolution should increase at higher buffer strengths due to decrease of EOF hence increase of resident time. Authors try to explain the observation as the increase of the ionic density at high ionic concentrations may lead to lower electrophoretic mobilities.

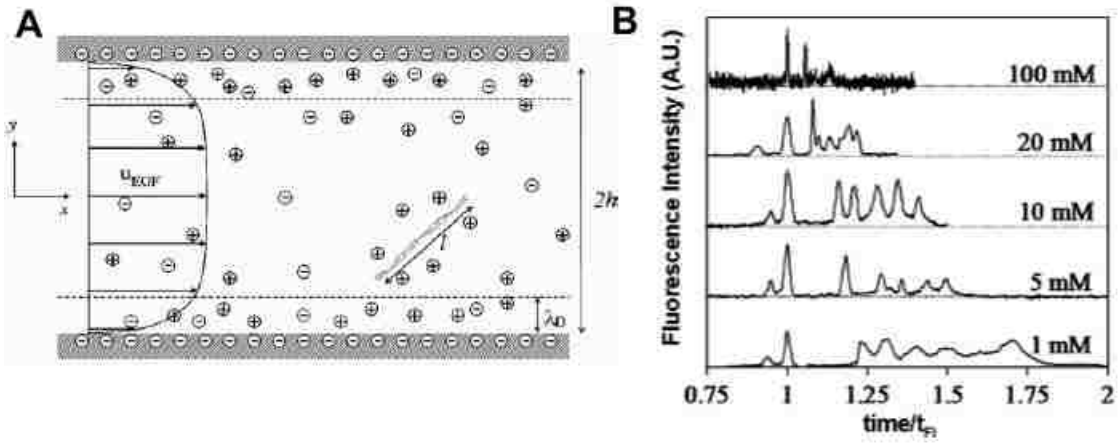

Figure 1.14 (A) Schematic of nanochannel electrophoresis of rod-like oligonucleotides. Important length scales are the depth of the channel ($2h$), the length of the dsDNA (l), and the Debye length (λ_D). (B) Measured electropherograms for electrokinetic separations of fluorescein, UTP, and a 10-100 bp oligonucleotide ladder in a 100 nm deep channel. Electropherograms are shown for separations in five different concentrations of sodium borate: 100 (top), 20, 10, 5, and 1 mM (bottom). t_{FI} is the residence time of fluorescein in each experiment (Reproduced from Pennathur *et al. Anal. Chem.* 2007)

At lower ionic concentrations (such as 1 mM) ion density and EDL coupling, two opposing factors contest each other to regulate the axial migration rate. Authors propose a substantial coupling between electromigration, bulk EOF in the both axil and transvers paths and steric-wall

interactions. Kaji *et al.*[148] developed a method to separate long DNA molecues based on their size using a quartz nano-pillar chip. Authors were able to separate DNA fragments of 1-38 kbps and large DNA fragments from λ DNA (48.5 kbps) and T4 DNA (168.5 kbps). The separation was achieved in 380 μm long nanopillar channel with a separation efficiency of 1000-3000 (0.7×10^6 - 2.1×10^6 plates/m) under 10 s.

Fu, Mao and Han extended the work of long DNA separation using entropic traps to investigate the possibility of separating SDS protein. Separation was carried out for sodium dodecyl sulfate (SDS) protein and dsDNA by size-fraction (weight fraction) using entropic trap and nanofilter arrays with gap size of 40-180 nm.[149] They were able to separate SDS protein under 90 V/cm field strength achieving 3×10^5 plates/m in 4 min while the separation for dsDNA was achieved in 10 min under 70 V/m. Authors suggest that electric potential energy of the dsDNA molecules and Ogston sieving induces entropic energy barrier compete with each other for separation. Schoch *et. al.*[154] investigated the diffusion characteristic of proteins in a nanochannel exploring an interesting approach to separate them. Adjusting the pH of the solution the charge of the protein can be controlled to be either negative or positive (pH < pI – positive net charge, pH > pI – negative net charge) which is called the Donnan effect. Using this approach they were managed to separate three lectin proteins having same molecular weight but different pI values in a 50 nm high nanochannel varying the pH from 6 to 11. Electrostatic interactions become significant with increasing surface charges in the nanochannel thus providing a mechanism for separation based on different diffusion coefficient values.

Separation of catecholamines samples from liposomes and separation of cytoplasmic samples from intact mammalian cell has been achieved in 770 nm inner diameter sized capillaries.[21] Riehn *et al.*[155] conducted enzyme studies in a nanochannel of 100-200 nm environment using

DNA and endonuclease enzyme facilitated by electrophoresis and diffusion of Mg^{2+} and EDTA. Mennard and Ramsey reported electrophoresis of λ-page DNA in 25 nm, 50 nm and 100 nm glass based nanochannels.[156] Uba *et. al*.[157] reported the electrophoresis of λ- DNA in 100 nm ×100 nm polymer nanochannels under 2.0x and 0.5x TBE buffer concentrations.

1.5 Experimental Methods for Studying Transport in Nanochannels

Nanochannels for analysis of DNA has been performed in a wide variety of applications as discussed in the earlier section. Nanochannels with smaller dimensions are able to linearize DNA molecules to extract the structural information. There are two main detection modalities that can be identified, optical modality and electrical modality. However, each of them has their own advantages and disadvantages.

In an optical detection modality, DNA backbone is stained with an intercalating dye fluorescent dye and it is detected with high-resolution microscopy system with higher magnification. Optical detection will allow the researcher to visualize the undergoing physical and chemical phenomena inside the nanochannel thus have a better perceptive about the experiment. The main two problems with staining DNA with fluorescent dye is that photobleaching and photoniking. After staining once it is exposed to the excitation light source it gradually decreases its intensity over time. This is called photo bleaching of the dye, which may impact experiments that requires long period of times. Also, exposing to an excitation source may lead photonic DNA in to small fragments. Electrical modality is capable of detecting unstained DNA as well as stained DNA by electric readouts. Electrical signal can be made when a DNA molecule enters the nanochannel by longitudinally or transversely using planar pair of electrodes.

1.5.1 Single-Molecule Imaging in Nanochannels

Optical imaging studies of single molecules in nanochannels can be classified in to two main categories as imaging by confinement and tracking of single molecules. Both these study areas are vastly investigated due to the ability to extract immense amount of information about single molecules. Conventional microscopy techniques as well as most recently, super resolution microscopy techniques are two approaches to study single molecules with different optical resolutions. DNA studies were more popular in nano electrophoresis because of their linearity inside nanochannel, charged, rigid structure that can be easily stained with intercalating dyes thus easy to drive and detect inside a nanochannel using a microscope. Generally, the most popular intercalating dye in use to stain dsDNA is YOYO-1. In combination with 2% - 4% of β-mercaptoethanol or Trolox to the DNA-dye complex solution, photobleaching can be minimized.[151, 158] Kim *et. al.*[159] reported that even though, anti-photobleaching agents prevent photobleaching; it has a negative impact in increasing the ionic concentration of the buffer due to proton loss in thiol groups at a pK_a of 9.6.[160] Also, it has been reported that there is an increase of the extension length of dsDNA once it is stained by an intercalating dye. For dsDNA stained with YOYO-1 dye, ~20% increase of extension in contour and persistence length was observed.[105]

Tracking single molecules with a fluorescence signature in nanochannels has been used to obtain information about separation, adsorption-desorption with wall interaction and transport dynamics, which was discussed in previous section in detail. This section will provide a summary of the different detection methods that has been incorporate to fulfill the studies. There are reports about DNA electrophoresis in late 70's.[161] Craighead group studied the separation of DNA based on size in entropic traps using optical microscopy.[20, 44, 151-153, 162] Santiago group

investigated the possibility of separating oligos based on there size in nanochannels using 60x objective and 488 laser illumination.[95, 150]

Confining DNA in nanochannel and stretching them to a length close to its full contour length was studies extensively by Reisner *et. al.*[105] TOTO-1 was used to stain DNA 1:10 dye to bp ratio, which increase L_c from 13%. In 0.5X TBE buffer, λ DNA (48.5 kbps, L_c =16.5 μm) extension length L_{dye} was 18.6 μm, for T2 DNA (164 kbps, L_c =55.8 μm) the extension length L_{dye} was 63 μm. Genomic mapping studies by optical detection were recently popular due to their ability in acquiring genetic spatial resolutions as well as epigenitc information. In 2010, Das *et. al.*[163] reported the possibility of identifying specific sequence regions via a nick-labeling scheme in dsDNA by stretching them in a nanochannel array device. (see Figure 1.15) They were able to create 3 Gbp human genomes reducing to ~50 Mbp of target sequence. For imaging 100x oil objective with 1.4 NA was used. DNA was stained with YOYO- and excited by 488 nm laser, Cy3 and Alexa 546 were excited by 543 nm laser and Alexa 647 was excited by 633 nm helium neon laser. By considering the frequency of occurrence in specific genomic sequence regions, they were able to acquire an interesting picture of the whole genome.

Lam and coworkers were able to identify specific sequence motifs in dsDNA molecules stretched in silicon nanochannel device array.[164] Nanochannel array devices are of 2 sizes, 120 nm × 120 nm and 45 nm × 45 nm. To prevent clogging at the entrance and to help uncoil DNA before entering in to the nanochannels, there is a gradient region with pillars. It makes an energetically favorable situation for DNA to enter the nanochannels. They were able to analyze 95 bacterial artificial chromosomes (BAC) clones using these devices, which consist in 4.7 Mb human major histocompatibility complex regions. They were able to 22 halotype differences,

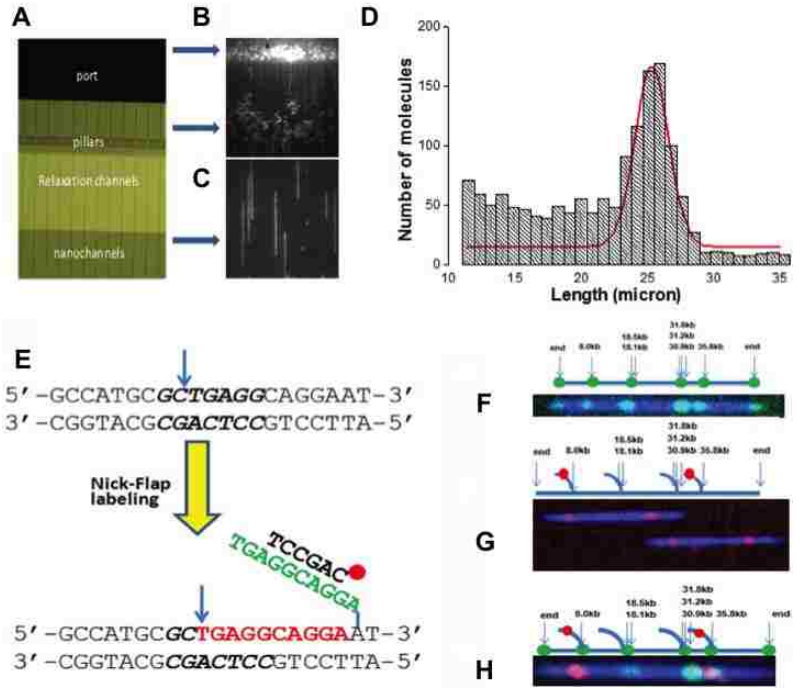

Figure 1.15 Image of the nano-channel array in a chip that has been used for the linearization of DNA. (A) Different regions of a nano-channel device. (B) Image showing the translocation of DNA through different areas (microstructure and nano-channel) of the chip. (C) Image of the relaxed and linearized DNA molecules inside nano-channel array. (D) Size distribution of BAC 3F5 DNA molecules inside nano-channel array; Schematic drawing of recognition sequence of nicking endonuclease Nb.BbvCI and the Nick–Flap labeling scheme. (E) After nicking (blue arrow) at the recognition sequence (GCTGAGG, Nb.BbvCI), fluorescent or non-labeled nucleotides (red) are incorporated using a polymerase with displacement activity but lacking 5'-> 3' exonulcease activity. As a result, the native sequences are displaced (green) downstream. A ssDNA structure (flap) is generated and can be interrogated with various chemistry including hybridization probes. For example, an oligo probe (black) can hybridize to the flap. (F) Nick-labeling of λ-DNA molecules. The top graph shows the distribution of the seven nick endonuclease Nb.BbvCI recognition sites of λ-DNA. The solid blue line represents the backbone of the λ-DNA, the arrow indicates the positions of the predicted Nb.BbvCI sites and the green dots represent the potential tagging sites. The bottom graph shows a single labeled λ-DNA molecule. Backbone was labeled with YOYO-1 (blue) and nicking sites were labeled with Alexa-546 dUTP nucleotides and four internal labels were observed and matched well with predicted sites. (G) Flap-labeling. Two labeled flap sites are shown in red dots on a solid line peeling off the DNA backbone in top graph. The bottom graph shows two λ-DNA molecules, whose flap sites at 8 and 35.5 kb were hybridized and labeled with probes Cy3-AAGGTCTTGAGCAGGCCGTT-Cy3 and Cy3-TCCAACTATATAATTT-GACCAGAGAACAAG-Cy3, respectively. In this case the nicking sites were not labeled. (H) Nick–flap labeling. All nicking sites of λ-DNA molecules were labeled with Alexa 647 dUTP (green) and two flap sequences at nicking sites of 8 kb and 35.5 kb were selectively hybridized and labeled with green probes Cy3-AAGGTCTTGA-GCAGGCCGTT-Cy3 and Cy3-TCCAACTATATAA-TTTGACCAG AGAACAAG-Cy3, respectively (Reporduced from Das *et. al. Nucl. Acid Res.* 2010)

with 9 kb average between the labels. Figure 1.16 shows a representation of the genomic mapping of 95 BACs.

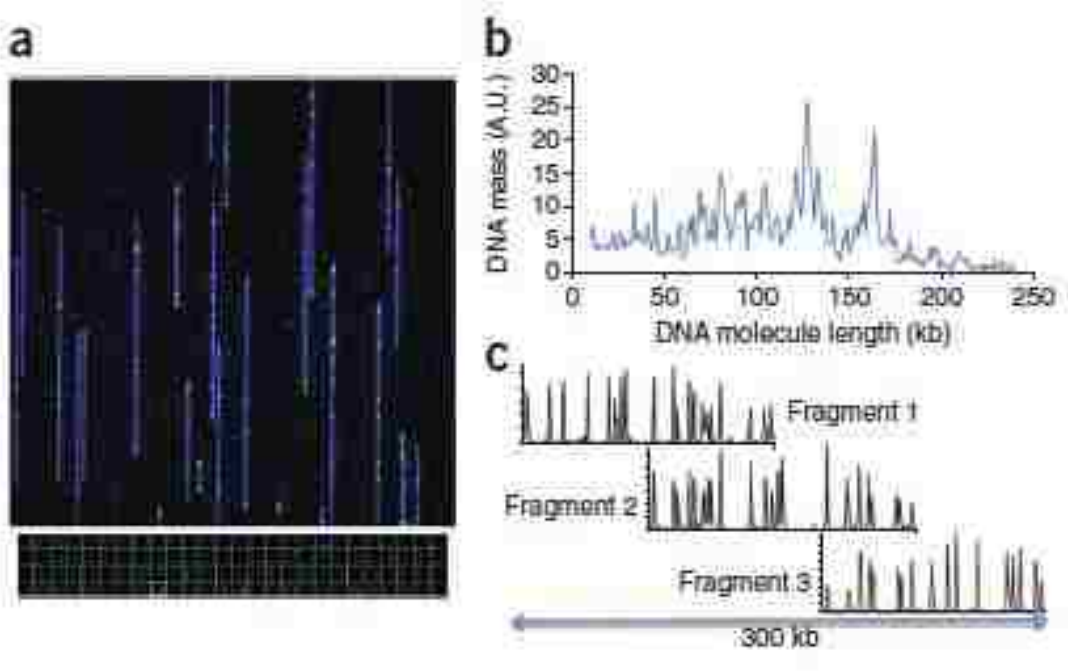

Figure 1.16 Genome mapping of mixtures of 95 BACs from the PGF and COX libraries. (a) Image of a single field of view (FOV 73 . 73 μm) containing a mixture of nick-labeled DNA molecules in the nanoarray. This FOV is part of 108 FOVs shown in the bottom part of the panel (outlined in green). Each FOV can accommodate up to 250 kb of a DNA molecule from top to bottom. The images of four FOVs are stitched together so that longer molecules (up to 1 Mb) in a single channel can be analyzed whole. In all, there are 27 sets of four vertical FOVs per array scan. (b) The distribution of the DNA molecules imaged on the nanoarray by length. The majority of the molecules are 100–170 kb in length as expected from the BAC-clone sizes. (c) After clustering of DNA molecules based on nick-labeling patterns, consensus maps with overlapping patterns are assembled into contiguous-sequence motif maps. In this example, three overlapping consensus maps (each ~150 kb long) are assembled into a 300-kb map. (Reproduced from Lam *et. al. Nat. Biotech.* 2012)

The fragmentation frequencies were plotted and identify the nicklabeling pattern of fragmentations. This process is followed by overlapping maps assembling in to contiguous-sequence motif maps. They achieved 23,000 molecules per optical load, which corresponds to 3 Gb of DNA sequence and as expected from BAC clones, 100-170 kb length fragments gave the highest frequency from the sizes ranging 20 -220 kb.[165] Using this technique there was a recent

commercialization of the technology at BioNano Genomics Inc. They were able to produce devices with more than 4000 nanochannels in a single Si chip to sequence dsDNA using the above technique.

Some recent publications in-line with this work can be useful in further investigations about genomic mapping.[166-167] In recent reviews, Michaeli, Levy-Sakin and Ebenstein has discussed about optical mapping of DNA to visualize the structural properties and copy number as beads on a stretched DNA in nanochannels.[165, 168] They further discuss about the current available techniques to optical genome mapping including nanochannel based stretching (Figure 1.17) and their resolution in terms of human genome depth, precision and throughput method.

1.5.2 Electric Detection of Single Molecules in Nanochannels

Electrical detection of biomolecules is studied by measuring the current in longitudinal or transverse method. The measured current can be in the form of blockade, resistance, conductance, impedance or capacitance. The electrical signature induced can be due to the biomolecules or the relative change in current of the buffer. Electrical signature for single molecular detection is more popular than existing optical methods due to their ability to detect biomolecules in their native state, compatibility in size and technology as well as the ability to measure with low cost simple instrumentation.

Longitudinal method of electrical detection is similar to a behavior of a nanopore. When a biomolecule blocks a nanogap it results in change in the ion flux inside the nanochannel. This change generates a change in current. In a recent publication, electrophoretic mobilities of different size Hepatitis B Virus (HBV) capsids were measured using the above method.[169] They were able to separate T= 3 HBV capsids (o.d. 32 nm) and T= 4 HBV capsids (o.d. 35 nm) capsids with a fully resolved amplitude distribution using resistive-pulse sensing. The devices

consists with nanochannels with the dimensions of 300 nm wide, 100 nm deep and 2.5 μm long nanochannel and nanopores were 45 nm deep and 45 nm wide. (see Figure 1.18)

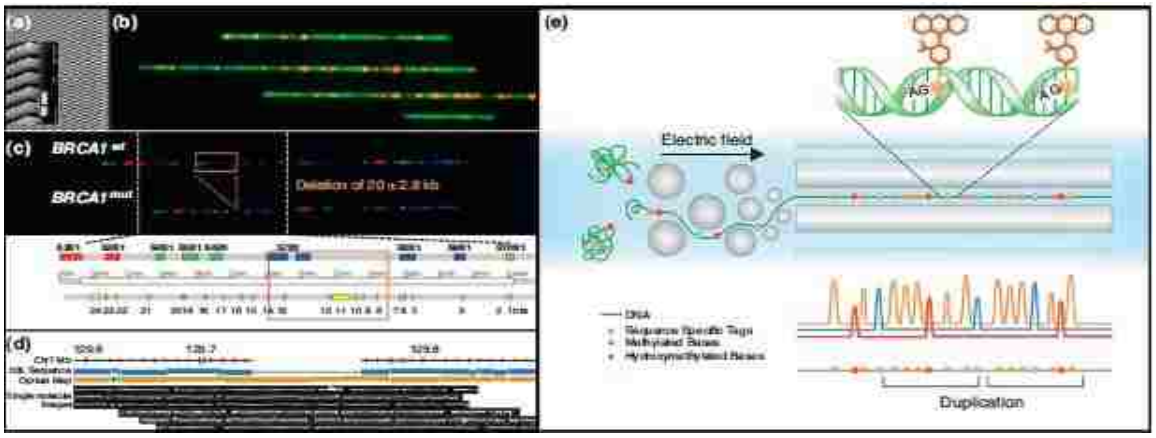

Figure 1.17 Optical mapping schemes. (a) Scanning electron microscope (SEM) image of a highly parallel nanochannel-array chip (source: BioNano Genomics, with permission). (b) BAC DNA molecules (green) are nicked by an enzyme at specific sequence motifs and repaired by a polymerase that incorporates fluorescently labeled nucleotides (orange dots) and imaged in nanochannel-array (Ebenstein lab, unpublished data). (c) DNA molecular combing. Large rearrangements in BRCA1 are detected in breast cancer patients. Del ex 8–13 is visible as a deletion of the blue signal S7B1 (modified from DeLeener *et. al.* with permission, John Wiley and Sons). (d) Restriction-optical mapping. A 90 kbp insertion is detected (red arrows). Included below the map is a montage of several of the single-molecule images that give evidence to support this insertion (adapted from Teague *et. al.* with permission). (e) Future perspective for optical mapping in nanochannels: DNA molecules (green) are specifically labeled with different colored probes revealing different genomic/epigenomic information such as sequence motifs and methylation sites (colored dots). An applied electric field drives the molecules through a series of progressively smaller nanoscale obstacles (gray circles) that funnel the molecules into nanochannels. Once DNA is stretched and confined within the channels, the distances between labels can be accurately measured using a fluorescence microscope. Software is used to generate a consensus map of the sequence motifs overlaid with the epigenetic patterns of individual molecules. The maps facilitate the analysis of structural and epigenetic variation, such as sequence duplications and methylation patterns (modified from Michaeli *et. al.*, with permission, Nature Publishing Group (Reprinted from Levy-Sakin *et. al.*)

In the transverse electrical detection method, the change of current is measured when a molecule passes through the detection gap by either the nano electrodes or electrical conductance change of the background electrolyte. Liang and Chou studied the electrical signal using pair of Au nanowires with 45 nm width and 18 nm thickness in a 45 nm × 45 nm nanochannel.[170] The

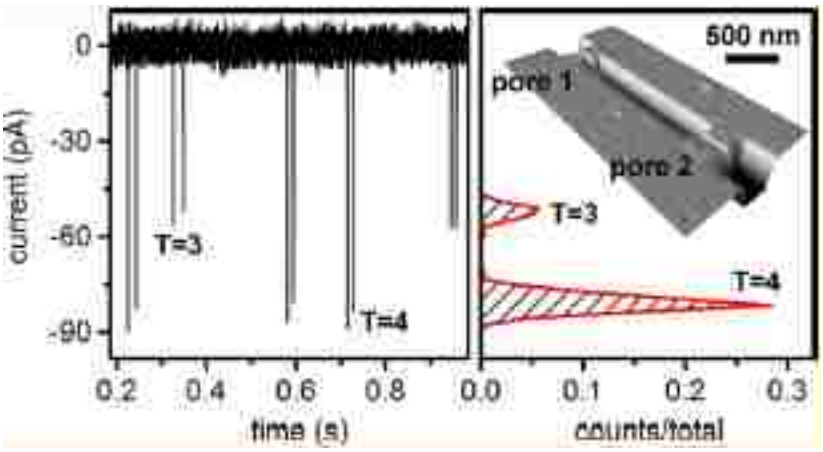

Figure 1.18 Representation of the electric signature for T= 3 HBV capsids (o.d. 32 nm) and T= 4 HBV capsids (o.d. 35 nm) in a 300 nm wide, 100 nm deep and 2.5 μm long nanochannel and 45 nm deep and 45 nm wide nanopore structure. (Reproduced from Harms *et. al. Anal. Chem.* 2015)

gap sizes vary from 9 nm to 20 nm while the gap heights vary from 16 nm to 30 nm. For the 9 nm gap size detecting 1.1 kbp DNA, the signal increased by ~200% and it was reported to be~350 pA. Kawai and coworkers measured the electrical current using DNA sized AuNPs (2 nm) and λ-DNA.[171-172] They performed there study win a device with nanogap dimensions of a 50 nm in width, 60 nm in depth and 200 nm in length using 0.1 M KCl solution. The current observed was in the range of 35 pA to 75 pA for λ-DNA. Menard and Ramsey[173] reported a method to monitor current when DNA is translocating through a nanochannel via a shorter orthogonal channel (see Figure 1.19).

The transport nanochannel widths and depths varied from ~50 nm to ~200 nm while transverse nanochannel depths and widths were ranging from ~40-160 nm and 25 – 35 nm over 3 devices. The current amplitude measured were 35 ± 5 pA for (~5% of baseline) for device A and 271 ± 53 pA (~27% of baseline) for device B in 1 M KCl solution. Moreover, optical measurements added further explanation to their reported results.

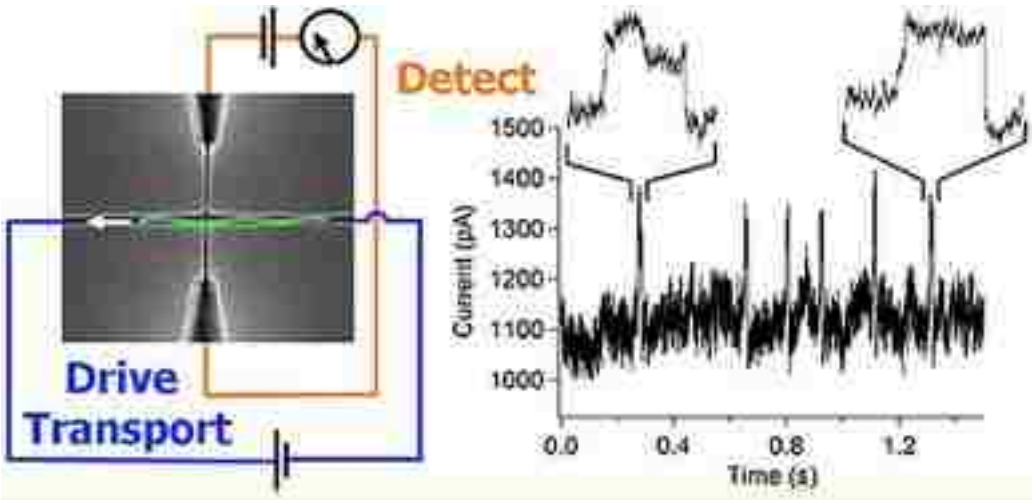

Figure 1.19 Electrical monitoring of the translocation of single DNA molecule using orthogonal nanochannels in 1M KCl solution (Menard *et. al. ACS Nano* 2012)

1.6 References

1. Maxam, A. M.; Gilbert, W., A new method for sequencing DNA. *Proceedings of the National Academy of Sciences* 1977, *74* (2), 560-564.

2. Sanger, F.; Coulson, A. R., A rapid method for determining sequences in DNA by primed synthesis with DNA polymerase. *Journal of Molecular Biology* 1975, *94* (3), 441-448.

3. Thomas, G. A., Farquar, H.D., Sutton, S., Hammer, R.P., Soper, S.A., Biomedical Microelectromechanical Systems (BioMEMS) using Electrophoresis for the Analysis of Genetic Mutations. *Molecular Review Diagnostics* 2002, *2*, 429-447.

4. Manz, A.; Harrison, D. J.; Verpoorte, E. M. J.; Fettinger, J. C.; Paulus, A.; Lüdi, H.; Widmer, H. M., Planar chips technology for miniaturization and integration of separation techniques into monitoring systems: Capillary electrophoresis on a chip. *Journal of Chromatography A* 1992, *593* (1-2), 253-258.

5. Whitesides, G. M., The origins and the future of microfluidics. *Nature* 2006, *442* (7101), 368-373.

6. Dharmasiri, U.; Witek, M. A.; Adams, A. A.; Soper, S. A., Microsystems for the Capture of Low-Abundance Cells. *Annual Review of Analytical Chemistry* 2010, *3* (1), 409-431.

7. Adams, A. A.; Okagbare, P. I.; Feng, J.; Hupert, M. L.; Patterson, D.; Göttert, J.; McCarley, R. L.; Nikitopoulos, D.; Murphy, M. C.; Soper, S. A., Highly Efficient Circulating Tumor Cell Isolation from Whole Blood and Label-Free Enumeration Using Polymer-Based Microfluidics with an Integrated Conductivity Sensor. *Journal of the American Chemical Society* 2008, *130* (27), 8633-8641.

8. Becker, H.; Gärtner, C., Polymer microfabrication methods for microfluidic analytical applications. *ELECTROPHORESIS* 2000, *21* (1), 12-26.

9. Wood, J., Microfluidics begins to realize its potential. *Nano Today* 2007, *2* (1), 16-16.

10. Dolník, V.; Liu, S.; Jovanovich, S., Capillary electrophoresis on microchip. *ELECTROPHORESIS* 2000, *21* (1), 41-54.

11. Pumera, M.; Wang, J.; Grushka, E.; Polsky, R., Gold Nanoparticle-Enhanced Microchip Capillary Electrophoresis. *Analytical Chemistry* 2001, *73* (22), 5625-5628.

12. Kinsella, A.; Minteer, S., Microchip Devices for Bioanalysis. In *Molecular Biomethods Handbook*, Walker, J.; Rapley, R., Eds. Humana Press: 2008; pp 851-859.

13. Nilsson, C.; Birnbaum, S.; Nilsson, S., Use of nanoparticles in capillary and microchip electrochromatography. *Journal of Chromatography A* 2007, *1168* (1–2), 212-224.

14. Osiri, J. K.; Shadpour, H.; Park, S.; Snowden, B. C.; Chen, Z.-Y.; Soper, S. A., Generating high peak capacity 2-D maps of complex proteomes using PMMA microchip electrophoresis. *ELECTROPHORESIS* 2008, *29* (24), 4984-4992.

15. Osiri, J.; Shadpour, H.; Soper, S., Ultra-fast two-dimensional microchip electrophoresis using SDS μ-CGE and microemulsion electrokinetic chromatography for protein separations. *Anal Bioanal Chem* 2010, *398* (1), 489-498.

16. Lin, C.-H.; Lee, G.-B.; Chen, S.-H.; Chang, G.-L., Micro capillary electrophoresis chips integrated with buried SU-8/SOG optical waveguides for bio-analytical applications. *Sensors and Actuators A: Physical* 2003, *107* (2), 125-131.

17. Abgrall, P.; Nguyen, N. T., Nanofluidic Devices and Their Applications. *Analytical Chemistry* 2008, *80* (7), 2326-2341.

18. Turner, S. W.; Cabodi, M.; Craighead, H. G., Confinement-induced entropic recoil of single DNA molecules in a nanofluidic structure. *Physical review letters* 2002, *88* (12), 128103.

19. Danelon, C.; Santschi, C.; Brugger, J.; Vogel, H., Fabrication and Functionalization of Nanochannels by Electron-Beam-Induced Silicon Oxide Deposition†. *Langmuir* 2006, *22* (25), 10711-10715.

20. Han, J.; Craighead, H. G., Separation of Long DNA Molecules in a Microfabricated Entropic Trap Array. *Science* 2000, *288* (5468), 1026-1029.

21. Woods, L. A.; Gandhi, P. U.; Ewing, A. G., Electrically Assisted Sampling across Membranes with Electrophoresis in Nanometer Inner Diameter Capillaries. *Analytical Chemistry* 2005, *77* (6), 1819-1823.

22. Bayley, H.; Martin, C. R., Resistive-Pulse SensingFrom Microbes to Molecules. *Chemical Reviews* 2000, *100* (7), 2575-2594.

23. Kemery, P. J.; Steehler, J. K.; Bohn, P. W., Electric Field Mediated Transport in Nanometer Diameter Channels. *Langmuir* 1998, *14* (10), 2884-2889.

24. Kuo, T.-C.; Sloan, L. A.; Sweedler, J. V.; Bohn, P. W., Manipulating Molecular Transport through Nanoporous Membranes by Control of Electrokinetic Flow: Effect of Surface Charge Density and Debye Length. *Langmuir* 2001, *17* (20), 6298-6303.

25. Kasianowicz, J. J.; Brandin, E.; Branton, D.; Deamer, D. W., Characterization of individual polynucleotide molecules using a membrane channel. *Proceedings of the National Academy of Sciences* 1996, *93* (24), 13770-13773.

26. Akeson, M.; Branton, D.; Kasianowicz, J. J.; Brandin, E.; Deamer, D. W., Microsecond Time-Scale Discrimination Among Polycytidylic Acid, Polyadenylic Acid, and Polyuridylic Acid as Homopolymers or as Segments Within Single RNA Molecules. *Biophysical Journal* 1999, *77* (6), 3227-3233.

27. Meller, A.; Nivon, L.; Brandin, E.; Golovchenko, J.; Branton, D., Rapid nanopore discrimination between single polynucleotide molecules. *Proceedings of the National Academy of Sciences* 2000, *97* (3), 1079-1084.

28. Meller, A.; Nivon, L.; Branton, D., Voltage-Driven DNA Translocations through a Nanopore. *Physical Review Letters* 2001, *86* (15), 3435.

29. Meller, A.; Branton, D., Single molecule measurements of DNA transport through a nanopore. *ELECTROPHORESIS* 2002, *23* (16), 2583-2591.

30. Deamer, D. W.; Branton, D., Characterization of Nucleic Acids by Nanopore Analysis. *Accounts of Chemical Research* 2002, *35* (10), 817-825.

31. Tian, P.; Smith, G. D., Translocation of a polymer chain across a nanopore: A Brownian dynamics simulation study. 2003, *119* (21), 11475-11483.

32. Kasianowicz, J. J.; Henrickson, S. E.; Weetall, H. H.; Robertson, B., Simultaneous Multianalyte Detection with a Nanometer-Scale Pore. *Analytical Chemistry* 2001, *73* (10), 2268-2272.

33. Storm, A. J.; Chen, J. H.; Ling, X. S.; Zandbergen, H. W.; Dekker, C., Fabrication of solid-state nanopores with single-nanometre precision. *Nat Mater* 2003, *2* (8), 537-540.

34. Rhee, M.; Burns, M. A., Nanopore sequencing technology: research trends and applications. *Trends in Biotechnology* 2006, *24* (12), 580-586.

35. Lagerqvist, J.; Zwolak, M.; Di Ventra, M., Fast DNA Sequencing via Transverse Electronic Transport. *Nano Letters* 2006, *6* (4), 779-782.

36. Lagerqvist, J.; Zwolak, M.; Di Ventra, M., Influence of the Environment and Probes on Rapid DNA Sequencing via Transverse Electronic Transport. *Biophysical Journal* 2007, *93* (7), 2384-2390.

37. Zikic, R.; Krstić, P. S.; Zhang, X. G.; Fuentes-Cabrera, M.; Wells, J.; Zhao, X., Characterization of the tunneling conductance across DNA bases. *Physical Review E* 2006, *74* (1), 011919.

38. Zwolak, M.; Di Ventra, M., Colloquium: Physical approaches to DNA sequencing and detection. *Reviews of Modern Physics* 2008, *80* (1), 141.

39. Davis, L. M.; Fairfield, F. R.; Harger, C. A.; Jett, J. H.; Keller, R. A.; Hahn, J. H.; Krakowski, L. A.; Marrone, B. L.; Martin, J. C.; Nutter, H. L.; Ratliff, R. L.; Shera, E. B.; Simpson, D. J.; Soper, S. A., Rapid DNA sequencing based upon single molecule detection. *Genetic Analysis: Biomolecular Engineering* 1991, *8* (1), 1-7.

40. Wu, H.-C.; Astier, Y.; Maglia, G.; Mikhailova, E.; Bayley, H., Protein Nanopores with Covalently Attached Molecular Adapters. *Journal of the American Chemical Society* 2007, *129* (51), 16142-16148.

41. Clarke, J.; Wu, H.-C.; Jayasinghe, L.; Patel, A.; Reid, S.; Bayley, H., Continuous base identification for single-molecule nanopore DNA sequencing. *Nat Nano* 2009, *4* (4), 265-270.

42. Astier, Y.; Braha, O.; Bayley, H., Toward Single Molecule DNA Sequencing: Direct Identification of Ribonucleoside and Deoxyribonucleoside 5‘-Monophosphates by Using an Engineered Protein Nanopore Equipped with a Molecular Adapter. *Journal of the American Chemical Society* 2006, *128* (5), 1705-1710.

43. Li, Y.; Xu, J.; Li, D., Molecular dynamics simulation of nanoscale liquid flows. *Microfluid Nanofluid* 2010, *9* (6), 1011-1031.

44. Han, J.; Turner, S. W.; Craighead, H. G., Entropic Trapping and Escape of Long DNA Molecules at Submicron Size Constriction. *Physical Review Letters* 1999, *83* (8), 1688-1691.

45. Martin, F.; Walczak, R.; Boiarski, A.; Cohen, M.; West, T.; Cosentino, C.; Ferrari, M., Tailoring width of microfabricated nanochannels to solute size can be used to control diffusion kinetics. *Journal of Controlled Release* 2005, *102* (1), 123-133.

46. Lam, L.; Iino, R.; Tabata, K. V.; Noji, H., Highly sensitive restriction enzyme assay and analysis: a review. *Analytical & Bioanalytical Chemistry* 2008, *391* (7), 2423-2432.

47. Mao, P.; Han, J., Fabrication and characterization of 20 nm planar nanofluidic channels by glass-glass and glass-silicon bonding. *Lab on a Chip* 2005, *5* (8), 837-844.

48. Steinmann, P., Fabrication of sub-5?nm gaps between metallic electrodes using conventional lithographic techniques. *J. Vac. Sci. Technol. B* 2004, *22* (6), 3178.

49. Ercolessi, F., *A molecular dynamics primer*. Spring College in Computational Physics, ICTTP, Trieste, Italy: International School for Advanced Studies (SISSA-ISAS), Trieste, Italy, 1997; p 56.

50. Frenkel, D., *Molecular Dynamics Simulations*. Van't Hoff Laboratory, Utercht University: Utercht , The Netherlands, 1993; p 85.

51. Liu, L.; Zhao, J.; Yin, C.-Y.; Culligan, P. J.; Chen, X., Mechanisms of water infiltration into conical hydrophobic nanopores. *Physical Chemistry Chemical Physics* 2009, *11* (30), 6520-6524.

52. Mitchell, M. J.; Qiao, R.; Aluru, N. R., Meshless analysis of steady-state electro-osmotic transport. *Microelectromechanical Systems, Journal of* 2000, *9* (4), 435-449.

53. Qiao, R., Ion concentrations and velocity profiles in nanochannel electroosmotic flows. *J. Chem. Phys.* 2003, *118* (10), 4692.

54. Ermakov, S. V.; Jacobson, S. C.; Ramsey, J. M., Computer Simulations of Electrokinetic Transport in Microfabricated Channel Structures. *Analytical Chemistry* 1998, *70* (21), 4494-4504.

55. Freund, J., Electro-osmosis in a nanometer-scale channel studied by atomistic simulation. *J. Chem. Phys.* 2002, *116* (5), 2194.

56. Conlisk, A. T., Modeling Biomolecular Transport at the Nanoscale BioMEMS and Biomedical Nanotechnology. Ferrari, M.; Lee, A. P.; Lee, L. J., Eds. Springer US: 2006; pp 399-434.

57. Bonthuis, D. J.; Meyer, C.; Stein, D.; Dekker, C., Conformation and Dynamics of DNA Confined in Slitlike Nanofluidic Channels. *Physical Review Letters* 2008, *101* (10), 108303.

58. Luan, B.; Afzali, A.; Harrer, S.; Peng, H.; Waggoner, P.; Polonsky, S.; Stolovitzky, G.; Martyna, G., Tribological Effects on DNA Translocation in a Nanochannel Coated with a Self-Assembled Monolayer. *The Journal of Physical Chemistry B* 2010, *114* (51), 17172-17176.

59. Su, T. X.; Purohit, P. K., Entropically driven motion of polymers in nonuniform nanochannels. *Physical Review E* 2011, *83* (6).

60. Min, S. K.; Cho, Y.; Mason, D. R.; Lee, J. Y.; Kim, K. S., Theoretical Design of Nanomaterials and Nanodevices: Nanolensing, Supermagnetoresistance, and Ultrafast DNA Sequencing. *The Journal of Physical Chemistry C* 2011, *115* (33), 16247-16257.

61. Wang, Y. W.; Tree, D. R.; Dorfman, K. D., Simulation of DNA Extension in Nanochannels. *Macromolecules* 2011, *44* (16), 6594-6604.

62. Steve, P., Fast Parallel Algorithms for Short-Range Molecular Dynamics. *Journal of Computational Physics* 1995, *117* (1), 1-19.

63. Schlick, T.; Collepardo-Guevara, R.; Halvorsen, L. A.; Jung, S.; Xiao, X., Biomolecular modeling and simulation: a field coming of age. *Quarterly Reviews of Biophysics* 2011, *44* (02), 191-228

64. Cornell, W. D.; Cieplak, P.; Bayly, C. I.; Gould, I. R.; Merz, K. M.; Ferguson, D. M.; Spellmeyer, D. C.; Fox, T.; Caldwell, J. W.; Kollman, P. A., A Second Generation Force Field for the Simulation of Proteins, Nucleic Acids, and Organic Molecules. *Journal of the American Chemical Society* 1995, *117* (19), 5179-5197.

65. Foloppe, N.; MacKerell, J. A. D., All-atom empirical force field for nucleic acids: I. Parameter optimization based on small molecule and condensed phase macromolecular target data. *Journal of Computational Chemistry* 2000, *21* (2), 86-104.

66. McDonald, D. Q.; Still, W. C., AMBER torsional parameters for the peptide backbone. *Tetrahedron Letters* 1992, *33* (50), 7743-7746.

67. MacKerell, A. D.; Wiorkiewicz-Kuczera, J.; Karplus, M., An all-atom empirical energy function for the simulation of nucleic acids. *Journal of the American Chemical Society* 1995, *117* (48), 11946-11975.

68. Scott, W. R. P.; Hünenberger, P. H.; Tironi, I. G.; Mark, A. E.; Billeter, S. R.; Fennen, J.; Torda, A. E.; Huber, T.; Krüger, P.; van Gunsteren, W. F., The GROMOS Biomolecular Simulation Program Package. *The Journal of Physical Chemistry A* 1999, *103* (19), 3596-3607.

69. Dubbeldam, D.; Calero, S.; Vlugt, T. J. H.; Krishna, R.; Maesen, T. L. M.; Smit, B., United Atom Force Field for Alkanes in Nanoporous Materials. *The Journal of Physical Chemistry B* 2004, *108* (33), 12301-12313.

70. Nath, S., A new united atom force field for ?-olefins. *J. Chem. Phys.* 2001, *114* (8), 3612.

71. Malhotra, A.; Harvey, S. C., A Quantitative Model of the Escherichia coli 16 S RNA in the 30 S Ribosomal Subunit. *Journal of Molecular Biology* 1994, *240* (4), 308-340.

72. Feig, M.; Pettitt, B. M., Structural Equilibrium of DNA Represented with Different Force Fields. *Biophysical Journal* 1998, *75* (1), 134-149.

73. Ricci, C. G.; de Andrade, A. S. C.; Mottin, M.; Netz, P. A., Molecular Dynamics of DNA: Comparison of Force Fields and Terminal Nucleotide Definitions. *The Journal of Physical Chemistry B* 2010, *114* (30), 9882-9893.

74. Wang, J.; Cieplak, P.; Kollman, P. A., How well does a restrained electrostatic potential (RESP) model perform in calculating conformational energies of organic and biological molecules? *Journal of Computational Chemistry* 2000, *21* (12), 1049-1074.

75. Duan, Y.; Wu, C.; Chowdhury, S.; Lee, M. C.; Xiong, G.; Zhang, W.; Yang, R.; Cieplak, P.; Luo, R.; Lee, T.; Caldwell, J.; Wang, J.; Kollman, P., A point-charge force field for molecular mechanics simulations of proteins based on condensed-phase quantum mechanical calculations. *Journal of Computational Chemistry* 2003, *24* (16), 1999-2012.

76. Reuss, F. F., Memoires de la Societe Imperiale de Naturalistes de Moscou. 1809, *2*, 327.

77. Wiedemann, G., *Pogg. Ann.* 1852, *87*, 321.

78. Helmholtz, H., *Ann.* 1879, *7*, 337.

79. Smoluchowski, M., *Krak. Anz.* 1903, 182.

80. Burgreen, D.; Nakache, F. R., Electrokinetic Flow in Ultrafine Capillary Slits1. *The Journal of Physical Chemistry* 1964, *68* (5), 1084-1091.

81. Kirby, B. J. Micro- and Nanoscale Fluid Mechanics - Transport in Microfluidic Devices. July 2010.

82. Jorgenson, J. W.; Lukacs, K. D., Capillary Zone Electrophoresis. *Science* 1983, *222* (4621), 266-272.

83. Paul, P. H.; Garguilo, M. G.; Rakestraw, D. J., Imaging of Pressure- and Electrokinetically Driven Flows through Open Capillaries. *Analytical Chemistry* 1998, *70* (13), 2459-2467.

84. Rice, C. L.; Whitehead, R., Electrokinetic Flow in a Narrow Cylindrical Capillary. *The Journal of Physical Chemistry* 1965, *69* (11), 4017-4024.

85. Altria, K. D., *Capillary Electrophoresis Guidebook : Principles, Operation and Applications*. Humana P: New York, 1995.

86. Kirby, B. J.; Hasselbrink, E. F., Zeta potential of microfluidic substrates: 1. Theory, experimental techniques, and effects on separations. *ELECTROPHORESIS* 2004, *25* (2), 187-202.

87. Grahame, D. C., The Electrical Double Layer and the Theory of Electrocapillarity. *Chemical Reviews* 1947, *41* (3), 441-501.

88. Helmholtz, H., Ueber einige Gesetze der Vertheilung elektrischer Ströme in körperlichen Leitern mit Anwendung auf die thierisch-elektrischen Versuche. *Annalen der Physik und Chemie* 1853, *165* (6), 211-233.

89. Guoy, G., Sur la constitution de la electrique ´ a l ` a surface d'un electrolyte. *J. Phys. Radium* 1910, *9*, 457–468.

90. Chapman, D., A contribution to the theory of electroencapillarity. *Philos. Mag* 1913, *25* (6), 475-481.

91. Stern, O. Z., *Electrochem* 1924, *30*, 508.

92. Lyklema, J., *Fundamentals of Interface and Colloid Science - Solid-Liquid Interfaces*. 1st ed.; Academic Press: London, England, 1995; Vol. 2.

93. Russel, W. B., Saville, D.A. and Schowalter, W. R., *Colloidal Dispersions*. Cambridge University Press: Cambridge, UK, 1989.

94. Pennathur, S.; Santiago, J. G., Electrokinetic Transport in Nanochannels. 1. Theory. *Analytical Chemistry* 2005, *77* (21), 6772-6781.

95. Pennathur, S.; Santiago, J. G., Electrokinetic Transport in Nanochannels. 2. Experiments. *Analytical Chemistry* 2005, *77* (21), 6782-6789.

96. Kirby, B. J.; Hasselbrink, E. F., Zeta potential of microfluidic substrates: 2. Data for polymers. *Electrophoresis* 2004, *25* (2), 203-213.

97. Mijatovic, D.; Eijkel, J. C. T.; van den Berg, A., Technologies for nanofluidic systems: top-down vs. bottom-up-a review. *Lab on a Chip* 2005, *5* (5), 492-500.

98. Nallathamby, P. D.; Lee, K. J.; Xu, X.-H. N., Design of Stable and Uniform Single Nanoparticle Photonics for In Vivo Dynamics Imaging of Nanoenvironments of Zebrafish Embryonic Fluids. *ACS Nano* 2008, *2* (7), 1371-1380.

99. Lee, K. J.; Nallathamby, P. D.; Browning, L. M.; Osgood, C. J.; Xu, X.-H. N., In Vivo Imaging of Transport and Biocompatibility of Single Silver Nanoparticles in Early Development of Zebrafish Embryos. *ACS Nano* 2007, *1* (2), 133-143.

100. Huang, T.; Nallathamby, P. D.; Xu, X.-H. N., Photostable Single-Molecule Nanoparticle Optical Biosensors for Real-Time Sensing of Single Cytokine Molecules and Their Binding Reactions. *Journal of the American Chemical Society* 2008, *130* (50), 17095-17105.

101. Xu, X.-H. N.; Brownlow, W. J.; Kyriacou, S. V.; Wan, Q.; Viola, J. J., Real-time probing of membrane transport in living microbial cells using single nanoparticle optics and living cell imaging. *Biochemistry* 2004, *43* (32), 10400-10413.

102. Huang, T.; Xu, X.-H. N., Synthesis and characterization of tunable rainbow colored colloidal silver nanoparticles using single-nanoparticle plasmonic microscopy and spectroscopy. *Journal of materials chemistry* 2010, *20* (44), 9867-9876.

103. Watson, J. D.; Crick, F. H. C., Molecular structure of nucleic acids. *Nature* 1953, *171* (4356), 737-738.

104. Reisner, W.; Morton, K. J.; Riehn, R.; Wang, Y. M.; Yu, Z.; Rosen, M.; Sturm, J. C.; Chou, S. Y.; Frey, E.; Austin, R. H., Statics and Dynamics of Single DNA Molecules Confined in Nanochannels. *Physical Review Letters* 2005, *94* (19), 196101.

105. Reisner, W.; Beech, J. P.; Larsen, N. B.; Flyvbjerg, H.; Kristensen, A.; Tegenfeldt, J. O., Nanoconfinement-Enhanced Conformational Response of Single DNA Molecules to Changes in Ionic Environment. *Physical Review Letters* 2007, *99* (5), 058302.

106. Walter, R.; Jonas, N. P.; Robert, H. A., DNA confinement in nanochannels: physics and biological applications. *Reports on Progress in Physics* 2012, *75* (10), 106601.

107. Hays, J. B.; Magar, M. E.; Zimm, B. H., Persistence length of DNA. *Biopolymers* 1969, *8* (4), 531-536.

108. Manning, G. S., Three persistence lengths for a stiff polymer with an application to DNA B-Z junctions. *Biopolymers* 1988, *27* (10), 1529-1542.

109. Manning, G. S., The Persistence Length of DNA Is Reached from the Persistence Length of Its Null Isomer through an Internal Electrostatic Stretching Force. *Biophysical Journal* 2006, *91* (10), 3607-3616.

110. Pray, L., Discovery of DNA structure and function: Watson and Crick. *Nature Education* 2008, *1* (1).

111. Flory, P. J., Principles of polymer chemistry. 1953.

112. Schaefer, D. W.; Joanny, J. F.; Pincus, P., Dynamics of Semiflexible Polymers in Solution. *Macromolecules* 1980, *13* (5), 1280-1289.

113. Tegenfeldt, J. O.; Prinz, C.; Cao, H.; Chou, S.; Reisner, W. W.; Riehn, R.; Wang, Y. M.; Cox, E. C.; Sturm, J. C.; Silberzan, P.; Austin, R. H., The dynamics of genomic-length DNA molecules in 100-nm channels. *Proceedings of the National Academy of Sciences of the United States of America* 2004, *101* (30), 10979-10983.

114. Odijk, T., The statistics and dynamics of confined or entangled stiff polymers. *Macromolecules* 1983, *16* (8), 1340-1344.

115. Odijk, T., DNA confined in nanochannels: Hairpin tightening by entropic depletion. *The Journal of Chemical Physics* 2006, *125* (20), 204904.

116. Movahed, S.; Li, D., Electrokinetic transport through nanochannels. *ELECTROPHORESIS* 2011, *32* (11), 1259-1267.

117. Baldessari, F.; Santiago, J., Electrophoresis in nanochannels: brief review and speculation. *Journal of Nanobiotechnology* 2006, *4* (1), 12.

118. Schoch, R. B.; Han, J.; Renaud, P., Transport phenomena in nanofluidics. *Reviews of Modern Physics* 2008, *80* (3), 839-883.

119. Napoli, M.; Eijkel, J. C. T.; Pennathur, S., Nanofluidic technology for biomolecule applications: a critical review. *Lab on a Chip* 2010, *10* (8), 957-985.

120. Piruska, A.; Gong, M.; Sweedler, J. V.; Bohn, P. W., Nanofluidics in chemical analysis. *Chemical Society Reviews* 2010, *39* (3), 1060-1072.

121. Plecis, A.; Schoch, R. B.; Renaud, P., Ionic Transport Phenomena in Nanofluidics: Experimental and Theoretical Study of the Exclusion-Enrichment Effect on a Chip. *Nano Letters* 2005, *5* (6), 1147-1155.

122. Karnik, R.; Fan, R.; Yue, M.; Li, D.; Yang, P.; Majumdar, A., Electrostatic Control of Ions and Molecules in Nanofluidic Transistors. *Nano Letters* 2005, *5* (5), 943-948.

123. Yuan, Z.; Garcia, A. L.; Lopez, G. P.; Petsev, D. N., Electrokinetic transport and separations in fluidic nanochannels. *ELECTROPHORESIS* 2007, *28* (4), 595-610.

124. Pu, Q.; Yun, J.; Temkin, H.; Liu, S., Ion-Enrichment and Ion-Depletion Effect of Nanochannel Structures. *Nano Letters* 2004, *4* (6), 1099-1103.

125. Manning, G. S., Electrostatic Free Energies of Spheres, Cylinders, and Planes in Counterion Condensation Theory with Some Applications. *Macromolecules* 2007, *40* (22), 8071-8081.

126. Jones, C.; Patel, A.; Griffin, S.; Martin, J.; Young, P.; O'Donnell, K.; Silverman, C.; Porter, T.; Chaiken, I., Current trends in molecular recognition and bioseparation. *Journal of Chromatography A* 1995, *707* (1), 3-22.

127. Muthukumar, M., Mechanism of DNA Transport Through Pores. *Annual Review of Biophysics and Biomolecular Structure* 2007, *36* (1), 435-450.

128. Giddlings, J. C., *Unified Separation Science*. John Wiley & Sons: New York, 1991.

129. Jones, T. B., *Electromechanics of Particles*. Cambridge University Press: Cambridge, 1995.

130. Kovarik, M. L.; Jacobson, S. C., Integrated Nanopore/Microchannel Devices for ac Electrokinetic Trapping of Particles. *Analytical Chemistry* 2008, *80* (3), 657-664.

131. Janssen, K. G. H.; Hoang, H. T.; Floris, J.; de Vries, J.; Tas, N. R.; Eijkel, J. C. T.; Hankemeier, T., Solution Titration by Wall Deprotonation during Capillary Filling of Silicon Oxide Nanochannels. *Analytical Chemistry* 2008, *80* (21), 8095-8101.

132. Squires, T. M., Induced-charge electrokinetics: fundamental challenges and opportunities. *Lab on a Chip* 2009, *9* (17), 2477-2483.

133. Hibara, A.; Saito, T.; Kim, H.-B.; Tokeshi, M.; Ooi, T.; Nakao, M.; Kitamori, T., Nanochannels on a Fused-Silica Microchip and Liquid Properties Investigation by Time-Resolved Fluorescence Measurements. *Analytical Chemistry* 2002, *74* (24), 6170-6176.

134. Blom, M. T.; Chmela, E.; Oosterbroek, R. E.; Tijssen, R.; van den Berg, A., On-Chip Hydrodynamic Chromatography Separation and Detection of Nanoparticles and Biomolecules. *Analytical Chemistry* 2003, *75* (24), 6761-6768.

135. Garcia, A. L.; Ista, L. K.; Petsev, D. N.; O'Brien, M. J.; Bisong, P.; Mammoli, A. A.; Brueck, S. R. J.; Lopez, G. P., Electrokinetic molecular separation in nanoscale fluidic channels. *Lab on a Chip* 2005, *5* (11), 1271-1276.

136. Xuan, X.; Xu, B.; Li, D., Accelerated Particle Electrophoretic Motion and Separation in Converging−Diverging Microchannels. *Analytical Chemistry* 2005, *77* (14), 4323-4328.

137. Xuan, X.; Li, D., Electrokinetic transport of charged solutes in micro- and nanochannels: The influence of transverse electromigration. *ELECTROPHORESIS* 2006, *27* (24), 5020-5031.

138. Xuan, X.; Raghibizadeh, S.; Li, D., Wall effects on electrophoretic motion of spherical polystyrene particles in a rectangular poly(dimethylsiloxane) microchannel. *Journal of Colloid and Interface Science* 2006, *296* (2), 743-748.

139. Qian, S.; Wang, A.; Afonien, J. K., Electrophoretic motion of a spherical particle in a converging–diverging nanotube. *Journal of Colloid and Interface Science* 2006, *303* (2), 579-592.

140. Napoli, M.; Atzberger, P.; Pennathur, S., Experimental study of the separation behavior of nanoparticles in micro- and nanochannels. *Microfluid Nanofluid* 2011, *10* (1), 69-80.

141. Kaji, N.; Ogawa, R.; Oki, A.; Horiike, Y.; Tokeshi, M.; Baba, Y., Study of water properties in nanospace. *Anal Bioanal Chem* 2006, *386* (3), 759-764.

142. Hoang, H. T.; Segers-Nolten, I. M.; Tas, N. R.; van Honschoten, J. W.; Subramaniam, V.; Elwenspoek, M. C., Analysis of single quantum-dot mobility inside 1D nanochannel devices. *Nanotechnology* 2011, *22* (27), 275201.

143. Han, R.; Wang, G.; Qi, S.; Ma, C.; Yeung, E. S., Electrophoretic Migration and Axial Diffusion of Individual Nanoparticles in Cylindrical Nanopores. *The Journal of Physical Chemistry C* 2012, *116* (34), 18460-18468.

144. Wynne, T.; Dixon, A.; Pennathur, S., Electrokinetic characterization of individual nanoparticles in nanofluidic channels. *Microfluid Nanofluid* 2012, *12* (1-4), 411-421.

145. Liu, Y.-W.; Pennathur, S.; Meinhart, C. D., Electrophoretic mobility of a spherical nanoparticle in a nanochannel. *Physics of Fluids* 2014, *26* (11), 112002.

146. Huang, C.-H.; Lee, E., Electrophoretic Motion of a Liquid Droplet in a Cylindrical Pore. *The Journal of Physical Chemistry C* 2012, *116* (28), 15058-15067.

147. Huang, C.-H.; Hsu, H.-P.; Lee, E., Electrophoretic motion of a charged porous sphere within micro-and nanochannels. *Physical Chemistry Chemical Physics* 2012, *14* (2), 657-667.

148. Kaji, N.; Tezuka, Y.; Takamura, Y.; Ueda, M.; Nishimoto, T.; Nakanishi, H.; Horiike, Y.; Baba, Y., Separation of Long DNA Molecules by Quartz Nanopillar Chips under a Direct Current Electric Field. *Analytical Chemistry* 2004, *76* (1), 15-22.

149. Fu, J.; Mao, P.; Han, J., Nanofilter array chip for fast gel-free biomolecule separation. *Applied Physics Letters* 2005, *87* (26), -.

150. Pennathur, S.; Baldessari, F.; Santiago, J. G.; Kattah, M. G.; Steinman, J. B.; Utz, P. J., Free-Solution Oligonucleotide Separation in Nanoscale Channels. *Analytical Chemistry* 2007, *79* (21), 8316-8322.

151. Han, J.; Craighead, H. G., Entropic trapping and sieving of long DNA molecules in a nanofluidic channel. *Journal of Vacuum Science & Technology A* 1999, *17* (4), 2142-2147.

152. Cabodi, M.; Turner, S. W. P.; Craighead, H. G., Entropic Recoil Separation of Long DNA Molecules. *Analytical Chemistry* 2002, *74* (20), 5169-5174.

153. Han, J.; Craighead, H. G., Characterization and Optimization of an Entropic Trap for DNA Separation. *Analytical Chemistry* 2002, *74* (2), 394-401.

154. Schoch, R. B.; Bertsch, A.; Renaud, P., pH-Controlled Diffusion of Proteins with Different pI Values Across a Nanochannel on a Chip. *Nano Letters* 2006, *6* (3), 543-547.

155. Riehn, R.; Lu, M.; Wang, Y.-M.; Lim, S. F.; Cox, E. C.; Austin, R. H., Restriction mapping in nanofluidic devices. *Proceedings of the National Academy of Sciences of the United States of America* 2005, *102* (29), 10012-10016.

156. Menard, L. D.; Ramsey, J. M., Electrokinetically-Driven Transport of DNA through Focused Ion Beam Milled Nanofluidic Channels. *Analytical Chemistry* 2013, *85* (2), 1146-1153.

157. Soper, S. A.; Uba, F. I.; Pullaguria, S.; Sirasunthorn, N.; Wu, J.; Park, S.; Chantiwas, R.; Cho, Y.; Shin, H., Surface Charge, Electroosmotic Flow and DNA Extension in Chemically Modified Thermoplastic Nanoslits and Nanochannels. *Analyst* 2014.

158. Cordes, T.; Vogelsang, J.; Tinnefeld, P., On the Mechanism of Trolox as Antiblinking and Antibleaching Reagent. *Journal of the American Chemical Society* 2009, *131* (14), 5018-5019.

159. Kim, Y.; Kim, K. S.; Kounovsky, K. L.; Chang, R.; Jung, G. Y.; de Pablo, J. J.; Jo, K.; Schwartz, D. C., Nanochannel Confinement: DNA Stretch Approaching Full Contour Length. *Lab on a chip* 2011, *11* (10), 1721-1729.

160. Hsieh, C.-C.; Balducci, A.; Doyle, P. S., Ionic Effects on the Equilibrium Dynamics of DNA Confined in Nanoslits. *Nano Letters* 2008, *8* (6), 1683-1688.

161. Schellman, J. A.; Stigter, D., Electrical double layer, zeta potential, and electrophoretic charge of double-stranded DNA. *Biopolymers* 1977, *16* (7), 1415-1434.

162. Turner, S. W. P.; Cabodi, M.; Craighead, H. G., Confinement-Induced Entropic Recoil of Single DNA Molecules in a Nanofluidic Structure. *Physical Review Letters* 2002, *88* (12), 128103.

163. Das, S. K.; Austin, M. D.; Akana, M. C.; Deshpande, P.; Cao, H.; Xiao, M., Single molecule linear analysis of DNA in nano-channel labeled with sequence specific fluorescent probes. *Nucleic Acids Research* 2010.

164. Lam, E. T.; Hastie, A.; Lin, C.; Ehrlich, D.; Das, S. K.; Austin, M. D.; Deshpande, P.; Cao, H.; Nagarajan, N.; Xiao, M.; Kwok, P.-Y., Genome mapping on nanochannel arrays for structural variation analysis and sequence assembly. *Nat Biotech* 2012, *30* (8), 771-776.

165. Michaeli, Y.; Ebenstein, Y., Channeling DNA for optical mapping. *Nature biotechnology* 2012, *30* (8), 762-763.

166. Cao, H.; Hastie, A. R.; Cao, D.; Lam, E. T.; Sun, Y.; Huang, H.; Liu, X.; Lin, L.; Andrews, W.; Chan, S., Rapid detection of structural variation in a human genome using nanochannel-based genome mapping technology. *GigaScience* 2014, *3* (1), 34.

167. Hastie, A. R.; Dong, L.; Smith, A.; Finklestein, J.; Lam, E. T.; Huo, N.; Cao, H.; Kwok, P.-Y.; Deal, K. R.; Dvorak, J., Rapid genome mapping in nanochannel arrays for highly complete and accurate de novo sequence assembly of the complex Aegilops tauschii genome. *PloS one* 2013, *8* (2), e55864.

168. Levy-Sakin, M.; Ebenstein, Y., Beyond sequencing: optical mapping of DNA in the age of nanotechnology and nanoscopy. *Current Opinion in Biotechnology* 2013, *24* (4), 690-698.

169. Harms, Z. D.; Haywood, D. G.; Kneller, A. R.; Selzer, L.; Zlotnick, A.; Jacobson, S. C., Single-Particle Electrophoresis in Nanochannels. *Analytical Chemistry* 2015, *87* (1), 699-705.

170. Liang, X.; Chou, S. Y., Nanogap Detector Inside Nanofluidic Channel for Fast Real-Time Label-Free DNA Analysis. *Nano Letters* 2008, *8* (5), 1472-1476.

171. Tsutsui, M.; He, Y.; Furuhashi, M.; Rahong, S.; Taniguchi, M.; Kawai, T., Transverse electric field dragging of DNA in a nanochannel. *Scientific Reports* 2012, *2*, 394.

172. Tsutsui, M.; Taniguchi, M.; Kawai, T., Transverse Field Effects on DNA-Sized Particle Dynamics. *Nano Letters* 2009, *9* (4), 1659-1662.

173. Menard, L. D.; Mair, C. E.; Woodson, M. E.; Alarie, J. P.; Ramsey, J. M., A Device for Performing Lateral Conductance Measurements on Individual Double-Stranded DNA Molecules. *ACS Nano* 2012, *6* (10), 9087-9094.

CHAPTER 2. SINGLE PARTICLE SEPARATIONS OF NANOSCALE ELECTROPHORESIS USING LOCALIZED SURFACE PLASMON RESONANCE (LSPR) DETECTION[1]

2.1 Introduction

Over the past decade, microchip capillary electrophoresis (microchip-CE) has gained relevance because of its unique operating characteristics, such as the ability to assay hundreds of samples simultaneously, low sample and reagent consumption and the ease of integrating multiple sample processing steps into a single platform.[1-7] However, the electrophoretic separation process in microchip-CE is fundamentally similar to capillary-based CE; the separation resolution depends primarily on differences in the electrophoretic mobilities of the targets and reducing zonal dispersion, which is primarily determined by longitudinal diffusion in well-designed systems. In some cases, the lack of separation in free solution is circumvented by using buffer additives. For instance, because of the free draining behavior of single and double-stranded DNA molecules in free solution, electrophoretic separations require the incorporation of a 3D porous gel. Alternative additives are surfactants used above their critical micelle concentration to form pseudo-stationary phases.

Nanofluidics, which utilizes structures with one (nanoslits) or two (nanochannels) critical dimensions <150 nm, have provided platforms for unique electrophoretic phenomena that are not available in microscale environments.[8-9] Nanochannels and/or nanoslits have been applied in many different analytical separations,[10-11] manipulation and detection of single molecules,[12] and control of molecular transport.[13-14] Nanofluidics has also been used for electrophoresis as well. For example, it has been shown that dsDNA fragments can be separated in glass-based nanoslits

[1] This chapter is submitted to ACS Analytical Chemistry journal and it is sunder peer-review. Authors; Kumuditha M. Weerakoon-Ratnayake, Franklin I. Uba, Nyoté J. Oliver-Calixte, and Steven A. Soper

without the need for a sieving gel when the channel dimensions are on the order of the Debye length (λ_D).[15]

There have been a few studies discussing the theoretical basis of nanoscale electrophoresis.[16-18] The challenge here is that existing theories applicable to microscale systems do not necessarily describe fundamental nanoscale phenomena. Theories and experimental studies relevant to nanoscale electrokinetic separations have appeared in several reports.[19-20] For example, ion transport with d/λ_D (d = channel critical dimension) ratios ranging from 1-10 show anomalous transport behavior, such as charge-dependent ion mobilities due to transverse electromigration (TEM) resulting from solute/wall electrostatic effects[15, 21-22] with the maximum resolution occurring when the column diameter is 1-10 times λ_D.[23] Pennathur and Santiago showed that electrokinetic separations in nanoslits were dependent on ion valence, ζ (zeta potential), ion mobility and λ_D.[15, 21] Garcia *et al.*[24] reported the electrokinetic separation of Alexa 488 (negatively charged) and rhodamine B (neutral) fluorescent dyes in glass-based nanochannels with widths between 35 and 200 nm. The mobility of the fluorescent dyes varied with their inherent charge and wall interactions.

Glass and quartz have been widely used as substrates for micro- and nanofluidic devices because of their well-established surface chemistry, excellent optical properties and well-developed fabrication technologies. All of the aforementioned nanoscale electrophoresis studies were performed in glass-type devices. These materials ensure an electrical insulating interface and provide relatively large amounts of surface charge when in contact with aqueous solutions generating a relatively large electroosmotic flow (EOF).[25]

Recently, thermoplastics have generated interest as nanofluidic devices because of their biocompatibility, optical properties comparable to glass substrates in some cases and their ability

to be manufactured in a high production mode at low-cost using nano-replication modalities, such as nanoimprint lithography (NIL). NIL has proven to be successful in patterning structures to sub-10 nm scales,[26-29] with the ultimate resolution seemingly determined by the minimum feature size associated with the molding tool.[30] Several researchers have reported the fabrication of nanofluidic devices in thermoplastics.[31-33] We recently reported a low-cost, high throughput scheme for the production of nanochannels and nanoslits in thermoplastics.[34-35]

Previous work has shown the ability to separate submicron-sized particles based on their unique electrophoretic mobility.[36] Liu *et al.*[37] was able to separate silver nanoparticles (AgNPs) in the presence of an SDS surfactant using microscale CE. However, they were unable to achieve separation without the addition of SDS to the running buffer. While there have been reports on the separation of spherical nanoparticles using conventional or microchip CE, only a few studies have reported the electrophoretic transport behavior of noble metal nanoparticles in nanofluidic domains;[17-18, 38] these studies used glass-based devices.

Herein, we report the separation of single AgNP in thermoplastic nanoslit devices. AgNPs were used in this study because the localized surface plasmon resonance (LSPR) of these particles coupled with dark-field microscopy could be used to track their transport properties free from photobleaching artifacts.[7] In this manuscript, we discuss the effects of polymer-based nanoslit depth (150 and 400 nm), salt concentration and field strength on the electrophoretic properties of 60 and 100 nm diameter AgNPs.

2.2 Experimental Methods

2.2.1 Materials

Silicon <100> (Si) wafers were purchased from University Wafers (Boston, MA). Poly(methylmethacrylate), PMMA, substrates and cover plates were purchased from Good

Fellow (Berwyn, PA) and cyclic olefin copolymer (COC 6017) was purchased from TOPAS Advanced Polymers (Florence, KY). The anti-adhesion coating material, (tridecafluoro – 1,1,2,2-tetrahydrooctyl) tricholorosilane (T-silane), was purchased from Gelest, Inc. (Morrisville, PA). Citrate capped AgNPs (60 nm and 100 nm in diameter) were purchased from Nanocomposix®, Inc. (San Diego, CA) and suspended in an aqueous 2 mM citrate buffer (Fisher Scientific®, Philadelphia, PA). The concentrations of the AgNP solutions were adjusted so that single particle events could be tracked. All dilutions were performed using 18 MΩ/cm milliQ water (Millipore) with citrate buffer (pH = 7.0). The final concentrations were approximately 10^8 particles/μL. All solutions were filtered through 0.2 μm membranes (Thermo Scientific® Nalgene syringe filters) prior to use. Particle size variation was reported by the manufactures to be <10% (CV).

2.2.2 Fabrication of Nanofluidic Devices

Access microchannels were fabricated in a Si substrate using optical lithography and nanoslits (150 nm or 400 nm deep with a 5 μm width) were patterned using a Ga focused ion beam (FIB; Helios NanoLab 600 Dual Beam Instrument, FEI) milling as previously reported by our group.[32, 34-35, 39] The pattered Si master was then coated with an anti-adhesion monolayer of T-silane in a desiccator under vacuum for 2 h. The pattern on the Si master was then transferred to a UV curable resin (TPGA 68% w/w as base, TMPA 28% w/w as a cross linker and Irgacure 651 4% w/w as a photo initiator) with the unpolymerized resin sandwiched between the Si master and a cyclic olefin copolymer (COC) back plate. The resin was cured using 365 nm UV light (10 J/m^2) for 6 min (CL-1000 Ultraviolet Cross linker). After curing, the resin stamp was carefully demolded to from the Si master.

The resin stamp was then used to imprint structures into a 1.5 mm thick PMMA substrate. Imprinting of structures was performed with a JenOptik Hex03 instrument at 127°C under 1850

kN/m^2 pressure for 120 s. The substrate and a 125 μm thick cover plate (PMMA cover plate, used for enclosing the nanofluidic device) were activated under oxygen plasma (Femto, Diener Electronic) at 50 W for 30 s and 10 sccm oxygen flow. After activation of the surfaces, devices were assembled at 80°C for 400 s under 680 kN/m^2 force (see Figure 2.1).

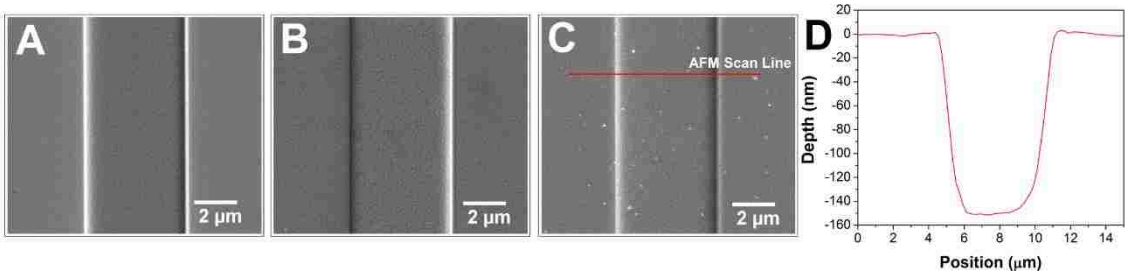

Figure 2.1 Scanning electron micrographs (SEMs) of the: (A) Si master; (B) UV-resin stamp; and (C) PMMA substrate containing a patterned nanoslit. (D) Atomic force microscope (AFM) profile taken across the nanoslit showing a nanoslit depth of ~150 nm and 5 μm width. Note: The debri seen on the SEM image in (C) of the PMMA substrate arose from artifacts resulting from coating with 3 nm AuPd for SEM imaging.

2.2.3 Dark-Field Microscopy Imaging

Dark-field microscopy was used to track single AgNPs electrophoretically moving through nanoslits under an applied electric field. Noble metal nanoparticles such as Ag, Au and Cu have unique surface plasmon resonances that depend on their size, shape and dielectric constant of the surrounding medium.[40-41] The AgNPs used herein have high yields for LSPR scattering. Compared to a single fluorescent molecule such as R6G, a 2 nm AgNP has a 10^4 fold higher photon signal yield making them easily tracked for long periods of times without photobleaching issues. [40-42]

A schematic of the imaging system is shown in section A of Figure 2.2. It consisted of an inverted microscope (Leica DMIRB) operated in a dark-field imaging mode, a COOLSNAP B/W EMCCD (Photometric), an excitation condenser with a high numerical aperture (NA = 0.9) and a 100× oil immersion objective with an adjustable numerical aperture (1.4 – 0.6) operated at

low NA values (NA = 0.6). A 100 W halogen lamp was used as the excitation source. The filtered excitation light was incident onto the device and the scattered light from the AgNPs was transmitted through the objective and focused onto an EMCCD camera. All events were acquired at 3 ms exposure time with a 650 × 50 pixel region of interest that spans the entire length and width of the nanoslit. A custom designed image-J macro was used to sort out signals from aggregates of AgNPs from that of the monodispersed nanoparticles. The measured electrophoretic migration times were used to compute electrophoretic parameters of the AgNPs such as their electrophoretic mobilities, plate numbers and resolution.

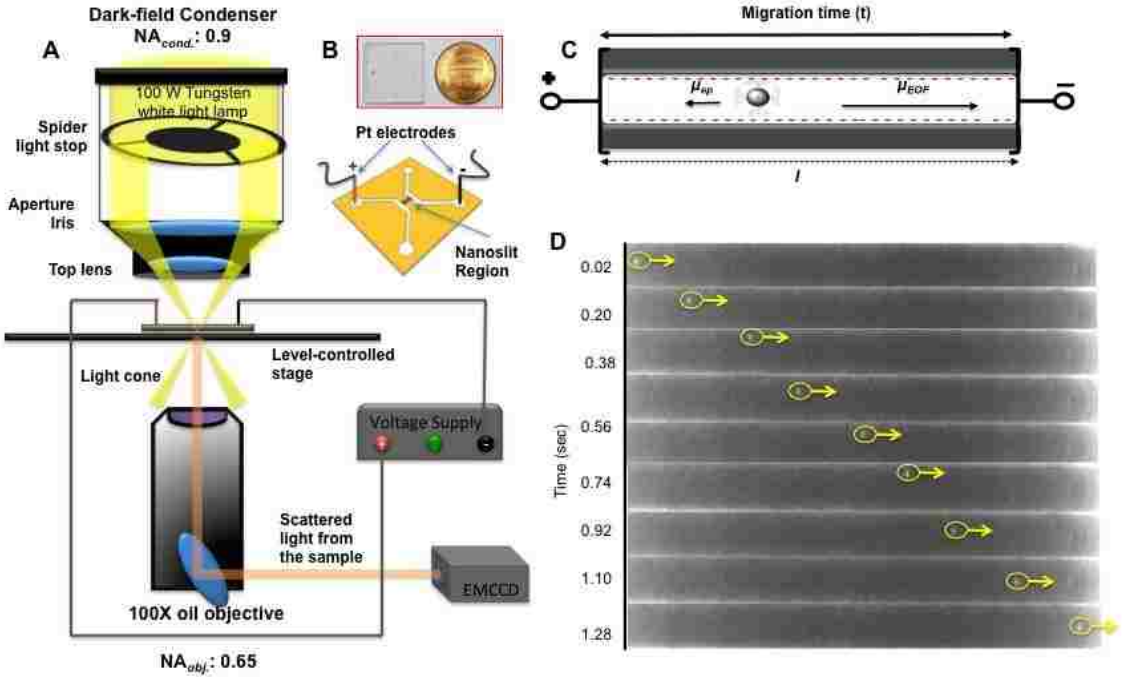

Figure 2.2 (A) Schematic of the dark field microscopy and the experimental setup. Sample is mounted on a level-controlled stage. While the spider stop controlled white light misses the objective, only scattered light from the sample enters the objective. (B) Image of actual PMMA chip and a schematic of the device with nanoslits and Pt electrodes on reservoirs, which are connected to a DC voltage unit. (C) Schematic of the nanoslits when an external electric field is applied. Electroosmotic flow is from anode to cathode while the electrophoretic mobility of negatively charged AgNP is towards anode. (D) A representation of real time translocation event of 60 nm AgNP in a nanoslit captured by DFM. Time-lapse image sequence of a single event at external field strength of 200 V/cm with respect to time. Apparent mobility was observed from anode to cathode (same direction as EOF) in 1.28 s. Dimensions of the nanoslits are 100 μm in length and 150 nm deep.

2.2.4 Nanoscale Electrophoretic Separation

The PMMA nanofluidic device was mounted on a sample holder and placed on a leveled sample stage of the dark-field microscope. Two platinum electrodes were inserted into reservoirs and an electric potential was applied longitudinally to the nanoslit using a DC-power supply (see B in Figure 2.2). The electric fields used in these experiments ranged between 100 V/cm and 1500 V/cm. Prior to the electrophoresis, the assembled nanofluidic device, which was made in PMMA, was initially primed with a 50% v/v methanol/water mixture followed by multiple water rinses prior to introduction of the running buffer. After the channels were completely filled, the AgNP solution prepared in citrate buffer was injected into an access microchannel poised on the nanofluidic device and electrophoresed using the appropriate field strength through the nanoslit.

2.3 Results and Discussion

2.3.1 Device Fabrication

The devices were developed following a method previously reported by our group. [34, 43-44] Two devices with different depths, 150 nm and 400 nm, were used in these studies to investigate the effects of nanoslit geometry on the mobilities of the AgNP. The width and lengths of the nanoslits were set to 5 μm and 100 μm, respectively, to prevent scattering background from the channel wall from overwhelming the scattering from the AgNP during translocation.

Figure 2.1 shows SEMs of the fabricated 150 nm nanoslits in the Si master, UV resin stamp and PMMA substrate. The master was used to make UV curable resin stamps that were subsequently used to imprint the nanoslits into the PMMA substrate via thermal imprinting (see Figure 2.1 B and C). The similar thermal expansion coefficients and Young's modulus of the UV resin stamp and PMMA helped to reduce thermal stress placed on the substrate during the imprinting step.[45]

Devices were assembled by thermal fusion bonding a PMMA cover plate to the substrate at a temperature slightly below the glass transition temperature of PMMA. Assembled devices were filled with 5 mM fluorescein isothiocyanate (FITC) in 1X TBE buffer solution to verify good sealing of the device. Figure 2.1 D shows SEMs and profilometer traces of the nanoslits used as columns for the electrophoresis. All tests revealed high fidelity of pattern transfer from the Si master into the resin stamp and finally, the PMMA substrate and also, with uniform sealing following thermal fusion bonding of the cover plate to the PMMA substrate. As previously reported by our group, each Si master can fabricate >20 UV resin stamps as well as each resin stamp generating >20 replicas without any notable deformation of the nanostructures.[34] As such, focused ion beam patterning of each device was not required.

2.3.2 Single Silver Nanopartile Tracking

The probability of occupancy (P_0) of an entity within a volume element can be calculated from;

$$P_o = D_v C \tag{2.1}$$

where C is the concentration of the targets (in this case, the number of AgNP per mL of solution) and D_v is the detection volume, which in this case was defined as the nanoslits electrophoresis column (75 fL for a 150 nm deep nanoslit with a width of 5 µm and column length of 100 µm). The concentration of AgNPs was adjusted to keep only a single particle resident within the electrophoresis column to aid in single particle tracking. If P_o = 0.01, the probability of double occupancy would be 0.01% and thus, almost all events could be ascribed to single particle events. At P_o = 0.01 and D_v = 75 fL, the particle concentration required to meet this criteria is 1.3 × 10^8/mL. Therefore, the particle concentration used in our experiments was set at 10^8 /mL, meaning that the probability of double occupancy was minimal.

In the absence of an electric field applied across the nanoslit, only Brownian motion of particles was observed. However, in the presence of an electric field, the AgNPs were electrophoretically transported through the nanoslits. We noted that the number of particles entering the nanoslits per unit time was found to increase with increases in the electric field. Wynne et al. observed similar behavior for negatively charged polystyrene beads electrophoresing through a glass nanofluidic device.[18] They hypothesized that for the case of negatively charged walls and negatively charged particles, as in our case, lower buffer concentrations should produce a thicker EDL resulting in particle exclusion from the nanoslit. However, using the PMMA nanoslit devices and buffer concentrations employed herein, we did not observe exclusion effects when a certain voltage threshold was reached (see below) in spite of the fact that the channel walls and AgNP carry negative charges.

2.3.3 Nanoscale Electrophoresis

Figure 2.2 C shows a representation of the electrophoretic transport of a single AgNP in a nanoslit using an electric field strength of 200 V/cm and D in Figure 2.2 shows selected frames from a time-lapse image sequence for the 60 nm AgNPs translocating through the nanoslit.

The average time for the AgNPs to migrate through the nanoslit (length = 100 μm) was 1.3 s at this field strength. This corresponded to a linear velocity of 0.0077 cm/s or an apparent electrophoretic mobility of 3.8×10^{-5} cm^2/Vs. We also observed that both the 60 and 100 nm AgNPs migrated from anode to cathode, suggesting that the electroosmotic flow (EOF) induced by the nanoslit was greater than the electrophoretic mobility of the AgNPs; citric acid is a tricarboxylic acid (pK_{a1} 3.13, pK_{a2} 4.77, pK_{a3} 6.4).[46] At pH 7.4, ~90.9% of the carboxyl groups of the citrate caps associated with the AgNPs are deprotonated; hence, imposing an overall negative charge to the AgNPs inducing an electrophoretic mobility of cathode to anode movement with an

EOF moving from anode to cathode due to the negative surface charge of PMMA following O_2 plasma treatment.[34]

Figure 2.3 shows histograms (100 events) of the observed electrophoretic migration times for the 60 nm (blue stripes) and 100 nm (red stripes) AgNPs transported electrokinetically through a 150 nm nanoslit in 0.05 mM citrate buffer using applied electric fields of 100, 200, 500, 1500 V/cm.

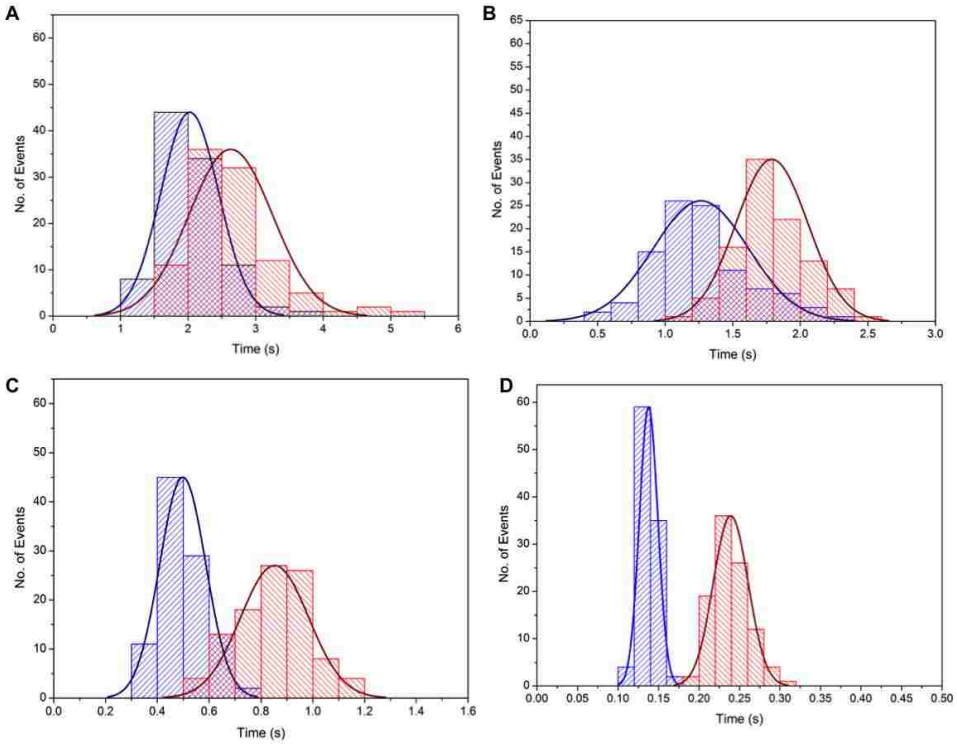

Figure 2.3 Histograms corresponding to the translocation events of 60 nm AgNPs (blue) and 100 nm AgNPs (red) in 150 nm nanoslits in 0.05 mM citrate buffer. Each histogram includes 100 events at a bias voltage of (A) 100 V/cm (B) 200 V/cm (C) 500 V/cm and (D) 1500 V/cm. Note that the time axes has different scale depending on the bias voltage.

We observed "stick/slip" motion of the AgNPs at electric field strengths of 100 and 200 V/cm. This effect was previously observed for DNA translocation studies in nanocolumns,[34, 44, 47] and arose from adsorption/desorption behavior of the solute with the channel walls.[48-50] When a negatively charged particle electrophoretically translocates through nanoscale columns with negatively charged walls under low buffer ionic strengths, it interacts both hydrodynamically and

electrically with the channel walls.[34] Under low electric fields (<200 V/cm), Brownian motion dominates with the possibility of inducing potential wall interactions, even when the solute carries a net charge similar to the column walls, which in this case consisted of PMMA that had been O_2 plasma treated.[34] However, under high fields, electrokinetic forces become dominant and the particle travels predominately longitudinally with minimal wall interactions (see Figure 2.4).

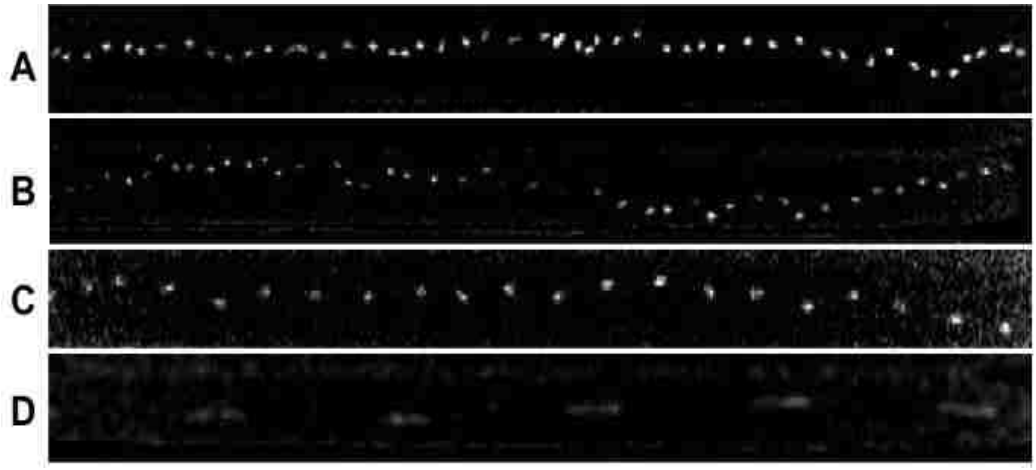

Figure 2.4 Frame-to-frame images of 60 nm AgNPs electrophoretically translocating through a 100 μm long and 150 nm deep nanoslit in a buffer concentration of 0.05 mM citrate. A, B, C, D represent translocation events corresponding to electric field strengths of 100 V/cm, 200 V/cm, 500 V/cm and 1500 V/cm field strengths, respectively.

For O_2 plasma activated PMMA surfaces, the surface charge density has been reported to be -38.3 mC/m^2, yielding ζ (zeta potential) = -57.1 mV, but these values are highly dependent on the dosing level of the plasma (time and power).[34] For O_2 plasma treated PMMA nanofluidic devices, there was a propensity for the negatively charged particles to not enter the nanoslits until a threshold (on-set) voltage was reached, which allowed the AgNPs to be injected into the nanoslit. This on-set voltage was found to be higher using low ionic strength buffers because of the thicker EDL compared to higher ionic strength buffers. For the 150 nm nanoslits, the on-set voltage was found to be ~10 V/cm in a 2.0 mM citrate buffer while in 0.05 mM buffer, this

value increased to ~20 V/cm for the same nanoslit device. In all nanoscale electrophoresis experiments performed using PMMA devices, we did not observe concentration polarization effects at the nanoslit entrance as noted above. We also note that in all cases, the AgNPs traveled from anode to cathode irrespective of the nanoslits dimensions and carrier electrolyte composition, meaning that the electroosmotic flow (EOF) was greater than the electrophoretic mobility of the AgNP.

The apparent mobility (μ_{app}) of the particles is the summation of their electrophoretic mobility (μ_{ep}; the negative sign indicates flow in the direction of the anode, equation 2) and the EOF (μ_{EOF}). The apparent mobility can be calculated from the nanoslit length, *L*, the applied external electric field, *V*, and the migration time, *t* (see equation 2.2).

$$\mu_{app} = \mu_{EOF} + (-\mu_{ep}) = \frac{L^2}{Vt} \tag{2.2}$$

Figure 2.5 shows μ_{app} of AgNPs under different electrokinetic operating conditions (additional histograms are shown in Figure 2.6). The μ_{app} values observed were in the range of 2.0×10^{-5} to 9.0×10^{-5} cm^2/Vs. For the high ionic strength carrier electrolyte, the apparent mobility of the AgNPs was higher compared to the use of a lower ionic strength buffer for both AgNP sizes. In addition, we noticed that as the nanocolumns depth approached the particle diameter, a reduction in the electrophoretic mobility of the AgNPs was observed (B in Figure 2.5)

The electrophoretic velocity of a particle can be calculated using;

$$v_{ep} = -f_H \frac{\varepsilon_0 \varepsilon_r \zeta_p}{\eta} E \tag{2.3}$$

where ζ_p is the zeta potential of the particle and f_H is Henry's function, which depends on *r* (radius) of the particle and its λ_D and represents the retardation effect of particles in

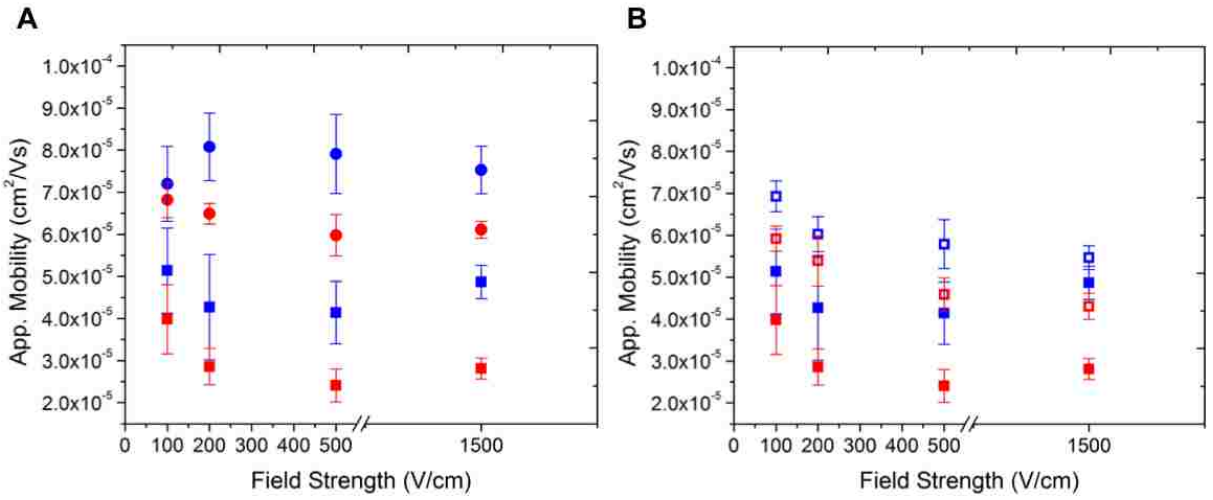

Figure 2.5 Apparent mobilities of AgNPs by nanoelectrophoresis in PMMA nanoslits. Data points corresponding to 60 nm AgNPs are represented in blue while 100 nm AgNPs are represented in red. Each data point represents the mean of 100 translocation events with the error bars depicting the standard deviation. Closed squares correspond to the electrophoresis data at 0.05 mM citrate buffer concentration in 150 nm nanoslits. Closed circles represent data of a 150 nm nanoslits with a running buffer of 2.0 mM citrate. Open squares represent data using 400 nm nanoslits in 0.05 mM citrate buffer. A) Comparison of apparent mobility based on the buffer concentrations of 0.05 mM versus 2.0 mM. B) Comparison of apparent mobilities based on the channel heights, 150 nm versus 400 nm.

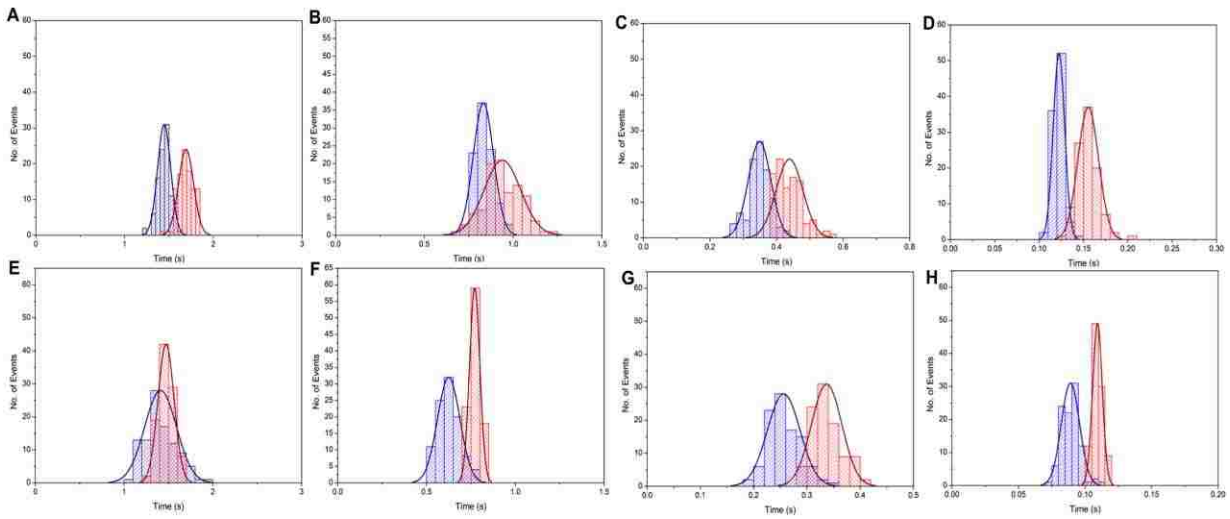

Figure 2.6 Histograms representing electrophoretic translocation events of 60 nm AgNPs (blue strips) and 100 nm AgNPs (red strips). A, B, C, D correspond to events electrophoresed in 0.05 mM buffer using 400 nm deep nanoslits while E, F, G, H correspond to a 2.0 mM buffer in the 150 nm deep nanoslits. Histograms in A and E, B and F, C and G, D and F were secured using field strengths of 100 V/cm, 200 V/cm, 500 V/cm and 1500 V/cm, respectively.

electrophoresis. In systems with a thick λ_D, the effective electric field within the EDL cannot be considered uniform and depends on ζ_p and the ratio of r and λ_D.[17, 51]

When AgNPs are in an ionic buffer such as citrate, the surface is covered with citrate ions acting as a capping agent to prevent agglomeration of the AgNPs. The surface groups induce a charge on the particle, which is represented by ζ_p. At 2.0 mM citrate buffer concentrations, ζ_p of the 60 nm AgNPs was approximately -49.9 mV and for the 100 nm AgNPs, it was -42.6 mV (data from the manufacturer). ζ_p plays a role in determining the particle's electrophoretic mobility (see equation 2.3).[17] Based on the direction of the EOF in these O_2 plasma treated PMMA devices and the observed apparent mobilities, we would expect the 60 nm particles to possess a smaller electrophoretic mobility compared to the 100 nm particles (see equation 2.2). Thus, based on equation 3 and dividing v_{ep} by E, which represents the particle's electrophoretic mobility, we would expect the 60 nm particles to have a larger electrophoretic mobility compared to the 100 nm particles based solely on differences in ζ_p (ζ_p = -49.9 mV and -42.6 mV, for the 60 and 100 nm particles, respectively). Thus, f_H for the 60 nm particles should be considerably smaller than that for the 100 nm AgNPs because the apparent mobility of the 60 nm particles is larger than that of the 100 nm AgNP (*i.e.,* the electrophoretic mobility difference is dominated by differences in the retardation factor as opposed to differences based on ζ_p).

Napoli et al.[17] reported 100 nm polystyrene beads possessed a higher apparent mobility than 50 nm beads in 1 mM buffer concentration and 250 nm deep nanoslits. There were two effects that governed the particle velocity; viscous retardation near a non-conducting boundary, which is described by f_H, and the electric field effects on the particle.[17, 52-53] By tuning the concentration of the buffer, which had an effect on the particles' and channel walls' EDL, it was possible to separate nanoparticles based on differences in their size.[54]

Liu and coworkers were unable to separate AgNPs based on their size (17 nm AgNPs versus 49 nm AgNPs; % size difference = 49%; % size difference = (size difference) / (average particle size)) using conventional CE; the separation was successful only upon addition of SDS to the running electrolyte.[37] We were able to separate the 60 and 100 nm AgNPs (% size difference = 50%) using free solution electrophoresis and 150 nm polymer nanoslits (see Figure 2.3).

2.3.4 Determining the Nanoconfined Diffusion Coefficient

The effective diffusion coefficient (D_{eff}) defines the spatial distribution function of a particle with time. For a particle that undergoes Brownian motion only, the Stokes-Einstein relation[55] can be used to calculate the diffusion coefficient, D_T;

$$D_T = \frac{k_B T}{\gamma} \tag{2.4}$$

where k_B is Boltzmann's constant, T is the absolute temperature of the solution and γ is the hydrodynamic Stokes drag coefficient of the particle, which is given by $\gamma = 6\pi\eta r$ where r is the particle radius. D_T values for 60 nm AgNPs ranged from 7.27 x 10^{-12} to 9.04 x 10^{-12} m^2s^{-1} and for 100 nm AgNPs it was 4.30 × 10^{-12} to 5.33 × 10^{-12} m^2s^{-1} (particle diameter distribution provides the range for D_T values). Experimentally, the diffusion coefficient can also be determined by the electrophoretic peak variance (σ^2) when the peak is fit to a Gaussian function.

The effective diffusion coefficient (D_{eff}) from the Gaussian distribution is given by;

$$D_{eff} = \frac{\sigma^2}{2t} \tag{2.5}$$

$$\sigma^2(t) = 2D_{eff}t \tag{2.6}$$

It should be noted that D_{eff} varies with other factors such as ζ, λ_D and r.[51, 56] We sought to evaluate the effects of nanoconfinement on D_{eff} for the 60 and 100 nm AgNPs.

The variation of time taken by single AgNPs to electrokinetically move through the nanoslits resulted in histograms that could be fit to a Gaussian function (see Figure 2.3). Thus, the variance (σ^2), which is given by the overall width of the Gaussian electrophoretic peak, allowed for determination of D_{eff}. It should be noted that in this case, the electrophoretic peak is defined by a histogram of single AgNP translocation times through the PMMA nanoslits (see Figure 2.3).

The time a single particle takes to travel through a nanoslit is given by equation (2.2) and the variance of particle travel times is given by equation (2.6). Combining equations (2.2) and (2.6), the following relationship could be derived;

$$\sigma^2 = \left(\frac{2D_{eff}L^2}{\mu_{app}}\right)\left(\frac{1}{V}\right) \tag{2.7}$$

For each voltage, the standard deviation (σ), which is the square root of the variance, could be extracted from the width of a Gaussian electrophoretic peak at the point of inflection. $\sigma(t)$ values obtained as such were converted to $\sigma(l)$ by multiplying each σ value with the average velocity at a particular voltage. The particle variance (σ^2) when traveling through the nanoslits under a certain bias voltage could be plotted based on equation (2.7) (Figure 2.7) and the slope of the graph used to calculate D_{eff} values. Not too surprisingly, calculated D_{eff} values indicated that at high applied voltages, spatial diffusion was minimal (see Table 2.1) giving rise to lower σ^2 values. At lower voltages, however, diffusion due to Brownian motion became dominant compared to the electrophoretic force, giving rise to stick/slip motion and thus larger values of σ^2.

The D_{eff} values from Table 2.1 show that they differ by approximately one order of magnitude (larger) compared to the D_T value for each particle diameter. The D_{eff} values can be related to D_T if diffusion is the major contributor to σ^2 during the particle's electrophoretic migration through the nanoslit. However, other factors can contribute to σ^2, such as the

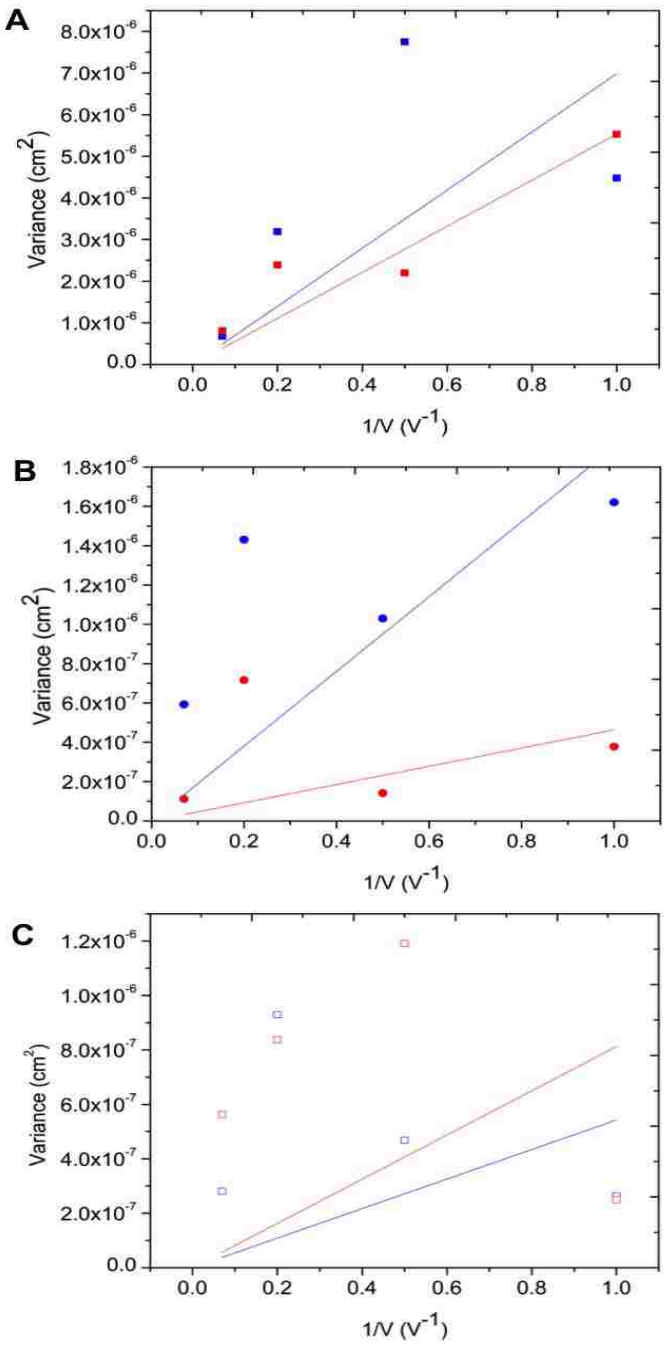

Figure 2.7 Variance (σ^2; cm^2) change of 60 nm (blue) and 100 nm (red) AgNPs as a function of the reciprocal of the bias voltage. The slope of each fitted line represented ($2DL^2/\mu_{app.avg}$). (A) The running buffer was 0.05 mM citrate buffer with the nano-electrophoresis carried out using a 150 nm deep nanoslit with ($slope_{60}$) = 6.98×10^{-6} cm^2V^{-1} and ($slope_{100}$) = 5.53×10^{-6} cm^2V^{-1}. (B) Nano-electrophoresis using a 2.0 mM citrate and 150 nm deep nanoslit device with ($slope_{60}$) = 1.90×10^{-6} cm^2V^{-1} and ($slope_{100}$) = 4.63×10^{-7} cm^2V^{-1}. (C) Nano-electrophoresis using 0.05 mM citrate buffer in a 400 nm deep nanoslits device with ($slope_{60}$) = 5.42×10^{-7} cm^2V^{-1} and ($slope_{100}$) = 8.12×10^{-7} cm^2V^{-1}.

Table 2.1 Comparison of calculated diffusion coefficient and variance for each experimental condition

Nanoslit size	Citrate Buffer Concentration	AgNP size r (nm)	Applied Voltage V (V)	Standard Deviation $\sigma(t)$ (s)	Variance $\sigma^2(l)$ (cm^2)	Diffusion Coefficient D_{exp} (m^2s^{-1})
150 nm	0.05 mM	60	1	0.4284	4.48E-6	1.54E-10
			2	0.3520	7.75E-6	
			5	0.0889	3.19E-6	
			15	0.0113	6.77E-7	
		100	1	0.6189	5.53E-6	8.10E-11
			2	0.2655	2.20E-6	
			5	0.1319	2.39E-6	
			15	0.0215	8.11E-7	
150 nm	2.00 mM	60	1	0.1795	1.62E-6	7.18E-11
			2	0.0633	1.03E-6	
			5	0.0307	1.43E-6	
			15	0.0069	5.93E-7	
		100	1	0.0905	3.78E-7	1.46E-11
			2	0.0291	1.42E-7	
			5	0.0285	7.16E-7	
			15	0.0037	1.12E-7	
400 nm	0.05 mM	60	1	0.0741	2.63E-7	1.64E-11
			2	0.0569	4.68E-7	
			5	0.0336	9.29E-7	
			15	0.0065	2.81E-7	
		100	1	0.0846	2.50E-7	2.04E-11
			2	0.1025	1.19E-6	
			5	0.0402	8.38E-7	
			15	0.0117	5.63E-7	

heterogeneity in the particle size during manufacturing. According to the manufacturer, the particle diameter for 60 nm AgNPs was 60.8 ±6.6 nm (RSD = 10.9%) and for the 100 nm AgNPs, it was 103.0 ±11.0 nm (RSD = 10.7%). Therefore, variations in particle size can affect σ^2 as well. Also, because particles of similar size may contain different numbers of citrate groups due to initiators and adsorbed inhibitors on the surface,[17] this can result in differences in the apparent mobility as well.

2.3.5 Separation Efficiency and Resolution of Nanoscale Electrophoresis

Nanoscale electrophoresis performance can be evaluated from the number of theoretical plates, *N*, given by;

$$N = \frac{\mu_{avg\ app}\mathrm{V}}{2D_T} = \frac{L^2}{2D_T t_{avg}} \tag{2.8}$$

In Table 2.2, *N* is presented as a function of different nano-CE operating conditions. Here we considered that D_{eff} was limited to Brownian motion only and thus, $D_{eff} \approx D_T$. Even though it contained a level of uncertainty, using D_T provided sufficient information about the efficiency of the separation due to heterogeneous particle sizes as employed herein.[57] At high electric field strengths it was noticed that *N* increased for both the 60 nm and 100 nm particles as compared to lower electric field strengths (see Figure 2.8). But, *N* did depend upon the ratio of the particle's apparent mobility and D_T. Even though it was expected that a higher plate number should result for larger particles (higher *r* and thus lower D_T from equation (2.4)), it is evident that the apparent mobility played a significant role in determining the plate numbers for the separation (see Table 2.2).

In our experiment, we evaluated *N* at field strengths up to 1500 V/cm for columns that were 100 μm in length. In conventional CE, Joule heating limits the electric field strength that can be used. But, because of the high surface-to-volume ratio in nanoslits, heat dissipation is efficient

Table 2.2 Basic electrophoretic parameters for 60 nm and 100 nm AgNPs at different nanoslits dimensions and different buffer concentrations.

Nanoslit dimension	Citrate Buffer Concentration	Field Strength (V/cm)	AgNP size (nm)	Plate Number (N)	Variance (σ^2) × 10^{-12}	Resolution (R)
150 nm	0.05 mM	100	60	303	33.00	0.2190
			100	233	43.00	
		200	60	486	20.60	0.3333
			100	570	17.50	
		500	60	1224	8.17	0.7447
			100	1200	8.33	
		1500	60	4371	2.29	1.1111
			100	4250	2.35	
150 nm	2.00 mM	100	60	836	13.82	0.0889
			100	694	14.41	
		200	60	1093	10.13	0.7692
			100	1325	7.55	
		500	60	2661	4.25	0.5714
			100	3000	3.33	
		1500	60	7650	1.47	0.6667
			100	9273	1.08	
400 nm	0.05 mM	100	60	422	23.70	0.5854
			100	371	27.00	
		200	60	737	13.60	0.2651
			100	1085	9.20	
		500	60	1749	5.72	0.5143
			100	2318	4.31	
		1500	60	5100	1.96	0.6154
			100	6375	1.57	

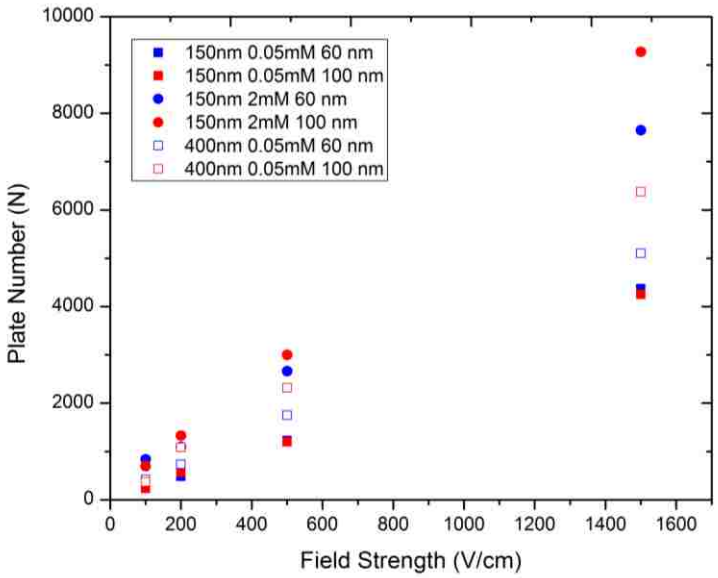

Figure 2.8 The efficiency of the column in terms of plate number with respect to the applied in the field strengths. At each experimental condition, data points corresponding to both 60 nm and 100 nm shows a linear increase with increasing field strength.

resulting in lower thermal effects compared to larger size columns, for example microchannels.[58] Hence, potentially higher voltages can be used for nanoscale columns without observing deleterious effects in *N*. From the data, *N* increased linearly with the electric field strength and at 1500 V/cm, the efficiency of the nanoscale electrophoresis increased 10^3 fold compared to *N* observed at 200 V/cm (see Figure 2.8 and Table 2.2). We could not test higher electric field strengths due to the limited frame rate we could achieve with our CCD camera.

When two species electrophorese in a column with average migration times, t_{R1} and t_{R2}, the resolution of the separation is given by;

$$R_S = \frac{2(t_{R1} - t_{R2})}{1.7(W_{0.5,1} + W_{0.5,2})} \tag{2.9}$$

where $W_{0.5,1}$ and $W_{0.5,2}$ corresponds to the width of the two peaks at the half maximum of the Gaussian peaks obtained from the histograms shown in Figure 2.3. The calculated resolution values are presented in Table 2.2. A R_S of 1.1 was achieved in 150 nm nanoslits in 0.05 mM

citrate using an electric field strength of 1500 V/cm. We noted a decrease in resolution at lower electric field strengths most likely due to a combination of longitudinal diffusion and stick/slip motion that occurred at lower electric fields.

It has been reported that a decrease in R_S results when transitioning from micro- to nanoscale electrophoresis for multiple particle occupancy within the nanoslit.[17-18] For example, Napoli and Pennathur noticed a decrease in plate numbers resulting in lower R_S for polystyrene beads in glass nanoslits. They suggested that the negatively charged particles and negatively charged channel walls played a significant role in affecting R_S.[17] Also, electrostatic repulsion of the polystyrene beads from the channel walls pushed the nanoparticles to the center of the channel, which increased the local concentration of the beads within the center of the channel leading to changes in viscous retardation. In our case, the probability of finding more than one particle in the nanoslit was below 0.01% (see equation 2.1). Therefore, we did not expect to see changes in the viscous retardation.

EOFs are typically higher in non-modified glass electrophoresis devices compared to PMMA devices that have been activated with an O_2 plasma.[34] The surface charge characteristics and the effects of pH on the EOF of polymer devices has been discussed in detail in a recent publication by our group.[34] For PMMA nanoslits of 50 nm (depth) × 3 μm (width), the surface charge was found to be –38.3 mC/m^2 with a ζ value of -57.1 mV. The measured EOF in the nanoslits was 0.93 ±0.02 × 10^{-4} cm^2/Vs. This value was lower than that reported for fused silica.[59] Considering that the migration time of a given particle is affected by the EOF and μ_{ep}, a negatively charged particle will spend more time in a channel under high EOF conditions giving rise to lower plate numbers and therefore, reduced resolution. Therefore, compared to untreated glass devices, we expect polymer-based nanofluidic devices to provide improved resolution for negatively charged

entities in nanoscale electrophoretic separations due to the associated lower EOF. Also, because of the ability to control the surface charge by controlled dosing of the channel walls with the O_2 plasma, polymer nanoslits and nanochannels obviate the deleterious effects of concentration polarization.

2.4 Conclusions

AgNPs were used as a model system to investigate the utility of nanoscale electrophoresis using thermoplastics as the substrate material that was activated using O_2 plasma that generated negatively charged functional groups (carboxylic acids) that could support an EOF. Free solution mobility differences for 60 nm and 100 nm AgNPs was observed using PMMA nanoslits that were ~100 µm in length that could not be achieved using a microchannel column.[37] A separation of AgNPs based on size using PMMA-based nanoslit columns was demonstrated with 10^3 fold improvement in N and R_s >1 in less than 2 s when using E > 200 V/cm. Further improvements in the electrokinetic separation could be realized by using higher electric field strengths and smaller sized column cross-sectional areas that could provide the ability to use extremely high electric field strengths that would further eliminate deleterious effects produced by stick/slip motion and/or zonal dispersion generated by longitudinal diffusion.

2.5 References

1. Dolník, V.; Liu, S.; Jovanovich, S., Capillary electrophoresis on microchip. *ELECTROPHORESIS* 2000, *21* (1), 41-54.

2. Pumera, M.; Wang, J.; Grushka, E.; Polsky, R., Gold Nanoparticle-Enhanced Microchip Capillary Electrophoresis. *Analytical Chemistry* 2001, *73* (22), 5625-5628.

3. Kinsella, A.; Minteer, S., Microchip Devices for Bioanalysis. In *Molecular Biomethods Handbook*, Walker, J.; Rapley, R., Eds. Humana Press: 2008; pp 851-859.

4. Nilsson, C.; Birnbaum, S.; Nilsson, S., Use of nanoparticles in capillary and microchip electrochromatography. *Journal of Chromatography A* 2007, *1168* (1–2), 212-224.

5. Osiri, J. K.; Shadpour, H.; Park, S.; Snowden, B. C.; Chen, Z.-Y.; Soper, S. A., Generating high peak capacity 2-D maps of complex proteomes using PMMA microchip electrophoresis. *ELECTROPHORESIS* 2008, *29* (24), 4984-4992.

6. Osiri, J.; Shadpour, H.; Soper, S., Ultra-fast two-dimensional microchip electrophoresis using SDS μ-CGE and microemulsion electrokinetic chromatography for protein separations. *Anal Bioanal Chem* 2010, *398* (1), 489-498.

7. Lin, C.-H.; Lee, G.-B.; Chen, S.-H.; Chang, G.-L., Micro capillary electrophoresis chips integrated with buried SU-8/SOG optical waveguides for bio-analytical applications. *Sensors and Actuators A: Physical* 2003, *107* (2), 125-131.

8. Turner, S. W.; Cabodi, M.; Craighead, H. G., Confinement-induced entropic recoil of single DNA molecules in a nanofluidic structure. *Physical review letters* 2002, *88* (12), 128103.

9. Danelon, C.; Santschi, C.; Brugger, J.; Vogel, H., Fabrication and Functionalization of Nanochannels by Electron-Beam-Induced Silicon Oxide Deposition†. *Langmuir* 2006, *22* (25), 10711-10715.

10. Han, J.; Craighead, H. G., Separation of Long DNA Molecules in a Microfabricated Entropic Trap Array. *Science* 2000, *288* (5468), 1026-1029.

11. Woods, L. A.; Gandhi, P. U.; Ewing, A. G., Electrically Assisted Sampling across Membranes with Electrophoresis in Nanometer Inner Diameter Capillaries. *Analytical Chemistry* 2005, *77* (6), 1819-1823.

12. Bayley, H.; Martin, C. R., Resistive-Pulse SensingFrom Microbes to Molecules. *Chemical Reviews* 2000, *100* (7), 2575-2594.

13. Kemery, P. J.; Steehler, J. K.; Bohn, P. W., Electric Field Mediated Transport in Nanometer Diameter Channels. *Langmuir* 1998, *14* (10), 2884-2889.

14. Kuo, T.-C.; Sloan, L. A.; Sweedler, J. V.; Bohn, P. W., Manipulating Molecular Transport through Nanoporous Membranes by Control of Electrokinetic Flow: Effect of Surface Charge Density and Debye Length. *Langmuir* 2001, *17* (20), 6298-6303.

15. Pennathur, S.; Santiago, J. G., Electrokinetic Transport in Nanochannels. 2. Experiments. *Analytical Chemistry* 2005, *77*, 6782-6789.

16. Pennathur, S.; Santiago, J. G., Electrokinetic Transport in Nanochannels. 1. Theory. *Analytical Chemistry* 2005, *77* (21), 6772-6781.

17. Napoli, M.; Atzberger, P.; Pennathur, S., Experimental study of the separation behavior of nanoparticles in micro- and nanochannels. *Microfluid Nanofluid* 2011, *10* (1), 69-80.

18. Wynne, T.; Dixon, A.; Pennathur, S., Electrokinetic characterization of individual nanoparticles in nanofluidic channels. *Microfluid Nanofluid* 2012, *12* (1-4), 411-421.

19. Baldessari, F.; Santiago, J., Electrophoresis in nanochannels: brief review and speculation. *Journal of Nanobiotechnology* 2006, *4* (1), 12.

20. Yuan, Z.; Garcia, A. L.; Lopez, G. P.; Petsev, D. N., Electrokinetic transport and separations in fluidic nanochannels. *ELECTROPHORESIS* 2007, *28* (4), 595-610.

21. Pennathur, S.; Santiago, J. G., Electrokinetic Transport in Nanochannels. 1. Theory. *Analytical Chemistry* 2005, *77*, 6772-6781.

22. Xuan, X.; Li, D., Electrokinetic transport of charged solutes in micro- and nanochannels: The influence of transverse electromigration. *Electrophoresis* 2006, *27*, 5020-5031.

23. Xuan, X., Ion separation in nanofluidics. *Electrophoresis* 2008, *29*, 3737-3743.

24. Garcia, A. L.; Ista, L. K.; Petsev, D. N.; O'Brien, M. J.; Bisong, P.; Mammoli, A. A.; Brueck, S. R. J.; Lopez, G. P., Electrokinetic molecular separation in nanoscale fluidic channels. *Lab on a Chip* 2005, *5* (11), 1271 - 1276.

25. Guo, L. J. C. a. L. J., Ionic current rectification, breakdown, and switching in heterogeneous oxide nanofluidic devices. *ACS Nano* 2009, *3*, 575-584.

26. Austin, M. D.; Ge, H. X.; Wu, W.; Li, M. T.; Yu, Z. N.; Wasserman, D.; Lyon, S. A.; Chou, S. Y., Fabrication of 5 nm linewidth and 14 nm pitch features by nanoimprint lithography. *Applied Physics Letters* 2004, *84* (26), 5299-5301.

27. Chou, S. Y.; Krauss, P. R., Imprint lithography with sub-10 nm feature size and high throughput. *Microelectronic Engineering* 1997, *35* (1-4), 237-240.

28. Chou, S. Y.; Krauss, P. R.; Renstrom, P. J., IMPRINT OF SUB-25 NM VIAS AND TRENCHES IN POLYMERS. *Applied Physics Letters* 1995, *67* (21), 3114-3116.

29. Chou, S. Y.; Krauss, P. R.; Renstrom, P. J., Nanoimprint lithography. *Journal of Vacuum Science & Technology B* 1996, *14* (6), 4129-4133.

30. Gates, B. D.; Whitesides, G. M., Replication of vertical features smaller than 2 nm by soft lithography. *Journal of the American Chemical Society* 2003, *125* (49), 14986-14987.

31. Abgrall, P.; Low, L.-N.; Nguyen, N.-T., Fabrication of planar nanofluidic channels in a thermoplastic by hot-embossing and thermal bonding. *Lab on a Chip* 2007, *7* (4), 520-522.

32. Chantiwas, R.; Hupert, M. L.; Pullagurla, S. R.; Balamurugan, S.; Tamarit-Lopez, J.; Park, S.; Datta, P.; Goettert, J.; Cho, Y. K.; Soper, S. A., Simple replication methods for producing nanoslits in thermoplastics and the transport dynamics of double-stranded DNA through these slits. *Lab Chip* 2010, *10*, 3255-3264.

33. Thamdrup, L. H.; Klukowska, A.; Kristensen, A., Stretching DNA in polymer nanochannels fabricated by thermal imprint in PMMA. *Nanotechnology* 2008, *19*, 125301.

34. Uba, F. I.; Pullagurla, S. R.; Sirasunthorn, N.; Wu, J.; Park, S.; Chantiwas, R.; Cho, Y.-K.; Shin, H.; Soper, S. A., Surface charge, electroosmotic flow and DNA extension in chemically modified thermoplastic nanoslits and nanochannels. *Analyst* 2015, *140* (1), 113-126.

35. Uba, F. I.; Hu, B.; Weerakoon-Ratnayake, K.; Oliver-Calixte, N.; Soper, S. A., High process yield rates of thermoplastic nanofluidic devices using a hybrid thermal assembly technique. *Lab on a Chip* 2015, *15* (4), 1038-1049.

36. Radko, S. P.; Chrambach, A., Capillary electrophoresis of subcellular-sized particles. *Journal of Chromatography B: Biomedical Sciences and Applications* 1999, *722* (1–2), 1-10.

37. Liu, F.-K.; Ko, F.-H.; Huang, P.-W.; Wu, C.-H.; Chu, T.-C., Studying the size/shape separation and optical properties of silver nanoparticles by capillary electrophoresis. *Journal of Chromatography A* 2005, *1062* (1), 139-145.

38. Harms, Z. D.; Selzer, L.; Zlotnick, A.; Jacobson, S. C., Monitoring Assembly of Virus Capsids with Nanofluidic Devices. *ACS Nano* 2015, *9* (9), 9087-9096.

39. Wu, J. H.; Chantiwas, R.; Amirsadeghi, A.; Soper, S. A.; Park, S., Complete plastic nanofluidic devices for DNA analysis via direct imprinting with polymer stamps. *Lab on a Chip* 2011, *11* (17), 2984-2989.

40. Huang, T.; Nallathamby, P. D.; Xu, X.-H. N., Photostable Single-Molecule Nanoparticle Optical Biosensors for Real-Time Sensing of Single Cytokine Molecules and Their Binding Reactions. *Journal of the American Chemical Society* 2008, *130* (50), 17095-17105.

41. Nallathamby, P. D.; Lee, K. J.; Xu, X.-H. N., Design of Stable and Uniform Single Nanoparticle Photonics for In Vivo Dynamics Imaging of Nanoenvironments of Zebrafish Embryonic Fluids. *ACS Nano* 2008, *2* (7), 1371-1380.

42. Lee, K. J.; Nallathamby, P. D.; Browning, L. M.; Osgood, C. J.; Xu, X.-H. N., In Vivo Imaging of Transport and Biocompatibility of Single Silver Nanoparticles in Early Development of Zebrafish Embryos. *ACS Nano* 2007, *1* (2), 133-143.

43. Wu, J.; Chantiwas, R.; Amirsadeghi, A.; Soper, S. A.; Park, S., Complete plastic nanofluidic devices for DNA analysis via direct imprinting with polymer stamps. *Lab on a Chip* 2011, *11* (17), 2984-2989.

44. Chantiwas, R.; Hupert, M. L.; Pullagurla, S. R.; Balamurugan, S.; Tamarit-Lopez, J.; Park, S.; Datta, P.; Goettert, J.; Cho, Y.-K.; Soper, S. A., Simple replication methods for producing nanoslits in thermoplastics and the transport dynamics of double-stranded DNA through these slits. *Lab on a Chip* 2010, *10* (23), 3255-3264.

45. Amirsadeghi, A.; Lee, J. J.; Park, S., Surface adhesion and demolding force dependence on resist composition in ultraviolet nanoimprint lithography. *Applied Surface Science* 2011, *258* (3), 1272-1278.

46. Goldberg, R. N.; Kishore, N.; Lennen, R. M., Thermodynamic Quantities for the Ionization Reactions of Buffers. *Journal of Physical and Chemical Reference Data* 2002, *31* (2), 231-370.

47. Campbell, L. C.; Wilkinson, M. J.; Manz, A.; Camilleri, P.; Humphreys, C. J., Electrophoretic manipulation of single DNA molecules in nanofabricated capillaries. *Lab on a Chip* 2004, *4* (3), 225-229.

48. Luan, B.; Afzali, A.; Harrer, S.; Peng, H.; Waggoner, P.; Polonsky, S.; Stolovitzky, G.; Martyna, G., Tribological Effects on DNA Translocation in a Nanochannel Coated with a Self-Assembled Monolayer. *The Journal of Physical Chemistry B* 2010, *114* (51), 17172-17176.

49. Novak, B. R.; Moldovan, D.; Nikitopoulos, D. E.; Soper, S. A., Distinguishing Single DNA Nucleotides Based on Their Times of Flight Through Nanoslits: A Molecular Dynamics Simulation Study. *The Journal of Physical Chemistry B* 2013, *117* (12), 3271-3279.

50. Xia, K.; Novak, B. R.; Weerakoon-Ratnayake, K. M.; Soper, S. A.; Nikitopoulos, D. E.; Moldovan, D., Electrophoretic Transport of Single DNA Nucleotides through Nanoslits: A Molecular Dynamics Simulation Study. *The Journal of Physical Chemistry B* 2015.

51. Henry, D. C., The Cataphoresis of Suspended Particles. Part I. The Equation of Cataphoresis. *Proceedings of the Royal Society of London A: Mathematical, Physical and Engineering Sciences* 1931, *133* (821), 106-129.

52. Xuan, X.; Xu, B.; Li, D., Accelerated Particle Electrophoretic Motion and Separation in Converging−Diverging Microchannels. *Analytical Chemistry* 2005, *77* (14), 4323-4328.

53. Xuan, X.; Raghibizadeh, S.; Li, D., Wall effects on electrophoretic motion of spherical polystyrene particles in a rectangular poly(dimethylsiloxane) microchannel. *Journal of Colloid and Interface Science* 2006, *296* (2), 743-748.

54. Schnabel, U.; Fischer, C.-H.; Kenndler, E., Characterization of colloidal gold nanoparticles according to size by capillary zone electrophoresis. *Journal of Microcolumn Separations* 1997, *9* (7), 529-534.

55. Einstein, A., On the movement of small particles suspended instationary liquids required by the molecular-kinetic theory ofheat. *Annalen der Physik* 1905, *17*, 549–560.

56. Kirby, B. J.; Hasselbrink, E. F., Zeta potential of microfluidic substrates: 1. Theory, experimental techniques, and effects on separations. *ELECTROPHORESIS* 2004, *25* (2), 187-202.

57. Palanisami, A.; Miller, J. H., Simultaneous sizing and electrophoretic mobility measurement of sub-micron particles using Brownian motion. *ELECTROPHORESIS* 2010, *31* (21), 3613-3618.

58. Jorgenson, J. W.; Lukacs, K. D., Capillary Zone Electrophoresis. *Science* 1983, *222* (4621), 266-272.

59. Menard, L. D.; Mair, C. E.; Woodson, M. E.; Alarie, J. P.; Ramsey, J. M., A device for performing lateral conductance measurements on individual double-stranded DNA molecules. *ACS nano* 2012, *6* (10), 9087-9094.

CHAPTER 3. HYRID NANOFLUIDIC DEVICES AND THEIR APPLICATIONS FOR SINGLE MOLECULAR FLUORESCENE DETECTION

3.1 General Introduction

The following chapter contains two main sections. The first section discusses a hybrid thermal assembly process, a method we recently developed in our laboratory. The fabrication methodology has been developed with a high glass transition substrate that can be sealed to a low glass transition cover plate in order to facilitate optical detection with better optical clarity and utilize tracking of single molecules with enhanced resolution. The hybrid assembly approach also prevents distortion of the formed nanostructures during the assembly process. A provisional patent for this approach has been submitted for the approval.[2,3]

The second section discusses about an application based on the hybrid nanofluidic device assembly. This study has shown that the hybrid devices can be used for single molecule imaging with better signal to noise ratio and resolution. Specifically, the focus on this study is to build an assay for chemotherapeutically induced damage site detection using the hybrid nanofluidic devices. DNA with chemotherapeutically induced damage sites (AP sites) are stretched in nanochannels and the AP sites are detected using dual color fluorescence detection. Preliminary studies have shown the importance and ease of use of the assay compared to the available conventional assays, which will be further discussed in this chapter.

[2] Provisional patent filed on September 15, 2014 in the United States Patent and Trademark Office (U.S. Provisional application number 62/050, 237); Inventors: Kumuditha M. Weerakoon-Ratnayake, Franklin I. Uba, Nyote J. Oliver-Calixte, Steven A. Soper

[3] This section is originally published in Lab-On-a-Chip (2015), *15* (4), 1038-1049, DOI: 10.1039/C4LC01254B; Featured in December HOT article and inside back cover page DOI: 10.1039/C5LC90025E; Author list includes Uba, F. I.; Hu, B.; Weerakoon-Ratnayake, K.; Oliver-Calixte, N.; Soper, S. A.

3.2 High Process Yield Rates of Thermoplastic Nanofluidic Devices using a Hybrid Thermal Assembly Technique

3.2.1 Introduction

Nanofluidic devices have generated great interest for investigating several unique physical and chemical phenomena that are not readily obtainable in micro-scale environments. For example, nanofluidic devices have served as viable platforms for the analysis of biopolymers, especially DNAs.[1-2] When a double-stranded DNA (dsDNA) is contained in a microchannel, it will assume a randomly coiled-state (low entropy) with a radius of gyration (R_g) defined by the ionic strength of the solution and the contour length of the molecule.[3] However, when confined in a nanochannel with dimensions (width x depth) comparable to its persistence length, ~50 nm for a dsDNA, the molecule stretches with the degree of stretching inversely proportional to the nanochannel dimensions.[4-7] This phenomenon has generated interesting applications such as rapid probing of conformational, dynamic and entropic properties of DNA molecules for the determination of the spatial location of genetic information,[8] identification of methylation patterns within dsDNA,[9] restriction mapping of genomic DNA,[10] DNA fragment sizing,[11] localization of transcription factors for protein synthesis to a specific gene or binding site,[12] and high signal-to-noise ratio detection of DNA with minimal multiple occupancy artifacts.[13]

Recently, polymer-based materials, especially thermoplastics – linear or branched polymers with high molecular weights – have become viable substrates for the fabrication of nanofluidic devices. Thermoplastics such as poly(methyl methacrylate) (PMMA), polycarbonate (PC), cyclo-olefin copolymer (COC) and polyethylene terephthalate (PET) possess glass transition temperatures (T_g) that are significantly smaller than glass allowing for the fabrication of nanostructures using nanoimprint lithography (NIL), which is conducive to high production rates at low-cost and with good replication fidelity.[14] NIL has been successful in patterning structures

down to the sub-10 nm scale with the ultimate resolution seemingly determined by the minimum feature size associated with the molding tool.[15-18] Other modalities that can be used to fabricate thermoplastic nanochannels include proton beam writing,[19] thermomechnical deformation,[20] compression of microchannels,[21] sidewall lithography and hot embossing,[22] UV-lithography/O_2 plasma etching,[23] hot embossing with thermoplastic molding tools,[24] refill of microchannels,[25] and the use of silica nanowire templates.[26]

The aforementioned techniques for producing nanochannels in thermoplastics employed a top-down approach and as such, require an assembly step to enclose the fluidic network. Unfortunately, challenges associated with assembling devices with the cover plates have limited the use of thermoplastic-based nanofluidic devices with the smallest operational 2D thermoplastic nanochannel reported till date being 71 × 77 nm (width × depth). In a typical fluidic device production pipeline, the final step involves bonding the thermoplastic substrate possessing the fluidic network to a second plastic material (cover plate) that encloses the channels. The common modes employed for enclosing thermoplastic nanochannels are thermal or solvent-assisted fusion bonding.[27] Thermal fusion bonding the substrate to a cover plate of the same material has been executed by; (i) heating the substrate and cover plate to slightly above its T_g while applying a constant pressure, thereby allowing polymer chains to diffuse between the contact surfaces; or (ii) bonding at a temperature lower than the T_g of the material by using UV or oxygen plasma treatment of the substrate and cover plate prior to chip assembly, thereby reducing the T_g of the first few layers of material.[16-18, 28-29] Although both approaches have been reported to produce high tensile strengths between the cover plate and substrate, the first approach is typically discouraged for assembly of thermoplastic nanofluidic devices because it results in bulk polymer flow and significant deformation or collapse of the nanochannels (40%

and 60% deformation for PMMA and COC, respectively) rendering devices unusable in most cases. The second approach is commonly used for enclosing thermoplastic nanochannels; however, the resulting bond strength is often lower than desired and thus, are unable to withstand high pressure or electric fields for extended periods of time.[16] Preliminary results obtained from our group have revealed that nanochannels experience reduction in depths (6% for PMMA and 9% for COC) when sealed with cover plates of the same material by fusion bonding at a temperature below its bulk T_g after plasma treatment.[16] Unfortunately, these channel dimensional changes increased as the nanochannel dimensions dropped below 50 nm and resulted in low process yield rates (*i.e.,* low rates of producing successful devices). Likewise, solvent-assisted bonding suffers from problems associated with dimensional stability because the solvent can soften and embrittle the plastic material leading to material dissolution.[27] Hence, there remains the need for the development of methods for sealing thermoplastic nanochannels with high bond strength while maintaining structural integrity and producing high process yield rates.

Herein, we report a robust mode for the assembly of thermoplastic nanofluidic devices in which a high T_g thermoplastic substrate possessing the nanofluidic structures is bonded to a cover plate with a T_g lower than that of the substrate. Although, a similar scheme was proposed for sealing COC-based microsystems[30] and recently reported for sealing PMMA nanochannels using a PET cover plate,[31] the smallest assembled nanochannels were ~85 nm and the functionality of these devices for biological applications were not demonstrated. In this study, COC (T_g = 75ºC) was used as the cover plate due to its excellent optical transmissivity (with low propagation loss at λ >300 nm), low autofluorescence,[32-33] excellent biocompatibility, low moisture uptake (< 0.01%), high temperature tolerance, chemical resistance and ease of surface modification via UV activation or plasma treatment. The T_g of COC depends on the norbornene

content and can range from 65 – 180°C for norbornene contents ranging from 60 – 85 wt%, respectively.[30, 34] Nanofluidic channels were fabricated in a substrate (PMMA; T_g = 105°C or COC; T_g = 178°C) via a single imprinting step as previously reported.[35] Device assembly was achieved by bonding the plasma treated cover plate (COC; T_g = 75°C) to the untreated substrate at a temperature ~5°C lower than the T_g of the cover plate. In contrast to the high temperature, time-consuming and long processing steps required for enclosing glass nanofluidic devices,[36-37] our assembly process was performed directly on the thermoplastic substrate following embossing without the need of pre-cleaning or cleanroom conditions in a total time of 15 min. With this assembly approach, we demonstrated the utilization of sub-50 nm thermoplastic nanochannels for high SNR fluorescent imaging and DNA stretching. Bond strengths higher than those of the native polymers assembled at a temperature above its T_g were achieved with a process yield – percent of working assembled devices that retained the nanochannel dimensions predefined in the original Si master – >90% without deformation or collapse of the nanostructures. Finally, nanochannels were successfully modified via UV-activation through the cover plate post-assembly and the functionality of the assembled devices was assessed by investigating the transport dynamics of dsDNA through the nanochannels.

3.2.2 Experimental Methods

3.2.2.1 Materials and Reagents

PMMA sheets (T_g = 105°C), 1.5 mm and 0.175 mm thick, were purchased from Good Fellow (Berwyn, PA). Cyclic olefin copolymer (COC) 6017 ($T_g \approx$ 178°C), 5010 ($T_g \approx$ 108°C) and 8007 ($T_g \approx$ 78°C; 0.13 mm) sheets were purchased from TOPAS Advanced Polymers (Florence KY). Si <100> wafers were purchased from University Wafers (Boston, MA). Tripropylene glycol diacrylate (TPGA), trimethylolpropane triacrylate (TMPA), Irgacure 651 (photo-initiator), 50%

potassium hydroxide (KOH), hydrochloric acid (HCl) and potassium chloride (KCl) were obtained from Sigma-Aldrich (St. Louis, MO). The anti-adhesion monolayer of (tridecafluoro – 1,1,2,2 – tetrahydrooctyl) tricholorosilane (T-silane) was purchased from Gelest, Inc. Tris buffer (pH = 8.0) was obtained from Fisher Scientific (Houston, TX). All dilutions were performed using 18 MΩ/cm milliQ water (Millipore).

3.2.2.2 Device Fabrication

Nanofluidic structures were fabricated in thermoplastic substrates using a scheme previously reported by our group.[35] Briefly, access microchannels and nanochannels were fabricated in a Si wafer (master) by optical lithography and focused-ion beam milling, respectively. Next, resin stamps were produced from the Si master by curing a UV-resin (68 wt% TPGA, 28 wt% TMPA and 4 wt% Irgacure 651) under 365 nm light coated onto a COC 6017 plate. Subsequently, fluidic structures were imprinted into the polymer substrate by thermal embossing at 125^{o}C for 120 s under 1910 kN/m^2 pressure using a Hex03 hot embosser (JenOptik). In the final fabrication step, fluidic structures were enclosed with a low T_g thermoplastic cover plate using the setup shown in Figure 3.1.

The assembly scheme used an untreated substrate possessing the fluidic structures and an oxygen plasma treated cover plate that were brought into conformal contact and then placed in a vacuum seal bag for 20 min to eliminate air pockets from the contacted substrate/cover plate. Next, the partially bonded device (determined by the lack of Newton rings) was sandwiched between a pair of polyimide films, rubber sheets and placed between the platens of the thermal embosser (see (a) in Figure 3.1). We found that the rubber sheets promoted bond uniformity across the entire surfaces while the polyimide film prevented sticking of the thermoplastic nanofluidic device to the rubber sheets. The temperature, pressure and time were found to be

important process parameters, which depended primarily on the thermal, mechanical, physical and surface properties of the cover plate.

As shown in (b) of Figure 3.1, the temperature–pressure process program used for enclosing the fluidic structures was partitioned into six stages:

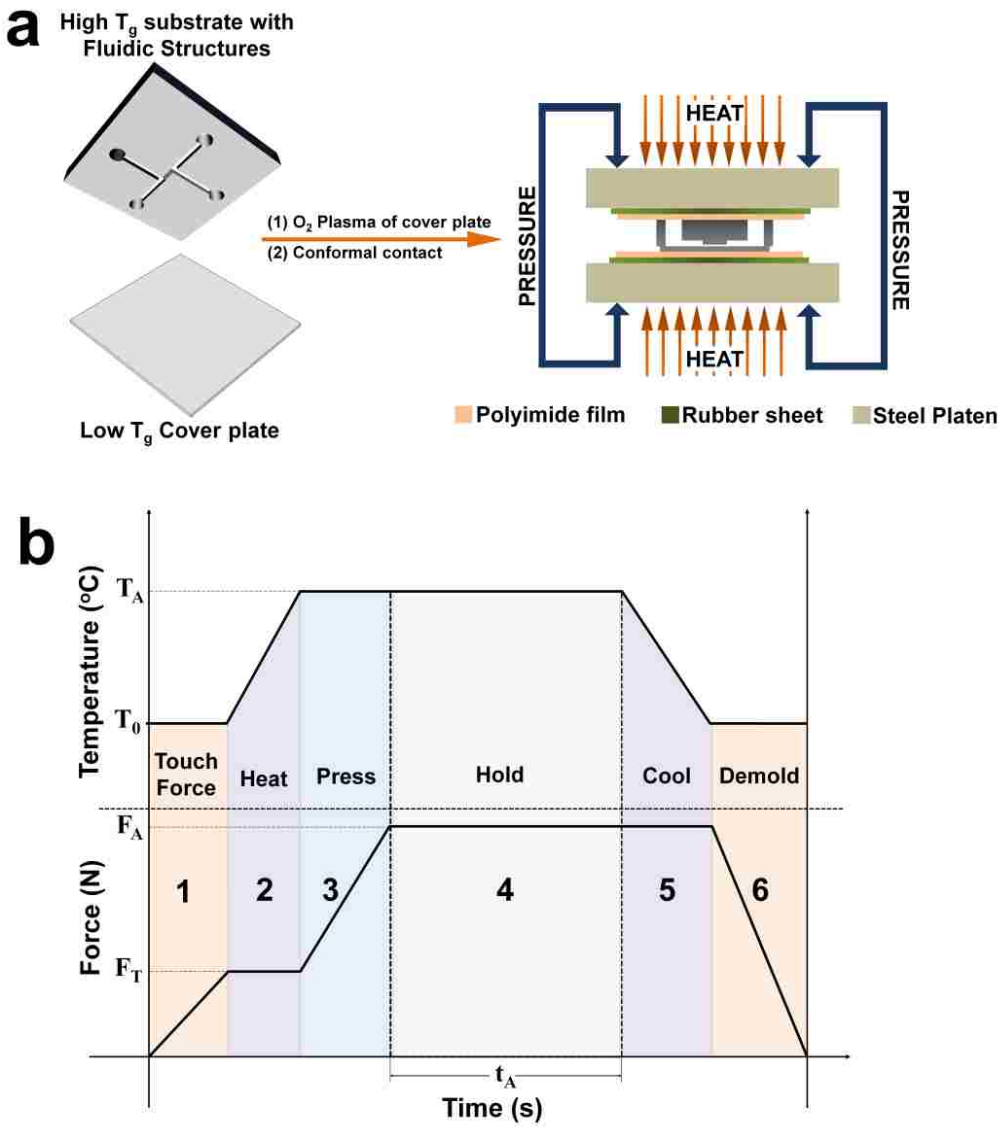

Figure 3.1 (a) Schematic illustration of the device assembly using the thermal press instrument. (b) Temperature-pressure process profile showing the six stages for the bonding cycle.

(1) Touch force stage – This was incorporated to facilitate heat conduction across the surfaces prior to thermal fusion bonding. The top and bottom embosser platens were advanced

towards the assembly and used to clamp the pre-assembled substrate and cover plate near room temperature at a pressure of 180kN/m^2, which was lower than the required assembly pressure.

(2) Heating Stage – The top and bottom platens were heated to the optimized assembly temperature (70^{o}C when using the COC 8007 cover plate) at a defined ramp rate of 3^{o}C/s while holding the clamped device at the touch force.

(3) Pressure stage – Once the desired assembly temperature was reached, the pressure was immediately increased to the intended optimum pressure of 680 kN/m^2.

(4) Holding stage – The assembly temperature and pressure were maintained for 900 s.

(5) Cooling stage – Once assembly was complete, the temperature was gradually reduced to ≤35^{o}C at a rate of 1^{o}C/s while holding the device at the assembly pressure. This reduced stress imposed on the cover plate and prevented collapse into the fluidic channels.

(6) Demolding stage – After the assembled device was cooled, the platens were slowly withdrawn.

3.2.2.3 Water Contact Angle Measurements

The wettability of the polymer surfaces, effect of plasma power and exposure time and the ageing of the cover plate were assessed by water contact angle measurements using a VCA Optima instrument (AST Products). A volume of 2.0 μL nanopure water (18.2 MΩ·cm at 25^{o}C) was dispensed onto 1 cm × 1 cm thermoplastic surfaces and a photograph of each droplet captured immediately for analysis using the software provided by the manufacturer. The measurements were repeated five times at different positions on the substrate with the values reported as the mean ±one standard deviation.

3.2.2.4 Bond Strength Measurements

A common technique used to evaluate the bond strength is the double cantilever beam test also known as the crack opening method.[38-39] In this technique, a razor blade of known thickness t_b is inserted between the bonded substrate and cover plate inducing an interfacial fracture (or equilibrium crack) with a length L from the edge of the razor. If the elastic moduli of the substrate and cover plate is represented by E_s and E_p, respectively, the bond strength γ (J/cm^2) defined by the interfacial surface energy is given by;

$$\gamma = \frac{3t_b^2 E_s t_s^3 E_p t_p^3}{16L^4\left(E_s t_s^3 + E_p t_p^3\right)} \tag{3.1}$$

where t_s and t_p are the thicknesses of substrate and cover plate, respectively. In this work, all tests were performed using a stainless steel single edge razor blade with a thickness of 0.009" and the crack lengths were measured using a calibrated upright microscope with a 5× objective lens. Bond strengths were calculated using equation 1 with elastic moduli of 3.3 GPa for PMMA, 2.60 GPa for COC 8007 and 3.0 GPa for COC 5010 as provided by the manufacturer of the thermoplastics. Measurements were performed in triplicate and values were plotted against the assembly temperature (^{o}C), time (s) and pressure (N/m^2).

3.2.2.5 Surface Charge Measurements

Direct current (DC) conductance measurements were used to evaluate the surface charge density in the nanochannel before and after UV activation. Conductance plots were generated using KCl solutions in the concentration range of 10^{-6} to 0.1 M KCl following the procedure previously reported.[35, 40] For UV activation of the nanochannels, assembled devices were placed in a 265 nm UV chamber with the cover plate facing the light source, then exposed to a 350 *m*J/cm^2 dose of UV light through the COC cover plate. In all cases, fluidic devices were initially flushed with a binary mixture of methanol/ultrapure water (50% v/v) followed by rinsing with

deionized water. Pre-cleaned devices were filled with KCl solutions with Ag/AgCl electrodes immersed into the access reservoirs poised at the ends of microchannels. Electrolyte solutions were allowed to equilibrate for 3-5 min as evidenced by a stable current value under a fixed bias voltage. Current-voltage plots were generated by fitting the slope of the ionic current as a function of the applied voltage stepped from -0.5 V to 0.5 V with 50 mV steps and a 5 s holding time. All measurements were performed using the Axopatch 200B amplifier coupled to a Digidata 1440A digitizer with signal acquisition and analysis performed with the pClamp10 software. The average conductance generated from five trials was plotted against the electrolyte concentration in a log-log plot and the surface charge (σ_s) determined by fitting the graphs with the conductance equation;[35]

$$G_T = 10^3\left(\mu_{K^+} + \mu_{Cl^-}\right) c\, N_A\, e \cdot \frac{n\, w\, h}{L} + 2\, \mu_{opp} \sigma_s\, n \frac{(w + h)}{L} \tag{3.2}$$

where G_T is the total measured conductance in the nanochannel, w, L and h are the nanochannel width, length and height, respectively, N_A is Avogadro's number, e is the electron charge (1.602×10^{-19} C), c is the electrolyte concentration in mol/L, n is the number of nanochannels in the device and μ_{K+} and μ_{Cl^-} are the ion mobilities of K^+ and Cl^- ions, respectively ($\mu_{K+} = 7.619 \times 10^{-8}$ m^2/V s and $\mu_{Cl^-} = 7.912 \times 10^{-8}$ m^2/V s) and $\mu_{opp} \approx \mu_{K+}$ for the deprotonated carboxyl surface. Finally, we assessed the effects of electrolyte pH on the surface conductance using KCl solutions prepared over a pH range of 5 – 9 adjusted using HCl or KOH solutions.

3.2.2.6 Atomic Force Microscopy (AFM) and Scanning Electron Micrograms (SEMs)

The topologies of the nanofluidic channels and the roughness of the polymer surfaces were investigated using an Asylum Research MFP-3D Atomic Force Microscope (tip radius ~2 nm) in repulsive tapping mode at a rate of 1.0 Hz. The Tap300A1-G cantilever tips (Ted Pella) had a frequency of 300 kHz and force constant of 40 N/m. For SEM, the non-conductive resin stamps

and thermoplastic substrates were pre-coated with a 2-3 nm Au/Pd layer and imaged using a FEI Helios FIB/SEM.

3.2.2.7 Nanofluidic Devices and DNA Translocation

All fluorescence imaging experiments were performed using an inverted microscope (Olympus IX81 TIRF microscope, Olympus, Pennsylvania, PA) equipped with a 100×/1.49 NA oil immersion objective and 488 nm laser light for excitation, Sedat laser filter set (LF488/561-2X2M-B-000, Semrock) and a Hamamatsu EMCCD digital camera with Metamorph software for data acquisition. All images were analyzed using Fiji software. λ-DNA (Promega Corporation) and T4 DNA (Wako Chemcials) were stained with the bis-intercalating dye, YOYO-1 (Molecular Probes, Eugene, OR) at a base-pair/dye ratio of 5:1 in an electrolyte solution of 1× TBE (89 mM Tris, 89 mM Borate, 1 mM EDTA) with the addition of 4% v/v β-mercaptoethanol as a radical scavenger to minimize photo-induced damage (photobleaching and/or photonicking).

Nanochannels with depths between 25 and 200 nm were fabricated in PMMA and sealed using the assembly scheme previously described. Devices were seeded with 5 mM FITC in 1× TBE and allowed to equilibrate for 3 min before imaging through the cover plate with an exposure time of 2 s. Unprocessed images were imported into Fiji software and the fluorescence SNR was computed for each nanochannel using the relation;[41]

$$\mathrm{SNR} = 0.655\ \frac{S_{avg}}{\sigma_{noise}} \tag{3.3}$$

where S_{avg} is the mean pixel intensity of the signal and σ_{noise} is the standard deviation in the background pixel intensity. The factor 0.655 arises because the (Gaussian) noise present on the raw data is centered about zero.[41] The selected area in all cases was 18 μm^2 and the measured

σ_{noise} under these imaging conditions were respectively ~2.589 and 5.822 for the COC and PMMA cover plates.

We investigated the degree of extension of T4-DNA molecules confined in nanochannels designed with a range of predefined sizes. The DNA molecules were driven from the microchannels into the nanochannel under low field strengths. Once they had fully entered the nanochannel, the DC field was switched off. The molecule was allowed to relax until it reached its equilibrium extension length before an image was acquired. The end-to-end distance of the fluorescence image was measured using Fiji software. Although the total contour length (L_c) of an unstained λ-DNA molecule (166 kbp) is ~56.6 μm, at our intercalating dye concentration, the expected length is ~64 μm.[42] Finally, the velocities of λ-DNA molecules (0.75 pM) electrokinetically driven through an untreated and UV-activated hybrid device was evaluated from time-lapse images acquired at ~120 fps.

3.2.3 Results and Discussion

3.2.3.1 Water Contact Angle Measurements

In a typical nanofluidic device assembly process, the maximum bond strength between the substrate and cover plate is in part a function of the difference in hydrophobicitiy/hydrophilicity of the surfaces in contact. In our initial bonding tests performed using a low T_g untreated COC cover plate and the high T_g untreated substrate, we were only able to achieve bonding when the devices were assembled at temperatures greater than the T_g of the cover plate by 5^{o}C or more (data not shown). However, at these temperatures the nanochannels were severely deformed and the cover plate completely collapsed, rendering the device nonfunctional. Therefore, before device assembly, oxygen plasma was used to pre-activate the hydrophobic COC cover plate to

make it more hydrophilic and thus, improve its adhesion to the PMMA substrate, which was not plasma activated.

It is well-established that oxygen plasma generates oxygen-containing polar functional groups on thermoplastic surfaces by inducing free radical reactions between the polymer chains and atomic oxygen in the plasma.[43-44] It also known that as the plasma power and treatment times are increased, the surface not only becomes richer in oxygen containing groups but also rougher. The RMS roughness is a parameter that can result in distortion of the electroosmotic flow in nanochannels, especially when the ratio of the RMS roughness to the electric double layer (EDL) thickness >1.[40] For these reasons, water contact angle and AFM measurements were used to assess the hydrophilicity and surface roughness, respectively, for determining the optimum plasma RF power and exposure time for treatment of the COC cover plate under a constant oxygen gas flow of 10 sccm.

Figure 3.2 (a) shows the relationship between the water contact angle and the plasma power at a 10 s exposure time. As shown in the graph, oxygen plasma treatment resulted in a decrease in the water contact angle of 96.4 ±2.1^{o} for the untreated COC surface to 46.9 ±1.4^{o} and 45.2 ±0.7^{o} for surfaces treated at 20 W and 80 W RF power, respectively, indicating an increase in the surface energy.[44]

However, we observed that the effect of the plasma RF power on the hydrophilicity of the COC surface was not very significant when compared to the exposure time. The black trace in Figure 3.2 (b) shows the variation of the water contact angle with the exposure time in the range of 6 to 60 s at 50 W plasma power. As can be seen, there was a distinct decrease in the contact angle from 45.6 ±1.1^{o} to 41.7 ±1.0^{o} when the treatment time was increased from 6 s to 30 s. Above 30 s, the contact angle slightly decreased to a constant value of 40.8 ±0.7^{o} at 54 s.

However, as shown in Figure 3.2 (c) (blue trace), the surface roughness increased almost linearly from 0.49 ±0.03 nm for the untreated COC surface to 1.06 ±0.06 nm for the surface treated for

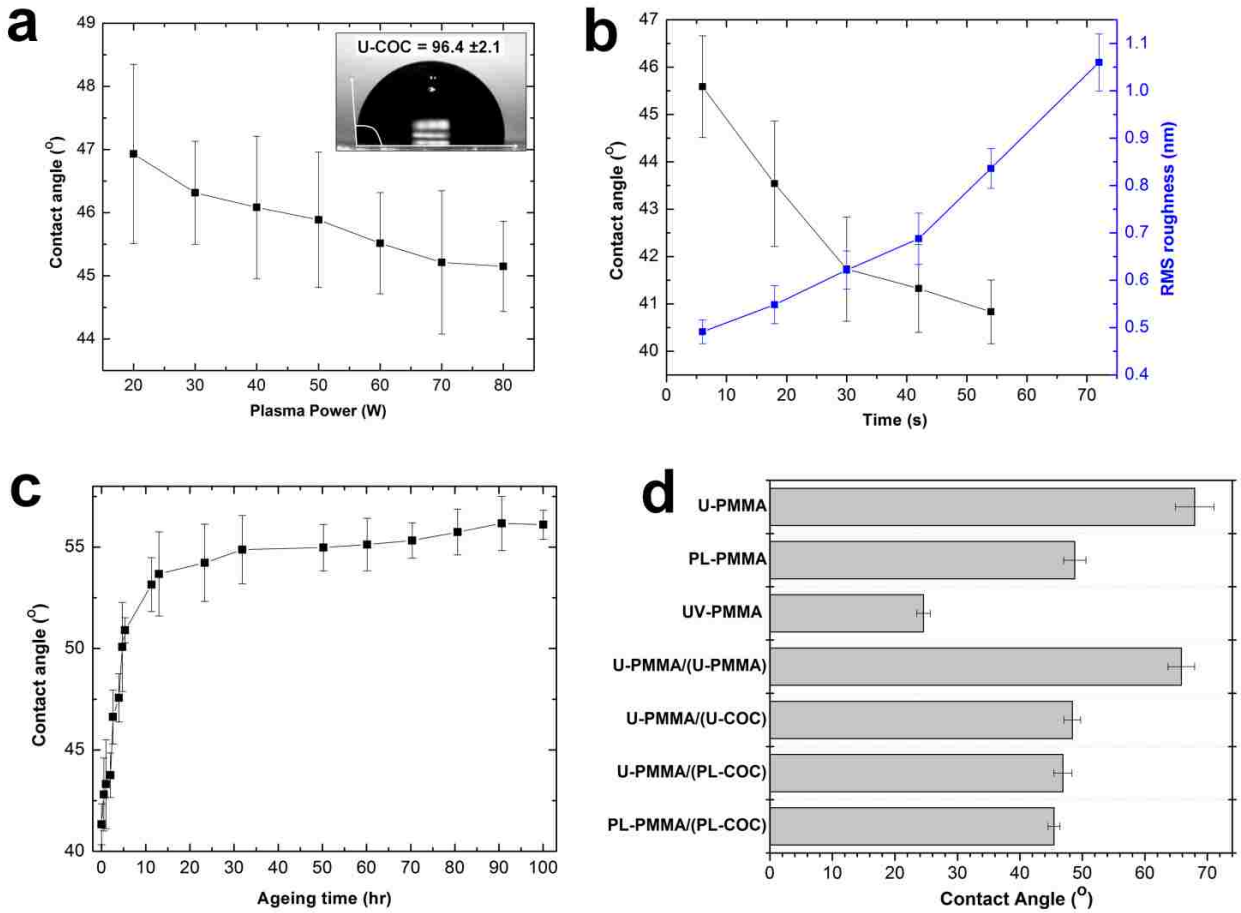

Figure 3.2 (a) Plot of the variation between the contact angle and RF power of the oxygen plasma at 10 sccm gas flow and a constant exposure time of 10 s. (b) Plot of the relationship between the water contact angle (black trace) and the RMS roughness (blue trace) versus the plasma exposure time at 50 W for 10 sccm gas flow. (c) Effect of ageing under room temperature conditions on the water contact angle of treated COC cover plate surface for plasma treatments condition of 50 W at 30 s under 10 sccm oxygen flow rate. (d) Water contact angle measurements on the PMMA substrate under different surface modification conditions with and without the COC cover plate. ('U-PMMA' is untreated PMMA substrate, 'PL-PMMA' is plasma treated PMMA substrate, 'UV-PMMA' is UV-activated PMMA substrate, 'U-PMMA/(U-PMMA)' is untreated PMMA substrate UV-activated through an untreated PMMA cover plate, 'U-PMMA/(U-COC)' is untreated PMMA substrate UV-activated through an untreated COC cover plate, 'U-PMMA/(PL-COC)' is untreated PMMA substrate UV-activated through a plasma treated COC cover plate and 'PL-PMMA/(PL-COC)' is plasma treated PMMA substrate UV-activated through a plasma treated COC cover plate).

60 s. As a result, we used an oxygen plasma condition of 50 W RF power with a 30 s exposure time under 10 sccm oxygen flow rate to treat the COC cover plate.

Because the EDL thickness for most ionic solutions used in nanofluidics varies between 1-100 nm and the RMS roughness of the COC surface treated at the above plasma condition was low (~0.62 ±0.04 nm), we speculate that distortions in the EOF profile arising from the surface roughness on the nanochannel cover plate would be minimal while still maintaining high adhesive capacity. Based on XPS data from previous reports, the density of polar functional groups on COC at this treatment condition is relatively low when compared to higher exposure times and gas flow rates.[44]

Although the surface properties of thermoplastics can be modified by plasma treatment without affecting its bulk properties, treated surfaces have been shown to undergo ageing when stored in air. This is due to reorientation of the polar surface functional groups causing their movement into the bulk thermoplastic or movement of small chain polymer segments into the bulk causing the thermoplastic surface to lose its hydrophilic property.[40, 45] Ageing studies were performed on treated COC cover plates to determine whether oxidation continued to occur after assembly and if assembled nanofluidic devices could be stored under vacuum conditions to improve shelf-life. The results obtained after treating the COC cover plate with 50 W RF power and 30 s exposure time are shown in Figure 3.2 (c). These results revealed that the contact angle changed from 41.33 ±1.00^{o} to 53.15 ±1.33^{o} during the first 10 h following treatment. Over a period of 100 h, the contact angle remained at 56.10 ±0.72^{o}. The hydrophilicity was not completely lost over the storage time evaluated as the contact angle was still 35-40^{o} lower than that of the untreated COC surface. Also, we did not experience any difficulty in filling devices

used 5 days after assembly and these devices yielded results similar to those obtained from the devices that were used immediately after sealing.

Because we were interested in post-assembly modification of the nanochannels by UV-activation through the COC cover plate, we assessed the wettability of a PMMA substrate before and after exposure to UV light with and without a COC cover plate. We used U-, PL- and UV- prefixes to indicate untreated, plasma treated and UV-activated surfaces, respectively, and represented the assembled devices as 'substrate/(cover plate)'. For example, untreated PMMA substrate bonded to an oxygen plasma treated COC cover plate was represented as 'U-PMMA/(PL-COC)'. As can be seen in Fig. 3.2d, U-PMMA showed a water contact angle of 68.0 ±3.1^{o}. Direct exposure to RF oxygen plasma under the above conditions resulted in a decrease in the contact angle to 48.8 ±1.8^{o}. However, direct exposure to 350 *m*J/cm^{2} of UV light resulted in a reduction in the contact angle to 24.6 ±1.1^{o} with an observed yellowing of the polymer. When the PMMA substrate was activated through an untreated PMMA cover plate, the measured water contact angle was 65.9 ±2.1^{o}, a value similar to that obtained for U-PMMA. This was not surprising considering that PMMA has been shown to only transmit 10-15% of light at a wavelength of 265 nm.[32] The measured contact angles for U-PMMA/(U-COC) and U-PMMA/(PL-COC) were 48.4 ±1.3^{o} and 46.9 ±1.5^{o}, respectively; these contact angles were not statistically different but were lower than U-PMMA by 15-20^{o}. These results not only revealed that the underlying PMMA substrates were successfully activated through the COC cover plate by the UV light, but also showed that plasma treatment of the cover plate had no considerable effect on the bulk transmittance of the material, because it only affects 5-15 nm of the polymer surface.[44] When the PMMA substrate was plasma treated prior to UV-activation through the plasma treated COC cover plate, the measured water contact angle was 45.5 ±0.9^{o}. Because this

value was slightly lower than that obtained for U-PMMA/(U-COC), it is either likely that under UV-activation, more polar groups were incorporated onto the PMMA surface[46] or less polar groups generated on the PMMA via plasma activation[43] were converted to more polar hydrophilic groups via free-radical pathways.

3.2.3.2 Bond Strength Determination

The critical parameters in any fusion bonding scheme adopted for enclosing fluidic devices are the bonding pressure, temperature and time. In this work, we optimized these parameters to obtain high bond strengths while retaining the structural integrity of the nanochannels. Before device assembly, the COC cover plate was treated with oxygen plasma consisting of 50 W RF power for 30 s and 10 sccm gas flow rate while the PMMA substrate remained untreated. Variations between the bonding temperature and the bond strength at a constant bonding pressure of 680 kN/m^2 and a bonding time of 15 min are shown in Figure 3.3 (a). The result

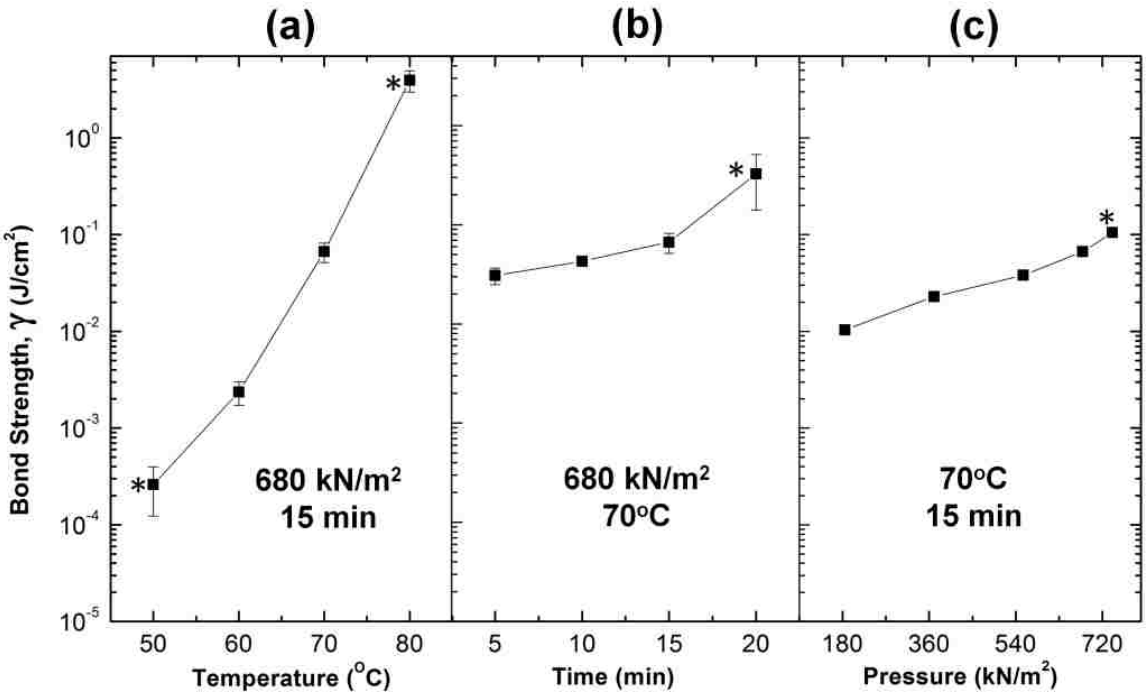

Figure 3.3 Variation of the bond strength with the (a) temperature, (b) bonding time, and (c) pressure for the hybrid assembly scheme.

revealed that the bond strength varied linearly with the bonding temperature. Based on the work of Tsao *et al,*[39] bond strengths for our nanofluidic devices were comparable to those of microfluidic devices. While the bond strength at 80^{o}C seemed impressively high, our data revealed that bonding at this temperature resulted in unusable devices. This is likely a result of bulk flow of the cover plate material into the nanochannels due to the bonding temperature being greater than its bulk T_g. In subsequent studies, 70^{o}C was selected as the optimum bonding temperature.

Next we studied the effect of bonding time on the bond strength using the optimum temperature of 70^{o}C and a constant force of 680 kN/m^2. As shown in Figure 3.3 (b), bond strengths were greater than those previously reported in applications involving electrokinetic transport in thermoplastic nanochannels[16, 35] when devices were bonded between 5 and 20 min assembly times.

However, we observed that devices bonded at 20 min did not yield reproducible results. We speculate that this may be due to minor deformations in the nanochannels or sagging of the cover plate into the channels similar to previous observations.[31] Therefore, 15 min was selected as the optimal assembly time. Lastly, (c) in Figure 3.3 shows the effect of bonding pressure on the bond strength under an optimum bonding temperature of 70^{o}C and a bonding time of 15 min. Bond strengths achieved in the pressure range under study were sufficiently greater than that previously reported for electrokinetic flow in nanofluidic devices[16] and comparable to the homogenous polymers bonded at a temperature greater than their T_g.[39] However, to prevent sagging of the cover plate into the nanochannels, we selected 680 kN/m^2 as the optimum pressure to minimize this artifact. Based on the aforementioned results, untreated high T_g

substrates were bonded to plasma treated low T_g COC cover plates using a bonding pressure, temperature and time of 680 kN/m^2, 70^{o}C and 15 min, respectively.

Similarly, we evaluated the bond strengths of PL-PMMA, PL-COC and U-COC (COC 5010) substrates bonded to the low T_g COC cover plate. The results are summarized in Table 3.1. Devices 1 – 4 were bonded at the optimized bonding pressure, temperature and time as previously noted. Device 5 was bonded using a pressure of 370 kN/m^2 at 80^{o}C for ~7 min, as previously reported by our group.[35] Device 6 was bonded using a pressure of 370 kN/m^2 at 105^{o}C for ~7 min and the bond strength was 0.143 ±0.071 mJ/cm^2 for the U-COC/(PL-COC) device. This bond strength was too low for performing fluidic experiments, because we experienced difficulty in filling the assembled device due to the hydrophobic nature of the untreated substrate. When the COC substrate was treated with oxygen plasma prior to device assembly, there was an increase in the bond strength to 1.04 ±0.01 mJ/cm^2 and an improvement in the wettability. However, using untreated and plasma treated PMMA as the substrates produced devices with bond strengths of 65.92 ±7.13 *m*J/cm^2 and 67.92 ±6.97 mJ/cm^2 for U-PMMA/(PL-COC) and PL-PMMA/(PL-COC), respectively, that easily filled easily by capillary action. Though it remains unclear why the bond strength was greater in U-PMMA/(PL-COC) than PL-COC/(PL-COC), we conclude from these results that the bond strength not only depends on the surface wettability - PL-COC has a water contact angle less than U-PMMA - but also on the chemical nature of the surfaces in contact. Nevertheless, U-PMMA/(PL-COC) devices, which we refer to as the hybrid devices, were used in our subsequent experiments.

For comparison, we evaluated the bond strengths from assembled PL-PMMA/(PL-PMMA) and U-PMMA/(U-PMMA) devices. As shown in Table 3.1, in both cases, the measured bond strengths were lower than that of the hybrid devices. Though PL-PMMA/(PL-PMMA) devices

have been useful for surface modification and DNA transport studies,[16-17, 35] the process yield rate for both devices was relatively low (<50% for PL-PMMA/(PL-PMMA) and <10% for U-PMMA/(U-PMMA)) due primarily to deformation and collapse of the nanochannels following thermal fusion bonding and possible delamination of the cover plate during an experiment.[16]

Table 3.1 A summary of the bond strength tests obtained for devices assembled with different substrates and cover plates.

No	Assembled device	Bond Strength (*m*J/cm^2)
1	U-COC/(PL-COC)	0.143 ±0.071
2	PL-COC/(PL-COC)	1.035 ±0.007
3	U-PMMA/(PL-COC)	65.921 ±7.131
4	PL-PMMA/(PL-COC)	67.918 ±6.966
5	PL-PMMA/(PL-PMMA) [80^{o}C]	1.244 ±0.003
6	U-PMMA/(U-PMMA) [106^{o}C]	1.897 ±0.053

As a comparison, using the optimized thermal fusion bonding conditions noted above for U-PMMA/(PL-COC) devices, the process yield was >90% with a similar value noted for devices consisting of U-COC/(PL-COC). AFM measurements taken from the 5 μm × 120 nm nanoslits utilized for the surface charge measurements after removing the cover plate post-assembly revealed no change in the nanoslit dimensions. This was not surprising since device assembly was performed at a temperature ~35^{o}C less than the T_g of the PMMA substrate.

3.2.3.3 Surface Charge Measurements

We recently reported the surface charge density in PL-PMMA/(PL-PMMA) nanofluidic devices assembled under slightly different plasma conditions (5.5 sccm, 35 s and 50 W).[35] Herein we evaluated the surface charge density of the hybrid U-PMMA/(PL-COC) devices assembled with the optimum conditions reported above.

Ionic conductance plots were used to evaluate the surface charge density of assembled nanofluidic devices comprising an array of five nanoslits, each 5 μm wide, 120 nm deep and 148 μm long. It is well-known that carboxylic acid moieties can be generated on PMMA or COC surfaces following plasma treatment[40, 45] or UV-activation.[46] Figure 3.4 (a) shows the conductance traces measured in PL-PMMA/(PL-COC) compared to PL-PMMA/(PL-PMMA) devices. In the high ionic strength regime (KCl concentrations $>10^{-2}$ M), the ionic conductance in both devices fit linearly to the theoretical bulk conductance with high reproducibility for both devices. This confirmed that there was no change in the dimensions of the nanochannels during thermal embossing and after assembly for the devices tested. At the low ionic concentration (or surface-charge governed) regime, there was a significant difference in the measured conductance between these devices. For the PL-PMMA/(PL-PMMA) device, the surface charge density $|\sigma_s|$ estimated from the fitted curve was 43.2 mC/m^2 while for the hybrid device, $|\sigma_s|$ was 57.3 mC/m^2, ~32.6% greater than the former. This difference in surface charge density is likely due to the fact that more carboxyl groups are generated on COC compared to PMMA when treated under similar oxygen plasma conditions.[40, 45] Figure 3.4 (b) shows the conductance traces measured in the hybrid device U-PMMA/(PL-COC) before (blue trace) and after (red trace) exposure to UV light. The average conductance in the low ionic strength regime for the unexposed devices was 1.45×10^{-9} S with $|\sigma_s|$ equal to 40.7 *m*C/m^2. After the device was exposed to 350 *m*J/cm^2 of 265 UV light through the plasma-treated COC cover plate, there was a 47.2% increase in $|\sigma_s|$ (59.9 *m*C/cm^2) as evidenced by the increase in conductance to 1.89×10^{-9} S. This suggested that post-assembly UV activation induced more carboxyl groups on the walls of the nanoslits, in particular for the unmodified PMMA substrate. Also, the surface charge density in the UV activated hybrid devices were 4.5% higher than devices with plasma treated substrate

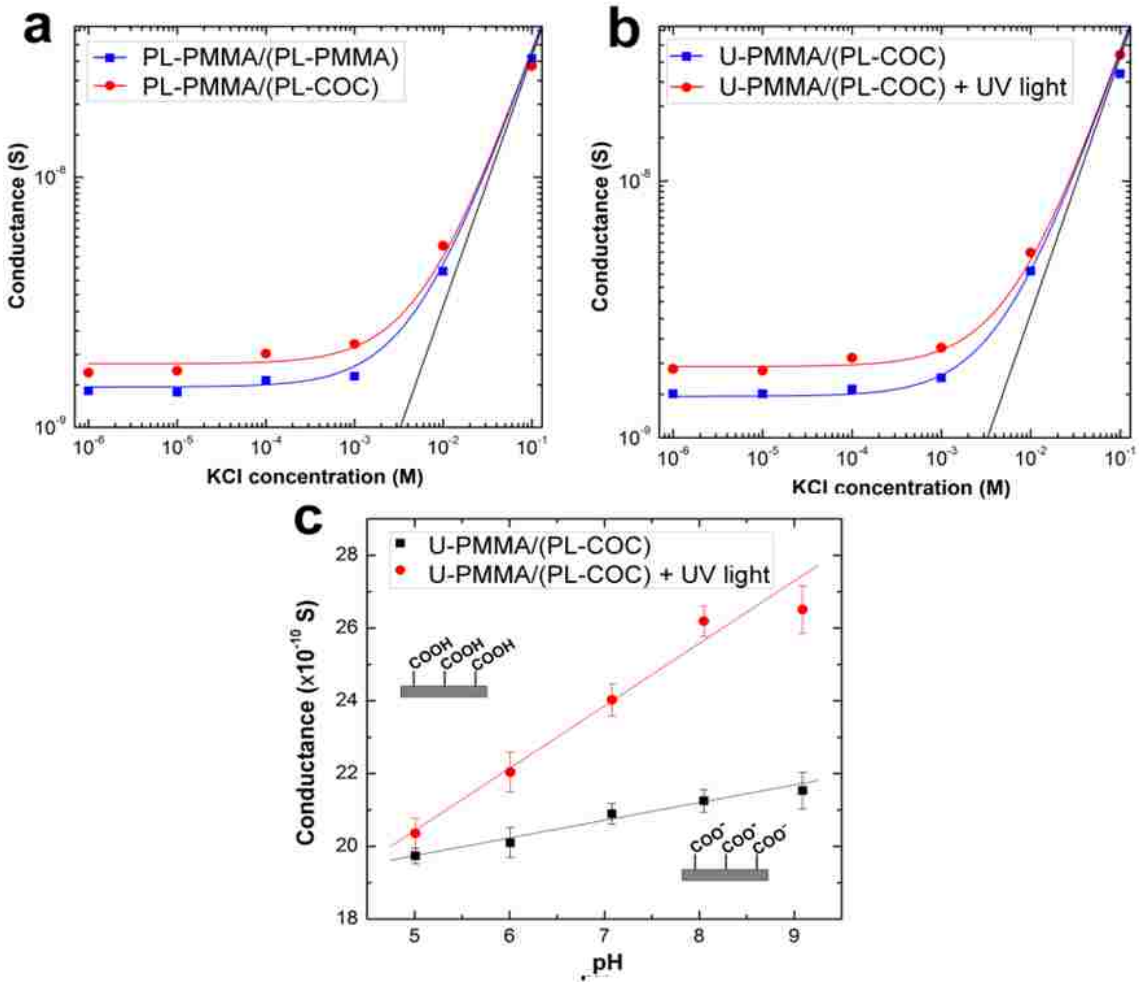

Figure 3.4 (a) Conductance plots for assembled devices with plasma treated PMMA substrate bonded to plasma treated PMMA cover plate, PL-PMMA/(PL-PMMA), and plasma treated PMMA substrate bonded to plasma treated COC cover plate, PL-PMMA/(PL-COC). The latter devices showed a higher conductance at the low ionic conductance regime because more carboxyl moieties are introduced on COC surfaces than PMMA when exposed to the same plasma conditions. (b) Conductance plots for the hybrid devices consisting of untreated PMMA substrate bonded to plasma treated COC cover plate, U-PMMA/(PL-COC), before (blue trace) and after (red trace) UV activation. The device used in all cases consists of an array of five nanoslits (each 5 μm wide, 120 nm deep and 148 μm long) connected to V-shaped assess microchannels at the input and output ends. Each data point represents an average of five measurements with a scatter in the data within 5-8% of the mean value and the solid black line represents the trace of the theoretical bulk conductance. (c) Plot showing the relationship between the conductance and the electrolyte pH for the assembled hybrid devices before (black) and after (red) UV activation. 10^{-4} M KCl solution adjusted to pH between 5.01 and 9.09 was used in the study.

(red trace in Figure 3.4 (a)). This is because the surface density of carboxylates generated on UV activated PMMA surfaces (14.7 ±2.6 *n*mol/cm^2)[46] is greater than that generated on plasma treated surfaces (2.7 ±0.5 *n*mol/cm^2).[47]

Figure 3.4 (c) shows the effects of solution pH on the measured conductance for the nanoslits before and after UV activation. As can be seen, in both cases the conductance increased linearly with the pH of the electrolyte. Prior to UV activation, there was an observed change in the measured conductance of the nanochannel from 13.7 (±0.2) × 10^{-10} S at pH 5.0 to 15.5 (±0.5) × 10^{-10} S at pH 9.09 (black trace). Because the PMMA substrate was untreated prior to device assembly, charge contributions from carboxyl moieties on the PMMA surfaces, especially at high pH, will be insignificant compared to that from the plasma treated COC cover plate.

Therefore, the change in conductance is predominantly due to deprotonation of the carboxyl groups on the cover plate. Nevertheless, after UV-activation of the same devices, there was a significant increase in the conductance, ~30% (15.4 (±0.4) × 10^{-10} S at pH 5.0 to ~21.6 (±0.6) × 10^{-10} S at pH 9.1), as evident by an increase in the slope of the red trace in Figure 3.4 (c). These results confirmed that the nanoslits were successfully functionalized via UV-activation after device assembly.

3.2.3.4 Operational Characteristics of Nanofluidic Devices

Finally, we assessed the performance of the assembled hybrid nanofluidic devices, for fluorescence imaging, DNA stretching and translocation relative to their non-hybrid counterparts. The stamp was used to imprint channels into a PMMA substrate with ~100% replication fidelity. AFM profiles shown in Figure 3.5 suggest effective transfer from Si master to UV resin.

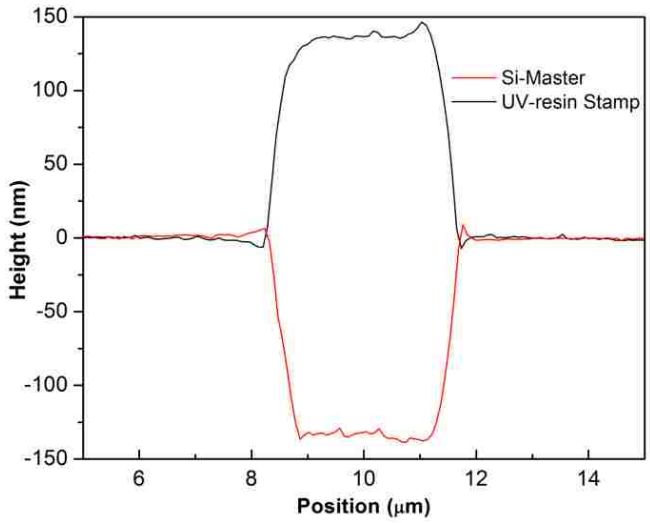

Figure 3.5 AFM profile of a nanoslit in a silicon (Si) master (red trace) and positive structure in the UV resin stamp (black trace) showing the replication fidelity in the structure.

Figure 3.6 indicates that there was no significant reduction in the stamp height channel depth even after twenty transfers. Figure 3.7 (a) shows an AFM profile and the SEM image (insert) of the UV curable resin stamp consisting of 2-D nanochannels with predefined widths (*w*) × depths (*d*) of 300 × 200 nm, 250 × 155 nm, 190 × 95 nm, 150 × 60 nm, 110 × 25 nm and 35 × 35 nm corresponding to *nc*1, *nc*2, *nc*3, *nc*4, *nc*5, and *nc*6, respectively.Using the unprocessed images obtained from the fluorescent seeding test with 5 mM FITC, we found that the average SNR was ~3× greater in *nc*1 – *nc*4 and ~4.5× greater in *nc*5 for U-PMMA/(PL-COC) than PL-PMMA/(PL-PMMA) ((b) in Figure 3.7). This enhancement in SNR is most likely due to the superior optical properties (high optical transmission, low autofluorescence/ background and high refractive index) of COC at 488 nm compared to PMMA.[32] The higher SNR observed for *nc*5 may be an indication of slight collapse of the nanochannel in the non-hybrid devices or an artifact from the high background fluorescence of PMMA. Figure 3.7 (c) shows unprocessed frames of T4 DNA molecules confined in *nc*1 – *nc*6 devices and imaged through the COC cover plate at 10 ms exposure time. The images revealed good contrast and excellent SNR with the

degree of polymer stretching increasing as the nanochannel size decreased. Figure 3.7 (d) shows a plot of the DNA extension (ε) versus the geometric average (D_{av}) nanochannel dimension with traces for the deGennes prediction, $\varepsilon_{deGennes} \approx \left(\omega_{eff}\, L_p / D_{av}^2\right)^{1/3}$ and the Odijk prediction,

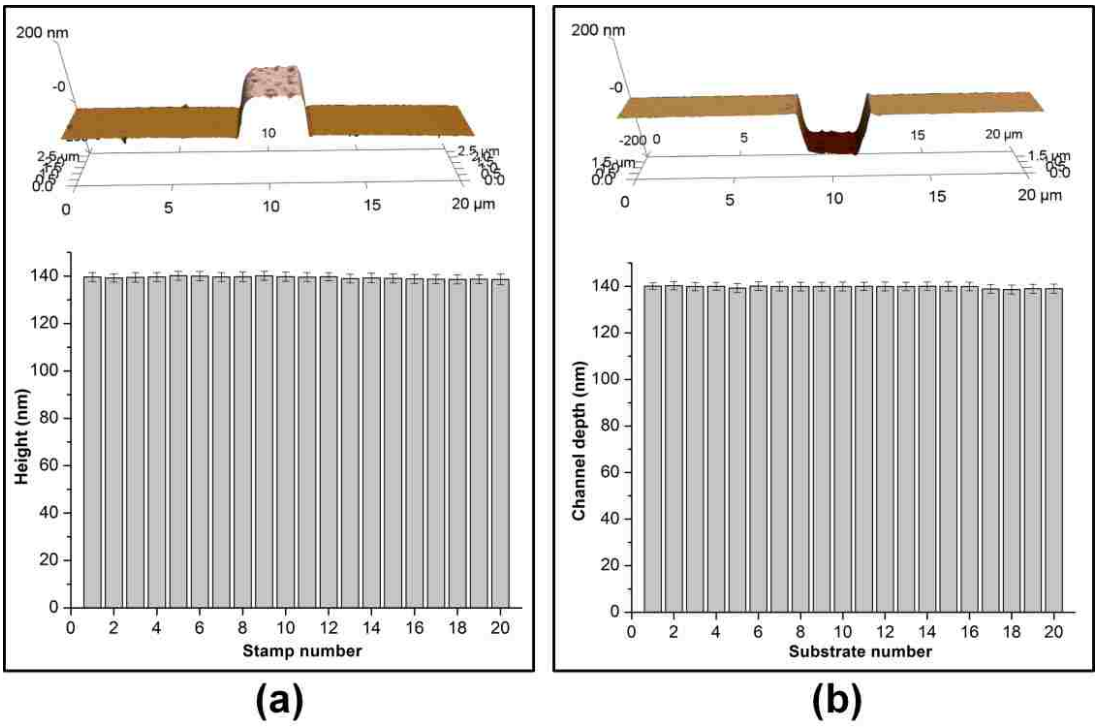

Figure 3.6 (a) Upper panel - AFM image of the first UV resin stamp produced from the Si master. Lower panel – Box plots of the stamp height measured with the AFM from 20 stamps produced from a single Si master. (b) Upper panel – AFM image of the first PMMA device generated after thermal imprinting using a UV-resin stamp. Lower panel – Box plots of the nanoslit depth measured with AFM from 20 substrates produced from a single UV-resin stamp. Both images reveal ~100% replication fidelity of nanostructures from the master to stamp to substrate.

$\varepsilon_{Odijk} \approx \left[1 - 0.361\left(D_{av}/L_p\right)^{2/3}\right]$, where $D_{av} = \sqrt{w \times d}$, ω_{eff} is the effective width (~3 nm) and L_p is the persistence length (50 nm) for dsDNA.[42]

As seen in (d) of Figure 3.7, the data for the channel with >200 nm D_{av} fits well with the deGennes regime while the nanochannel with D_{av} = 35 nm fits well to the Odijk regime. However, data for *nc*3 – *nc*5, though expected to fit to the deGennes regime, were observed to be

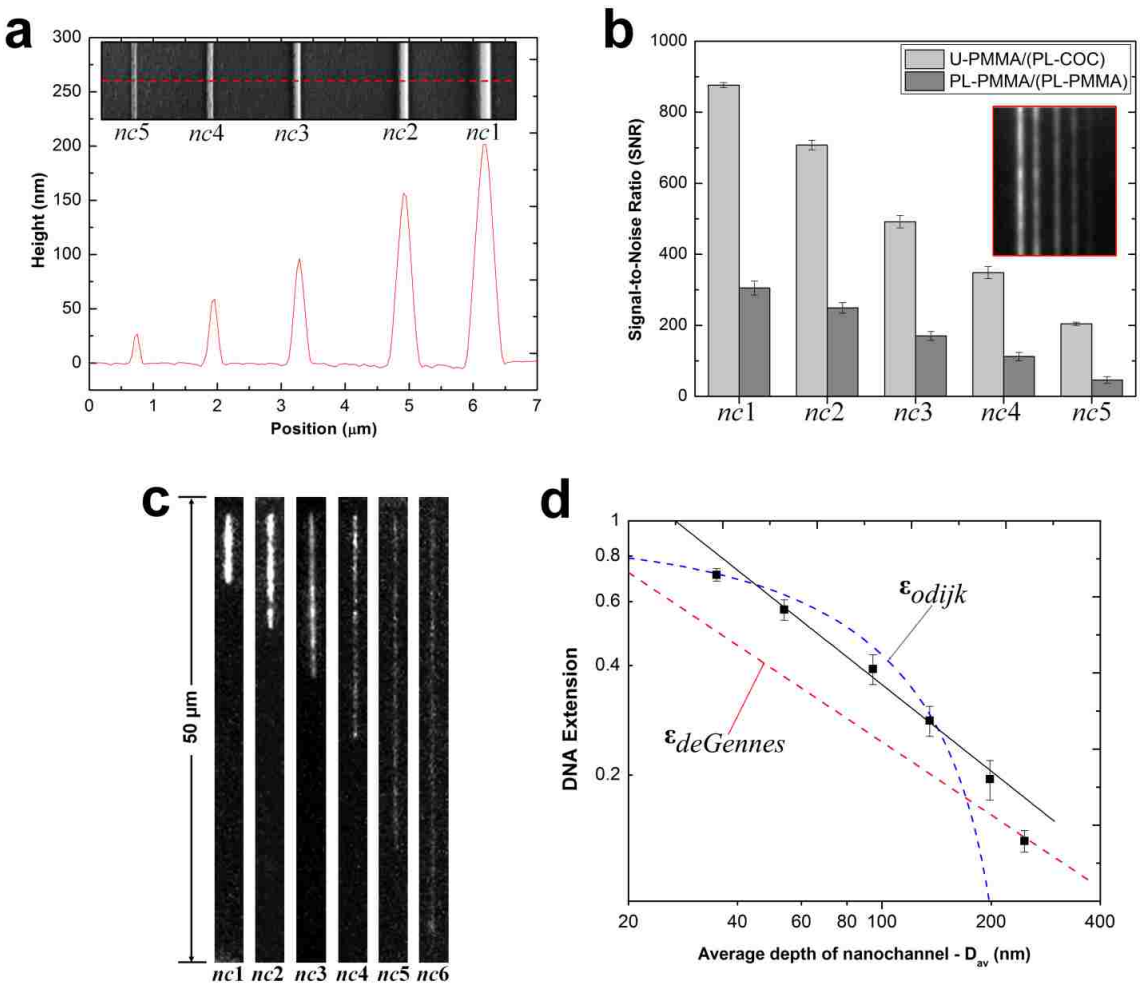

Figure 3.7 (a) AFM scan (and SEM image insert) of the UV curable resin stamp possessing the positive tones of the 2-D nanochannels. Channels were imprinted into PMMA with ~100% replication fidelity and the dimensions (width × depth) were *nc*1 ≈ 300 × 200 nm, *nc*2 ≈ 250 × 155 nm, *nc*3 ≈ 190 × 95 nm and *nc*4 ≈ 150 × 60 nm and *nc*5 ≈ 110 × 25 nm. (b) Bar graphs showing the signal-to-noise ratio (SNR) at 2 s exposure time for the devices with untreated PMMA substrate enclosed with a plasma treated COC cover plate, U-PMMA/(PL-COC), and plasma treated substrate enclosed with a plasma treated PMMA cover plate, PL-PMMA/(PL-PMMA) filled with 5 mM FITC solution. The error bar represents the standard deviation in measurements from ten separate devices. (Insert shows the unprocessed image of the seeding test for U-PMMA/(PL-COC)). The hybrid devices showed a background that was ~56% lower than that of the non-hybrid devices. (c) Unprocessed representative frames of T4 DNA molecules stretched in the enclosed nanochannels in the hybrid devices. Images were acquired at 10 ms exposure time with the driving field turned-off. (Note that *nc*6 ≈ 35 × 35 nm). (d) Log-log plot showing the T4 DNA extension as a function of the geometric average depth of the nanochannels. The DNA extension was normalized to a total contour length (L_c) of 64 μm for the dye labelled molecules. The red and blue dashed lines are the deGennes and Odijk predictions, respectively, with the respective equations inserted. The black solid line is the best power-law fit to the data points obtained from the nanochannels with an average geometric depth range of 53 nm to 200 nm.

greater than the deGennes prediction but less than the Odijk prediction. This enhancement in the degree of extension within this regime is likely due to the hydrophobicity of the nanochannel walls.[48]

Finally, we evaluated the effect of post-assembly UV-activation of the U-PMMA/(PL-COC) devices on the linear velocity of λ-DNA molecules electrokinetically driven through 100 × 100 nm nanochannels. As shown in Figure 3.8, in both cases there was a corresponding linear

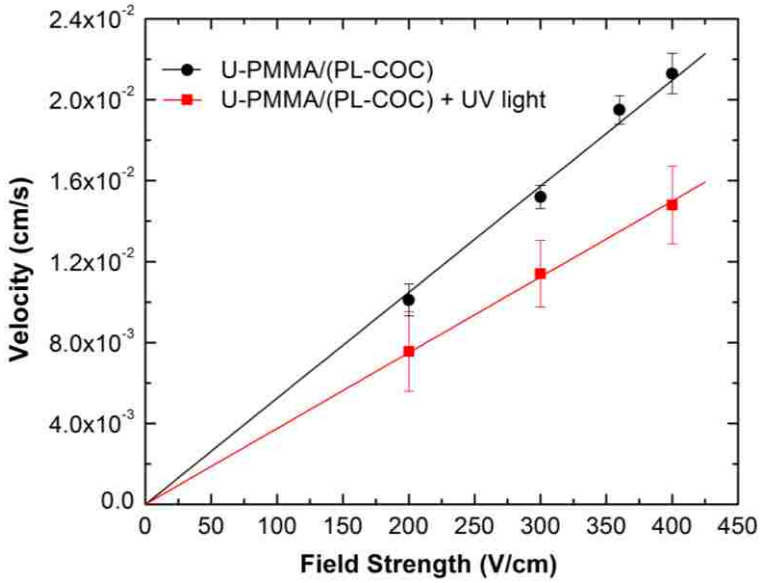

Figure 3.8 Graph showing the relationship between the translocation velocity (cm/s) and the field strength (V/cm) of λ-DNA translocating through the hybrid devices before and after activation with UV light. Each data point represents the mean of 20 events per device measured in 2× TBE buffer.

increase in the velocity of dsDNA as the driving voltage was increased. However, the DNA molecules were observed to migrate slower in the UV-activated devices. This is likely due to an increase in the EOF emanating from increases in the surface charge density after the incorporation of –COOH groups onto the wall of the nanochannel via UV activation.

3.2.4 Conclusion

In this work, we developed a low temperature hybrid bonding scheme useful for the assembly of thermoplastic devices and demonstrated the utility of these devices for DNA

elongation and translocation and post-assembly modification. With this scheme, we have addressed a significant challenge associated with the use of thermoplastics for nanofluidic – the relatively small Young's modulus associated with these materials makes cover plate assembly to the patterned substrate difficult due to cover plate collapse and/or nanostructure deformation using either thermal or chemical assisted bonding to enclose the fluidic network. Our assembly scheme will aid in generating nanofluidic devices with high process yield rates for many analyses that take advantage of the unique physics associated with nano-confinement. We are currently evaluating the extent of distortions in the EOF profile, if any, arising from hybrid nanochannels as has been shown in microchannels.[49] We also suspect that these distortions will be observed in PL-COC/(PL-COC) devices due to differences in the norbonene content of the substrate versus cover plate. We are also employing super resolution imaging techniques to assess the surface coverage and uniformity of carboxyl functional groups generated in these nanochannels via UV-activation.

3.3 Detection of Chemotherapeutic-Induced Damage in Genomic DNA using Hybrid Thermoplastic Nanochannel Sensors

3.3.1 Introduction

Current methods for selecting therapy for a cancer patient are based on results of previous clinical outcome studies performed on patients with tumors of the same type and clinical stage. Data on tumor type, stage, lymph node status and the presence of receptors for hormones or growth factors and genetic markers or gene expression changes are used to further classify the tumor with therapy selected based on the tumor classification. For example, by classifying a patient's breast cancer (BC), a treatment regimen is selected that clinical studies have shown to provide the best percentage of favorable outcomes within groups of BC patients with similar tumors.[50-53] Unfortunately, these optimized therapies are not equally effective for all patients

within specific tumor classifications.[54-57] For example, individuals with certain genetic variants in oxidative stress genes have been shown to have atypical chemo-resistance to a particular therapeutic drug.

Single-molecule imaging can provide assistance to determining the proper treatment regimen of cancer patients. For example, stretching DNA in nanochannels and imaging specific sites, which is called optical or genomic mapping has been extensively studied.[58-61] There have been several recent reports addressing optical/genomic mapping. In the early 20th century, reports exist about visualizing abasic (AP) sites in DNA by direct visualization through microscopy. Detection of AP sites on a 250 bp DNA with 2 abasic sites was performed using atomic force microscopy.[62] Hirose *et. al.*[63] reported a direct method to visualize abasic sites on a λ DNA stretched on a glass and Kim *et. al.*[64] reported a method using scanning near-field optical microscopy (SNOM). Recent reports have shown interest in identifying the specific damage sites in a DNA strand. Chastain and coworkers managed to map the frequency of abasic site lesions in genomic DNA by optically mapping DNA fiber on a glass slide.[65] A method to identify UV-induced single strand and double strand DNA breakage locations was reported by Lee *et. al.*[66]. The authors were able to map the specific sites to the expected breakage sites.

Nanopore-based identification of single abasic sites has also been reported. Burrows *et. al.*[67] reported a method to characterize individual abasic sites attached to crown ethers by a pulse like current signatures generated from electrolyte interactions when it passed through an α-hemolysin nanopore.[38, 67] Marshall *et. al.*[68] showed the electrophoretic dynamics of an apurinic site showed slower dynamics through a solid-state nanopore; thus, it can be used to identify the abasic sites in a single DNA molecule.

Damage of genomic DNA can be induced by therapeutic treatments, especially to chemotherapeutic drugs. Chemotherapy has been widely used as a treatment option for tumors to arrest the activity of the cancer cells comprising the tumor. Even though these treatments help patients to survive from their disease, they undergo the risk of double strand breaks of DNA, DNA crosslinking and formation of abasic sites. Current methodologies using optical visualization suffer from several shortcomings such as the inability to image a single molecule in real time, the need of extra processing before using optical imaging, and the inaccuracy generated by not stretching DNA to its full contour length.

We propose a new sensing platform for the direct reading of abasic sites, which consists of optical quantification following DNA stretching to near its full contour length using a hybrid thermoplastic nanochannel that is imprinted into a polymer substrate. Curved serpentine-shaped nanochannels and straight nanochannel structures, which have a cross section smaller than the persistent length of the double-stranded DNA molecule and a length longer than their full contour length is used to enhance the stretching for better optical readout in a single image even for chromosomal DNA. Our nanostructures are fabricated in poly(methyl) methacrylate, PMMA, using nanoimprint lithography (NIL). Imprinted channels <100 nm (in width and depth) and different designs have been employed to account for different length DNAs. Single DNA molecules are electrokinetically driven into the nanochannels by an external applied electric field. Abasic sites are labeled with a biotinylated aldehyde-reactive-probe (ARP), which is then associated to fluorescently labeled streptavidin molecules. Fluorescently labeled streptavidin molecules are optically visualized using total-internal reflection fluorescence (TIRF) microscopy with dual excitation; the entire DNA molecule labeled with an intercalating dye (YOYO-1) and an AlexaFluor dye is covalently attached to streptavidin for sensing the abasic sites. With full

stretching of the dsDNA molecule contained within the polymer nanochannel, abasic sites are more easily resolved to better provide quantitative data as to their number. We are also detecting the presence of abasic sites in cancer cells secured from breast cancer patients that are undergoing chemotherapeutic treatment. This section discusses the achievements and challenges in successfully building the nanofluidic-based sensor with the required specificity and sensitivity to monitor chemotherapy responses of cancer patients by carefully monitoring the frequency of AP sites generated in their DNA.

3.3.2 Materials and Methods

3.3.2.1 Materials and Reagents

Silicon <100> (Si) wafers were purchased from University Wafers (Boston, MA), poly (methyl methacrylate), PMMA (T_g = 105 ^{0}C), sheets were purchased from Good Fellow (Berwyn, PA) and cyclic olefin copolymer (COC 8007, T_g = 78 ^{0}C) cover plates were purchased from TOPAS Advanced Polymers (Florence, KY). The anti-adhesion coating material, (tridecafluoro – 1,1,2,2-tetrahydrooctyl) tricholorosilane (T-silane), was purchased from Gelest, Inc. (Morrisville, PA). Tripropylene glycol diacrylate (TPGA), trimethylolpropane triacrylate (TMPA), Irgacure 651 (photo-initiator), sodium citrate buffer (pH = 5.0), β-mercaptoethanol was purchased from Sigma-Aldrich (St Louis, MO). λ DNA (New England BioLabs, Ipswich MA) and T4 DNA (Wako Chemicals USA, Inc. Richmond VA) were also purchased and DNA damage quantification kit was purchased from Dojindo Molecular Technologies, Inc. Rockville MD. Aldehyde Reactive Probe with biotin (ARP-biotin), Streptavidin with Alexa Fluor® 594 Conjugate, Streptavidin with Alexa Fluor®647 conjugate, YOYO-1 were purchased from Life Technologies, Carlsbad, NY. Chroma spin TE-1000 columns were purchased from Clontech Laboratories, Inc. San Francisco CA. Aqueous citrate buffer and Tris-Borate-EDTA (TBE, 89

mM Tris, 89 mM Borate, 1 mM EDTA) buffer were purchased from Fisher Scientific®, Philadelphia, PA. All dilutions were performed using 18 MΩ/cm milliQ water (Millipore). All solutions were filtered through 0.2 μm filters (Thermo Scientific® Nalgene syringe filters) prior to use.

3.3.2.2 Fabrication of Nanofluidic Devices

Nanofluidic devices were fabricated using the procedure explained in the previous section of this chapter in detail. Briefly, the microstructures were fabricated into silicon (Si) substrate using photolithography and wet-etching techniques. Nanochannels were milled into a Si substrate by FIB milling (FEI Helios 600 Nanolab Dual Beam system). Different channel sizes and nanochannel designs, such as straight and serpentine, were fabricated to test the best structure for DNA confinement and imaging with fluorescently labeled abasic sites. The Si master was used to produce the UV-resin stamps and the patterns were transferred into a PMMA substrate by hot embossing at 125°C for 120 s under 1910 kN/m^2 (Hex 03, JenOptik). The structures were enclosed with a low T_g COC 8007 cover plate annealed at 70°C under a pressure of 680 kN/m^2 for 900 s.

3.3.2.3 Creating Abasic Sites in dsDNA

Abasic sites were created on λ DNA and T4 DNA by the heating method as previously reported [63-64, 69-70]. Heating genomic DNA to a temperature to 70°C for different times yields different number of abasic sites. For example, Kow *et al.* [70] reported treating DNA at 70°C for 10, 20, 30, 40 and 50 min would result in approximately 1, 2, 3, 4 or 5 AP sites. To prepare the DNA sample for the heat treatment, it was dialyzed in depurination buffer containing 100 mM NaCl and 10 mM sodium citrate buffer (pH ~ 5.0) at 4°C for 4 h. Prepared DNA samples were

then incubated at 70°C for 1 h to create abasic sites. AP DNA samples were then stored at 20°C until it was required for use.

3.3.2.4 Theory of ARP-Streptavidin Assay

Genomic DNA present in the cells can be damaged due to reactive oxygen species (ROS) present in the cell. ROS inside the cell can be generated by radiation, chlorinated compounds, ultraviolet light metal ions, peroxide compounds or chemotherapeutic drugs [65].

Generated abasic sites in DNA reside in equilibrium with a ring opened and a ring closed structure (Figure 3.9). It has been reported that 5% of the AP sites are in the ring-opened form. [70]

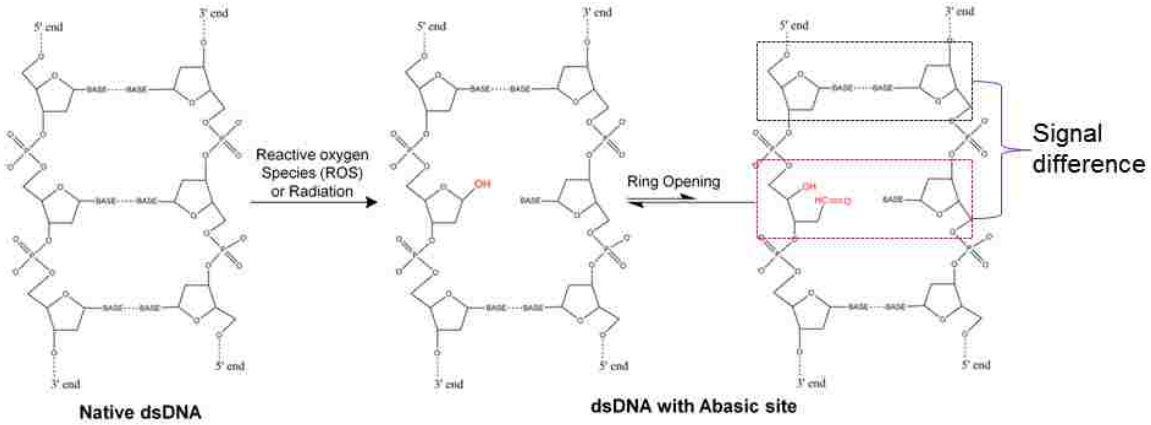

Figure 3.9 Reactive oxygen species inducing the double strand bond breakage followed by a ring opening generating an active carboxyl group exposed possible for conjugation.

Through the use of an extra amount of reactive species with the aldehyde group, it is possible to convert all the abasic sites into the open-ring form [70]. A biotinylated hydroxylamine called "aldehyde reactive probe" (ARP) readily conjugates to the active aldehyde group in the ring-opened form and attaches strongly by an imine bond (Figure 3.10). After labeling with ARP using the biotin group in ARP, it is possible to produce a complex with avidin or streptavidin. Horseradish peroxidase assays [70] and AlexaFluor labeled streptavidin assays [63-64] can be used to produce biotin-avidin or biotin-streptavidin complexes.

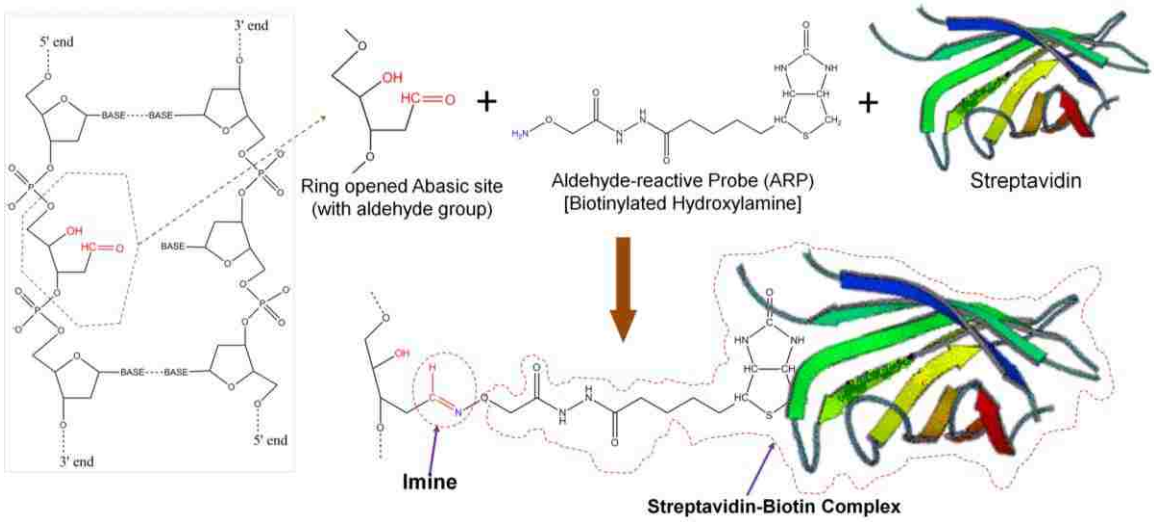

Figure 3.10 Aldehyde reactive probe (ARP) reacting with active aldehyde group in the ring-opened form of the abasic site. The biotin group in the ARP has a strong affinity to streptavidin which performs a strong covalent bond with Alexa Fluor labeled streptavidin making it possible to visualize abasic sites.

3.3.2.5 Preparation of ARP Conjugated AP DNA

The conjugation of aldehyde reactive probe (ARP) to AP DNA was carried out according to previous reports [63-64]. Prepared DNA solution concentration was adjusted to 100 ng/µL (this can be in the range of 50 -100 ng/µL). From the diluted DNA solution, 10 µL was mixed with 10 µL of 10 mM ARP-Biotin solution followed by incubation at 37^{o}C for 1 h. The excess DNA was removed by passing through a gel filtration column (Chroma spin TE-1000). Prepared ARP AP DNA was stored in 4^{o}C until further use.

3.3.2.6 Commercial Colorimetric Assay Protocol for Standard Abasic DNA [71]

Commercial DNA damage quantification kit was purchases from Dojindo Molecular Technologies, Inc. The standard abasic (AP) DNA is already labeled with aldehyde reactive probe (ARP). It includes calf-thymus DNA samples (0.5 µg/mL) with 0, 2.5, 5, 10, 20 and 40 ARP labeled AP sites. DNA binding solution, substrate solution, HRP-streptavidin, TE buffer

and washing buffer was also provided with the kit. Calibration curves were obtained using the standard protocol provided.

To prepare the colorimetric assay using DNA standards in a 96 well plate, 60 μL of each standard ARP-DNA was added in 3 wells for each sample. Then, 100 μL of DNA binding solution was mixed by pipetting in each well followed by overnight incubation at room temperature. The next day, 1/4000 diluted HRP-streptavidin solution was freshly prepared by mixing 10 μL of HRP-streptavidin in 40 mL of washing buffer (due to its instability, this solution was freshly prepared every time). Binding solutions were discarded and the wells were washed with washing buffer 5 times. After washing, 150 μL of diluted HRP-streptavidin was added to each well and incubated at 37^{o}C for 1 h. After incubation, the washing step was repeated. Then, 100 μL of substrate solution was added to each well and incubated at 37^{o}C for another 1 h. The optical density (OD) was recorded using a 96-well plate reader (SpectraMax M5 Multimode Plate Reader, Molecular Devices, LLC)

3.3.2.7 Choice of Fluorescence Dye for Abasic Site Tagging

Suitable dyes for direct imaging of the AP sites were selected prior to the experiment and the feasibility of imaging with the YOYO-1 was compared (YOYO-1 is an intercalating dye and is used to measure the DNA length to normalize the AP site frequency with respect to the DNA length). Figure 3.11 shows the excitation and emission spectra for YOYO-1, Alexa Fluor 594 and 647 dyes that can be excited with 488, 561 and 641 nm lasers equipped with emission filters 525/30, 605/15 and 678/29, respectively. YOYO-1 is excited with a 488 or 491 nm laser while 641 nm laser line is used to excite Alexa Fluor 647 and the 561 nm laser is used to excite Alexa Fluor 594 with minimal cross talk between these dyes and YOYO-1. Excitation and emission

filter sets can be adjusted to allow a certain fraction of light to pass through the filters and onto the camera.

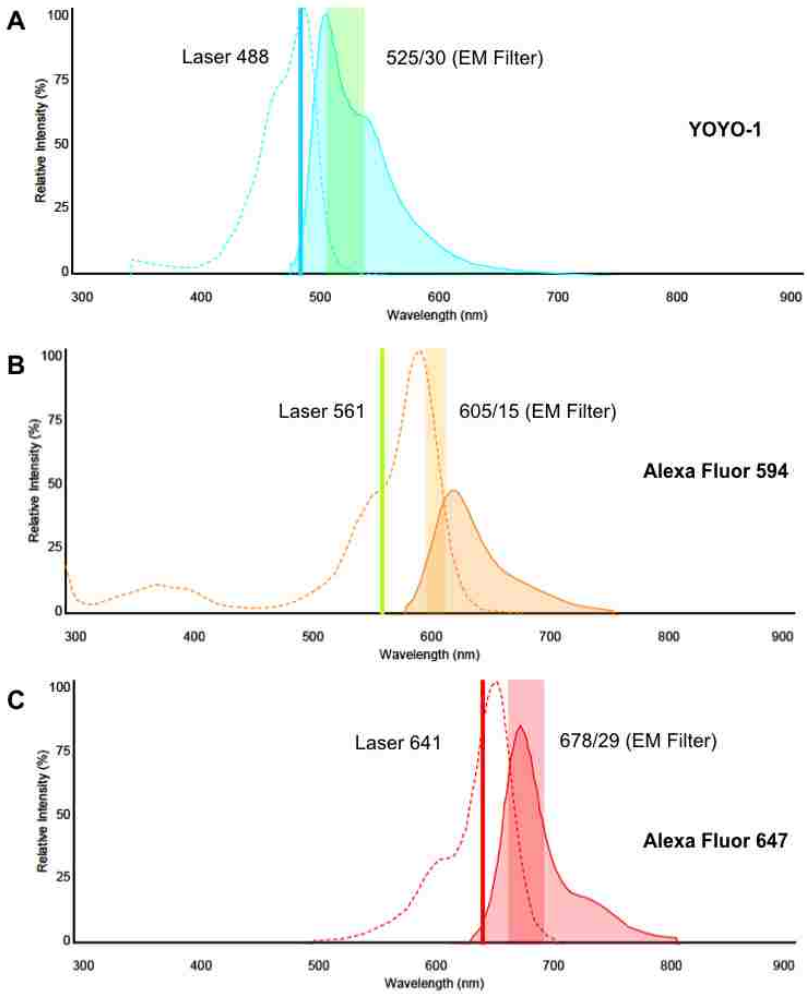

Figure 3.11 Excitation and emission spectra of A) YOYO-1 with 488 nm laser B) Alexa Fluor 594 with 561 nm laser and C) Alexa Fluor 647 with 641 nm laser. The emission filter sets are 525/30, 605/15 and 678/29, respectively. Emission spectra are normalized on the plot with respective to the emission

3.3.2.8 Labeling ARP AP DNA

ARP AP DNA was labeled with streptavidin that was loaded (covalently) with Alexa Fluor 594 or 647. The corresponding streptavidin molecule will react with the biotin group present in ARP to produce Alexa Fluor labeled abasic targets in the dsDNA. Figure 3.10 shows the amine

group of the ARP probe reacting with the aldehyde group of the open-ringed form to produce a strong imine bond.

Alexa Fluor labeled streptavidin solution was diluted by volume 1 to 5000. Mixed 10 μL of the diluted streptavidin solution with 10 μL of ARP AP DNA and the mixture was incubated at 37^{o}C for 1 h. Following this step, gel filtration was performed to remove the excess Alexa Fluor labeled streptavidin from the solution mixture. Finally, the DNA backbone was labeled with YOYO-1 dye at 5:1 bp/dye ratio in 1X TBE including 4% v/v β-mercaptoethanol as an anti-photobleaching agent.

3.3.2.9 DNA Extension, Confinement, Acquisition and Analysis of Abasic Sites

Prepared DNA samples were extended in the fabricated nanochannels driven into the nanochannel by an applied electric potential. When the DNA entered the nanochannel, the electric field supply was turned off such that the entered DNA would be confined and extended inside the nanochannel. DNA molecules were allowed to relax before acquisition of data. Fluorescence images were acquired using an inverted microscope (Olympus IX83 TIRF microscope system, Olympus, Pennsylvania PA) operated with a 100x oil immersion objective with a NA of 1.49 (WD = 0.19) and a 4-color laser system. The laser line used for this experiment was 491 nm (blue laser line), 561 nm (green laser line) and 641 nm (red laser line) with a Sedat filter set (LF488/561-2X2M-B-000, Semrock). Image acquisition was performed using a Hamamatsu Image EM Dual EMCCD camera (digital mode, 1024 ×1024 high resolution) with Metamorph software. High exposure times were used in order to achieve enough signal to detect the single molecule damage sites labeled in DNA strands.

3.3.3 Results and Discussion

3.3.3.1 Fabrication of Device

Fabrication steps are shown in Figure 3.12 as reported from our group.[17, 35] Briefly, this simplified method of NIL process shows the construction of UV resin stamp from nanochannel fabricated Si master by exposing to UV light. The constructed UV resin stamp was then used to

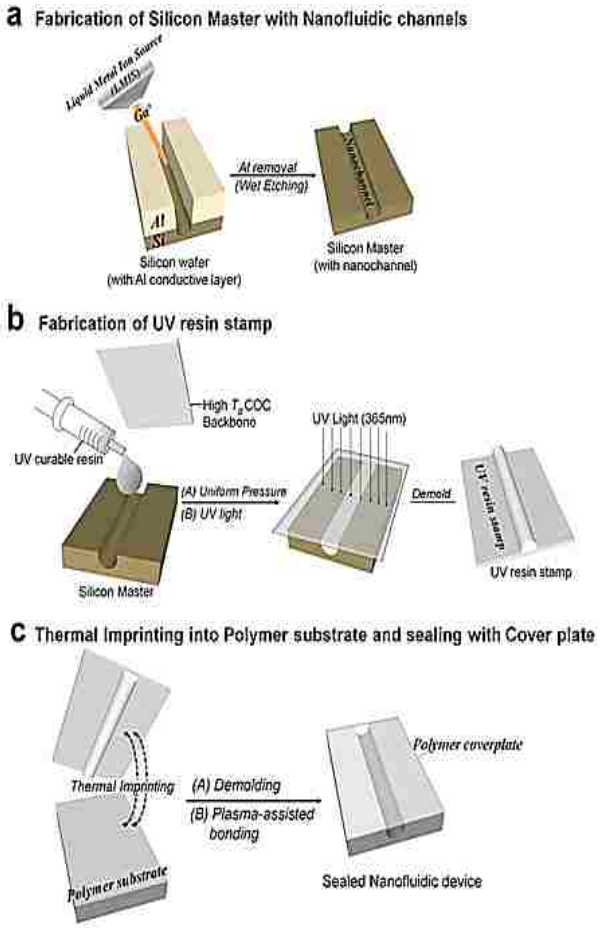

Figure 3.12 Process scheme for the fabrication and assembly of thermoplastic nanofluidic devices. (a) Fabrication of the Si master, which consisted of micron-scale access channels and the nanochannels/nanoslits; (b) fabrication of the protrusive polymer stamp in a UV-curable resin from the Si master; (c) generation of the fluidic structures in the thermoplastic substrate from the resin stamp by thermal embossing and plasma-assisted bonding of the substrate to the cover plate. (Reprinted from Uba *et. al.*)

stamp out nanofluidic devices in PMMA using thermal embossing. The devices were assembled with a cover plate using a low temperature bonding process and a COC cover plate.[72]

Nanochannel structures can be fabricated as straight nanochannel and/ or curvy (also called serpentine) nanochannels. Serpentine nanochannels have several advantages over straight channels for the present application. For example, serpentine nanochannels facilitate imaging a long DNA strand by confining it within the limited field-of-view (FoV) set by the microscope and its objective. Also, serpentine structures may assist the DNA molecule to confine inside the channel without an electric field to stretch it to its full contour length. It was reported that when DNA molecules were confined in straight nanochannels it undergoes molecular relaxation, thus reducing its stretched length inside nanochannel in the absence of an electrical field.[73] In serpentine nanochannels even though the relaxation phenomena occurs in straight region of the nanochannels, the turns may help the DNA to be hooked and keep the stretching in the absence of electric fields.

Different device designs were examined to find the most entropically favorable structure for DNA confinement and stretching to quantify the number of AP sites present in a single DNA molecule when read optically. Structures with serpentine architectures in different length scales and curvature differences were fabricated as well as straight nanochannels. Figure 3.13 shows fabricated test structure on a Si master, UV resin stamp and PMMA substrate.

Confinement of T4 DNA in the serpentine nanochannel structure was tested using the selected (3rd design from left on Figure 3.13) nanostructure. The dimension of the device was 120 nm × 120 nm. The goal of this experiment was to check the stretching percentage under the presence of an electric field and its behavior when the electric field is on verses at the absence of the electric field. The total channel length was calculated to be 95.45 μm (see Figure 3.14). DNA

confinement was tested using real-time imaging while it was translocating through the channel. The stretching at each condition was measured. Contour length of T4 DNA has been reported as 56.6 μm. But, it was reported that with the intercalating labeled YOYO-1, it could be increased by 13% (63.96 μm) to 32% (74.71 μm). [7, 74]

Stretching of the DNA was measured using ImageJ with the acquired images at the presence and absence of the electric field. The highest stretching was reported when the DNA was stretched under applied electric field strength of 35.6 V/cm with a length of 71.22 μm, which was 25% from its contour length. It was also found that the onset voltage for DNA to overcome the entropic barrier and enter the nanochannel was around 0.4 V, which translates to ~39 V/cm. It was observed at the absence of the electric field the stretching was almost the same and it was ~68 μm.

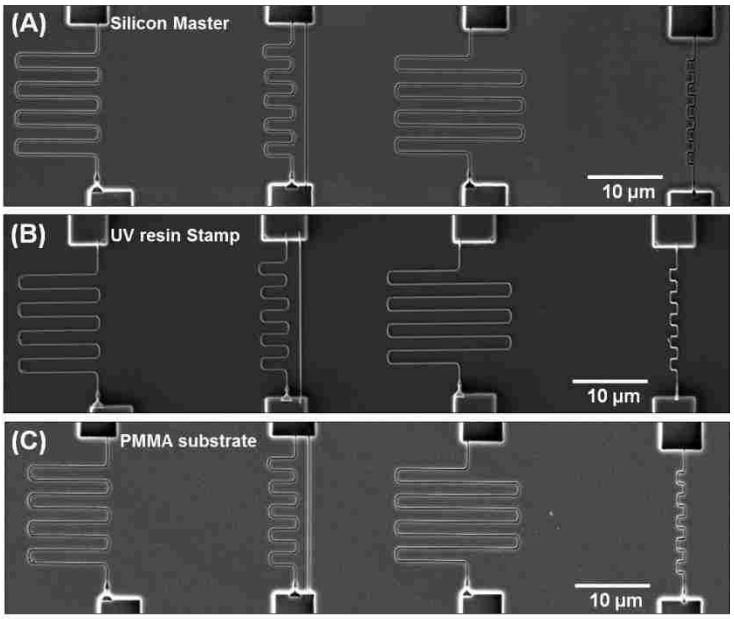

Figure 3.13 SEM images of A) Si master B) UV resin stamp C) PMMA substrate with thermal transferred serpentine nanochannel structures including different nanofluidic patterns. Preliminary results were collected using the above structures and analyzed to find the nanochannel that can confine DNA with minimal entropic stress.

Structure in Figure 3.14 was modified with the addition of two funnel entrances with pillars from both sides as shown in Figure 3.15. All the nanochannels are 120 nm × 120 nm while a different device was fabricated with narrower turns of 85 nm × 120 nm. The ease of translocation was checked using labeled λ and T4 DNA. The entrance funnel has a gradient with reducing depth from microchannel to the nanochannel entrance. The pillar regions help coiled DNA to pre-stretch and break the entropic barrier before entering the nanochannel.

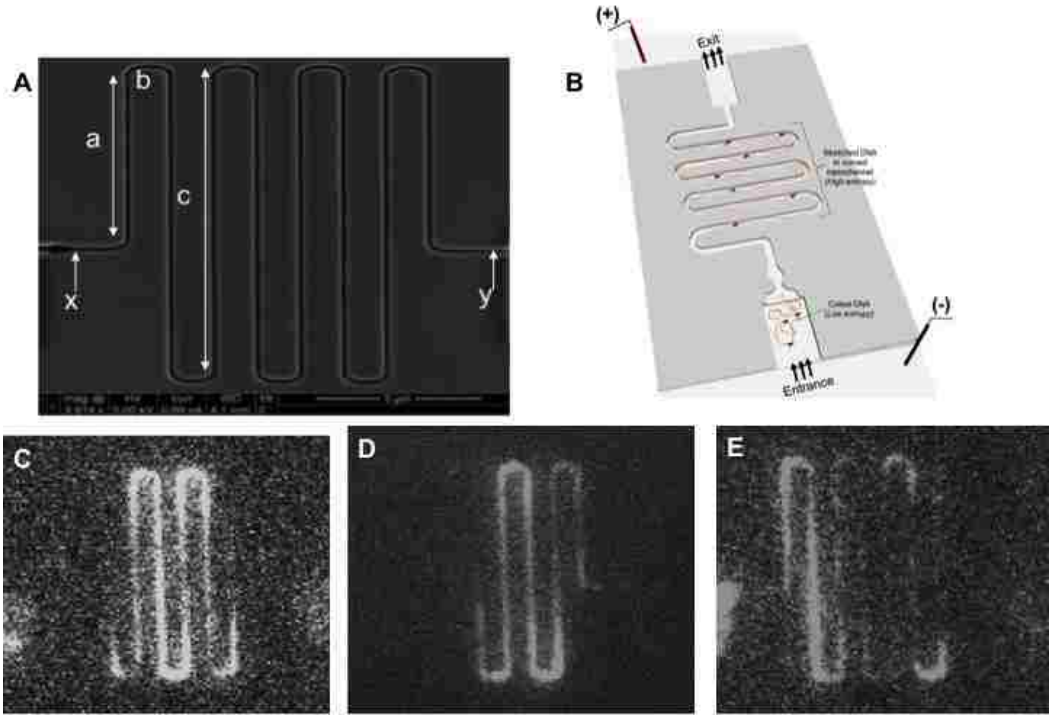

Figure 3.14 A) SEM images of chosen serpentine nanochannel device design to incorporate confinement of T4 DNA. The measured lengths of sections are a = 6.12 μm, b = 1.32 μm and c = 11.49 μm, which gives a total length of the channel from x to y as 95.45 μm. B) Schematic representation of T4 DNA driven electrokinetically into the serpentine nanochannel and confined for imaging. Percent stretching of T4 DNA under field strengths of C) 46.1 V/cm, D) 98.48 V/cm, E) 35.62 V/cm with measured stretching length 56.56 μm, 51.24 μm and 71.22 μm, respectively.

Figure 3.16 shows the T4 and λ DNA stretching in serpentine nanochannels. A maximum stretching of 51.24 μm (stained contour length = 56.6 μm) was reported for T4 DNA and 14.5 μm (stained contour length = 21.8 μm) was reported for λ DNA. From the preliminary studies

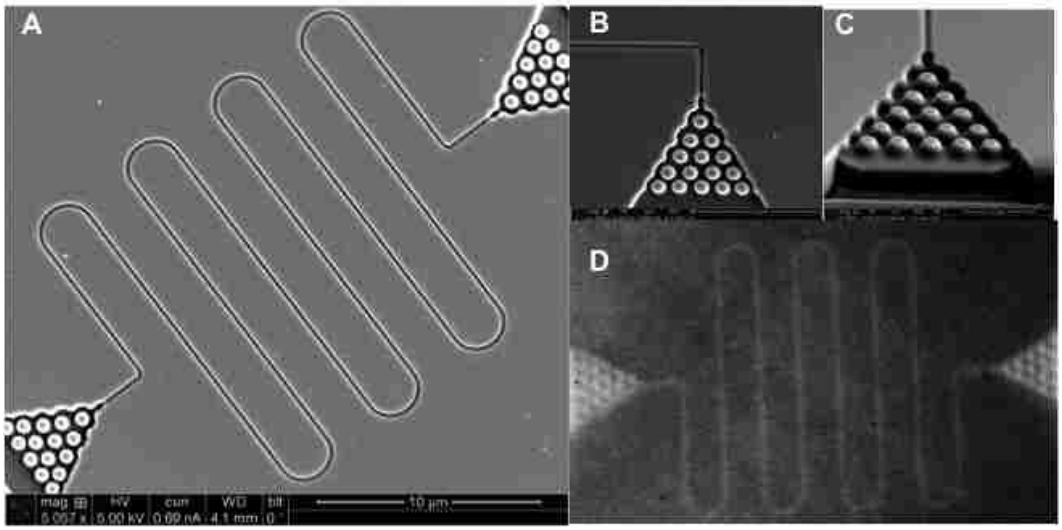

Figure 3.15 A) SEM images of the chosen serpentine nanochannel device design to incorporate confinement of T4 DNA with the funnel shape entrance with pillars. The measured lengths of sections are a = 6.875 µm, b = 2.5 µm and c = 14.375 µm, which gives a total length of the channel from x to y of 120 µm. Two devices designed with different curvature dimensions of 120 nm × and 85 nm × 120 nm. All the straight regions were 120 nm × 120 nm. B) and C) shows the funnel entrance with pillars. The diameters of the pillars are 300 nm and the spacing between the pillars is 150 nm. D) Sealing test to check the proper sealing of the device with 5 mM FITC dye in 1X TBE.

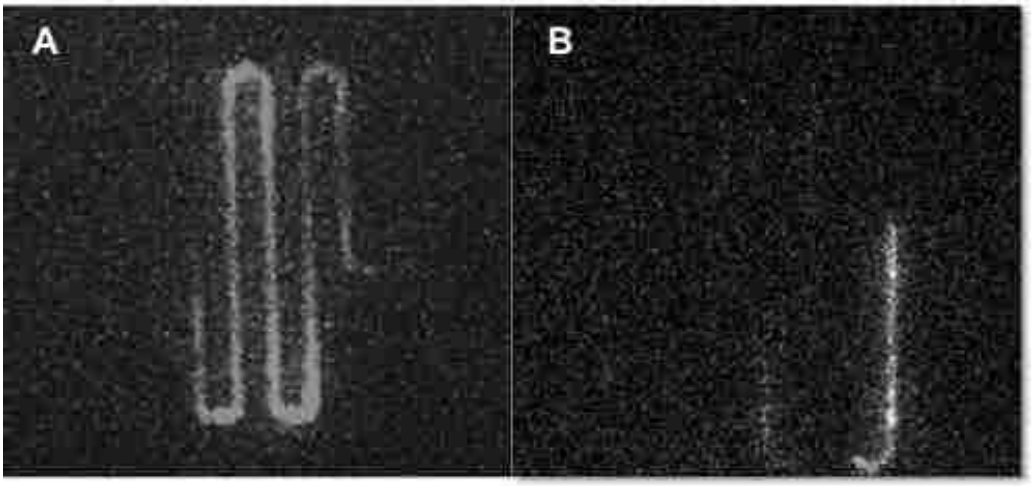

Figure 3.16 Images of A) T4 DNA stretched inside the serpentine nanochannels to a length of 51.24 µm B) λ DNA stretched to 14.5 µm length inside the serpentine nanochannel. Dimensions of the channels are 120 nm × 120 nm

about DNA confinement in serpentine nanochannels, it was evident that the entropic barrier for the DNA to enter the serpentine was high compared to that of the straight channels. Also, the

motion of DNA gained by the electrophoretic force was disturbed by the 90^0 turn as soon as the molecule entered the nanochannel. Also the entropic barrier it has to overcome to pass each turn was higher compared to the straight nanochannel thus DNA molecules seems to push itself extremely hard at the mentioned turns. As a result, it may break in to small fragments preventing to image the whole molecule stretched inside the nanochannel. Also, we observed the fragments tend to hook at the turns creating issues to clean the nanochannel for reuse. Also, from extensive studies in our group about the capture efficiency of DNA molecules in the presence of an electric field, it is higher when gradually decreasing funnel (3D funnel) entrances are ratified into the device design.

Therefore, the pillar geometry and gradual decreasing modality of the entrance has adapted to the next device design incorporating with straight nanochannels. Figure 3.17 A shows the nanofluidic device design with pillar region to facilitate the pre-stretching. Similar design has been previously reported to stretch and confine DNA in nanochannel arrays [60-61]. Fabricated nanochannels dimensions were 100 nm × 80 nm and 80 nm × 50 nm (B of Figure 3.17). The sealing of the device was confirmed by 5 mM FITC in TBE buffer as shown in C of Figure 3.17.

The functionality of the above device was verified with YOYO-1 dye. It was observed that the entrance pillars pre-stretched the λ DNA aiding them to λ DNA stained with enter the nanochannel more easily. Figure 3.18 shows the confinement of λ DNA in the 120 nm × 80 nm nanochannel array absence of the electric field. It was observed that DNA undergo molecular relaxation and move in a "spring-like" motion inside the nanochannel. Considering the dimensions of the nanochannel, we are observing DNA moleculae are extending in the deGennes regime reporting a maximum stretch of ~65% considering the total length of stained λ DNA is ~20 μm.

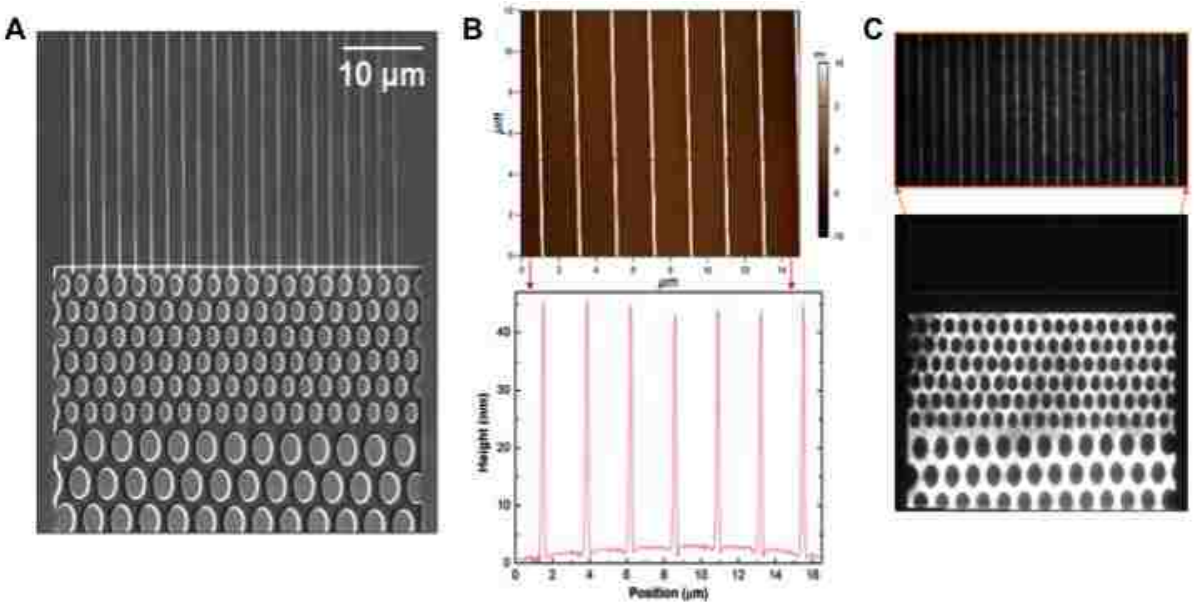

Figure 3.17 A) SEM images of the Si master with the device design. Device consists of entrance larger pillar structures followed by smaller pillar structures to incorporate the pre-stretching of DNA. The pillar region and the opposite microchannel are directly connected by the nanochannel array. B) AFM profile scanned across the nanochannel array showing a ~50 nm depth and 80 nm width. C) Sealing test with 5 mM FITC in 1X TBE buffer through a COC cover plate to ensure the nanofluidic structure patterns are transferred to PMMA with high integrity and minimal deformity.

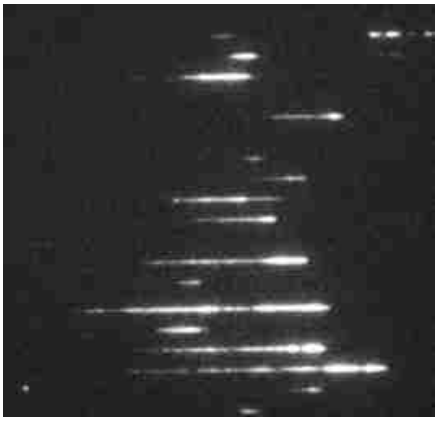

Figure 3.18 Stretching and confinement of λ DNA in the nanochannel array in the absence of electric field. Channel dimensions were 120 nm × 80 nm.

3.3.3.2 Optical Microscopy and Experimental Setup with Dual Color Laser System

Figure 3.19 shows the experimental setup for the AP site imaging. The bonded nanofluidic chip was place on the translational stage of the microscope. The DNA sample was introduced from the device reservoirs and it was driven into the nanochannels by the electrical potential supplied through the DC power supply. The onset voltage for the DNA to go into the nanochannels was found to be 0.4 V. The device design we are using with this setup is shown in

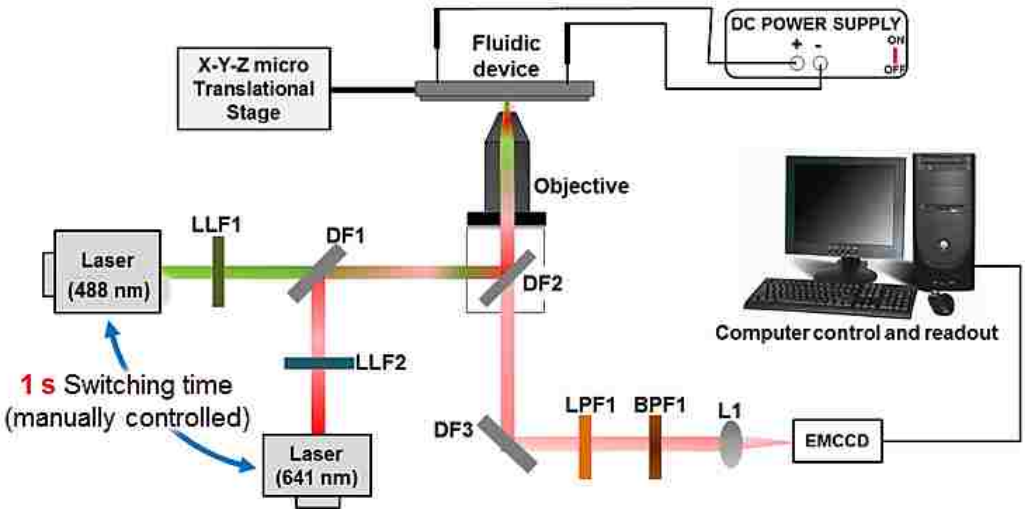

Figure 3.19 Schematic representation of the microscopy setup with two color laser system. Nanofluidic device is placed on the translational stage and the Pt electrodes supply the electric potential through a DC power supply. The switching between two lase lines is controlled manually with a 1s switching delay. All the acquired images were collected through the EMCCD camera by Metamorph software.

Figure 3.17. As soon as DNA entered the nanochannels, the voltage was turned off so that the molecules could be imaged within the nanochannel to maintain its stretched conformation. Imaging of YOYO-1 labeled DNA was performed with the EM gain setting of 250 and 100 ms exposure time under wide field mode. Likewise, images of Alexa Fluor streptavidin labeled AP sites were acquired at 300 EM gain and 2000 ms exposure time. The DNA lengths were measured and the fluorescence spots on the DNA strands were counted using FIJI software. The

measured fragmentation lengths and the AP site fluorescence signal were done using the available functions in FIJI software.

3.3.3.3 Alexa Flour conjugated Streptavidin

Streptavidin is a biotin binding non-glycosylated 52,800-dalton protein with 4 identical polypeptide chains found in cultured broth of bacterium *Streptomyces avidinii* with an isoelectric point close to neutral. Streptavidin has shown remarkable affinity towards biotin. Both biotin and streptavidin are in the size range of 2-3 nm.[75] Streptavidin-biotin complex (B in Figure 3.20) is highly stable over a wide pH range and temperatures (Dissociation constant, K_d is ~10^{-15}).[76]

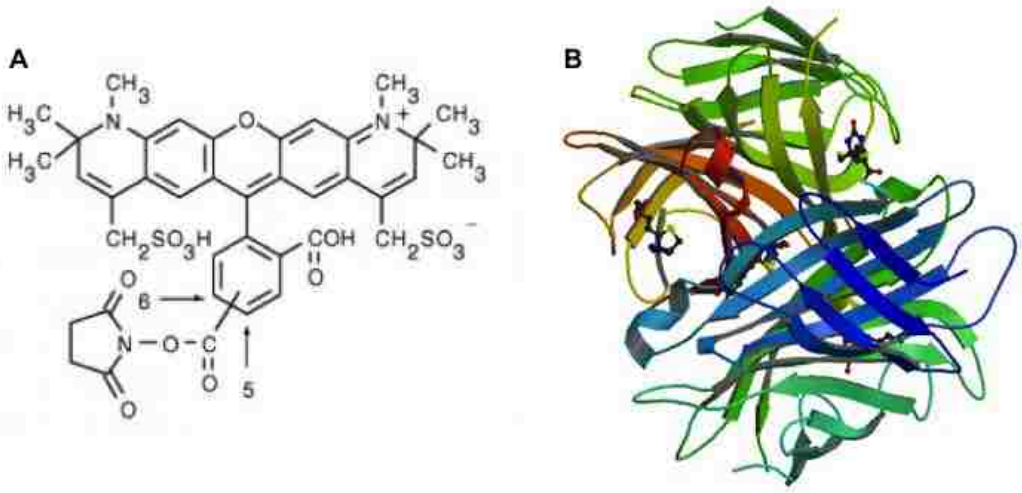

Figure 3.20 A) Structure of Alexa 594 with a net charge of negative 2. B) Crystal structure of streptavidin with two bonded biotin molecular system (Reproduced from www.biosyn.com and www.rcsb.org)

Although, irreversible denaturation of the protein can cause disruption of the complex.[77-78] Most critically, the low number of carbohydrate groups associated with streptavidin compared to avidin make it neutral (pI 5 - 6) and hence, more useful for studying various biological applications. Subsequently, it has shown less non-specific binding compared to avidin, which results in binding to specific targets presumably in applications such as DNA/ RNA analysis,

Western blots, Sothern blots, protein purifications and biotinylation of specific sites (abasic sites of DNA) [76, 79-80]. The composition of streptavidin is a homo-tetramer with 24-32 lysine residues in each tetramer. It doesn't contain cysteine or carbohydrate side chains. Even though, different synthesis protocols [81-82] can result in differences in the amino or carboxyl terminus and different chain lengths, monomer subunits of streptavidin usually synthesized with 183 amino acids.[83] According to Suter *et al.* [84], the extinction coefficient of streptavidin is found to be 32.

Alexa Flour dyes are usually used for labeling antibodies, nucleic acids, and as general probes for proteins, cytoskeletal elements, lipids, and general neuroscience. These dyes are synthetic fluorescent conjugate dyes, which has an excitation and emission spectra including mostly visible (and some infrared wavelengths) and higher wavelengths of ultra violet regions. These are known of their high stability and low photobleaching properties.[85] For example, Alexa Fluor 488 is a green fluorescent dye that is suitable for excitation by 488 nm laser line with an excitation max of 490 and an emission max of 525, whereas Alexa Fluor 594 (A in Figure 3.20) is a bright red fluorescent dye that is suitable for excitation using both 561 and 594 laser lines with an excitation max at 590 and emission max at 617.[86] Alexa dyes are negatively charged anions with a net charge of negative 2. [87-88]

In this experiment, Alexa Fluor 594 streptavidin conjugate and Alexa Fluor 647 streptavidin conjugate were used to label the damage sites of dsDNA. Thus, our perceptive is to understand the properties and dynamics of streptavidin labeled with Alexa Fluor dyes under the influence of an electric field which would help us clarifying preliminary assumptions in our experiment. Also, the static imaging techniques of these conjugates needs to be understood.

Figure 3.21 A shows the imaged Streptavidin Alexa Fluor 647 conjugate on a glass slide imaged with the 641 laser to explore the possibility of seeing a single conjugate and their

lifespan. Alexa Fluor 647 consists of 3 dye molecules and it was observed that before it completely photobleach, the fluorescence intensity reduced stepwise in intensity and blinked several times. ImageJ was used to calculate the fluorescent intensity and timespan of one streptavidin conjugate. Figure 3.21 B shows the fluorescence intensity spectrum corresponding to each dye molecule histogrammed in C in Figure 3.21. It is evident that most of the conjugates had a similar intensity value at the initial stage of excitation with the laser. The average timespan of the conjugate varied from 62 – 208 s providing a wide range due to the presence of 3 dye molecules per conjugate.

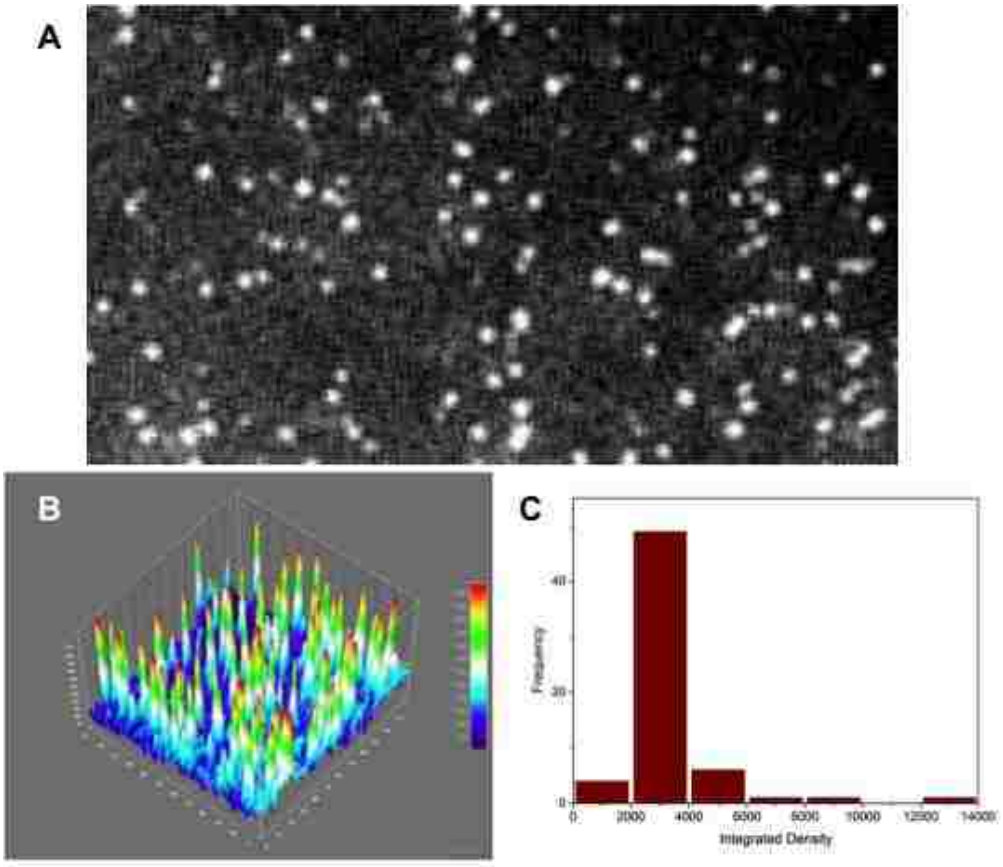

Figure 3.21 A) Images of Streptavidin Alexa Fluor 647 conjugate through a COC cover plate. Illumination was from 641 nm red laser using 100X (1.49 N/A) objective. B) Surface 3D plot showing the intensity of the individual streptavidin molecules. C) Number of occurrences of integrated intensity for all current voxels of single streptavidin molecules.

PMMA polymer nanoslits were filled with Alexa Fluor 594 labeled streptavidin and excited using the 563 nm green laser. An electric field was applied across the nanoslits. The travel direction of streptavidin molecules was noted. As Figure 3.22 elaborates, dye labeled streptavidin traveled from anode to cathode with the electroosmotic flow (EOF). Neutral streptavidin molecule consists of 2 dye molecules, which are both negatively charged (each -2 net charge), resulting -4 net charge on the molecule. Even though it is expected that the net

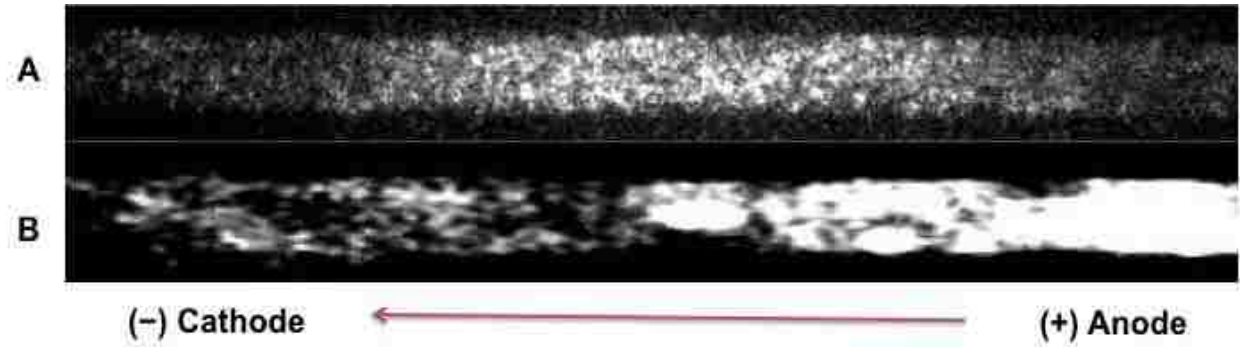

Figure 3.22 A) Alexa Fluor 594 labeled streptavidin inside PMMA nanoslits device (d = 150 nm) at 0 V B) Alexa Fluor 594 labeled streptavidin molecules moving from anode to cathode with the EOF at 20 V/cm

negative charge should direct the molecules towards the positively biased electrode, we observed the streptavidin traveling towards the negatively biased electrode with the EOF. This behavior has been previously reported by Gracia *et. al.*[88]. Electrokinetic transport behavior of dyes in micro scale would not necessarily be translated to the nanoscale.

The concentrations of Streptavidin Alexa Fluor used for labeling abasic sites are in the range of 0.2 -0.4 μg/mL. The emission spectra of the conjugate versus the concentrations were investigated to build a calibration curve using the fluorometer. It will be helpful to quantify the remaining streptavidin conjugate once the abasic sites are being labeled, and filtered to remove the excess. Figure 3.23 (left) shows the fluorescence maximum intensity in counts-per-second

versus the concentration when the streptavidin conjugates were excited at 561 nm. The fluorescence intensity increased with the increasing concentration (right figure of Figure 3.23).

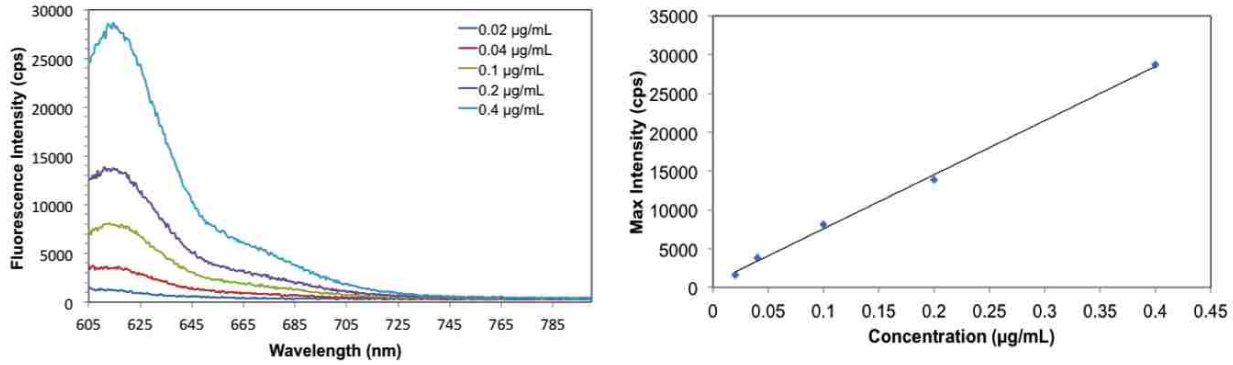

Figure 3.23 Emission spectrum fluorescence intensities of 0.02, 0.04, 0.1, 0.2, 0.4 µg/mL concentrations of streptavidin Alexa Fluor 594 emission spectrum in the wavelength range 605 - 805 nm. The units in y-axis are in counts-per-second (cps) (left). Calibration plot with the max intensity corresponding each concentration. Max intensity points were average values over 5 trials (right).

The lowest concentration of streptavidin conjugate that can be measured using the fluorometer was 0.08 µg/mL. Therefore it was compared to the actual concentration used in the experiment before and after the gel filtration. After labeling the abasic sites on the DNA, it was necessary to remove the excess streptavidin in free solution via a size-exclusion gel filtration column (Chroma spin TE-1000). This is a crucial step, because the free streptavidin may interfere with the imaging when the abasic DNA is confined in the nanochannel resulting in erroneous observations. The free flow of unbounded streptavidin in to the nanochannel and they being occupied in a region where the abasic DNA is confined may result in counting them as labeled abasic sites on the DNA strand.

Figure 3.24 (left) shows the fluorescence intensity measurements of 0.4 µg/mL concentration of streptavidin conjugate before and after the filtration step along with the similar results obtained for 0.008 µg/mL. Figure 3.24 (right) shows it for actual samples with 0 AP DNA and 40 AP DNA in comparison with 0.008 and 0.4 µg/mL concentrations of streptavidin conjugate. All

the results were acquired after performing the gel filtration step. From these observations it is obvious that the gel filtration step was successful in removing most of the unconjugated streptavidin from the free solution.

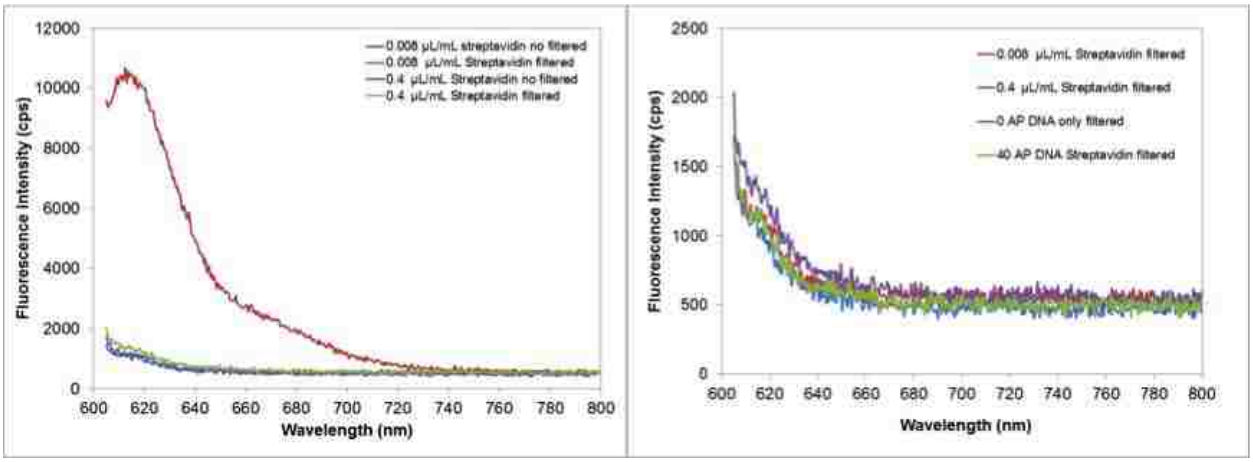

Figure 3.24 Fluorescence intensities of the emission spectrum corresponding to 0.008 and 0.4 µg/mL concentration solutions of streptavidin Alexa Fluor 594 before and after the filtration step (left). 0.008 and 0.4 µg/mL concentration solutions of streptavidin Alexa Fluor 594, 0-AP DNA, 40-AP DNA after the filtration step. Data are in the wavelength ranging from 600 to 800 nm (right). The units in y-axis is are counts-per-second (cps)

3.3.3.4 Development of Calibration Assay with Commercial Standard Abasic Site DNA Kit using Conventional Analytical Methodologies

There are commercial assays available to measure abasic DNA using conventional methods (such as colorimetric, absorption) and quantify based on the number of abasic sites. These methods are easy to use but the main disadvantage is lack of sensitivity in the single molecular level. Usually these assays require DNA samples in µL volumes for the accurate quantification, which requires thousands of cells.

The commercial DNA damage assay was purchased from Dojindo and standard protocol was followed to build the calibration curve using provided DNA standards. After following the steps in day1 and 2, the solutions in the wells turned in to blue color and absorbance was measured at

each well. Figure 3.25 shows the calibration curve for AP site determination using the colorimetric assay.

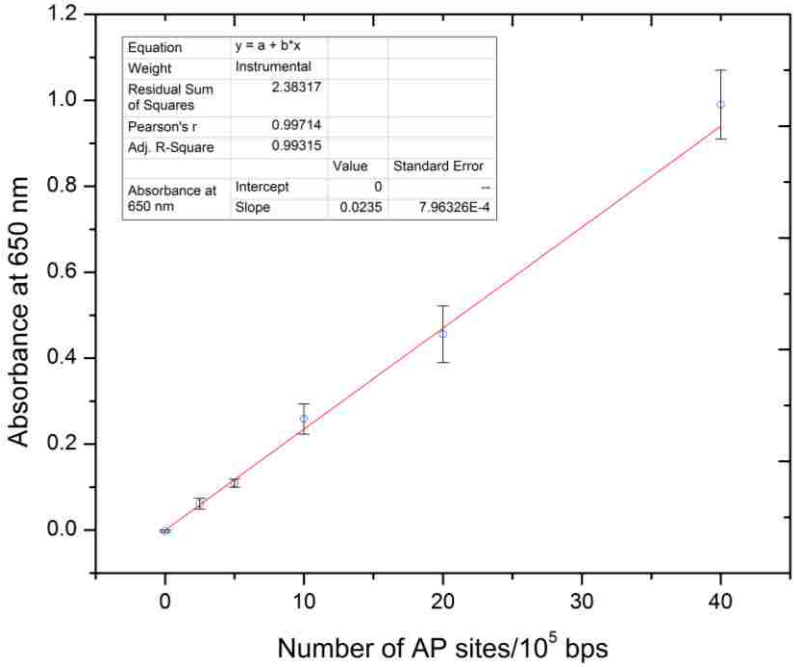

Figure 3.25 Calibration curve developed using colorimetric assay by measuring absorbance at 650 nm in a 96-well plate reader.

From the calibration curve it can be depicted that absorbance has a linear relationship with the number of abasic sites in the sample. The slope of the calibration curve is 0.0235 that reflects the sensitivity of the assay. Correlation coefficient was 0.99 corresponding to the obtained data set.

3.3.3.5 Single Molecule DNA Imaging

Commercial DNA standards and the AP ARP DNA prepared both can be labeled with Alexa Fluor streptavidin and YOYO-1 following the protocol described in the Material and Methods section. As preliminary data, the possibility of imaging abasic DNA stretched on poly-lysine (poly-L) glass slides was explored. Poly-L slides cationic nature allows anionic DNA backbone to adhere on to the surface and stretch when sandwiched between glass cover slip.

Figure 3.26 shows the calf-thymus DNA standards of 20 AP sites per 10^5 bp stretched on a poly-L glass slide. These images confirm that the labeling of the abasic sites was successful and from the acquired images there are 1-3 abasic sites that can be identified in these 7 images. It was expected that 20 abasic sites in 10^5 bp; that is approximately in 34 μm in length. However, the stretching on poly-L will not reach DNA's maximum contour length. Therefore, the labeled abasic sites visible on the DNA strand may be far less than what is expected. To overcome this challenge, it is critical to stretch the DNA in a nano-confined environment less than its persistence length.

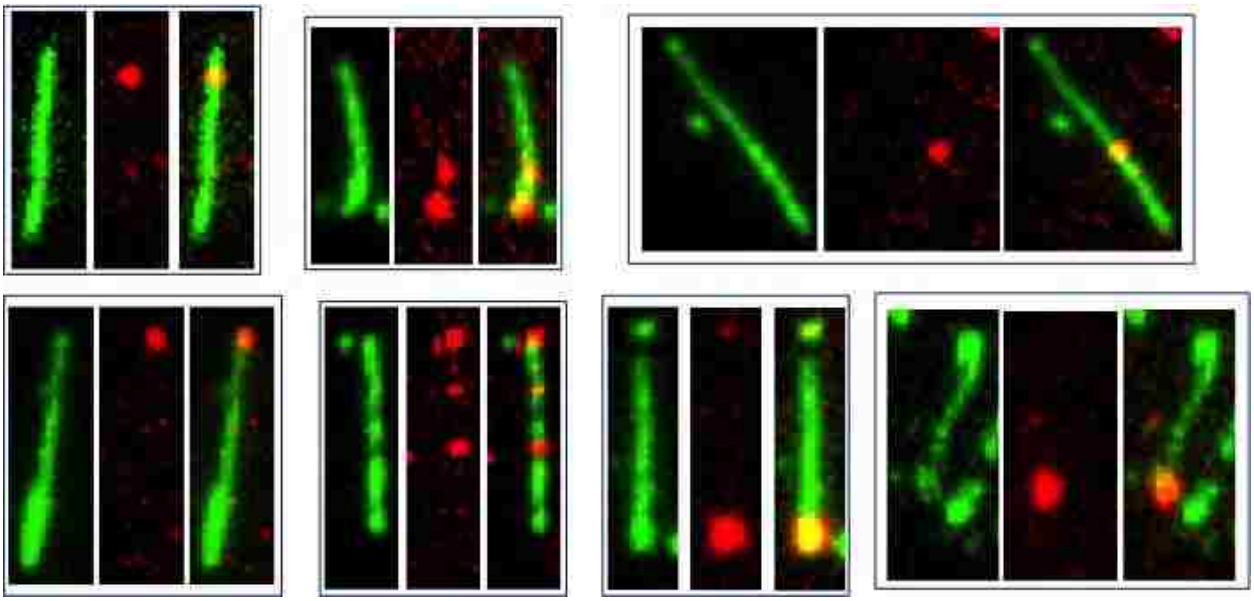

Figure 3.26 Images of 7 DNA molecules imaged by stretching on a poly-lysine glass slide from the 20 AP DNA standards. DNA backbone is labeled with YOYO-1 intercalating dye (green) and the abasic sites are labeled with Alexa Fluor 594 streptavidin (red). Composite image shows the abasic sites (yellow) in the DNA strand.

3.3.3.6 Hybrid Nanofluidic Device for Abasic Site Assay Development

Hybrid nanofluidic devices provide the perfect platform for imaging fluorescence single molecules because of its optical clarity through the COC cover plate compared to PMMA.[72]

Thus, it can be used to acquire images of single abasic sites with optimal resolution between two labeled sites.

Figure 3.27 shows the preliminary acquired images of 20 AP DNA/10^5 bp in a 120 nm × 80

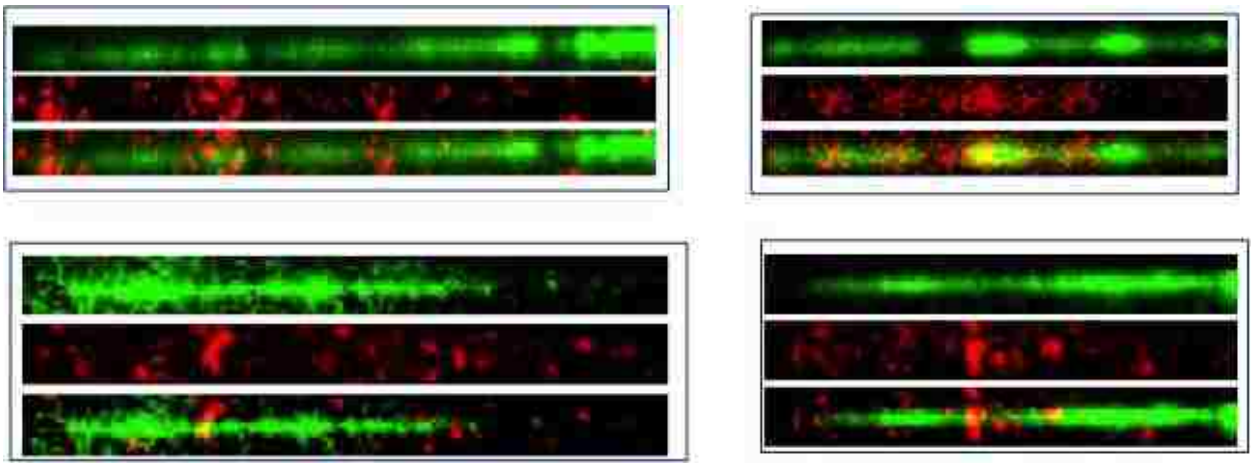

Figure 3.27 Images acquires on 20 AP DNA/10^5 bp confined on 120 nm × 80 nm nanochannels. DNA backbone is labeled with YOYO-1 intercalating dye (green) and the abasic sites are labeled with Alexa Fluor 594 streptavidin (red). Composite image shows the abasic sites (yellow) in the DNA strand.

nm nanochannel. However, these DNA cannot be stretched to its maximum length because their dimensions are higher than the persistence length. Nevertheless, acquired composite images can be image processed to enhance the abasic site fluorescence signal and remove the existing noise. ImageJ can be used to enhance the fluorescence signal from abasic sites. Figure 3.28 shows the

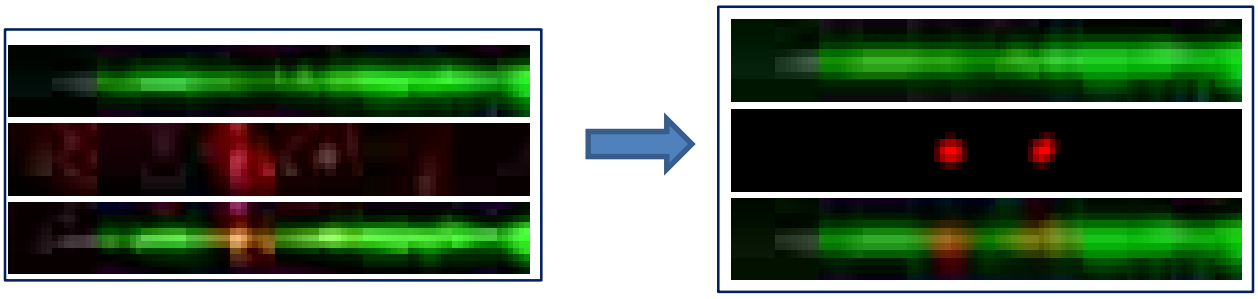

Figure 3.28 Images acquires on 20 AP DNA/10^5 bp confined on 120 nm × 80 nm nanochannels. DNA backbone is labeled with YOYO-1 intercalating dye (green) and the abasic sites are labeled with Alexa Fluor 594 streptavidin (red). Composite image shows the abasic sites (yellow) in the DNA strand.

enhanced signal removing the noise from the picture on left. Use of functions such as contrast enhancement, co-localization and Gaussian blur will help to produce more cleaner and enhanced images which will make it easy to identify the abasic sites in the DNA strand.

3.3.4 Conclusions and Future Work

It has been demonstrated that the use of serpentine nanochannel devices and straight nanochannel devices for DNA confinement. Imaging of abasic sites DNA, stretched in a glass slide and nanochannels has been demonstrated using the dual color laser system. Images for all the abasic standards will be collected using the hybrid nanochannel devices and the sensitivity of the calibration will be compared to the conventional methodologies available. Nanofluidic devices with smaller channel dimensions (smaller than persistence length) will be fabricated to accommodate full contour stretching of dsDNA. The genomic DNA will be isolated from patient samples undergoing chemotherapy treatments to identify the specific treatment regimes. Correlation with the patient abasic sample with the chemotherapy treatment will be identified.

3.4 References

1. Prakash, S.; Piruska, A.; Gatimu, E. N.; Bohn, P. W.; Sweedler, J. V.; Shannon, M. A., Nanofluidics: Systems and Applications. *Sensors Journal, IEEE* 2008, *8* (5), 441-450.

2. Abgrall, P.; Nguyen, N. T., Nanofluidic Devices and Their Applications. *Analytical Chemistry* 2008, *80* (7), 2326-2341.

3. Han, J.; Turner, S. W.; Craighead, H. G., Entropic Trapping and Escape of Long DNA Molecules at Submicron Size Constriction. *Phys. Rev. Lett.* 1999, *83* (8), 1688-1691.

4. Odijk, T., Scaling theory of DNA confined in nanochannels and nanoslits. *Physical Review E* 2008, *77* (6), 060901.

5. Guo, L. J.; Cheng, X.; Chou, C.-F., Fabrication of Size-Controllable Nanofluidic Channels by Nanoimprinting and Its Application for DNA Stretching. *Nano letters* 2003, *4* (1), 69-73.

6. Reisner, W., Statics and dynamics of single DNA molecules confined in nanochannels. *Phys. Rev. Lett.* 2005, *94* (19), 196101.

7. Reisner, W.; Beech, J. P.; Larsen, N. B.; Flyvbjerg, H.; Kristensen, A.; Tegenfeldt, J. O., Nanoconfinement-Enhanced Conformational Response of Single DNA Molecules to Changes in Ionic Environment. *Phys. Rev. Lett.* 2007, *99* (5), 058302.

8. Levy, S. L.; Craighead, H. G., DNA manipulation, sorting, and mapping in nanofluidic systems. *Chemical Society Reviews* 2010, *39* (3), 1133-1152.

9. Fang Lim, S.; Karpusenko, A.; Sakon, J. J.; Hook, J. A.; Lamar, T. A.; Riehn, R., DNA methylation profiling in nanochannels. *Biomicrofluidics* 2011, *5* (3).

10. Riehn, R.; Lu, M.; Wang, Y.-M.; Lim, S. F.; Cox, E. C.; Austin, R. H., Restriction mapping in nanofluidic devices. *Proceedings of the National Academy of Sciences of the United States of America* 2005, *102* (29), 10012-10016.

11. Foquet, M.; Korlach, J.; Zipfel, W.; Webb, W. W.; Craighead, H. G., DNA Fragment Sizing by Single Molecule Detection in Submicrometer-Sized Closed Fluidic Channels. *Analytical Chemistry* 2002, *74* (6), 1415-1422.

12. Li, W., Sacrificial polymers for nanofluidic channels in biological applications. *Nanotechnology* 2003, *14* (6), 578-583.

13. Tegenfeldt, J.; Prinz, C.; Cao, H.; Huang, R.; Austin, R.; Chou, S.; Cox, E.; Sturm, J., Micro- and nanofluidics for DNA analysis. *Anal Bioanal Chem* 2004, *378* (7), 1678-1692.

14. Chantiwas, R.; Park, S.; Soper, S. A.; Kim, B. C.; Takayama, S.; Sunkara, V.; Hwang, H.; Cho, Y.-K., Flexible fabrication and applications of polymer nanochannels and nanoslits. *Chemical Society Reviews* 2011, *40* (7), 3677-3702.

15. Chou, S. Y.; Krauss, P. R.; Renstrom, P. J., Imprint of sub- 25 nm vias and trenches in polymers. *Appl. Phys. Lett.* 1995, *67* (21), 3114-3116.

16. Chantiwas, R.; Hupert, M. L.; Pullagurla, S. R.; Balamurugan, S.; Tamarit-Lopez, J.; Park, S.; Datta, P.; Goettert, J.; Cho, Y.-K.; Soper, S. A., Simple replication methods for producing nanoslits in thermoplastics and the transport dynamics of double-stranded DNA through these slits. *Lab on a Chip* 2010, *10* (23), 3255-3264.

17. Wu, J.; Chantiwas, R.; Amirsadeghi, A.; Soper, S. A.; Park, S., Complete plastic nanofluidic devices for DNA analysis via direct imprinting with polymer stamps. *Lab on a Chip* 2011, *11* (17), 2984-2989.

18. Abgrall, P.; Low, L.-N.; Nguyen, N.-T., Fabrication of planar nanofluidic channels in a thermoplastic by hot-embossing and thermal bonding. *Lab on a Chip* 2007, *7* (4), 520-522.

19. Shao, P. E.; van Kan, A.; Wang, L. P.; Ansari, K.; Bettiol, A. A.; Watt, F., Fabrication of enclosed nanochannels in poly(methylmethacrylate) using proton beam writing and thermal bonding. *Appl. Phys. Lett.* 2006, *88* (9), -.

20. Sivanesan, P.; Okamoto, K.; English, D.; Lee, C. S.; DeVoe, D. L., Polymer Nanochannels Fabricated by Thermomechanical Deformation for Single-Molecule Analysis. *Analytical Chemistry* 2005, *77* (7), 2252-2258.

21. Li, J.-M.; Liu, C.; Ke, X.; Duan, Y.-j.; Fan, Y.; Li, M.; Zhang, K.-p.; Xu, Z.; Wang, L.-d., Fabrication of 1D nanochannels on thermoplastic substrates using microchannel compression. *Microsyst Technol* 2013, *19* (11), 1845-1850.

22. Cheng, E.; Zou, H.; Yin, Z.; Jurcicek, P.; Zhang, X., Fabrication of 2D polymer nanochannels by sidewall lithography and hot embossing. *J. Micromech. Microeng.* 2013, *23* (7).

23. Junshan, L.; Hongchao, Q.; Zheng, X.; Chong, L.; Junyao, W.; Liqun, D.; Xi, Z.; Liding, W., Fabrication of planar nanofluidic channels in thermoplastic polymers by O₂ plasma etching. *Micro & Nano Letters, IET* 2012, *7* (2), 159-162.

24. Liu, J.; Jin, X.; Sun, T.; Xu, Z.; Liu, C.; Wang, J.; Chen, L.; Wang, L., Hot embossing of polymer nanochannels using PMMA moulds. *Microsyst Technol* 2013, *19* (4), 629-634.

25. Li, J.-m.; Liu, C.; Ke, X.; Xu, Z.; Duan, Y.-j.; Fan, Y.; Li, M.; Zhang, K.-p.; Wang, L.-d., Microchannel refill: a new method for fabricating 2D nanochannels in polymer substrates. *Lab on a Chip* 2012, *12* (20), 4059-4062.

26. Zhang, L.; Gu, F.; Tong, L.; Yin, X., Simple and cost-effective fabrication of two-dimensional plastic nanochannels from silica nanowire templates. *Microfluid Nanofluid* 2008, *5* (6), 727-732.

27. Cho, Y. H.; Park, J.; Park, H.; Cheng, X.; Kim, B. J.; Han, A., Fabrication of high-aspect-ratio polymer nanochannels using a novel Si nanoimprint mold and solvent-assisted sealing. *Microfluid Nanofluid* 2010, *9* (2-3), 163-170.

28. Lasse, H. T.; Anna, K.; Anders, K., Stretching DNA in polymer nanochannels fabricated by thermal imprint in PMMA. *Nanotechnology* 2008, *19* (12), 125301.

29. Hu, X.; He, Q.; Zhang, X.; Chen, H., Fabrication of fluidic chips with 1-D nanochannels on PMMA substrates by photoresist-free UV-lithography and UV-assisted low-temperature bonding. *Microfluid Nanofluid* 2011, *10* (6), 1223-1232.

30. Bilenberg, B.; Hansen, M.; Johansen, D.; Özkapici, V.; Jeppesen, C.; Szabo, P.; Obieta, I. M.; Arroyo, O.; Tegenfeldt, J. O.; Kristensen, A., Topas-based lab-on-a-chip microsystems fabricated by thermal nanoimprint lithography. *Journal of Vacuum Science & Technology B* 2005, *23* (6), 2944-2949.

31. Cheng, E.; Yin, Z.; Zou, H.; Chen, L., Surface modification-assisted bonding of 2D polymer-based nanofluidic devices. *Microfluid Nanofluid* 2014, 1-9.

32. Piruska, A.; Nikcevic, I.; Lee, S. H.; Ahn, C.; Heineman, W. R.; Limbach, P. A.; Seliskar, C. J., The autofluorescence of plastic materials and chips measured under laser irradiation. *Lab on a Chip* 2005, *5* (12), 1348-1354.

33. Khanarian, G.; Celanese, H., Optical properties of cyclic olefin copolymers. *OPTICE* 2001, *40* (6), 1024-1029.

34. Jena, R.; Yue, C. Y.; Lam, Y. C., Micro fabrication of cyclic olefin copolymer (COC) based microfluidic devices. *Microsyst Technol* 2012, *18* (2), 159-166.

35. Uba, F. I.; Pullagurla, S.; Sirasunthorn, N.; Wu, J.; Park, S.; Chantiwas, R.; Cho, Y.-K.; Shin, H.; Soper, S. A., Surface charge, electroosmotic flow and DNA extension in chemically modified thermoplastic nanoslits and nanochannels. *Analyst* 2014, *139*.

36. Suni, T.; Henttinen, K.; Suni, I.; Mäkinen, J., Effects of Plasma Activation on Hydrophilic Bonding of Si and SiO2. *Journal of The Electrochemical Society* 2002, *149* (6), G348-G351.

37. Tong, Q. Y.; Gösele, U., A Model of Low- Temperature Wafer Bonding And Its Applications. *Journal of The Electrochemical Society* 1996, *143* (5), 1773-1779.

38. Ramm, P.; Lu, J. J.-Q.; Taklo, M. M., *Handbook of Wafer Bonding*. John Wiley & Sons: 2012.

39. Tsao, C. W.; Hromada, L.; Liu, J.; Kumar, P.; DeVoe, D. L., Low temperature bonding of PMMA and COC microfluidic substrates using UV/ozone surface treatment. *Lab on a Chip* 2007, *7* (4), 499-505.

40. Vesel, A.; Mozetic, M., Surface modification and ageing of PMMA polymer by oxygen plasma treatment. *Vacuum* 2012, *86* (6), 634-637.

41. Firbank, M. J.; Coulthard, A.; Harrison, R. M.; Williams, E. D., A comparison of two methods for measuring the signal to noise ratio on MR images. *Physics in Medicine and Biology* 1999, *44* (12), N261.

42. Reisner, W.; Morton, K. J.; Riehn, R.; Wang, Y. M.; Yu, Z.; Rosen, M.; Sturm, J. C.; Chou, S. Y.; Frey, E.; Austin, R. H., Statics and Dynamics of Single DNA Molecules Confined in Nanochannels. *Phys. Rev. Lett.* 2005, *94* (19), 196101.

43. Chai, J.; Lu, F.; Li, B.; Kwok, D. Y., Wettability Interpretation of Oxygen Plasma Modified Poly(methyl methacrylate). *Langmuir* 2004, *20* (25), 10919-10927.

44. Hwang, S.-J.; Tseng, M.-C.; Shu, J.-R.; Her Yu, H., Surface modification of cyclic olefin copolymer substrate by oxygen plasma treatment. *Surface and Coatings Technology* 2008, *202* (15), 3669-3674.

45. Roy, S.; Yue, C. Y.; Lam, Y. C.; Wang, Z. Y.; Hu, H., Surface analysis, hydrophilic enhancement, ageing behavior and flow in plasma modified cyclic olefin copolymer (COC)-based microfluidic devices. *Sensors and Actuators B: Chemical* 2010, *150* (2), 537-549.

46. Jackson, J. M.; Witek, M. A.; Hupert, M. L.; Brady, C.; Pullagurla, S.; Kamande, J.; Aufforth, R. D.; Tignanelli, C. J.; Torphy, R. J.; Yeh, J. J.; Soper, S. A., UV activation of polymeric high aspect ratio microstructures: ramifications in antibody surface loading for circulating tumor cell selection. *Lab on a Chip* 2014, *14* (1), 106-117.

47. Xu, F.; Datta, P.; Wang, H.; Gurung, S.; Hashimoto, M.; Wei, S.; Goettert, J.; McCarley, R. L.; Soper, S. A., Polymer Microfluidic Chips with Integrated Waveguides for Reading Microarrays. *Analytical Chemistry* 2007, *79* (23), 9007-9013.

48. Bensimon, D.; Simon, A. J.; Croquette, V.; Bensimon, A., Stretching DNA with a Receding Meniscus: Experiments and Models. *Phys. Rev. Lett.* 1995, *74* (23), 4754-4757.

49. Ross, D.; Johnson, T. J.; Locascio, L. E., Imaging of Electroosmotic Flow in Plastic Microchannels. *Analytical Chemistry* 2001, *73* (11), 2509-2515.

50. Kolarevic, D.; Tomasevic, Z.; Dzodic, R.; Gavrilovic, D.; Zegarac, M., Clinical and pathological response to induction chemotherapy used as a prognostic factor in inflammatory breast cancer. Single institution experience. *J BUON* 2012, *17* (1), 21-6.

51. Saadat, M.; Khalili, M.; Nasiri, M.; Rajaei, M.; Omidvari, S.; Saadat, I., Clinical response to chemotherapy in locally advanced breast cancer was not associated with several polymorphisms in detoxification enzymes and DNA repair genes. *Biochem Biophys Res Commun* 2012, *419* (1), 117-9.

52. Croshaw, R.; Shapiro-Wright, H.; Svensson, E.; Erb, K.; Julian, T., Accuracy of clinical examination, digital mammogram, ultrasound, and MRI in determining postneoadjuvant pathologic tumor response in operable breast cancer patients. *Ann Surg Oncol* 2011, *18* (11), 3160-3.

53. Esserman, L. J.; Berry, D. A.; Demichele, A.; Carey, L.; Davis, S. E.; Buxton, M.; Hudis, C.; Gray, J. W.; Perou, C.; Yau, C.; Livasy, C.; Krontiras, H.; Montgomery, L.; Tripathy, D.; Lehman, C.; Liu, M. C.; Olopade, O. I.; Rugo, H. S.; Carpenter, J. T.; Dressler, L.; Chhieng, D.; Singh, B.; Mies, C.; Rabban, J.; Chen, Y. Y.; Giri, D.; van 't Veer, L.; Hylton, N., Pathologic Complete Response Predicts Recurrence-Free Survival More Effectively by Cancer Subset: Results From the I-SPY 1 TRIAL--CALGB 150007/150012, ACRIN 6657. *Journal of clinical oncology : official journal of the American Society of Clinical Oncology* 2012.

54. Guiu, S.; Arnould, L.; Coudert, B.; Liegard, M.; Mayer, F.; Favier, L.; Fumoleau, P., Neoadjuvant Chemotherapy for Triple-Negative Breast Cancer: Pathologic Complete Response and Survival after Long-Term Follow-Up. *Cancer Research* 2009, *69* (24), 572S-572S.

55. Guiu, S.; Debled, M., Major challenges in the current management of metastatic cancer. *Oncologie* 2010, *12* (4), 278-284.

56. Guiu, S.; Gauthier, M.; Coudert, B.; Bonnetain, F.; Favier, L.; Ladoire, S.; Tixier, H.; Guiu, B.; Penault-Llorca, F.; Ettore, F.; Fumoleau, P.; Arnould, L., Pathological complete response and survival according to the level of HER-2 amplification after trastuzumab-based neoadjuvant therapy for breast cancer. *British journal of cancer* 2010, *103* (9), 1335-1342.

57. Humbert, O.; Berriolo-Riedinger, A.; Cochet, A.; Gauthier, M.; Charon-Barra, C.; Coudert, B.; Guiu, S.; Toubeau, M.; Cochet, I.; Fumoleau, P.; Brunotte, F., Prognostic relevance at 5 years of the early monitoring of neoadjuvant chemotherapy in luminal breast cancer, using 18F-FDG PET. *European Journal of Nuclear Medicine and Molecular Imaging* 2012, *39*, S283-S284.

58. Michalet, X.; Ekong, R.; Fougerousse, F.; Rousseaux, S.; Schurra, C.; Hornigold, N.; Slegtenhorst, M. v.; Wolfe, J.; Povey, S.; Beckmann, J. S.; Bensimon, A., Dynamic Molecular Combing: Stretching the Whole Human Genome for High-Resolution Studies. *Science* 1997, *277* (5331), 1518-1523.

59. Lin, J.; Qi, R.; Aston, C.; Jing, J.; Anantharaman, T. S.; Mishra, B.; White, O.; Daly, M. J.; Minton, K. W.; Venter, J. C.; Schwartz, D. C., Whole-Genome Shotgun Optical Mapping of Deinococcus radiodurans. *Science* 1999, *285* (5433), 1558-1562.

60. Cao, H.; Hastie, A. R.; Cao, D.; Lam, E. T.; Sun, Y.; Huang, H.; Liu, X.; Lin, L.; Andrews, W.; Chan, S., Rapid detection of structural variation in a human genome using nanochannel-based genome mapping technology. *GigaScience* 2014, *3* (1), 34.

61. Michaeli, Y.; Ebenstein, Y., Channeling DNA for optical mapping. *Nature biotechnology* 2012, *30* (8), 762-763.

62. Sun, H. B.; Qian, L.; Yokota, H., Detection of Abasic Sites on Individual DNA Molecules Using Atomic Force Microscopy. *Analytical Chemistry* 2001, *73* (10), 2229-2232.

63. Hirose, T.; Ohtani, T.; Muramatsu, H.; Tanaka, A., Direct Visualization of Abasic Sites on a Single DNA Molecule Using Fluorescence Microscopy¶. *Photochemistry and photobiology* 2002, *76* (2), 123-126.

64. Kim, J.; Muramatsu, H.; Lee, H.; Kawai, T., Near-field optical imaging of abasic sites on a single DNA molecule. *FEBS letters* 2003, *555* (3), 611-615.

65. Chastain, P. D.; Nakamura, J.; Rao, S.; Chu, H.; Ibrahim, J. G.; Swenberg, J. A.; Kaufman, D. G., Abasic sites preferentially form at regions undergoing DNA replication. *The FASEB Journal* 2010, *24* (10), 3674-3680.

66. Lee, J.; Park, H. S.; Lim, S.; Jo, K., Visualization of UV-induced damage on single DNA molecules. *Chemical Communications* 2013, *49* (42), 4740-4742.

67. An, N.; Fleming, A. M.; White, H. S.; Burrows, C. J., Crown ether–electrolyte interactions permit nanopore detection of individual DNA abasic sites in single molecules. *Proceedings of the National Academy of Sciences of the United States of America* 2012, *109* (29), 11504-11509.

68. Marshall, M. M.; Ruzicka, J. A.; Taylor, E. W.; Hall, A. R., Detecting DNA depurination with solid-state nanopores. 2014.

69. Fundador, E.; Rusling, J., Detection of labeled abasic sites in damaged DNA by capillary electrophoresis with laser-induced fluorescence. *Anal Bioanal Chem* 2007, *387* (5), 1883-1890.

70. Kow, Y. W.; Dare, A., Detection of abasic sites and oxidative DNA base damage using an ELISA-like assay. *Methods* 2000, *22* (2), 164-169.

71. Dojindo Molecular Technologies, I. DK02: -Nucleostain- DNA Damage Quantification Kit -AP Site Counting. http://www.dojindo.com/store/p/200-DNA-Damage-Quantification-Kit-AP-Site-Counting.html, (Retrieved on 07/12/2015).

72. Uba, F. I.; Hu, B.; Weerakoon-Ratnayake, K.; Oliver-Calixte, N.; Soper, S. A., High process yield rates of thermoplastic nanofluidic devices using a hybrid thermal assembly technique. *Lab on a Chip* 2015, *15* (4), 1038-1049.

73. Kim, Y.; Kim, K. S.; Kounovsky, K. L.; Chang, R.; Jung, G. Y.; Jo, K.; Schwartz, D. C., Nanochannel confinement: DNA stretch approaching full contour length. *Lab on a Chip* 2011, *11* (10), 1721-1729.

74. Walter, R.; Jonas, N. P.; Robert, H. A., DNA confinement in nanochannels: physics and biological applications. *Reports on Progress in Physics* 2012, *75* (10), 106601.

75. Swift, J. L.; Cramb, D. T., Nanoparticles as Fluorescence Labels: Is Size All that Matters? *Biophysical Journal* 2008, *95* (2), 865-876.

76. Chaiet, L.; Wolf, F. J., The properties of streptavidin, a biotin-binding protein produced by Streptomycetes. *Archives of Biochemistry and Biophysics* 1964, *106* (0), 1-5.

77. Bayer, E. A.; Ben-Hur, H.; Gitlin, G.; Wilchek, M., An improved method for the single-step purification of streptavidin. *Journal of Biochemical and Biophysical Methods* 1986, *13* (2), 103-112.

78. Hofmann, K.; Wood, S. W.; Brinton, C. C.; Montibeller, J. A.; Finn, F. M., Iminobiotin affinity columns and their application to retrieval of streptavidin. *Proceedings of the National Academy of Sciences* 1980, *77* (8), 4666-4668.

79. Life Technologies Avidin, NeutrAvidin and Streptavidin Conjugates—Section 7.6. http://www.lifetechnologies.com/us/en/home/references/molecular-probes-the-handbook/antibodies-avidins-lectins-and-related-products/avidin-streptavidin-neutravidin-and-captavidin-biotin-binding-proteins-and-affinity-matrices.html, (Retrieved on 07/12/2015).

80. Prozyme Streptavidin http://www.prozyme.com, (Retrieved on 07/12/2015).

81. Bayer, E. A.; Ben-Hur, H.; Hiller, Y.; Wilchek, M., Postsecretory modifications of streptavidin. *Biochem. J.* 1989, *259* (2), 369-376.

82. Pähler, A.; Hendrickson, W. A.; Kolks, M. A.; Argaraña, C. E.; Cantor, C. R., Characterization and crystallization of core streptavidin. *Journal of Biological Chemistry* 1987, *262* (29), 13933-7.

83. Argarana, C. E.; Kuntz, I. D.; Birken, S.; Axel, R.; Cantor, C. R., Molecular cloning and nucleotide sequence of the streptavidin gene. *Nucleic Acids Research* 1986, *14* (4), 1871-1882.

84. Suter, M.; Cazin Jr, J.; Butler, J. E.; Mock, D. M., Isolation and characterization of highly purified streptavidin obtained in a two-step purification procedure from Streptomyces avidinii grown in a synthetic medium. *Journal of Immunological Methods* 1988, *113* (1), 83-91.

85. Olympus Corporation Glossary of Terms in Fluorescence and Confocal Microscopy. http://www.olympusfluoview.com/theory/glossary.html, (Retrieved on 07/12/2015).

86. Life Technologies Fluorophore Selection. http://www.lifetechnologies.com/us/en/home/life-science/cell-analysis/fluorophores.html, (Retrieved on 07/12/2015).

87. Osiri, J. K.; Shadpour, H.; Park, S.; Snowden, B. C.; Chen, Z.-Y.; Soper, S. A., Generating high peak capacity 2-D maps of complex proteomes using PMMA microchip electrophoresis. *ELECTROPHORESIS* 2008, *29* (24), 4984-4992.

88. Garcia, A. L.; Ista, L. K.; Petsev, D. N.; O'Brien, M. J.; Bisong, P.; Mammoli, A. A.; Brueck, S. R. J.; Lopez, G. P., Electrokinetic molecular separation in nanoscale fluidic channels. *Lab on a Chip* 2005, *5* (11), 1271-1276.

CHAPTER 4. COMPUTER SIMULATION STUDIES

4.1 General Introduction

The following chapter is a collaboration project with Prof. Dorel Moldovan's group at Mechanical Engineering at LSU. We investigated the possibility of separating nucleotides in a nanoslit by molecular dynamics simulation study. It is an effort to provide guidance for the real time experiments performed on single molecular electrophoresis in nanochannel-based biosensors based on their time-of-flight (ToF) measurements. Corresponding study assisted to measure the efficiency and accuracy of nucleotide readouts occur in a nanotube. It will also revealed critical information about adsorption-desorption behavior of these nucleotides providing a platform to modify the polymer surfaces of our polymer devices to prevent non-specific adsorption and facilitate the optimum transport through the nanochannels.[4]

4.2 Electrophoretic Transport of Single DNA Nucleotides Through Nanoslits: Molecular Dynamics Simulation Study

4.2.1 Introduction

Automated DNA sequencing has attracted significant interest since the Human Genome Project began. A major goal is to develop a high-throughput and low-cost method to identify each DNA nucleotide in the correct sequence as it passes a sensor(s). There are three major sequencing approaches of this type under consideration. In some of these approaches intact DNA strands are used,[1] and in others individual nucleotides are first cleaved sequentially from DNA by an exonuclease.[2-3] The first approach involves modification of the nucleotides so optical detection methods can be used. In the second approach, a DNA strand or single nucleotides from

[4] This section is published in J. Phys. Chem. B, 2015, 119 (35), pp 11443–11458 DOI: 10.1021/acs.jpcb.5b02798 on August 03, 2015. Authors are as follows; Xia, Kai; Novak, Brian; Weerakoon-Ratnayake, Kumuditha; Soper, Steven; Nikitopoulos, Dimitris; Moldovan, Dorel.

a disassembled strand are passed through a nanopore and the identity of each nucleotide is determined as it passes.[4-8] The final approach involves passing single nucleotides from disassembled strands through a nanochannel containing multiple detectors. In this approach the flight times of the nucleotides between detectors are used to identify them. [9]

There are also several methods of detection under consideration for use with the above approaches. In optical methods, fluorescence is used.[10] If an electric field is used to drive DNA or nucleotides through a nanopore, a current associated with the flow of other ions through the pore exists. Part of this current is blocked when a nucleotide is in the pore,[11-12] and the magnitude of the blockage depends upon the nucleotide type. Electrodes might be placed in a nanopore to measure the transverse conductance[10, 13-19] or transverse differential conductance[20] associated with each nucleotide as it passes. Sequence specific hysteresis effects were observed when using an AC field with a nanopore.[21] Graphene nanoribbons have been used with nanopores since the currents induced in the nanoribbons from their interaction with each passing nucleotide are orders of magnitude higher than ion blockage currents.[22-25] For flight time based sequencing, the detectors will likely have to involve a restriction similar to a nanopore. In fact, two nanopore systems have been used to measure the mobility of DNA[26] molecules and to analyze virus capsids.[27-28] The detection method will also likely be similar to those being considered for the nanopore based methods. The difference is that in the flight-time-based method, only the presence of a nucleotide needs to be detected, not its identity; a noisier signal can be tolerated.

Optical methods rely on fluorescent labeling to distinguish the nucleotides. Color discrimination has been used to distinguish each nucleotide of an enzymatically disassembled DNA strand with fluorescently labeled nucleotides.[29-31] In another method, each nucleotide is

substituted for by a unique group of 16 nucleotides, then each of these oligonucleotides are hybridized to a fluorescently labeled strand, and finally a nanopore is used to remove the fluorescent strand and detect the oligonucleotide type and therefore the identity of the original nucleotide.[10, 32] A third method follows the incorporation of fluorescently labeled nucleotide triphosphates as they are added to a growing DNA strand by polymerases.[33]

In nanopore based sequencing methods, the nanopores act to help constrain the configurations of DNA, as the housing for electrodes, or as a constriction to create a blockage in ion current. The reliability and cost for the manufacturing of devices containing nanopores will play an important role in whether these types of DNA sequencing will be successful. Nanopores may be biological or synthetic. Biological pores include the membrane proteins α-hemolysin[2, 11-12, 34-37] or porin A.[38] Pores composed of synthetic DNA nanostructures[39-40] or carbon nanotubes[41] spanning a lipid bilayer have been studied. Synthetic pores constructed in silicon nitride[11, 42-43] or hafnium oxide,[44] or in 2D materials such as boron nitride,[45-46] graphene,[47-53] or molybdenum sulfide[54] provide additional flexibility including the ability to adjust the pore size and chemically modify the nanopore surfaces or entrap other structures such as synthetic DNA nanostructures[40] within them, and improved mechanical stability compared to membrane-bound systems.

Nanopore sequencing has limitations. For intact DNA, the measured signal may be a convolution of multiple adjacent nucleobases.[55] One advantage of using nanopores composed of 2D materials is that they can potentially overcome this problem since a single or a few sheets are of a similar or smaller depth than the depth of a single nucleotide. Another challenge is to improve the resolution to make detection more reliable. It only takes several microseconds for each nucleotide to move through a nanopore and it could be in a variety of different conformations, thus it is difficult to extract useful signals from background noise, particularly

when ion blockage currents are used due to their small magnitude. Solutions to this problem include reducing the traveling velocity of the DNA or single nucleotides or controlling the conformations of DNA while in the pores using various means[2, 37, 56-61] or creating two detection sites within nanopores.[62] Other detection methods such as transverse conductance and graphene nanoribbons discussed above are less susceptible to this problem due to the larger currents compared to ion blockage currents.

In this research we focus on the flight time based approach for DNA sequencing, which involves sequential, enzymatic DNA disassembly into single nucleotides. These nucleotides are driven through a nanochannel with detectors placed at multiple locations. The enzymes used would be λ–exonucleases covalently attached to pillars. λ–exonucleases have been attached to poly(methyl methacrylate) (PMMA) pillars and the activity of the attached enzymes was slightly higher than for free enzymes.[63] λ–exonucleases disassemble one strand of double stranded DNA into single nucleotides with phosphate groups on their 5' ends, deoxynucleotide 5'-monophosphates (dNMPs). The identity of each different type of dNMP; deoxyadenosine 5'-monophosphate (dAMP), deoxycytidine 5'-monophosphate (dCMP), deoxyguanosine 5'-monophosphate (dGMP), deoxythymidine 5'-monophosphate (dTMP), and the epigenetically modified dNMP deoxy-5-methylcytidine 5'-monophosphate (dMCMP) is determined by using the time(s) taken for it to travel between the different detectors (flight time(s) or time(s) of flight) as well as the detector signals themselves. The flight times have a specific distribution for each type of dNMP.

The following is a discussion of the advantages and disadvantages of the flight time based approach to sequencing. The main advantage of this method is that the detectors only need to determine the presence of a dNMP rather than its identity. The problem of trying to distinguish

closely spaced nucleotides in intact DNA does not exist when the DNA is disassembled. However, disassembling the DNA also has disadvantages. The first is simply the complication of having to introduce immobilized λ-exonuclease enzymes into the system. The use of free dNMPs instead of intact DNA allows for the possibility of misordering due to one dNMP passing another one. This can be minimized by changing the magnitude of the driving force or the rate at which the enzyme disassembles the DNA by altering solution conditions such as temperature and pH. Another issue is that diffusion broadens the flight time distributions leading to longer channel lengths and analysis times per dNMP.[9] To reduce this, it is desirable for the magnitude of the driving force to be as large as is practical. If the nucleotide-wall interactions are relied upon to separate the flight time distributions, then the channels should be as narrow as possible so that the dNMPs are in contact with them for a large fraction of the time. The channel walls should also be as homogeneous as possible both chemically and physically since heterogeneities will lead to varying dNMP-wall adsorption energies and broadening of the flight time distributions. The adsorption energies should also be small enough that the dNMPs do not become stuck on the walls for long periods of time since that could lead to misordering.

Since all the nucleotides are anionic for a pH above about 3.2,[64-66] the simplest way to drive DNA or single dNMPs through nanopores or nanochannels is by using an electric field to cause electrophoresis and, if the channel walls are charged, an electrokinetic flow.

In this study we investigated the electrophoretically driven transport of the four major DNA nucleotide monophosphates or dNMPs (dAMP, dCMP, dGMP, and dTMP) through nanoslits composed of disordered carbon atoms using all-atom, explicit solvent, molecular dynamics (MD) simulations. The main goals include development of fundamental understanding of the mechanism of the dNMP transport and assessment of the likelihood of this type of hydrophobic

surface, with no specific dNMP-surface interactions, for being suitable for discriminating the flight time distributions of the different types of dNMPs and therefore being useful for flight time based DNA sequencing. The variables considered were the electric field strength and wall roughness.

Various factors influencing the transport of the dNMPs through nanoslits were examined. The strength of the interaction of the dNMPs with the slit walls and their adsorption and desorption behavior is an important factor determining the channel length required to distinguish the flight time distributions of the four dNMP types. Association of counter ions with the phosphate group of the dNMPs can lead to a significant change in dNMP velocity along a channel. An understanding of these factors can provide guidance for the design of nanochannel surfaces.

4.2.2 Methodology

The simulation system consisted of a dNMP and sodium chloride in water confined between two slit walls. Periodic boundary conditions were used in the directions tangential to the walls. The wall slabs had dimensions of 5 × 5 nm in the tangential directions. Smooth wall slabs had a depth of 1.2 nm (see Figure 4.1).

For smooth walls, the atoms in the slit walls were placed outside two planes parallel to the *xy* plane, located at $z = \pm h_{slit}/2$ nm. The centers of the wall atoms were located at $z \leq -h_{slit}/2$ nm and $z \geq h_{slit}/2$ nm. Slit walls were composed of atoms with Lennard-Jones 12-6 parameters for a carbonyl carbon atom ($\varepsilon_{carbon\text{-}carbon}$ = 0.11 kcal/mol, $\sigma_{carbon\text{-}carbon} = 0.4/2^{1/6}$ nm). The mass of the wall atoms was increased from 12.011 to 14.30226 amu, which is the average mass of the atoms in a united atom (no hydrogen atoms, but increased mass of atoms that would have hydrogen

atoms bonded to them) representation of PMMA. The details on constructing the smooth slit walls are given in our previous work.[9]

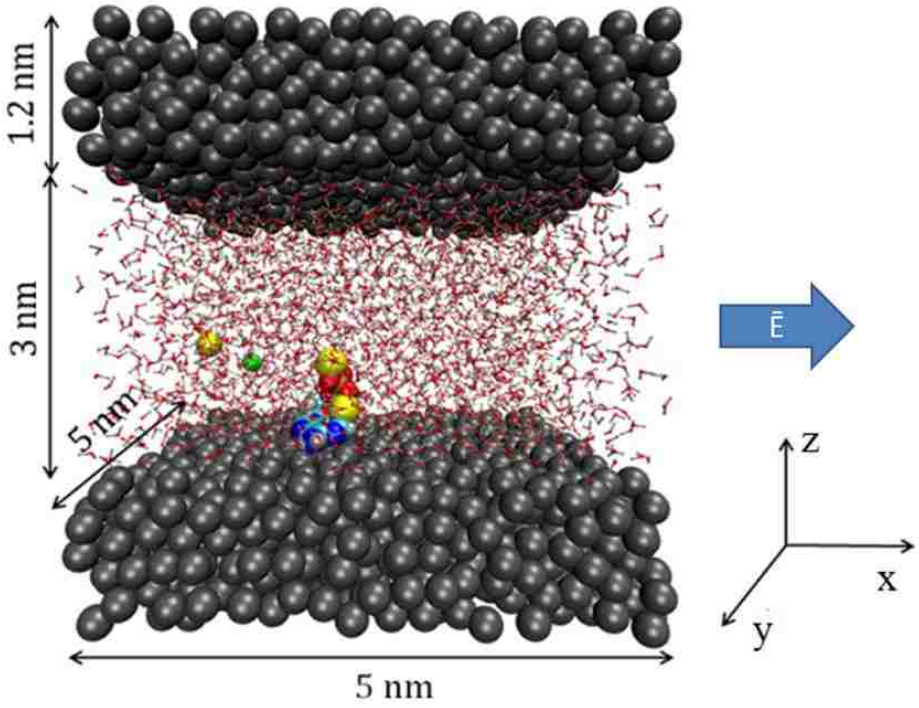

Figure 4.1 Simulation system with smooth walls. Carbon atoms (gray), sodium ions (yellow), chloride ion (green), and dNMP atoms are represented as large spheres. The water molecules are in a ball and stick representation. The electric field was applied in the positive x direction which caused the dNMP to move in the negative x direction on average.

The slit width of 3.0 nm was chosen to maximize the contact of the dNMPs with the slit walls while still having bulk solvent near the slit center plane. Real channels with dimensions smaller than 5.0 nm have been fabricated.[67] Note that small, hydrophobic nano-scale geometries are not practical due to the difficulty for aqueous solvent to enter them. The nature of the slit walls was chosen for simplicity in our initial studies. Future work will focus on more realistic walls composed of PMMA or modified PMMA. Ten slits were constructed with an average RMS roughness of 2.2708 nm. The spacing between the slit walls was chosen so that the volume accessible by the dNMPs was approximately the same as in the smooth wall cases.

Once the walls were constructed, dNMPs were placed between the slit walls and water and ions were added using the Visual Molecular Dynamics (VMD) software.[68] Constant pressure simulations could not be performed in LAMMPS using long-range electrostatics in the slab geometry, so the amount of water was determined by trial and error and interpolation. The *Solvate* function in VMD was used to add water. The *Solvate* settings used were: boundary = 2.4, *x* and *y* bounds = ±25.65 Å, *z* bounds = ±15 Å for the smooth wall cases, and boundary = 2.4, *x* and *y* bounds = ±25.44 Å, *z* bounds sufficient to be at or beyond the rough part of the slabs for the rough wall cases. These settings gave a reasonable equilibrium bulk density of water for the model that was used (1.015 g/cm^3 at the center of the slit) in equilibrium simulations containing only water and the slit walls. For the trial and error density calculation for the rough wall case, the slit with walls with an RMS roughness of 2.2747 nm was used. After using *Solvate*, some water molecules were replaced with two sodium ions to neutralize the system, and an extra sodium and chloride ion using the *Autoionize* function in VMD. Final configurations for the smooth wall cases contained between 2199 and 2233 water molecules. Final configurations for the rough wall cases contained between 2264 and 2356 water molecules. Ion concentrations ($[Na^+] + [Cl^-]$) were between 100.7 and 102.3 mM for smooth wall cases and between 95.5 and 99.4 mM for rough wall cases based on bulk water density to estimate the volume of solvent.

The CHARMM27 force field[69] was used for the dNMP and ion parameters. The rigid CHARMM TIP3P model was used for water. dNMPs with the phosphate group on their 5' end can be produced by cutting up double-stranded DNA using a λ-exonuclease enzyme. The λ-exonuclease enzyme that would be used for this would likely have the highest activity near the physiological pH of around 7.4. The pK_a for the first protonation of the phosphate groups of the dNMPs is around 6.8,[64] so the phosphate groups were simulated as non-protonated which gave

the dNMPs a net charge of -2*e* where *e* is the electron charge. The CHARMM27 topology file did not contain a terminal segment for DNA with a non-protonated phosphate on the 5' end. Construction of the required patch for a non-protonated phosphate on the 5' end was explained in previous work.[9] The chemical structure of the simulated dNMPs is shown in Figure 4.2.

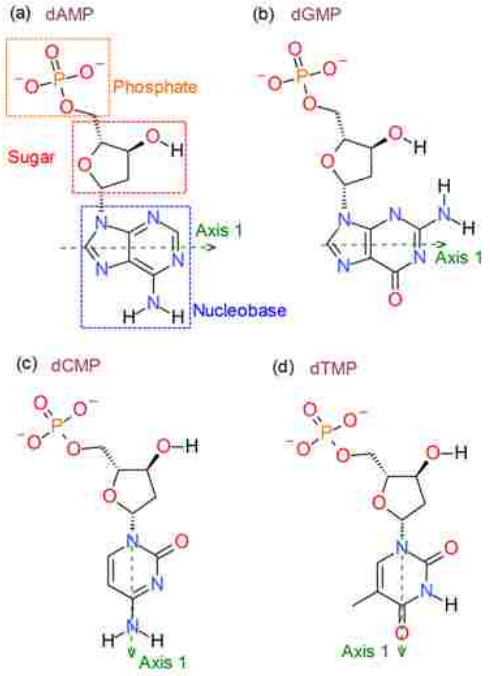

Figure 4.2 The structure of nucleotides with an un-protonated phosphate group attached to the 5' atoms of their sugars. Axis 1 was defined by atoms in the nucleobase rings, and some analysis of nucleobase configuration was based on it. If Axis 1 passes through an atom in the picture, then the position of that atom was one of the points used to define the axis. With dAMP and dGMP, the axis passes between two pairs of atoms. The geometric center of the pair furthest from the end of the nucleobase where the sugar is attached was used for the second point needed to define the axis.

Non-bonded interactions were treated as follows. The Lennard-Jones 12-6 interactions were switched to zero between 0.8 and 1.0 nm using the CHARMM switching function. The CHARMM force field uses Lorentz-Berthelot mixing rules to determine Lennard-Jones 12-6 parameters between atoms of different types. The short-range cutoff for electrostatic interactions was 1.0 nm. The 3-D particle-particle particle-mesh (PPPM) method corrected for a slab

geometry was used[70] with the minimum accuracy in the PPPM forces set to 10^{-5}. The box length for the PPPM in the non-periodic direction was three times the simulation box length in that direction.

Wall atoms were at a much higher density than Lennard-Jones particles would be at under the simulated conditions. Since a thermostat was applied to the wall atoms (see below), their positions could not be fixed. Therefore, to keep the walls intact, the wall atoms were attached to their initial positions by springs with force constants of 83,860 kJ/mol-nm^2.

Since the dNMPs have a net charge, they can be driven electrophoretically. For the non-equilibrium simulations, electric fields with strengths ranging from 0.0144 to 0.6 V/nm were applied to all atoms. The average steady state dNMP velocities in the direction of the applied field ranged from about 0.18 to 31.00 m/s. Simulation at high velocities relative to velocities typical of nano-scale flows is necessary in MD simulations to obtain statistically meaningful results in the relatively short time that can be simulated, nanoseconds to microseconds.

During non-equilibrium simulations, energy is continuously added to the system so a thermostat was used to remove it. To avoid any artifacts caused by thermostatting the flowing solvent and dNMP, only the wall atoms were thermostatted at 300 K using a Berendsen thermostat with a time constant of 0.1 ps. The fluid temperatures at steady state were no more than 10 K higher than the temperature of the thermostatted walls due to viscous heating of the fluid. Equilibrium simulations were thermostatted in the same way as the non-equilibrium simulations.

The following cases were simulated. Simulations with smooth walls were run for all four dNMPs with the electric field strengths of 0.0, 0.0144, and 0.1 V/nm. Five simulations with different starting configurations for the wall atoms[9] were run with 70 ns of production time for

each. Additional simulations with smooth walls were run for dTMP only with the electric field strengths of 0.3 and 0.6 V/nm using 5 different wall configurations for each electric field strength and 40 ns of production time per simulation. Finally, non-equilibrium simulations with rough walls were run for all nucleotide types with an electric field of 0.1 V/nm using 10 different wall configurations and with production times per simulation of 40 to 62 ns. The RMS roughnesses of the walls were 1.9799, 2.1131, 2.1967, 2.2085, 2.2747, 2.2926, 2.3326, 2.3412, 2.4411, and 2.5272 nm with an average of 2.2708 nm. The first 10 ns of each simulation was discarded to allow the simulation to reach a steady state or equilibrium state.

4.2.3 Results and Discussion

The primary variables for flight time based sequencing include the rate at which the enzyme disassembles a DNA strand, the nanochannel length, the number of detectors, the nanochannel dimensions, the magnitude and type of the driving force pushing the dNMPs through the nanochannel, and the interactions of the dNMPs with the channel walls and other species in solution. A secondary variable is the redundancy; how many times each DNA sequence is analyzed, either in serial or in parallel. A given identification accuracy can be obtained by modifying both the primary variables and the secondary variable; more redundancy means the time of flight distributions in each nanochannel do not have to be as well separated.

The goal is to reduce the time required to analyze each dNMP below some acceptable maximum value and to minimize the cost to analyze each dNMP. For a given set of flight time distributions over some length, the following conditions have to be met for sequencing to be successful: 1) the enzyme disassembly rate must be set so that the time between dNMPs being cleaved is at least equal to the time between the upper edge of the flight time distribution over the distance between the first and last detectors for the fastest dNMP type and the lower edge of

the flight time distribution over the distance between the first and last detectors for the slowest dNMP type to avoid the problem of misordering caused by dNMPs passing each other in the nanochannel, 2) either the nanochannel length must be long enough for the flight time distributions to be adequately separated for reliable identification of the dNMPs or the redundancy must be large enough for the chosen nanochannel length to obtain reliable identification of the dNMPs. In addition, the number of detectors should be as large as practical or cost effective since this additional redundancy improves the ability to identify each dNMP allowing for shorter nanochannel lengths and analysis times.

The flight time distributions are determined by the magnitude and type of the driving force, and by the interactions of the dNMPs with the rest of the system. The standard deviations of the flight time distributions decrease with increasing nanochannel length so assuming the distributions for each type of nucleotide are not exactly the same for a given length, they will eventually not overlap for long enough lengths. To obtain reasonable nanochannel lengths and analysis times, the flight time distributions for a given length need to be sufficiently separated. Since the dNMPs are charged, they can be driven electrophoretically. In that case, each nucleotide will have a different electrophoretic mobility. Unfortunately the different dNMP types are of similar size and have the same charge, so their mobilities are similar. Relying only on mobility differences would not provide good separation of the flight time distributions. Although the different dNMP types are similar in size, their nucleobase groups are chemically different which allows the interactions of the dNMPs with other parts of the system to be exploited to separate the flight time distributions. This is the factor exploited by chromatography, which can be used to separate or analyze different dNMP types from a solution containing multiple types.[71-72] The flight time based approach is essentially a single molecule version of chromatography.

Since this study only involved the motion of dNMPs through a nanoslit and did not involve the exonuclease enzyme or detectors, the factors of interest were the dNMP-wall and dNMP-counter ion interactions. Statistics and dynamics of the dNMP adsorption to and desorption from the slit walls were calculated. dNMP orientation during adsorption and desorption; fraction of time adsorbed; frequency of adsorption and desorption events; and the mean times, distances traveled by the dNMPs in the direction of the driving force, and velocities in the direction of the driving force while adsorbed and desorbed were calculated. The mean association numbers of the sodium ions with the dNMP phosphate groups were calculated as well as the characteristic relaxation times for states where 1 or 2 sodium ions were associated with the phosphate group. From the dNMP velocity distributions, the required channel lengths and minimum analysis times per dNMP were estimated. There were two parameters of interest; the strength of the electric field driving the dNMPs and the roughness of the slit walls. Uncertainties were 2 times the standard deviation of the mean unless otherwise indicated.

4.2.3.1 dNMP Adsorption and Desorption

In nanoscale geometries, the interaction of the solvent and the solutes in solution with the walls becomes more important since the volume of the solution-wall interfacial region becomes a significant fraction of the total solution volume. As mentioned above in the context of flight time based sequencing, the interaction of dNMPs with the nanochannel walls is important for distinguishing the flight time distributions of the different dNMP types. In nanopore based sequencing, the interaction of DNA or single dNMPs with the nanopore walls could also be important. The effect of binding of DNA to the polymer layer anchored on a nanochannel or directly on the surface of a nanochannel has been examined.[73-75] During the translocation process through nanochannels, DNA is subjected to a series of adsorptions and desorptions to and from

the wall surfaces. These transient adsorption events result in an effective mobility decrease. This adsorption and desorption phenomenon is also observed in the electrically facilitated transportation of proteins through large nanopores.[76] Our results presented below show that the dNMPs in our systems also undergo adsorption to, and desorption from the walls.

Figure 4.3 depicts the time dependence of the dNMP *Z*-coordinate (wall normal direction) trajectory of the four dNMPs driven by an electric field of 0.1 V/nm. Those plots show that all the dNMPs stayed adsorbed to the walls for periods of time between about 1 ns to 20 ns, then desorbed again. Thus based on the *Z*-coordinate of the center of mass of the dNMPs, a trajectory was decomposed into adsorbed states and desorbed states, which alternate with each other.

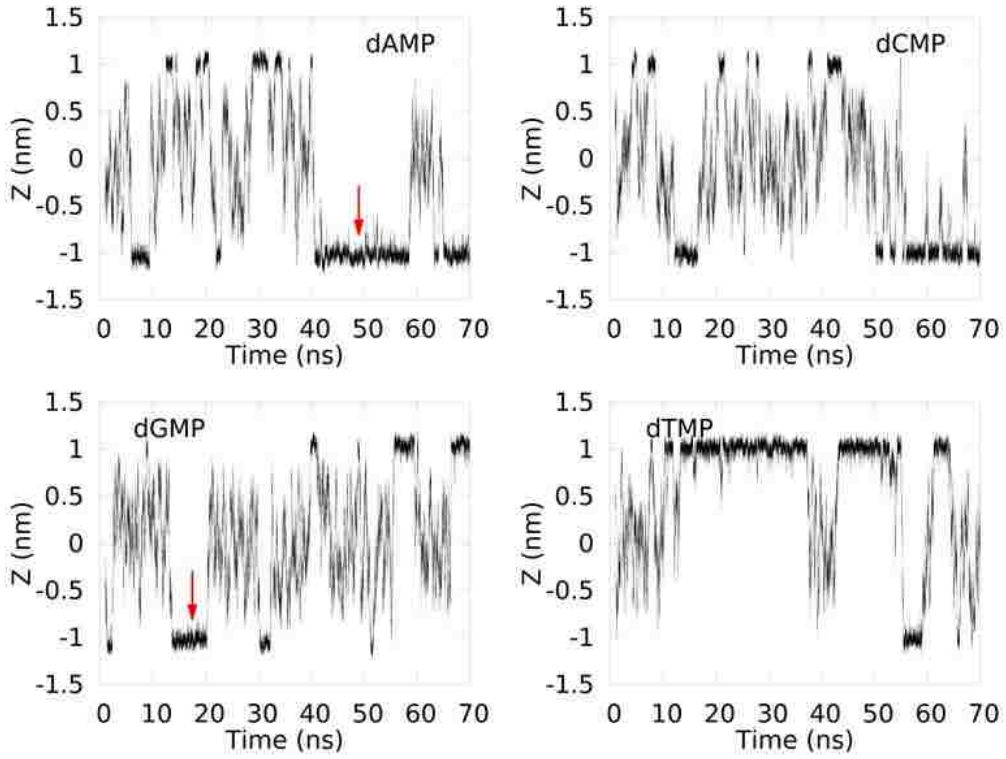

Figure 4.3 The position of the center of mass of the dNMPs driven by an electric field of 0.1 V/nm in the wall normal direction (*Z*) over 70 ns. The center of the slit is at $Z = 0$. Red arrows in the dAMP and dGMP trajectories indicate examples of periods when the dNMP was adsorbed to a slit wall.

In the adsorbed state, the hydrophobic nucleobase parts of the dNMPs tended to sit on the surface while the hydrophilic phosphate group pointed away from the surface. Figure 4.4 (a) shows a snapshot of dAMP with its nucleobase fully adsorbed on a wall. The end of the nucleobase furthest from the hydrophilic phosphate group was more apt to stick on the hydrophobic wall and thus the nucleobases were inclined to the wall surface when they were in the process of adsorbing to or desorbing from the walls as in Figure 4.4 (b) showing a snapshot of dAMP in the process of being adsorbed to a wall.

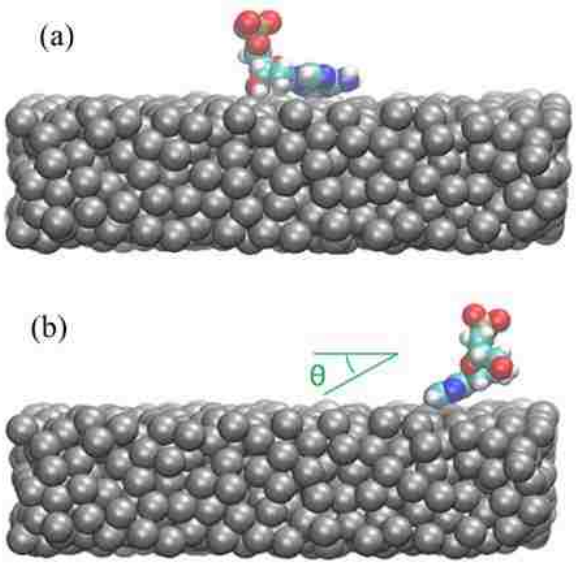

Figure 4.4 Snapshots of dAMP near a wall. (a) The nucleobase and sugar of dAMP are adsorbed. (b) The sugar is detached and the nucleobase is inclined with Axis 1 (see Figure 4.2) forming an angle θ with the wall plane during adsorption.

For the smooth wall cases the orientation of the dNMP nucleobases relative to the wall surface planes, and relative to the direction of the electric field were calculated during adsorption and desorption. Specifically, the angles between Axis 1 defined in Figure 4.2 with the wall surface planes and with the electric field direction were calculated. The periods for adsorption were defined to be from midway between the previous desorption instant and an adsorption instant until midway between that adsorption instant and the next desorption instant. The periods

for desorption were defined to be from midway between the preceding adsorption instant and desorption instant until midway between that desorption instant and the next adsorption instant. Adsorption and desorption instants are at the beginning of an adsorption or desorption instant, respectively.

The average angles (θ) of Axis 1 (see Figure 4.2) of the nucleobase parts of the dNMPs with the wall surfaces are plotted in Figure 4.5 as a function of distance from the nearest wall surface (d_w) for E = 0.1 V/nm. The behavior was similar for the electric field strengths of 0.0 and 0.0144 V/nm (Figure 4.6 and Figure 4.7), indicating that the electric field did not affect the mechanism of adsorption and desorption, at least at the lower field strengths that were studied.

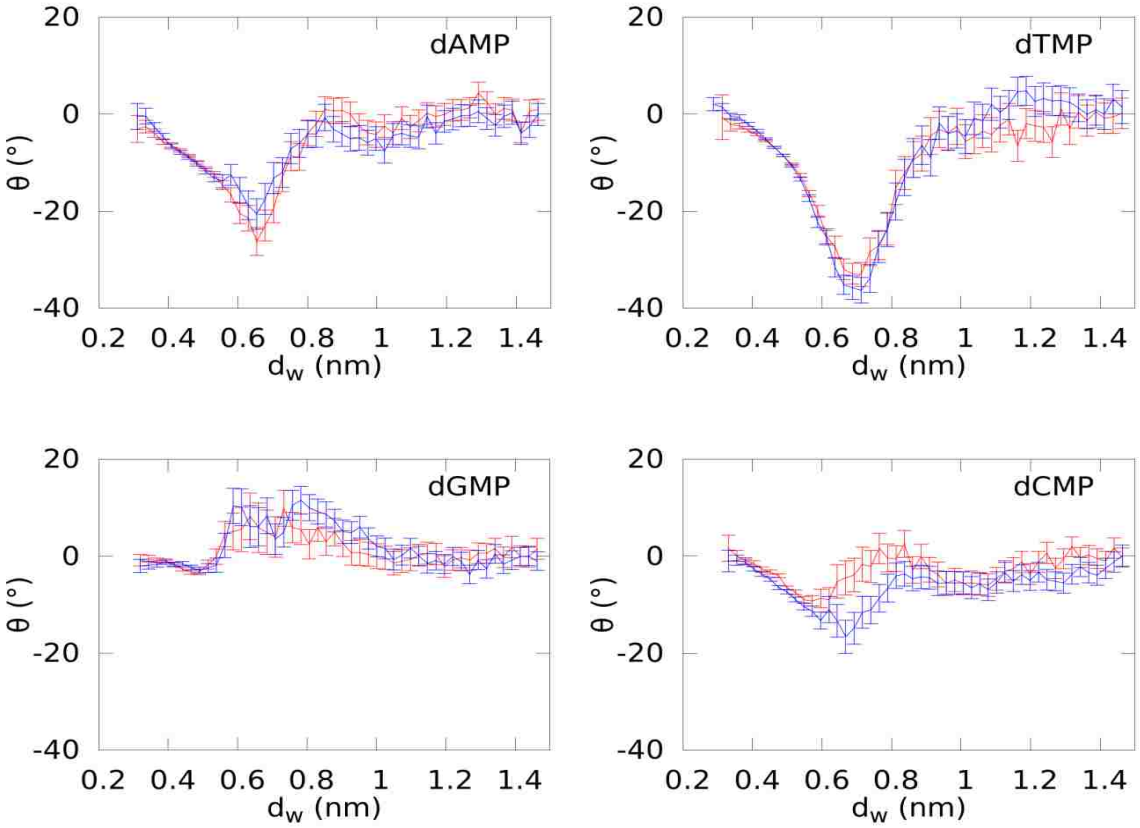

Figure 4.5 The angle between Axis 1 (see Figure 4.2) of the nucleobase and the wall surface as a function of d_w while the dNMP was adsorbing (red) and while the dNMP was desorbing (blue). E = 0.1 V/nm.

Negative values mean that the end of the nucleobase attached to the sugar was further away from the wall than the opposite end; Axis 1 pointed towards the wall plane. For d_w > 0.9 nm, the average angles for the four dNMPs were nearly 0. For d_w < 0.9 nm, dAMP, dCMP, and dTMP had minima in θ for both adsorption and desorption, indicating that the sugar adsorbed after the nucleobase and desorbed before the nucleobase.

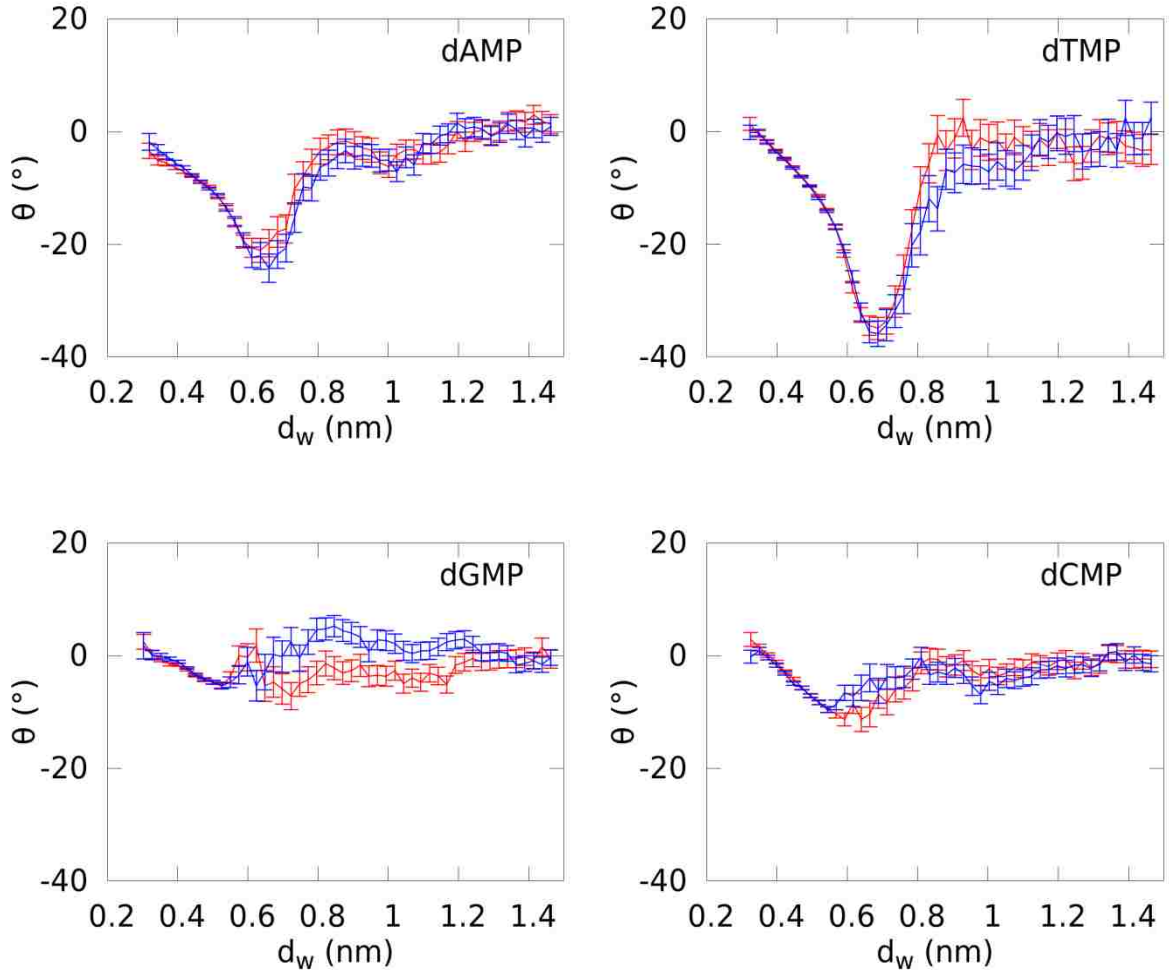

Figure 4.6 The angle between Axis 1 (see Figure 4.2) of the nucleobase and the wall surface as a function of d_w for adsorption (red) and desorption (blue). E = 0.0 V/nm.

The magnitude of the minima followed the order dCMP < dAMP < dTMP, which was consistent with the order of hydrophobicity of their nucleobases.[77-78] For d_w < 0.9 nm, dGMP had

a maximum in θ for both adsorption and desorption, indicating that the sugar adsorbed before the nucleobase and desorbed after the nucleobase. The different behavior of dGMP was likely because its nucleobase was the least hydrophobic.[77-78] The adsorption and desorption curves for each type of dNMP were similar to each other which indicated that adsorption and desorption occurred in a similar way.

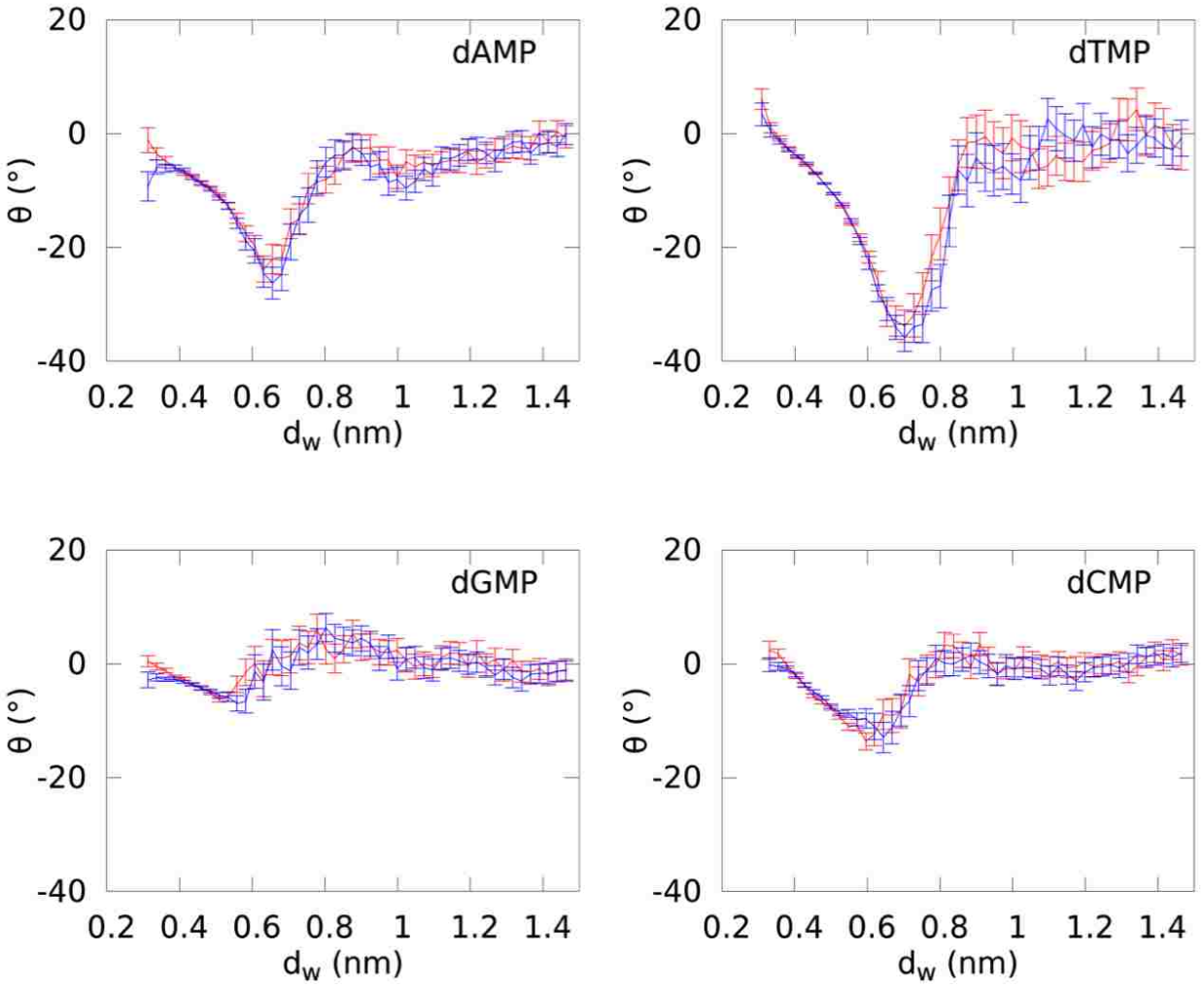

Figure 4.7 The angle between Axis 1 (see Figure 4.2) of the nucleobase and the wall surface as a function of d_w for adsorption (red) and desorption (blue). E = 0.0144 V/nm.

Figure 4.8 shows the average angle (ψ) between Axis 1 (see Figure 4.2) of the nucleobases of dNMPs with the electric field direction during adsorption as a function of d_w and Figure 4.9 shows it for desorption.

For an electric field of 0.0 V/nm, ψ was nearly 90º far from the wall since there was no reason for any orientation to be favored and ψ was defined between 0º and 180º. The dNMPs had

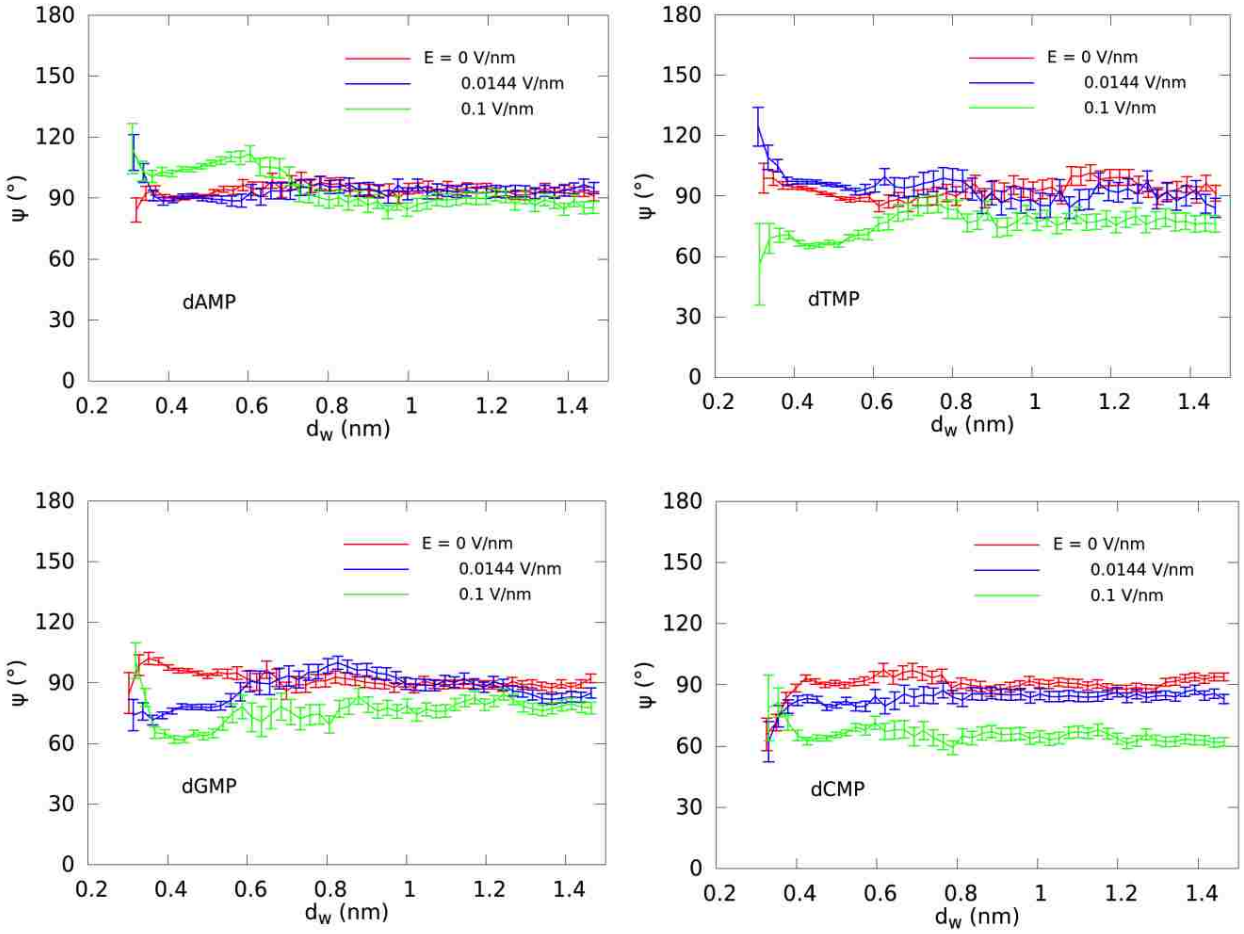

Figure 4.8 The average angles (ψ) between Axis 1 (see Figure 4.2) of the nucleobases of dNMPs with the electric field direction as a function of d_w during dNMP adsorption.

a net charge of -2*e* on the phosphate group therefore, for nonzero electric fields the phosphate group is pulled on average in the opposite direction of the electric field direction. This means that Axis 1 is more likely to point in the direction of the electric field, and ψ is expected to be

less than 90º far from the wall under non-zero electric field. This is not noticeable for most of the plots for E = 0.0144V/nm, but the average Axis 1 angle is clearly less than 90º for E = 0.1 V/nm far from the wall. This effect is smallest for the dNMPs with the largest nucleobases, dAMP and dGMP, and largest for the dNMP with the smallest nucleobases, dCMP. During adsorption and desorption when the nucleobases were very close to the wall, the nucleobase-wall interactions can make ψ far away from 90^0. The direction of this deviation depends on the identity of the dNMP, whether it was adsorbing or desorbing, and even on the magnitude of the electric field.

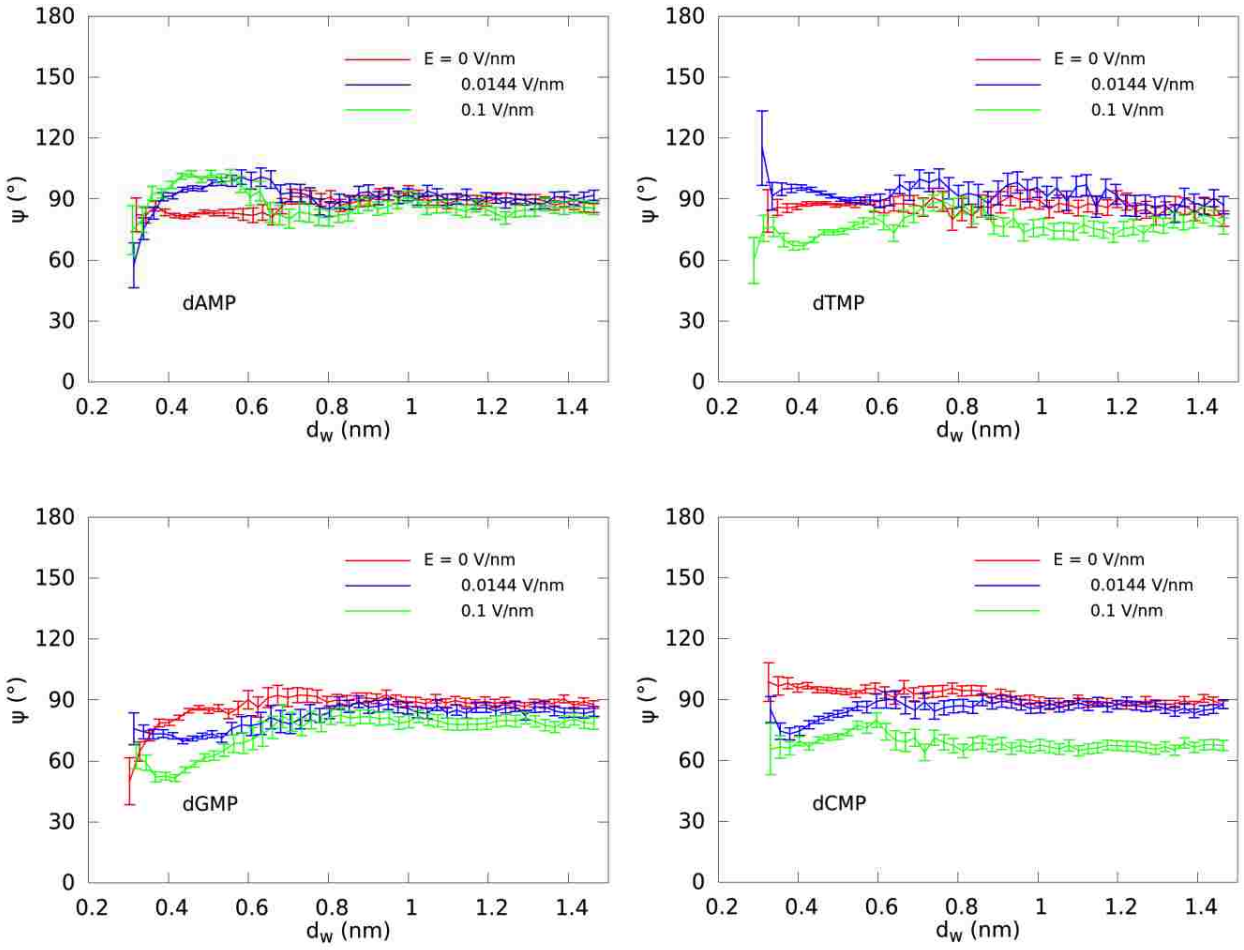

Figure 4.9 The average angles (ψ) between Axis 1 (see Figure 4.2) of the nucleobases of dNMPs with the electric field direction as a function of d_w during dNMP desorption.

Various statistics were calculated related to the adsorption of the dNMPs to the slit walls. The fraction of the total time that the dNMPs spent adsorbed, the frequency of dNMP adsorption events are shown in Figure 4.10 and the mean times per adsorption event, the mean distances the dNMPs traveled in direction of the driving force per adsorption event, and the mean dNMP velocities in the direction of the driving force while adsorbed are shown in Figure 4.11. Mean times per desorption event, mean distances the dNMPs traveled in the direction of the driving force per desorption event, and the mean dNMP velocities in the direction of the driving force while desorbed are shown in Figure 4.12.

Fractions of the total time during which the dNMPs were adsorbed to the slit walls ($f_{t,ads}$) are shown in (a) of Figure 4.10. The fraction of time adsorbed is larger for the more hydrophobic nucleotides (dAMP and dTMP) and generally decreased with increasing electric field strength. Rough walls reduce the fraction of the time adsorbed for dAMP, dCMP, and dGMP compared to smooth walls. However, the rough walls have little effect on $f_{t,ads}$ for dTMP. The dNMPs with the smaller pyrimidine nucleobases (dCMP and dTMP) are affected less by the roughness than the dNMPs with the larger purine nucleobases (dAMP and dGMP). As discussed previously, the nucleobase parts of the dNMPs tended to sit almost flat on the wall. When the wall was rough, the nucleobases had fewer locations where that was possible leading to more frequent desorption and a tendency toward reduced fraction of time adsorbed on the wall. The dTMP nucleobase was the most hydrophobic of the nucleobases. The dTMP nucleobase is the most hydrophobic of the nucleobases. Therefore even though it desorbed easier from rough walls than the smooth walls it will still re-adsorb very quickly so its fraction of time adsorbed is nearly the same as with smooth walls. This behavior is reflected in its much higher frequency of adsorption on rough walls compared to smooth walls which is shown in (b) of Figure 4.10 and discussed below.

The frequencies of adsorption events (F_{ads}) are shown in (b) of Figure 4.10. For smooth walls, higher frequency was correlated with a lower fraction of time adsorbed (see (a) of Figure 4.10), except for dGMP which has about the same frequency as dTMP. F_{ads} is generally higher

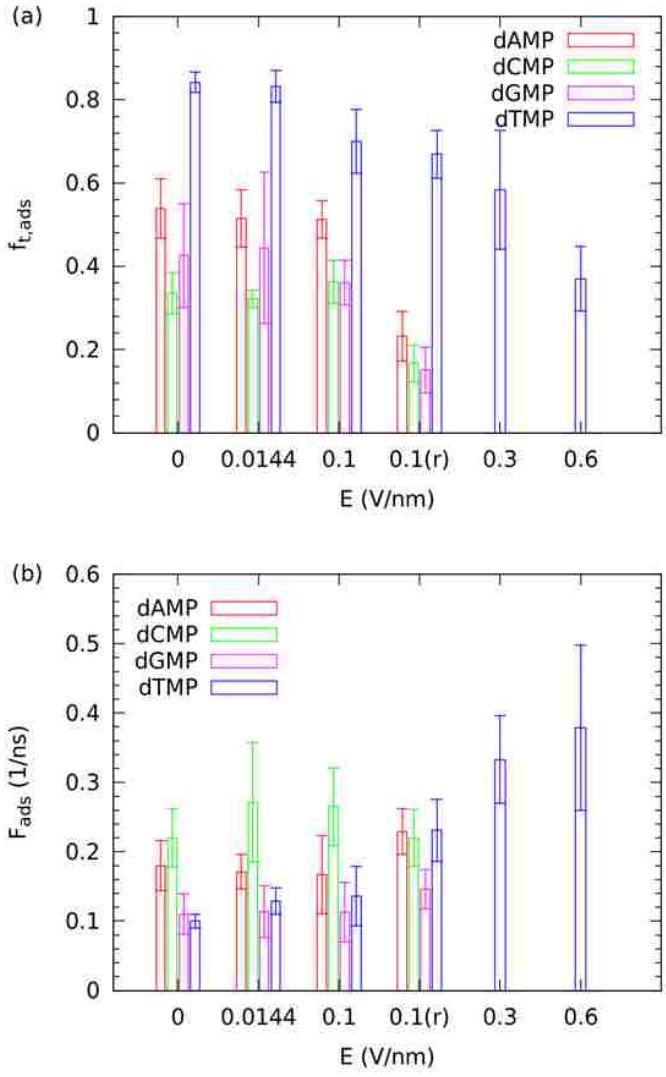

Figure 4.10 Statistics for the dNMPs while adsorbed. (a) Fractions of the total time that the dNMPs were adsorbed to the slit walls. (b) The frequency of adsorption events.

for the rough walls compared to the smooth walls with the same electric field strength while $f_{t,ads}$ is generally smaller for the rough walls. For dTMP, the adsorption frequency is significantly higher with the rough walls compared to the smooth walls which nearly overcome the fact that it is easier to desorb from the walls in the rough wall case so dTMP has almost the same fraction of

time adsorbed with rough and smooth walls. Frequency increases with increasing electric field strength; the frequencies for E = 0.3 and 0.6 V/nm are significantly higher than the frequencies for lower field strengths.

Mean times per adsorption event (t_{ads}) are shown in (a) of Figure 4.11. The trends are the same as for the fractions of time adsorbed. The mean time per adsorption event generally decreased with increasing electric field strength. Adding roughness to the slit walls caused a decrease of t_{ads} consistent with the F_{ads}.

Mean times per adsorption event (t_{ads}) are shown in (a) of Figure 4.11. The trends are the same as for the fractions of time adsorbed. The mean time per adsorption event generally decreases with increasing electric field strength. Adding roughness to the slit walls caused a decrease in t_{ads} consistent with the increase in F_{ads}.

The mean velocities of the dNMPs along the direction (-x) of the force driving them while adsorbed to the slit walls (v_{ads}) are shown in (b) of Figure 4.11. The velocities of the different dNMPs at a given electric field strength are similar. This means that despite the differences in the dNMP-wall interactions in the wall normal direction,[9] the interactions in the wall tangential directions were statistically similar for all dNMPs. The differences in the dNMP nucleobase sizes and in the mean sodium-dNMP association numbers (discussed later) also affected the velocities, but these effects are small. The velocities increased with increasing electric field strength. Making the slit walls rough reduces v_{ads} by a factor of about 1.5 to 2.

Mean distances traveled by the dNMPs in the direction (-x) of the force driving them while adsorbed to the slit walls (d_{ads}) are shown in (c) of Figure 4.11. The effect of the electric field strength on this distance was influenced by the competing effects of the increased dNMP velocity while adsorbed and the decreased time per adsorption event with increased electric field

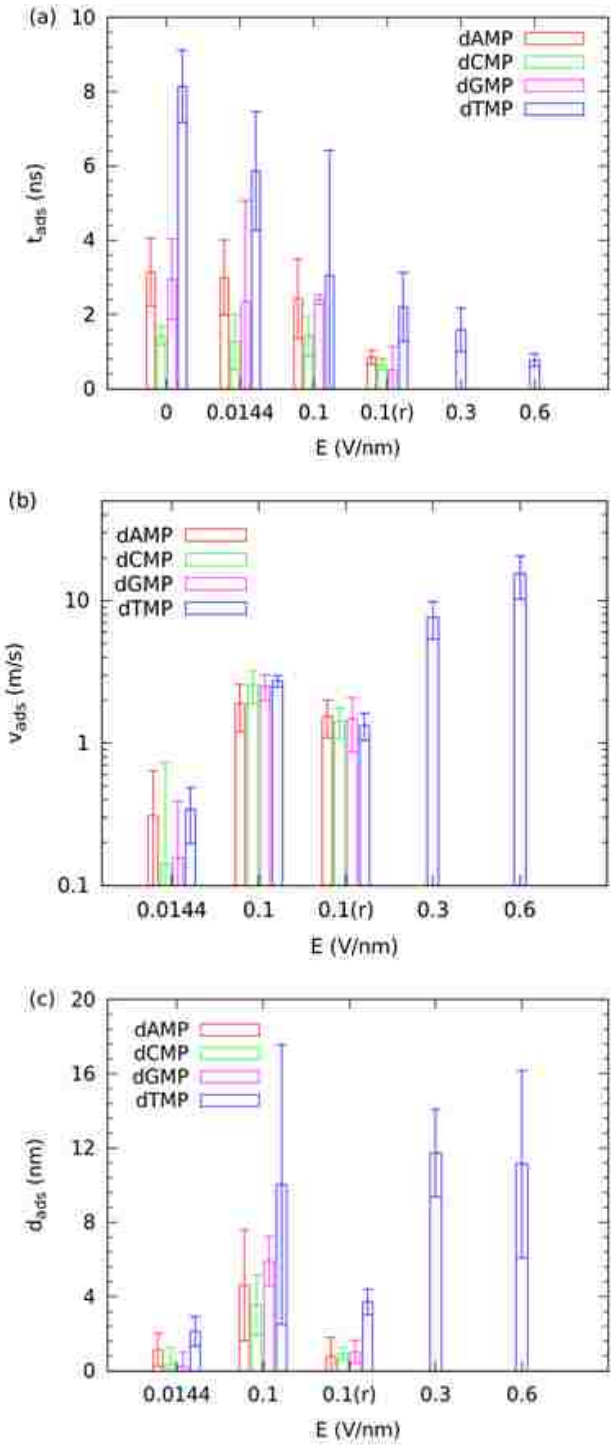

Figure 4.11 Statistics for the dNMPs while adsorbed. (a) The mean times per adsorption event. (b) Mean velocities of the dNMPs along the direction of the driving force on them (-*x*) while adsorbed to the slit walls. Note that the vertical axis is logarithmic. (c) Mean distances traveled by the dNMPs in the direction of the driving force on them (-*x*) while adsorbed to the slit walls.

strength. Mean distances per adsorption event of the dNMPs at E = 0.1 V/nm were higher than at E = 0.0144 V/nm. However, the distances at E = 0.3 V/nm and 0.6 V/nm were not much larger than at E = 0.1 V/nm; the increasing dTMP velocity while adsorbed was offset by the decreasing time per adsorption event. As with the time per adsorption event, rough walls decreased d_{ads} for dAMP, dCMP, and dGMP by much more than for dTMP.

Mean times per desorption event (t_{des}) are shown in (a) of Figure 4.12. The mean time per desorption event is not significantly affected by changing the electric field strength since it depended on the motion of the dNMPs in the wall normal direction and their adsorption and desorption dynamics, which as mentioned previously were not significantly affected by the electric field strength. Adding roughness to the slit walls also generally had little effect on t_{des}. The order for t_{des} for non-zero electric field was usually dTMP < dAMP ≤ dCMP < dGMP, which was the reverse of the hydrophobicity order of the nucleobases, G < C < A < T.[77-78] It is likely that greater hydrophobicity leads to a greater capture probability, the probability that when a dNMP comes near a wall that it will adsorb instead of bouncing off. A greater capture probability corresponds to a lower mean time per desorption event.

The mean distances traveled by the dNMPs in the direction of the force driving them (-x) while desorbed from the slit walls (d_{des}) are shown in (b) of Figure 4.12. The distances increase with increasing electric field strength. As with the time per desorption event, d_{des} is affected by the hydrophobicity of the dNMPs.

The mean velocities (v_{des}) of the dNMPs along the direction of the force driving them (-x) while desorbed from the slit walls are shown in (c) of Figure 4.12. As expected, the velocities are nearly the same for all the dNMPs at any given electric field strength. Any differences are due to the differing size of the dNMP nucleobases and the differences in the mean sodium-dNMP

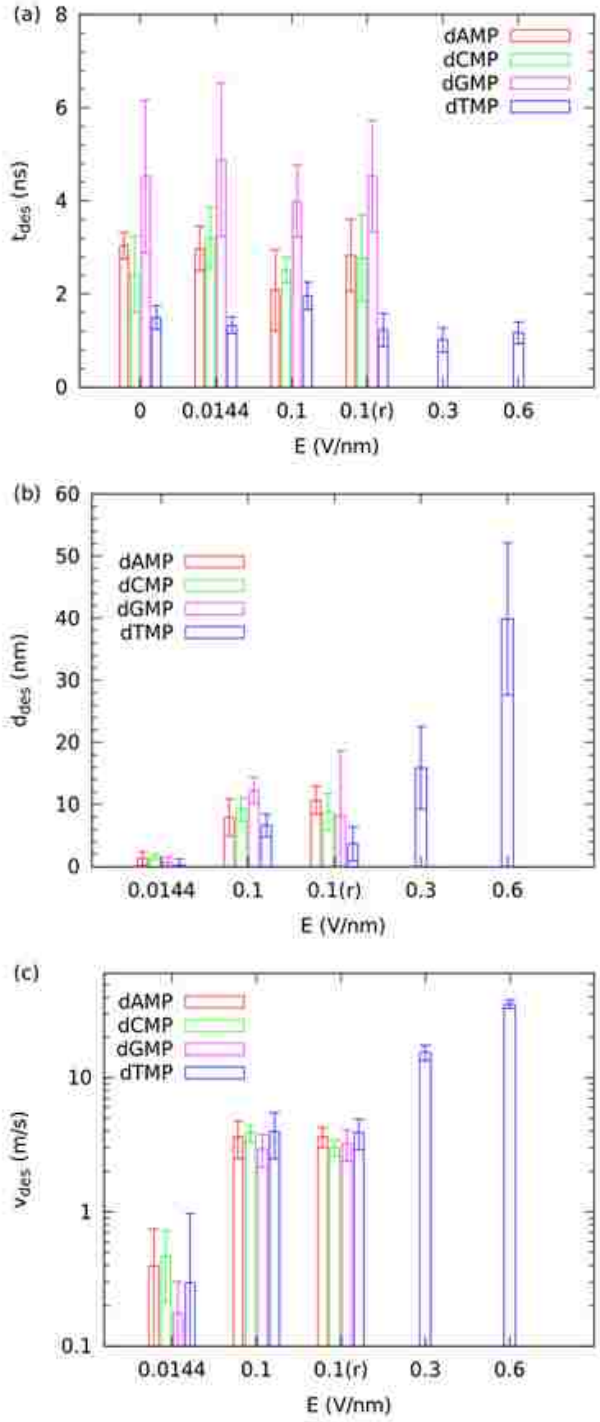

Figure 4.12 Statistics for the dNMPs while desorbed. (a) The mean times per desorption event. (b) Mean distances traveled by the dNMPs in the direction of the driving force on them (-*x*) while desorbed from the slit walls. (c) Mean velocities of the dNMPs along the direction of the driving force on them (-*x*) while desorbed from the slit walls. Note that the vertical axis is logarithmic.

association numbers which are discussed later. The velocities of the dNMPs increased with increased electric field strength. The walls have little effect on the dNMPs when they are desorbed, so v_{des} for the rough and smooth walls at E = 0.1 V/nm is approximately the same as expected.

4.2.3.2 dNMP Phosphate Association with Sodium Ions

Negatively charged DNA strongly interacts with positively charged counter ions which can form a stable layer near DNA in solution and play an important role in altering DNA structure and modulating the interaction between DNA and other molecules.[79-81] The counter ion layer is too stable to be removed by conventional deionization methods. However recent research found that an electric field can promote the dissociation of the DNA-ion complex during capillary electrophoresis resulting in irregular DNA migration velocity.[82] The interaction of cationic counter ions with the dNMPs is important since tightly bound ions can effectively reduce or even reverse the sign of the charge on the nucleic acid – counter ion complex which reduces or reverses the sign of the force on the complex due to the electric field. For example, smaller alkali metal cations bind to DNA more strongly; $Li^+ > Na^+ > K^+$. Kowalczyk et al.[58] exploited this by using Li^+ instead of Na^+ or K^+ to slow down the motion of single stranded DNA through a nanopore. Indeed our simulation results for the motion of dNMPs in nano-slits show that transient binding of sodium ions to the dNMPs lead to irregular dNMP velocities.

The phosphate groups of the dNMPs strongly interacted with sodium cations in solution and formed associations with 1, 2, and sometimes 3 sodium ions. This strong association is shown in Figure 4.13, which is a plot of the radial distribution function, *g(r)*, between the sodium cations and the phosphorus atom on the phosphate group of all dNMPs. The four dNMPs had similar distribution curves, indicating that their different nucleobase parts had little effect on the

association. All the distributions had major peaks with magnitudes between about 415 and 610, meaning that a very stable Na^+ shell was formed around the phosphate group. All the major peaks occurred at around r = 0.27 nm. There are small secondary peaks around r = 0.5 nm. The major peak widths were not affected by the electric field at all, but the peak height generally decreased with increasing electric field strength and thus the peaks were flattened slightly.

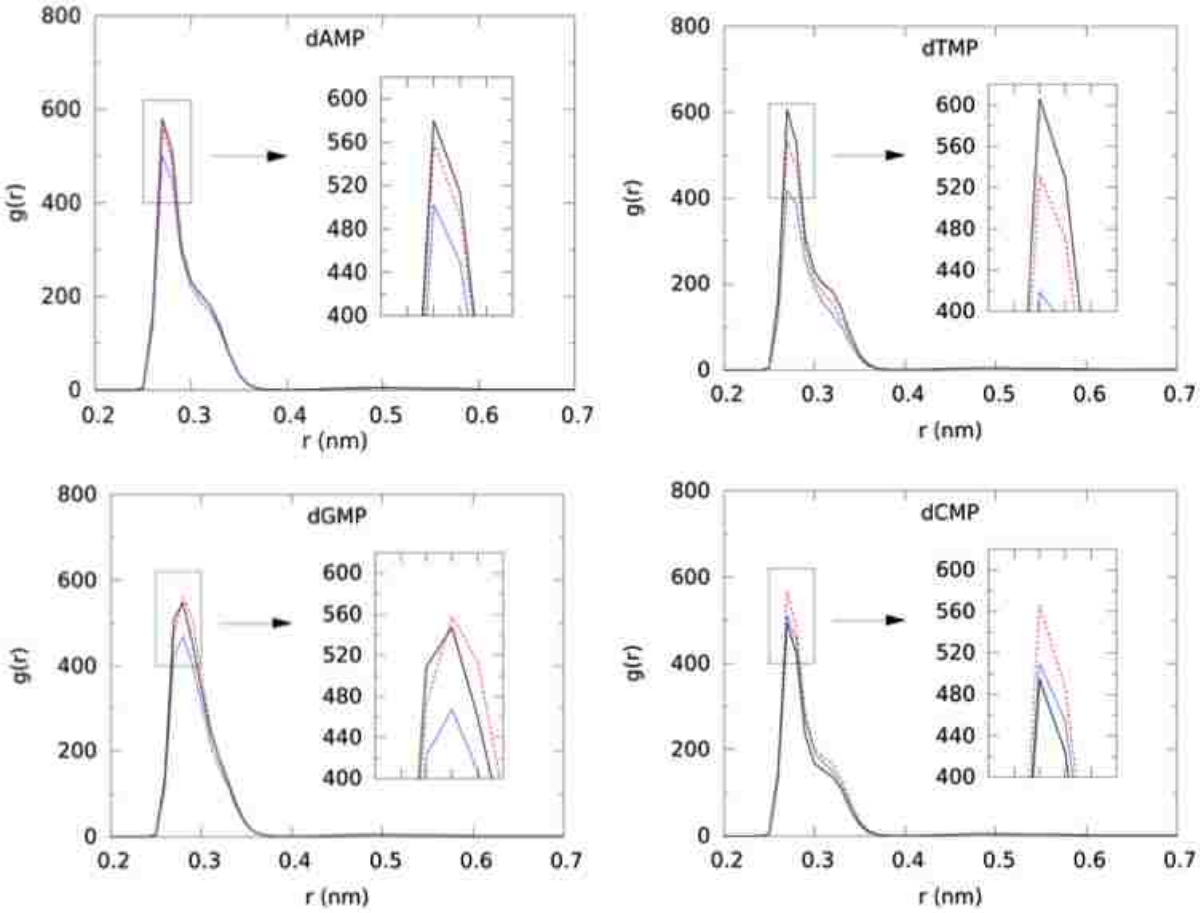

Figure 4.13 Radial distribution functions between the sodium cations and the phosphorus atom in the phosphate group of dNMPs. The abscissa r is the distance between the phosphorus atom and a sodium cation. Black solid lines, red dashed lines and blue dotted lines are, respectively, for the electric fields of 0.0 V/nm, 0.0144 V/nm and 0.1 V/nm.

To capture the entire major peak but not the secondary peak of *g(r)*, the cutoff distance to decide whether a Na^+ ion was associated with the phosphate group was chosen to be 0.4 nm. Use of a single cutoff distance lead to some very short association events because a sodium ion

crossed outside the cutoff distance and then right back inside it, or the reverse. This was avoided by only counting association states, which lasted longer than a minimum time of 0.4 ns. This time removed the noise due to the single cutoff distance, yet was still less than the mean time after a sodium dissociated from a dNMP until it passed the dNMP again through the periodic boundaries for electric field strengths of 0.0144 and 0.1 V/nm; use of this minimum time caused two association events to be counted as one. Use of a minimum time of 0.4 ns was equivalent to doing a 0.4 ns moving average on the association number trajectory followed by rounding to the nearest integer. Application of the minimum time had little effect on the mean association number, but affected dynamical quantities such as the mean relaxation time for association.

The association number versus time for one simulation for each dNMP with E = 0.1 V/nm is shown in Figure 4.14. The coordinates of the center of mass of the dNMPs in the direction of the driving force (-*x*) are also plotted in the same figures.

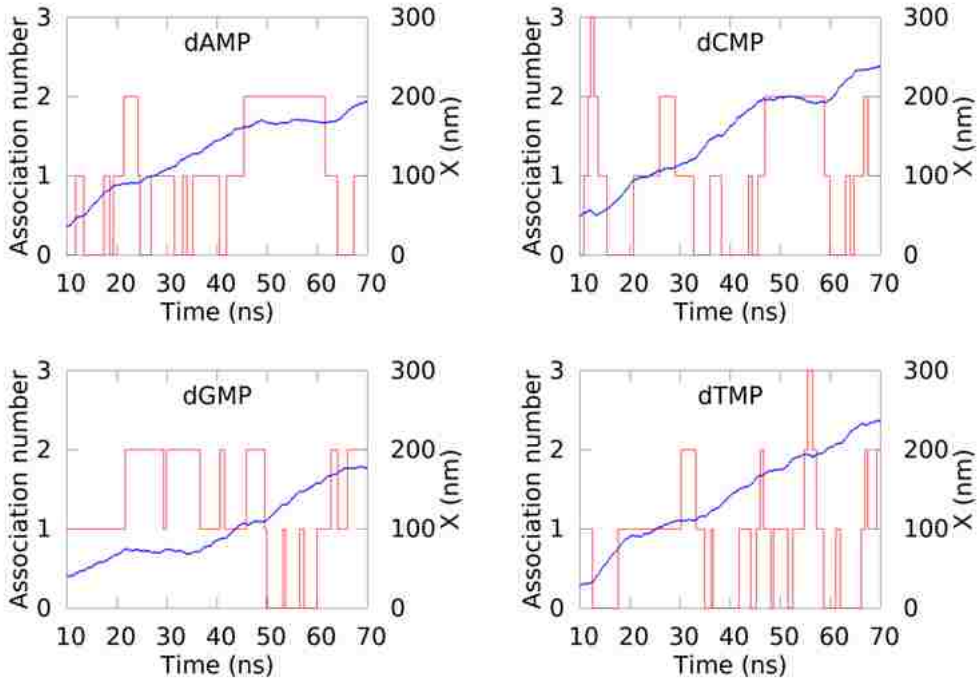

Figure 4.14 Association number of sodium cations with the dNMP phosphorus atom (red), and the -x coordinate (direction of the driving force) of the center of mass of dNMPs (blue) as a function of time. The electric field strength was 0.1 V/nm.

The figures show that the traveling velocity of dNMPs (i.e., the slope of *x*-coordinate versus time curve) was strongly influenced by the association formed between Na^+ and the dNMPs. Take dGMP for example and compare three time periods: from 10 ns to 20 ns the *x*-coordinate increased linearly with time and the association number was 1; from 20 ns to 36 ns the *x*-coordinate remained nearly the same and the association number was 2; from 50 ns to 60 ns the *x*-coordinate increases in time with a steeper slope than the first time period and the association number was generally 0, occasionally 1. The dNMPs were driven by the electric field so the driving force was proportional to the net charge on them. With no Na^+ bound, the net charge of the phosphate group was -2*e*. With one Na^+ ion bound to the phosphate group, the net charge of the aggregate was -1*e* and thus the driving force was reduced to half. If two Na^+ ions were associated simultaneously, the aggregate was electrically neutral and the driving force became zero, thus the *x*-coordinate remained the same in that time period.

Despite the effect of the individual sodium-phosphate association events on the dNMP velocity, overall the association did not have a significant effect since the mean association numbers were not affected much by the electric field strength or the roughness of the walls as shown in Figure 4.15. Even after averaging over all dNMPs for each case, the error bars still overlapped for all cases; none of the differences were significant. There appeared to be a small decrease in the association number averaged over all dNMPs with increased electric field strength from 0.0 to 0.1 V/nm. This is to be expected since the electric field pulled the sodium ions and dNMPs in opposite directions, which is not favorable for association. The association numbers for dTMP at electric fields E= 0.3 and 0.6 V/nm appeared to be slightly higher than for E = 0.1 V/nm and increasing with increased electric field strength, but this could be an artifact of the periodic boundary condition; once a sodium ion dissociated from a dNMP, it does not take

long before they passed each other again since they are moving at relatively high velocities in opposite directions which gave them little time to diffuse out of the path of each other and possibly increased the probability of re-association.

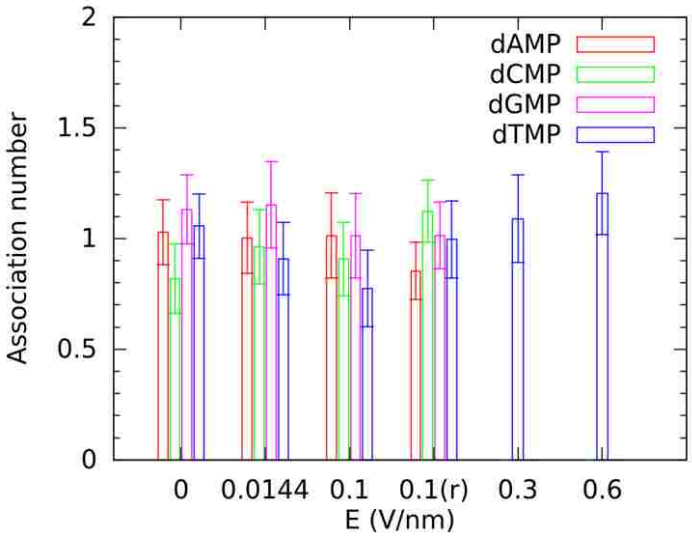

Figure 4.15 Mean association numbers for the dNMPs.

Figure 4.16 (a) shows the distribution of the Na^+-P association numbers (AN) averaged over all four dNMPs for E = 0.0, 0.0144, and 0.1 V/nm with smooth walls. The rough wall case with E = 0.1 V/nm is nearly identical to the smooth wall case with E = 0.1 V/nm, so the results for the rough wall are not shown. For all cases the order of the probabilities, AN=1 > AN=0 > AN=2 > AN=3. The probability of AN=3 is much lower than the other three states and doesn't have a significant influence on the traveling velocity of the dNMPs. The probability of AN=0 increased slightly and the probability of AN=1 decreases slightly with increasing E which lead to the overall decrease in association number with increasing E.

Figure 4.16 (b) shows the distribution of the Na^+-P association numbers averaged over the dNMPs with purine and pyrimidine nucleobases in the case of smooth walls with E = 0.1 V/nm. The dNMPs with pyrimidine nucleobases (dCMP and dTMP) had a higher probability of AN=0 and lower probability of AN=1 and AN=2 compared to the dNMPs with purine nucleobases

(dAMP and dGMP) which lead to the overall higher association number for dAMP and dGMP which can also be seen in Figure 4.15. Other cases showed similar behavior.

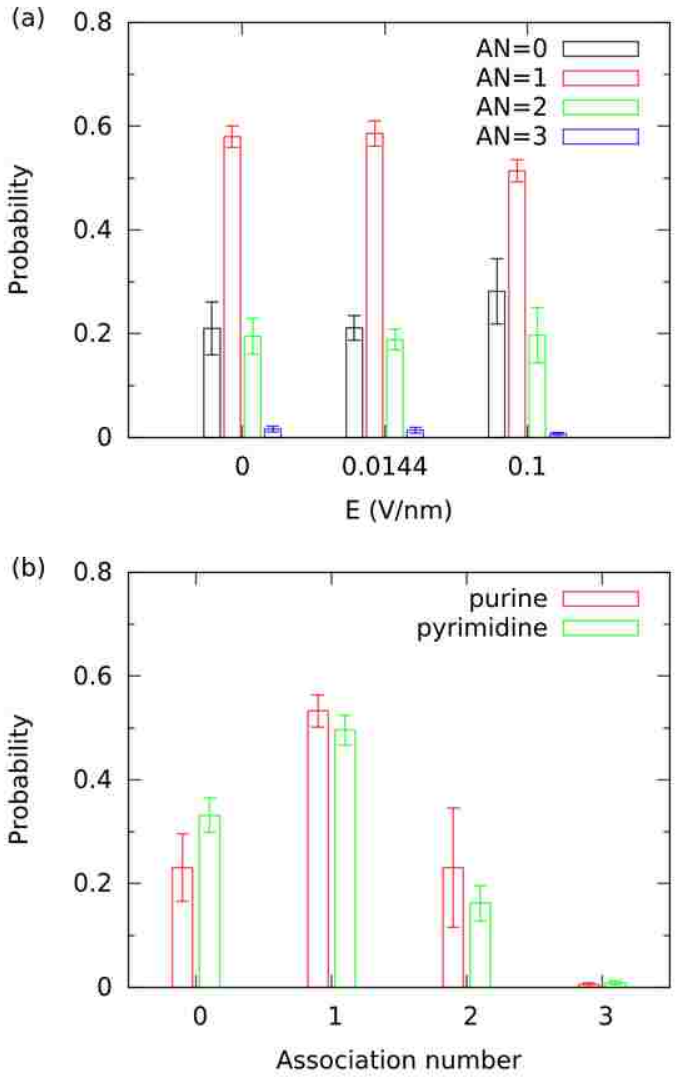

Figure 4.16 The distribution of the association numbers for (a) all of the dNMPs for the smooth wall cases with different electric fields, and for (b) the averages over the dNMPs with purine bases (dCMP and dTMP) and over the dNMPs with pyrimidine bases (dAMP and dTMP) with smooth walls and E = 0.1 V/nm.

The relaxation times for the association were estimated by integration of an aggregate existence autocorrelation function (AEACF) which is a generalization of the dimer existence autocorrelation function (DACF) described by Brehm and Kirchner.[83] Since there is only one

dNMP in our system, and therefore only one possible aggregate, the AEACF could be written in a simpler form.

$$AEACF(\Delta t) = \frac{\sum_{t=0}^{T_{sim}-\Delta t} \beta(t+\Delta t)\beta(t)}{\sum_{t=0}^{T_{sim}} \beta(t)} \tag{4.1}$$

The definition of β was also slightly different. For an association number of 1, the value of $\beta(t)$ was 1 if the association number was ≥ 1 at time t, and $\beta(t+\Delta t)$ became 0 once the association number became 0 and remained 0 for all subsequent Δt. For an association number of 2, the value of $\beta(t)$ was 1 if the association number was ≥ 2 at time t, and $\beta(t+\Delta t)$ became zero once the association number became 1 and remained 0 for all subsequent τ. For each association event, the numerator in Equation (4.1) contributes $N_i - \Delta t/\Delta t_{traj}$ to the sum, where N_i is the duration of event i in number of trajectory time steps of length Δt_{traj}. The denominator is equivalent to ΣN_i, which is just the sum of the duration of all events and was needed to normalize so that AEACF(0) = 1. The AEACF can therefore be thought of in terms of an average over events. For an event for an association number of 1 or 2, defined between the times that the association number changed from 0 to 1 or from 1 to 2 and the next time that the association number changed from 1 to 0 or from 2 to 1, the contribution to the AEACF was a line starting at a value of 1 at $\tau = 0$ and ending at 0 at the end of the event. The AEACF was the average of all the lines corresponding to each event.

$$AEACF(\Delta t) = \frac{1}{n_{events}} \sum_{i=1}^{n_{events}} \left(-\frac{\Delta t}{T_i} + 1\right) H\left[-\frac{\Delta t}{T_i} + 1\right] \tag{4.2}$$

$$AEACF_{fit}(t) = A_1 exp[-t/T_1] + A_2 exp[-t/T_2] + A_3 exp[-t/T_3] \tag{4.3}$$

$$t_r = \int_0^{\infty} AEACF_{fit}(t)\, dt = A_1T_1 + A_2T_2 + A_3T_3 \tag{4.4}$$

In Equation (4.2), T_i is the time duration of event i, Δt is the time elapsed from the beginning of an event, and H is the Heaviside step function. This allowed the events from multiple simulations to be combined to calculate single AEACFs for each dNMP. Once an AEACF was obtained it was fit to a function as shown in (4.3). The relaxation time is obtained by integrating the fitted AEACF function in Equation (4.4). Using the fitted function instead of the original AEACF function is because that it might underestimate the value of the integration due to its early decay to zero at the longest association event. Figure 4.17 shows AEACF curves for all the dNMPs for E = 0.1 V/nm and an association number of 1.

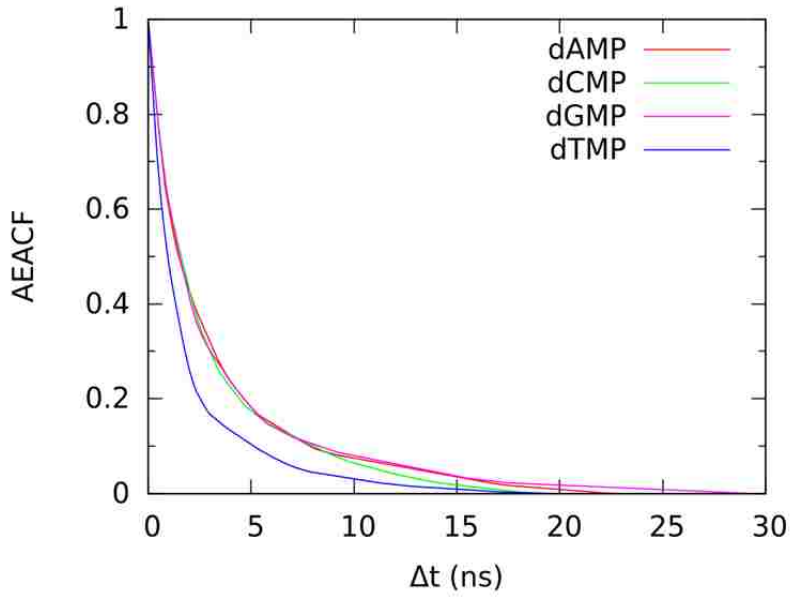

Figure 4.17 Aggregate existence autocorrelation functions (AEACFs) for the dNMPs with E = 0.1 V/nm and an association number of 1.

Figure 4.18 (a) shows the relaxation times for an association number of 1. The relaxation time generally decreased with increasing E because the electric field tends to pull the oppositely charged dNMPs and sodium ions apart. The rough wall case is similar to the smooth wall case at E = 0.1 V/nm except with dTMP. Figure 4.18(b) shows the relaxation times for an association

number of 2. There is not much difference in the relaxation times for E = 0.1 V/nm and lower for both the rough and smooth walls. The relaxation time decreased for E = 0.3 and 0.6 V/nm.

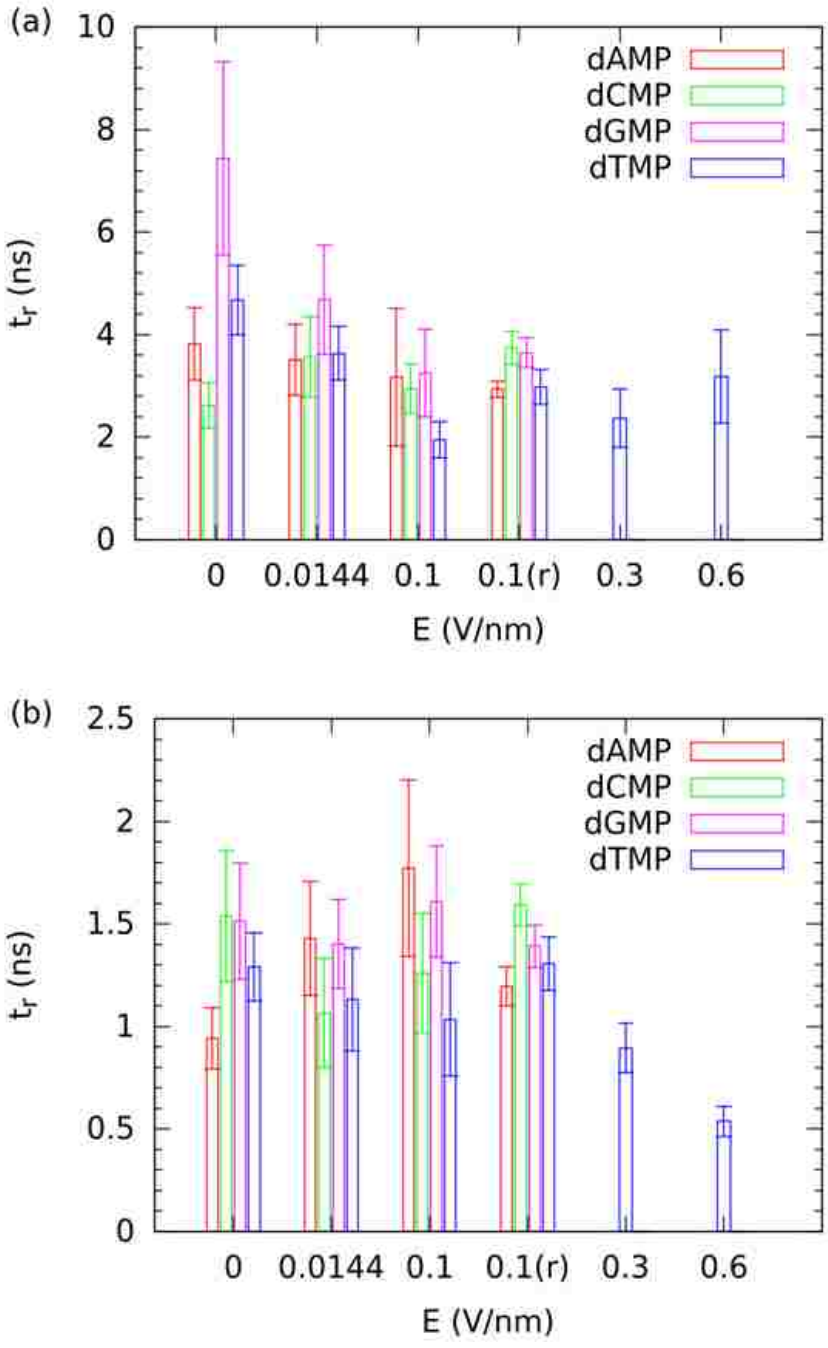

Figure 4.18 The mean relaxation times for a Na^+-P association number of (a) 1 and (b) 2.

4.2.3.1 dNMP Velocities

The mean velocities of the dNMPs give an indication of how well separated the flight time distributions will be. The mean velocities of the dNMPs in the nanoslit as a function of electric field strength and wall roughness are shown in Figure 4.19. At the lowest electric field of E =

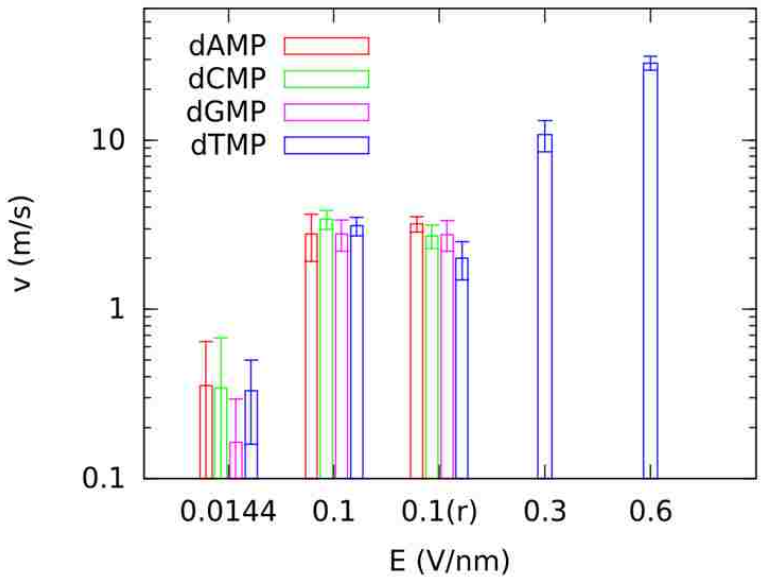

Figure 4.19 The average overall velocities of the dNMPs. Note that the vertical axis is logarithmic.

0.0144V/nm, the velocities of dNMPs are nearly equal except for dGMP although the dGMP velocity is still within the uncertainties of the other velocites. For dTMP, four different electric field strengths were used and the results showed that the velocities increased with electric field strength. The relationship between the average velocity and electric field is not linear, although the driving force on the dNMPs is linearly proportional to electric field. As discussed above, both adsorption to the walls and association between phosphate group and Na^+ ions also affected the traveling velocity of dNMPs. The super-linear increase in the velocity with increasing electric field strength was primarily due to reduction in the fraction of time adsorbed (see (a) of

Figure 4.10). A lower fraction of time adsorbed resulted in a larger velocity since the dNMP was slowed down less due to contact with the walls.

The large uncertainties in the velocities arise for several reasons. The first is that the velocities were much smaller than the thermal velocities especially for the lower electric fields. Simulation times for the smallest electric field would have to be much longer to reduce the uncertainties to the same relative uncertainty of around 10 percent or less obtained for the larger electric fields. A second factor contributing to the variability in the velocities is the variability in the time of each association event between the dNMP phosphate group and Na^+ cations. From Figure 4.14 it can be seen that the time of one association event ranged from less than 1 ns to 20 ns. The variability in the adsorption times and in the velocity while adsorbed due to the heterogeneity of the wall surface also contributed to variability in the velocities. The last two factors could also lead to biases as well if there are not enough association events or not enough adsorption events observed in the simulations. Of particular concern are that there are only a limited number of time periods during which the association number is equal to 2, and that especially for dTMP there are only a limited number of adsorption events.

4.2.3.2 Distance to Separate the dNMPs and Analysis of the Time of Flight per dNMP

In our previous work, the required channel length to achieve reliable separation of the time of flight distributions of the dNMPs was calculated from the distributions of the times of flight over 0.5 nm segments.[9] These times of flight were calculated for each simulation trajectory by starting from the first time step in the trajectory after equilibration, calculating the first time that a dNMP had advanced 0.5 nm beyond its initial position in the direction of the driving force, then repeating the process starting from the next time step in the trajectory after the end of the previous 0.5 nm segment until the end of the trajectory was reached. However, it was just as

valid to start at the second, third, etc. time steps after equilibration. This would lead to different sets of times of flight and different estimates of the required channel length. In addition, using only the single sets of flight times determined from the simulation did not lead to the best estimates of the distributions that would be obtained if in fact the simulations could have been extended until the actual distributions no longer overlapped. To fix the problems mentioned above, some modifications to the calculation were made. The distributions of the simulation mean dNMP velocities estimated using the moving block bootstrap method[84] were used instead of the time of flight distributions. Since the distributions of the mean velocities were nearly normal, a multiple of the standard deviation could be used as an estimate of the distribution widths instead of the distance between where the cumulative distribution function was equal to (1-separation efficiency)/2 and (1+separation efficiency)/2. The required distance for separating any pair of dNMPs (α and β) is $N_\alpha d_\alpha$ or $N_\beta d_\beta$. N_α can be determined using the Equation 4.5;

$$N_\alpha = Z^2 \frac{\left(s_{v_\alpha} + s_{v_\beta} \sqrt{\frac{\langle v_\beta \rangle \Delta T_\beta}{\langle v_\alpha \rangle \Delta T_\alpha}} \right)^2}{\left(\langle v_\alpha \rangle - \langle v_\beta \rangle \right)^2} \tag{4.5}$$

Table 4.1 shows the required distances for separation of the dNMP mean velocity distributions to 3 standard deviations. The maximum value was the minimum required channel length for that level of accuracy. These minimum channel lengths were about 166 μm, 107 μm, and 242 μm for the smooth wall case with E = 0.0144 V/nm, smooth wall case with E = 0.1 V/nm, and rough wall case with E = 0.1 V/nm, respectively. However, these values were very sensitive to the difference in the estimated overall mean velocities for the pair of dNMPs that determine them.

Since the estimated distribution of the mean velocities could be approximated as normal, the flight time distributions could be easily derived from the velocity distributions. The probability

density functions for the flight times over the required channel lengths for smooth walls with E = 0.0144 V/nm and E = 0.1 V/nm and rough walls with E = 0.1 V/nm are shown in Figure 4.20.

Table 4.1 Required distances (μm) to separate the time of flight distributions of the dNMP pair types to Z = 3 standard deviations from the means of the distributions for smooth walls with E = 0.1 V/nm and E = 0.0144 V/nm, and rough walls with E = 0.1 V/nm. The longest distances which are in bold are the minimum required channel lengths.

		dAMP	dCMP	dGMP	dTMP
E = 0.0144 V/nm	dAMP		165.8	1.2	0.2
	dCMP	165.8		1.3	52.2
	dGMP	1.2	1.3		0.4
	dTMP	0.2	52.2	0.4	
E = 0.1 V/nm (smooth)	dAMP		9.6	105.2	49.1
	dCMP	9.6		6.6	26.1
	dGMP	105.2	6.6		12.0
	dTMP	49.1	26.1	12.0	
E = 0.1 V/nm (rough)	dAMP		9.5	16.9	1.4
	dCMP	9.5		241.9	3.7
	dGMP	16.9	241.9		3.1
	dTMP	1.4	3.7	3.1	

In Figure 4.20, the order of the distributions was different in all three cases. For smooth walls with E = 0.1 V/nm, the dNMPs with the smaller pyrimidine nucleobases (dCMP and dTMP) moved faster than the dNMPs with the larger purine nucleobases (dAMP and dGMP). The order of the flight time distributions, dCMP < dTMP < dAMP < dGMP, was also the order of the surface area of the nucleobase part of the dNMPs and the order of the magnitudes of the potential

energies between the dNMPs and the wall calculated in previous simulations.[9] This would suggest that the order was simply determined by the interactions of the dNMPs with the walls, those with stronger interactions moved slower when adsorbed which lead to slower overall velocities. The trend in the velocities while adsorbed was dTMP > dCMP ≈ dGMP > dAMP (see (a) of Figure 4.11), but if this simple explanation were true, then the expected order would be dCMP > dTMP > dAMP > dGMP. The most important additional factor was the fraction of time adsorbed (see (a) of Figure 4.10) which was related to the hydrophobicity of the dNMP nucleobases.[77-78] dTMP was more hydrophobic than dCMP and spent a much larger fraction of time adsorbed than dCMP, so its overall velocity was lower than for dCMP even though it moved faster than dCMP while adsorbed. A similar argument holds for dGMP and dAMP; dAMP was more hydrophobic leading to a swapping in the order of their overall velocities compared to their velocities while adsorbed. For smooth walls with E = 0.0144 V/nm, the statistics were too poor and the order of the dNMPs may not be accurate. It may be that dGMP got stopped on the wall more often while adsorbed instead of sliding which could have lead to it having much longer flight times than the other dNMPs. However, it is unclear why dAMP would have the shortest flight times. For rough walls with E = 0.1 V/nm, the order of the dNMPs with purine nucleobases and pyrimidine nucleobases was switched compared to the case of smooth walls with E = 0.1 V/nm; the order of the flight times was dAMP < dGMP < dCMP < dTMP. This switching in the order was likely because the change in the fraction of time adsorbed (see (a) of Figure 4.10) decreased more in the rough wall case compared to the smooth wall case for dNMPs with purine nucleobases than for the dNMPs with pyrimidine nucleobases. The likely reason for this was simply geometric; the nucleobases had fewer locations where they could

adsorb strongly to the rough walls and this effect was greater for larger nucleobases. This was discussed earlier in the context of the fraction of time adsorbed.

It is desirable to have all the time of flight distributions about the same distance from each other to keep the minimum analysis time per dNMP small. Figure 4.20 shows that this was the case for a smooth wall with E = 0.1 V/nm and the analysis time is about 9 μs. For the rough walls with E = 0.1 V/nm, the distributions for dAMP and dTMP were not close to those for dGMP and dCMP and the analysis time was longer (about 46 μs). For a smooth wall with E = 0.0144 V/nm, the distribution for dGMP was very far from the other three, and the analysis time was about 582 μs. As with the channel length, the minimum analysis time per dNMP was also sensitive to the difference in the estimated mean velocities for the pair of dNMPs that were hardest to separate. Using the analysis mentioned previously in the context of channel length for the rough wall case gave a minimum value of about 15 μs, a maximum value of about 341 μs, and a median value of about 45 μs. There may be a significant difference between the E = 0.0144 V/nm case and the cases with E = 0.1 V/nm.

4.2.4 Summary and Conclusions

The electrophoretic transport of dNMPs in 3 nm wide slits composed of Lennard-Jones carbon atoms was studied using molecular dynamics simulations. The electric field strength (E) was varied, E = 0.0, 0.0144, 0.1, 0.3, or 0.6 V/nm, with atomically smooth, but disordered slit walls. In one case with E = 0.1 V/nm, slit walls with an RMS roughness on the order of the size of the dNMPs were also used. Quantities of interest related to the interactions of the dNMPs with the slit walls and the sodium ions in solution. Also of interest were the minimum channel lengths and analysis times per dNMP required to separate the time of flight distributions of the dNMPs to obtain a desired error rate for sequencing.

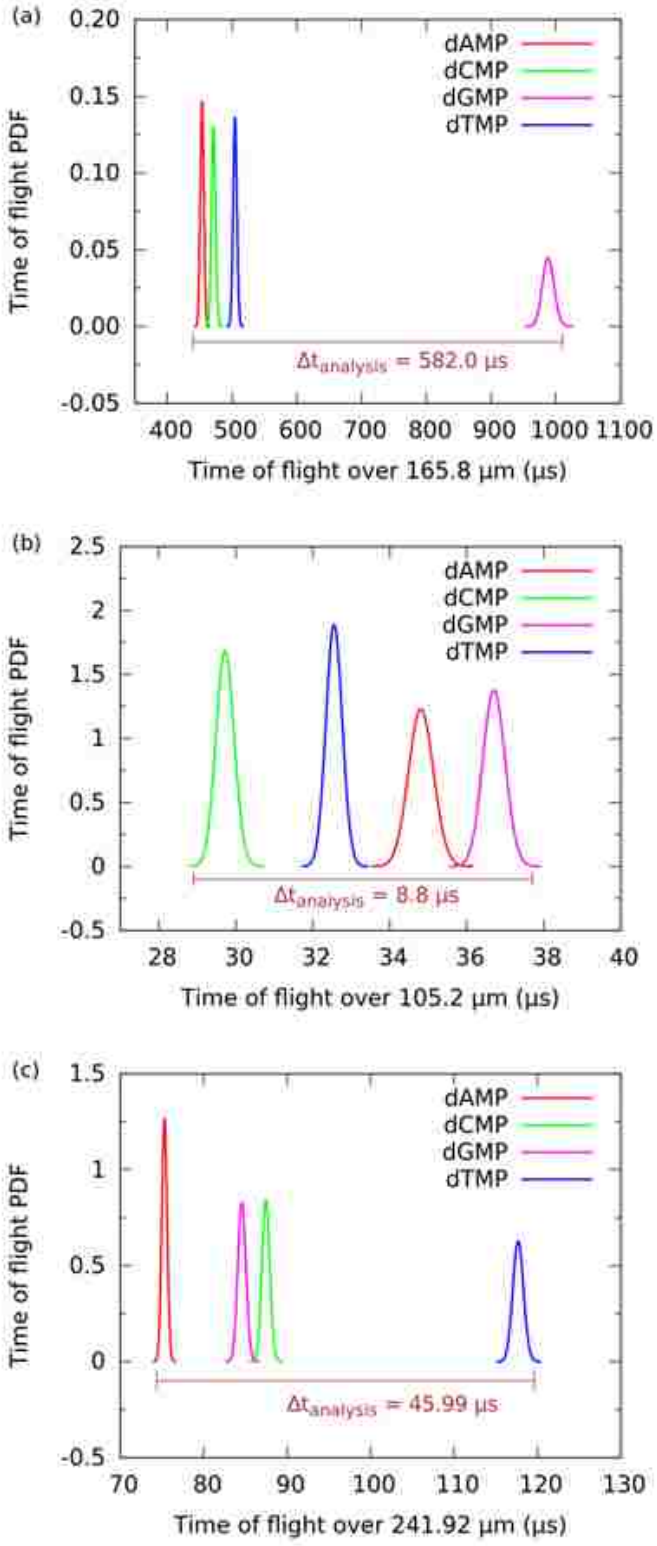

Figure 4.20 Probability density functions (PDFs) of the times of flight for each dNMP for (a) E = 0.0144 V/nm with smooth walls, (b) E = 0.1 V/nm with smooth walls, and (c) E = 0.1 V/nm with rough walls. The minimum required analysis times per dNMP are also shown on the plots.

The dNMP trajectories consisted of multiple adsorptions and desorptions to and from the slit walls with the dNMPs tending to adsorb with their nucleobase groups nearly flat on the surface. The orientations of the dNMP nucleobase groups relative to the wall surfaces as a function of distance from a slit wall during the adsorption and desorption processes were similar. The orientations were also similar as a function of E for E = 0.0, 0.0144, and 0.1 V/nm. This indicates that the mechanism of adsorption and desorption is not affected by the electric field if E is small enough. The orientation of the dNMPs relative to the direction of the electric field was influenced by the electric field. The dNMP was dragged by the negatively charged phosphate group, and with a large enough E, 0.1 V/nm, this effect is significant since the force due to the electric field is significant compared to thermal fluctuations.

Statistics related to adsorption and desorption were computed. The increasing electric field strength with smooth walls decreased the fraction of the total time that the dNMPs were adsorbed to the walls, decreased the mean time per adsorption event, increased the frequency of adsorption events, and increased the velocity of the dNMPs while adsorbed. Increased driving force made desorption more likely and sped up the sliding of the dNMPs on the slit walls. The mean distance traveled by the dNMPs in the direction of the driving force while adsorbed increased with increasing E up to E = 0.3 V/nm, but was about the same for E = 0.3 and 0.6 V/nm due to the competing effects of increasing velocity while adsorbed and decreased time per adsorption event with increasing E. Using rough walls generally made desorption more likely (decreased mean times and distances per adsorption event) and slowed down the sliding of the dNMPs on the walls (decreased velocity while adsorbed). The fractions of the total time that the dNMPs were adsorbed decreased for all dNMPs, but not significantly for dTMP. This was due to the large increase in the frequency of adsorption events for dTMP; its high hydrophobicity made

re-adsorption after desorption very fast. In general, the frequency of adsorption increased when using rough walls. The mean time per adsorption event for dTMP also decreased less than for the other dNMPs when comparing smooth and rough walls, again due to its high hydrophobicity. The velocity of the dNMPs in the direction of the driving force while desorbed was not a function of dNMP or wall roughness as expected. The mean time and distance per desorption event were not influenced by E or wall roughness, but decreased with increasing hydrophobicity of the nucleobase parts of the dNMPs due to faster re-adsorption for more hydrophobic dNMPs. The dNMP-wall interactions affected the frequency and duration of the dNMP adsorption and desorption periods as well as the dNMP velocities during those periods, which helped to separate the dNMP time of flight distributions.

Transient ion association between the anionic phosphate group of the dNMPs and the sodium cations in solution was observed with the number of associated sodium ions varying from 0 to 3. The average number of associated sodium ions was around 1. Due to the transient nature of the association, the force on the dNMP-sodium complex due the electric field also varied leading to changes in the dNMP velocity ranging from very fast with an association number of 0, approximately zero with an association number of 2, and even having the opposite sign with an association number of 3 (rare). The mean association numbers appeared to be a function of the electric field strength, but the differences were not significant considering the uncertainties. The dNMPs with pyrimidine nucleobases (dCMP and dTMP) had slightly fewer associated sodium ions on average compared to the dNMPs with purine nucleobases (dGMP and dTMP). Sodium association had a large effect on the instantaneous dNMP velocities, but little effect on the mean velocities and therefore helped little with separating their time of flight distributions.

The order of the mean velocities or times of flight was affected by the rough walls compared to the smooth walls. For smooth walls, the order of the times of flight was dCMP < dTMP < dAMP < dGMP; the larger dAMP and dGMP were slowed down more when adsorbed. For rough walls, the order of the times of flight was dAMP < dGMP < dCMP < dTMP; the dAMP and dGMP did not stay adsorbed as much and therefore moved faster overall since there were fewer favorable adsorption sites for them on rough walls. Walls with roughness having specific characteristics, or physically or chemically structured walls might be useful for improving the separation of the dNMP time of flight distributions.

4.3 References

1. Luan, B. Q.; Peng, H. B.; Polonsky, S.; Rossnagel, S.; Stolovitzky, G.; Martyna, G., Base-By-Base Ratcheting of Single Stranded DNA through a Solid-State Nanopore. *Phys. Rev. Lett.* 2010, *104* (23), 4.

2. Astier, Y.; Braha, O.; Bayley, H., Toward Single Molecule DNA Sequencing: Direct Identification of Ribonucleoside and Deoxyribonucleoside 5‘-Monophosphates by Using an Engineered Protein Nanopore Equipped with a Molecular Adapter. *Journal of the American Chemical Society* 2006, *128* (5), 1705-1710.

3. Clarke, J.; Wu, H. C.; Jayasinghe, L.; Patel, A.; Reid, S.; Bayley, H., Continuous base identification for single-molecule nanopore DNA sequencing. *Nature Nanotechnology* 2009, *4* (4), 265-270.

4. Miles, B. N.; Ivanov, A. P.; Wilson, K. A.; Dogan, F.; Japrung, D.; Edel, J. B., Single molecule sensing with solid-state nanopores: novel materials, methods, and applications. *Chemical Society Reviews* 2013, *42* (1), 15-28.

5. Haque, F.; Li, J.; Wu, H.-C.; Liang, X.-J.; Guo, P., Solid-state and biological nanopore for real-time sensing of single chemical and sequencing of DNA. *Nano Today* 2013, *8* (1), 56-74.

6. Yang, Y.; Liu, R.; Xie, H.; Hui, Y.; Jiao, R.; Gong, Y.; Zhang, Y., Advances in Nanopore Sequencing Technology. *Journal of Nanoscience and Nanotechnology* 2013, *13* (7), 4521-4538.

7. Nosik, V. L.; Rudakova, E. B., Prospects of biomolecule sequencing with the techniques of translocation through nanopores: A review. *Crystallogr. Rep.* 2013, *58* (6), 805-821.

8. Ying, Y.-L.; Zhang, J.; Gao, R.; Long, Y.-T., Nanopore-Based Sequencing and Detection of Nucleic Acids. *Angewandte Chemie International Edition* 2013, *52* (50), 13154-13161.

9. Novak, B. R.; Moldovan, D.; Nikitopoulos, D. E.; Soper, S. A., Distinguishing Single DNA Nucleotides Based on Their Times of Flight Through Nanoslits: A Molecular Dynamics Simulation Study. *Journal of Physical Chemistry B* 2013, *117* (12), 3271-3279.

10. Lee, J. W.; Meller, A., Rapid DNA Sequencing by Direct Nanoscale Reading of Nucleotide Bases on Individual DNA chains. In *Perspectives in Bioanalysis*, K., M., Ed. Elsevier, Amsterdam: 2007; Vol. 2.

11. Deamer, D. W.; Branton, D., Characterization of nucleic acids by nanopore analysis. *Accounts of Chemical Research* 2002, *35* (10), 817-825.

12. Kasianowicz, J. J.; Brandin, E.; Branton, D.; Deamer, D. W., Characterization of individual polynucleotide molecules using a membrane channel. *Proceedings of the National Academy of Sciences of the United States of America* 1996, *93* (24), 13770-13773.

13. Tsutsui, M.; Taniguchi, M.; Yokota, K.; Kawai, T., Identifying single nucleotides by tunnelling current. *Nature Nanotechnology* 2010, *5* (4), 286-290.

14. Fischbein, M. D.; Drndic, M., Sub-10 nm device fabrication in a transmission electron microscope. *Nano letters* 2007, *7* (5), 1329-37.

15. Zwolak, M.; Di Ventra, M., Electronic signature of DNA nucleotides via transverse transport. *Nano letters* 2005, *5* (3), 421-424.

16. Lagerqvist, J.; Zwolak, M.; Di Ventra, M., Fast DNA sequencing via transverse electronic transport. *Nano letters* 2006, *6* (4), 779-782.

17. Yokota, K.; Tsutsui, M.; Taniguchi, M., Electrode-embedded nanopores for label-free single-molecule sequencing by electric currents. *RSC Advances* 2014, *4* (31), 15886-15899.

18. Healy, K.; Ray, V.; Willis, L. J.; Peterman, N.; Bartel, J.; Drndić, M., Fabrication and characterization of nanopores with insulated transverse nanoelectrodes for DNA sensing in salt solution. *Electrophoresis* 2012, *33* (23), 3488-3496.

19. Fanget, A.; Traversi, F.; Khlybov, S.; Granjon, P.; Magrez, A.; Forró, L.; Radenovic, A., Nanopore Integrated Nanogaps for DNA Detection. *Nano letters* 2013, *14* (1), 244-249.

20. He, Y. H.; Shao, L. B.; Scheicher, R. H.; Grigoriev, A.; Ahuja, R.; Long, S. B.; Ji, Z. Y.; Yu, Z. A.; Liu, M., Differential conductance as a promising approach for rapid DNA sequencing with nanopore-embedded electrodes. *Appl. Phys. Lett.* 2010, *97* (4), 3.

21. Sigalov, G.; Comer, J.; Timp, G.; Aksimentiev, A., Detection of DNA sequences using an alternating electric field in a nanopore capacitor. *Nano letters* 2008, *8* (1), 56-63.

22. Bobadilla, A. D.; Seminario, J. M., Assembly of a Noncovalent DNA Junction on Graphene Sheets and Electron Transport Characteristics. *Journal of Physical Chemistry C* 2013, *117* (50), 26441-26453.

23. Puster, M.; Rodríguez-Manzo, J. A.; Balan, A.; Drndić, M., Toward Sensitive Graphene Nanoribbon–Nanopore Devices by Preventing Electron Beam-Induced Damage. *Acs Nano* 2013, *7* (12), 11283-11289.

24. Traversi, F.; Raillon, C.; Benameur, S. M.; Liu, K.; Khlybov, S.; Tosun, M.; Krasnozhon, D.; Kis, A.; Radenovic, A., Detecting the translocation of DNA through a nanopore using graphene nanoribbons. *Nature Nanotechnology* 2013, *8* (12), 939-945.

25. Rezapour, M. R.; Rajan, A. C.; Kim, K. S., Molecular Sensing Using Armchair Graphene Nanoribbon. *Journal of Computational Chemistry* 2014, *35* (26), 1916-1920.

26. Langecker, M.; Pedone, D.; Simmel, F. C.; Rant, U., Electrophoretic Time-of-Flight Measurements of Single DNA Molecules with Two Stacked Nanopores. *Nano letters* 2011, *11* (11), 5002-5007.

27. Harms, Z. D.; Haywood, D. G.; Kneller, A. R.; Selzer, L.; Zlotnick, A.; Jacobson, S. C., Single-Particle Electrophoresis in Nanochannels. *Analytical Chemistry* 2015, *87* (1), 699-705.

28. Harms, Z. D.; Mogensen, K. B.; Nunes, P. S.; Zhou, K. M.; Hildenbrand, B. W.; Mitra, I.; Tan, Z. N.; Zlotnick, A.; Kutter, J. P.; Jacobson, S. C., Nanofluidic Devices with Two Pores in Series for Resistive-Pulse Sensing of Single Virus Capsids. *Analytical Chemistry* 2011, *83* (24), 9573-9578.

29. Davis, L. M.; Fairfield, F. R.; Harger, C. A.; Jett, J. H.; Keller, R. A.; Hahn, J. H.; Krakowski, L. A.; Marrone, B. L.; Martin, J. C.; Nutter, H. L.; et al., Rapid DNA sequencing based upon single molecule detection. *Genetic analysis, techniques and applications* 1991, *8* (1), 1-7.

30. Goodwin, P. M.; Cai, H.; Jett, J. H.; IshaugRiley, S. L.; Machara, N. P.; Semin, D. J.; VanOrden, A.; Keller, R. A., Application of single molecule detection to DNA sequencing. *Nucleosides & Nucleotides* 1997, *16* (5-6), 543-550.

31. Zhu, L.; Stryjewski, W. J.; Soper, S. A., Multiplexed fluorescence detection in microfabricated devices with both time-resolved and spectral-discrimination capabilities using near-infrared fluorescence. *Anal. Biochem.* 2004, *330* (2), 206-218.

32. McNally, B.; Singer, A.; Yu, Z.; Sun, Y.; Weng, Z.; Meller, A., Optical Recognition of Converted DNA Nucleotides for Single-Molecule DNA Sequencing Using Nanopore Arrays. *Nano letters* 2010, *10* (6), 2237-2244.

33. Eid, J.; Fehr, A.; Gray, J.; Luong, K.; Lyle, J.; Otto, G.; Peluso, P.; Rank, D.; Baybayan, P.; Bettman, B.; Bibillo, A.; Bjornson, K.; Chaudhuri, B.; Christians, F.; Cicero, R.; Clark, S.; Dalal, R.; Dewinter, A.; Dixon, J.; Foquet, M.; Gaertner, A.; Hardenbol, P.; Heiner, C.; Hester, K.; Holden, D.; Kearns, G.; Kong, X. X.; Kuse, R.; Lacroix, Y.; Lin, S.; Lundquist, P.; Ma, C. C.; Marks, P.; Maxham, M.; Murphy, D.; Park, I.; Pham, T.; Phillips, M.; Roy, J.; Sebra, R.; Shen, G.; Sorenson, J.; Tomaney, A.; Travers, K.; Trulson, M.; Vieceli, J.; Wegener, J.; Wu, D.; Yang, A.; Zaccarin, D.; Zhao, P.; Zhong, F.; Korlach, J.; Turner, S., Real-Time DNA Sequencing from Single Polymerase Molecules. *Science* 2009, *323* (5910), 133-138.

34. Guy, A. T.; Piggot, T. J.; Khalid, S., Single-Stranded DNA within Nanopores: Conformational Dynamics and Implications for Sequencing; a Molecular Dynamics Simulation Study. *Biophysical Journal* 2012, *103* (5), 1028-1036.

35. Maglia, G.; Restrepo, M. R.; Mikhailova, E.; Bayley, H., Enhanced translocation of single DNA molecules through alpha-hemolysin nanopores by manipulation of internal charge. *Proceedings of the National Academy of Sciences of the United States of America* 2008, *105* (50), 19720-19725.

36. Rincon-Restrepo, M.; Milthallova, E.; Bayley, H.; Maglia, G., Controlled Translocation of Individual DNA Molecules through Protein Nanopores with Engineered Molecular Brakes. *Nano letters* 2011, *11* (2), 746-750.

37. Wu, H. C.; Astier, Y.; Maglia, G.; Mikhailova, E.; Bayley, H., Protein nanopores with covalently attached molecular adapters. *Journal of the American Chemical Society* 2007, *129* (51), 16142-16148.

38. Bhattacharya, S.; Derrington, I. M.; Pavlenok, M.; Niederweis, M.; Gundlach, J. H.; Aksimentiev, A., Molecular Dynamics Study of MspA Arginine Mutants Predicts Slow DNA Translocations and Ion Current Blockades Indicative of DNA Sequence. *Acs Nano* 2012, *6* (8), 6960-6968.

39. Langecker, M.; Arnaut, V.; Martin, T. G.; List, J.; Renner, S.; Mayer, M.; Dietz, H.; Simmel, F. C., Synthetic Lipid Membrane Channels Formed by Designed DNA Nanostructures. *Science* 2012, *338* (6109), 932-936.

40. Bell, N. A. W.; Keyser, U. F., Nanopores formed by DNA origami: A review. *Febs Letters* 2014, *588* (19), 3564-3570.

41. Liu, L.; Yang, C.; Zhao, K.; Li, J.; Wu, H.-C., Ultrashort single-walled carbon nanotubes in a lipid bilayer as a new nanopore sensor. *Nat Commun* 2013, *4*.

42. Rhee, M.; Burns, M. A., Nanopore sequencing technology: research trends and applications. *Trends in Biotechnology* 2006, *24* (12), 580-586.

43. Storm, A. J.; Chen, J. H.; Ling, X. S.; Zandbergen, H. W.; Dekker, C., Fabrication of solid-state nanopores with single-nanometre precision. *Nature Materials* 2003, *2* (8), 537-540.

44. Larkin, J.; Henley, R.; Bell, D. C.; Cohen-Karni, T.; Rosenstein, J. K.; Wanunu, M., Slow DNA Transport through Nanopores in Hafnium Oxide Membranes. *Acs Nano* 2013, *7* (11), 10121-10128.

45. Zhou, Z.; Hu, Y.; Wang, H.; Xu, Z.; Wang, W.; Bai, X.; Shan, X.; Lu, X., DNA Translocation through Hydrophilic Nanopore in Hexagonal Boron Nitride. *Sci. Rep.* 2013, *3*.

46. Liu, S.; Lu, B.; Zhao, Q.; Li, J.; Gao, T.; Chen, Y.; Zhang, Y.; Liu, Z.; Fan, Z.; Yang, F.; You, L.; Yu, D., Boron Nitride Nanopores: Highly Sensitive DNA Single-Molecule Detectors. *Advanced Materials* 2013, *25* (33), 4549-4554.

47. Wells, D. B.; Belkin, M.; Comer, J.; Aksimentiev, A., Assessing Graphene Nanopores for Sequencing DNA. *Nano letters* 2012, *12* (8), 4117-4123.

48. Wang, Y.; Yu, X. F.; Liu, Y. Y.; Xie, X.; Cheng, X. L.; Huang, S. M.; Wang, Z. M., Fabrication of Graphene Nanopores and a Preliminary Study on lambda-DNA Translocation. *Acta Chimica Sinica* 2014, *72* (3), 378-381.

49. Schneider, G. F.; Kowalczyk, S. W.; Calado, V. E.; Pandraud, G.; Zandbergen, H. W.; Vandersypen, L. M. K.; Dekker, C., DNA Translocation through Graphene Nanopores. *Nano letters* 2010, *10* (8), 3163-3167.

50. Garaj, S.; Hubbard, W.; Reina, A.; Kong, J.; Branton, D.; Golovchenko, J. A., Graphene as a subnanometre trans-electrode membrane. *Nature* 2010, *467* (7312), 190-U73.

51. Merchant, C. A.; Drndić, M., Graphene Nanopore Devices for DNA Sensing. In *Nanopore-Based Technology*, 2012; Vol. 870, pp 211-226.

52. Sadeghi, H.; Algaragholy, L.; Pope, T.; Bailey, S.; Visontai, D.; Manrique, D.; Ferrer, J.; Garcia-Suarez, V.; Sangtarash, S.; Lambert, C. J., Graphene Sculpturene Nanopores for DNA Nucleobase Sensing. *Journal of Physical Chemistry B* 2014, *118* (24), 6908-6914.

53. Liang, L.; Zhang, Z.; Shen, J.; Zhe, K.; Wang, Q.; Wu, T.; Agren, H.; Tu, Y., Theoretical studies on the dynamics of DNA fragment translocation through multilayer graphene nanopores. *Rsc Advances* 2014, *4* (92), 50494-50502.

54. Farimani, A. B.; Min, K.; Aluru, N. R., DNA Base Detection Using a Single-Layer MoS2. *Acs Nano* 2014, *8* (8), 7914-7922.

55. Carr, R.; Comer, J.; Ginsberg, M. D.; Aksimentiev, A., Microscopic Perspective on the Adsorption Isotherm of a Heterogeneous Surface. *J. Phys. Chem. Lett.* 2011, *2* (14), 1804-1807.

56. Keyser, U. F.; van der Does, J.; Dekker, C.; Dekker, N. H., Optical tweezers for force measurements on DNA in nanopores. *Rev. Sci. Instrum.* 2006, *77* (10).

57. Lu, B.; Hoogerheide, D. P.; Zhao, Q.; Zhang, H.; Tang, Z.; Yu, D.; Golovchenko, J. A., Pressure-Controlled Motion of Single Polymers through Solid-State Nanopores. *Nano letters* 2013, *13* (7), 3048-3052.

58. Kowalczyk, S. W.; Wells, D. B.; Aksimentiev, A.; Dekker, C., Slowing down DNA Translocation through a Nanopore in Lithium Chloride. *Nano letters* 2012, *12* (2), 1038-1044.

59. Zhang, H.; Zhao, Q.; Tang, Z.; Liu, S.; Li, Q.; Fan, Z.; Yang, F.; You, L.; Li, X.; Zhang, J.; Yu, D., Slowing Down DNA Translocation Through Solid-State Nanopores by Pressure. *Small* 2013, *9* (24), 4112-4117.

60. Belkin, M.; Maffeo, C.; Wells, D. B.; Aksimentiev, A., Stretching and Controlled Motion of Single-Stranded DNA in Locally Heated Solid-State Nanopores. *Acs Nano* 2013, *7* (8), 6816-6824.

61. He, Y.; Tsutsui, M.; Scheicher, R. H.; Bai, F.; Taniguchi, M.; Kawai, T., Thermophoretic Manipulation of DNA Translocation through Nanopores. *Acs Nano* 2012, *7* (1), 538-546.

62. Stoddart, D.; Maglia, G.; Mikhailova, E.; Heron, A. J.; Bayley, H., Multiple base-recognition sites in a biological nanopore: two heads are better than one. *Angew Chem Int Ed Engl* 2010, *49* (3), 556-9.

63. Oliver-Calixte, N. J.; Uba, F. I.; Battle, K. N.; Weerakoon-Ratnayake, K. M.; Soper, S. A., Immobilization of Lambda Exonuclease onto Polymer Micropillar Arrays for the Solid-Phase Digestion of dsDNAs. *Analytical Chemistry* 2014, *86* (9), 4447-4454.

64. Blackburn, G. M.; Gait, M. J., *Nucleic Acids in Chemistry and Biology*. IRL Press: Oxford, 1990.

65. Ts'o, P. O. P., Bases, Nucleosides, and Nucleotides. In *Basic Principles in Nucleic Acid Chemistry*, Ts'o, P. O. P., Ed. Academic Press: New York, 1974; Vol. 1, pp 454-584.

66. Close, D. M., Calculated pKa's of the DNA Base Radical Ions. *The Journal of Physical Chemistry A* 2012, *117* (2), 473-480.

67. Menard, L. D.; Ramsey, J. M., Fabrication of Sub-5 nm Nanochannels in Insulating Substrates Using Focused Ion Beam Milling. *Nano letters* 2011, *11* (2), 512-517.

68. Humphrey, W.; Dalke, A.; Schulten, K., VMD: Visual Molecular Dynamics. *Journal of Molecular Graphics* 1996, *14* (1), 33-38.

69. Foloppe, N.; MacKerell, A. D., All-atom empirical force field for nucleic acids: I. Parameter optimization based on small molecule and condensed phase macromolecular target data. *Journal of Computational Chemistry* 2000, *21* (2), 86-104.

70. Yeh, I. C.; Berkowitz, M. L., Ewald summation for systems with slab geometry. *Journal of Chemical Physics* 1999, *111* (7), 3155-3162.

71. Czarnecka, J.; Cieslak, M.; Michal, K., Application of solid phase extraction and high-performance liquid chromatography to qualitative and quantitative analysis of nucleotides and nucleosides in human cerebrospinal fluid. *Journal of Chromatography B-Analytical Technologies in the Biomedical and Life Sciences* 2005, *822* (1-2), 85-90.

72. Perrett, D.; Bhusate, L.; Patel, J.; Herbert, K., Comparative Performance of Ion-Exchange and Ion-Paired Reversed Phase High-Performance Liquid-Chromatography for the Determination of Nucleotides in Biological Samples. *Biomedical Chromatography* 1991, *5* (5), 207-211.

73. Castillo-Fernandez, O.; Salieb-Beugelaar, G. B.; van Nieuwkasteele, J. W.; Bomer, J. G.; Arundell, M.; Samitier, J.; van den Berg, A.; Eijkel, J. C. T., Electrokinetic DNA transport in 20 nm-high nanoslits: Evidence for movement through a wall-adsorbed polymer nanogel. *Electrophoresis* 2011, *32* (18), 2402-2409.

74. Mumper, R. J.; Wang, J. J.; Klakamp, S. L.; Nitta, H.; Anwer, K.; Tagliaferri, F.; Rolland, A. P., Protective interactive noncondensing (PINC) polymers for enhanced plasmid distribution and expression in rat skeletal muscle. *J. Control. Release* 1998, *52* (1-2), 191-203.

75. Kang, S. H.; Shortreed, M. R.; Yeung, E. S., Real-Time Dynamics of Single-DNA Molecules Undergoing Adsorption and Desorption at Liquid−Solid Interfaces. *Analytical Chemistry* 2001, *73* (6), 1091-1099.

76. Wu, L. Z.; Liu, H.; Zhao, W. Y.; Wang, L.; Hou, C. R.; Liu, Q. J.; Lu, Z. H., Electrically facilitated translocation of protein through solid nanopore. *Nanoscale Res. Lett.* 2014, *9*, 10.

77. Shih, P.; Pedersen, L. G.; Gibbs, P. R.; Wolfenden, R., Hydrophobicities of the Nucleic Acid Bases: Distribution Coefficients from Water to Cyclohexane. *Journal of Molecular Biology* 1998, *280* (3), 421-430.

78. Munoz-Muriedas, J.; Barril, X.; Lopez, J. M.; Orozco, M.; Luque, F. J., A Hydrophobic Similarity Analysis of Solvation Effects on Nucleic Acid Bases. *Journal of Molecular Modeling* 2007, *13*, 357-365.

79. MacKerell, A. D., Influence of magnesium ions on duplex DNA structural, dynamic, and solvation properties. *Journal of Physical Chemistry B* 1997, *101* (4), 646-650.

80. Mocci, F.; Laaksonen, A., Insight into nucleic acid counterion interactions from inside molecular dynamics simulations is "worth its salt". *Soft Matter* 2012, *8* (36), 9268-9284.

81. Shen, X.; Gu, B.; Che, S. A.; Zhang, F. S., Solvent effects on the conformation of DNA dodecamer segment: A simulation study. *Journal of Chemical Physics* 2011, *135* (3), 13.

82. Musheev, M. U.; Kanoatov, M.; Krylov, S. N., Non-uniform Velocity of Homogeneous DNA in a Uniform Electric Field: Consequence of Electric-Field-Induced Slow Dissociation of Highly Stable DNA-Counterion Complexes. *Journal of the American Chemical Society* 2013, *135* (21), 8041-8046.

83. Brehm, M.; Kirchner, B., TRAVIS - A Free Analyzer and Visualizer for Monte Carlo and Molecular Dynamics Trajectories. *Journal of Chemical Information and Modeling* 2011, *51* (8), 2007-2023.

84. Kunsch, H. R., The Jackknife and the Bootstrap for General Stationary Observations. *Annals of Statistics* 1989, *17* (3), 1217-1241.

85. Oostenbrink, C.; Villa, A.; Mark, A. E.; Van Gunsteren, W. F., A biomolecular force field based on the free enthalpy of hydration and solvation: The GROMOS force-field parameter sets 53A5 and 53A6. *Journal of Computational Chemistry* 2004, *25* (13), 1656-1676.

CHAPTER 5. ON-GOING DEVELOPMENT AND FUTURE DIRECTIONS

5.1 Introduction

The overall goal of the nanosensor project is to develop a novel innovative biosensor capable of sequencing biomolecules such as DNA, RNA and proteins in real-time in a rapid and efficient manner. The sequencing will be based on time-of-flight (ToF) measurements of the single monomer units migrating through 2D nanochannel devices after they being clipped by the clipping enzymes immobilized on the pillars. Depending on their interactions with the channel walls, a unique signature will be generated which can be used for differentiating the single monomers. The signature can be either optical which is measured by fluorescence or electrical which is measured by conductivity of the buffer. The realization of this project will be accomplished by integration of several individual modules.

The process of DNA sequencing module initiates with the immobilization of enzyme in the nanopillar. To accomplish this task, a clipping enzyme such as λ-exonuclease is tethered to the solid nanopillar support that can processively clip the single nucleotide units from the dsDNA strand. This bioreactor can be activated by the introduction of Mg^{2+} in to the fluidic channel.[1] Before the DNA strand reach the enzyme, its activity is manipulated using an entropic trap, which stores the DNA temporarily. These entropic traps also help DNA to elongate to support the sequencing. The clipped individual dNMPs travel through the nano flight tube in the presence of a electric field. Thus, in our group, we have shown the feasibility of separating them depending on their unique adsorption behavior with the carbon walls using molecular dynamics simulation.[2] We have also proven that surface modification of the nanochannel walls have a significant effect on the separation in nanotubes.[3]

As depicted in

Figure 5.1, single dNMPs are translocated through channels fabricated on polymer devices. In our group, we innovated a new method for produce polymer device hybrid bonding scheme.[4] These channels will have dimensions less than 20 nm and the electrical readouts will be recoded through fabricated transverse electrodes at the entrance and exit of the nano tube.

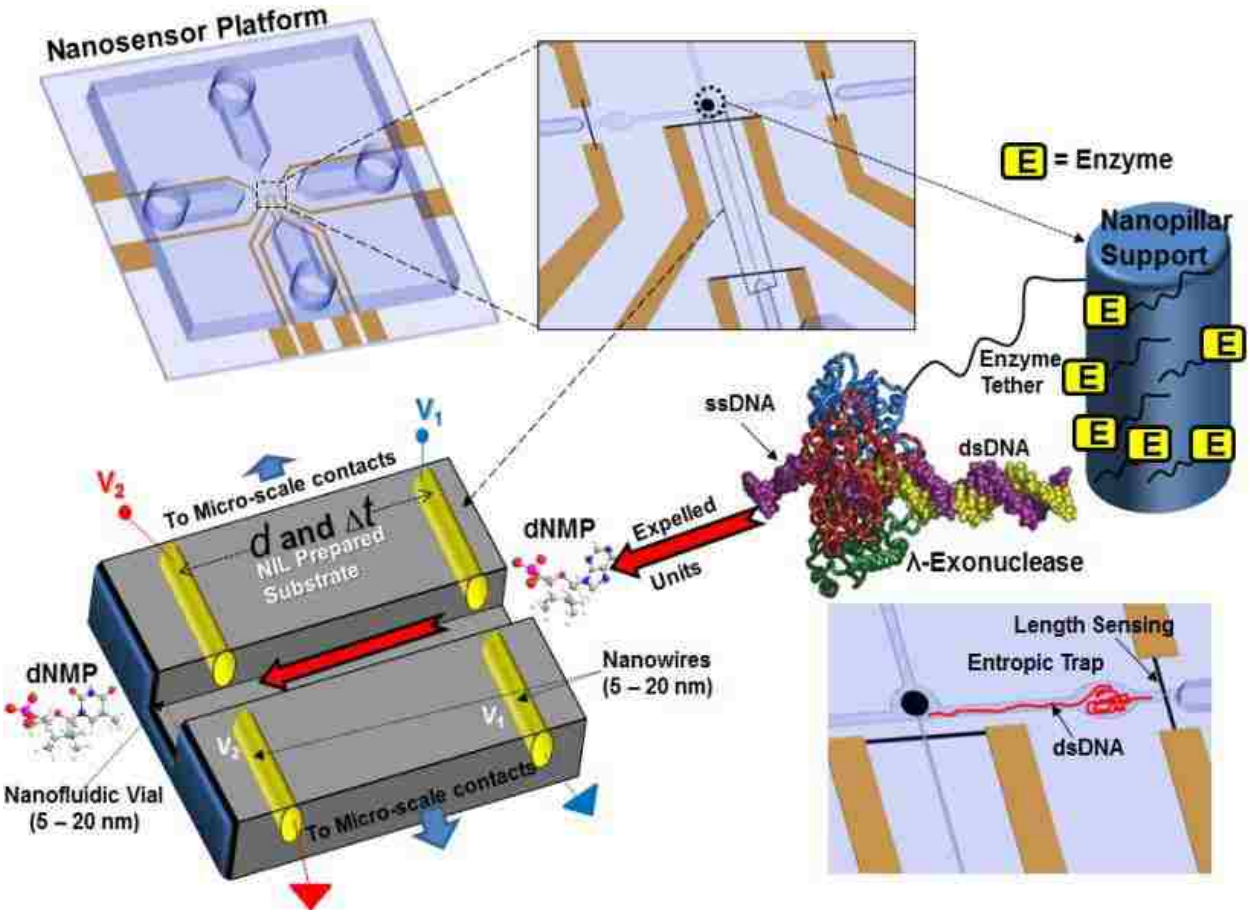

Figure 5.1 Schematic of the nanosensor that accepts dsDNA input molecules and deduces their primary sequence by the sequential clipping of the input dsDNA molecule using an exonuclease enzyme. The single dNMPs generated are moved through a nanochannel that produces a molecular-dependent flight-time used for dNMP identification. The flight-time is measured using a pair of nanoelectrodes poised at the input and output ends of the nanochannel, which is made from the appropriate polymeric material to suit the application need and the structures produced via micro- and nano-replication technologies. The nanosensor uses electrical signatures to monitor the input of dsDNA, immobilized exonuclease to complex the dsDNA, entropic traps to stretch the dsDNA and identify the clipped dNMPs using flight-times through 2D nanochannels.

5.2 On-going Developments

5.2.1 Fabrication of Nanopore Devices for Abasic DNA Readouts

Recent work has shown that DNA confinement in nanochannels or nanopores can be used to search for methylation [5-7] or AP sites [8]. For nanochannels, elongation to near a DNA's full contour length can be achieved either through the proper choice in nanochannel dimensions and/or the carrier electrolyte composition [9-11]. While most elongation experiments were undertaken using glass-based devices fabricated with dry etching following nano-patterning, electron beam lithography or focused ion beam milling [9, 11-17], we have developed a simple replication-based method to produce nanochannels directly in polymers with dimensions near or below the persistence length of double-stranded DNAs [18-19]. The advantage of this approach is that nanofluidic devices can be produced at lower cost and higher production modes making such devices appropriate for diagnostics.

Our fluidic bioprocessor will provide unique capabilities for detecting AP sites as an approach for assessing response to therapy in cancer patients. As can be seen from Table 5.1, the performance metrics predicted for our system compared to our slide-based system [20] and Next Generation Sequencing are noteworthy. The integrated system will not only automate the entire sample processing pipeline, but also reduce assay cost and increase throughput. We estimate that the time required for processing a single blood sample for DNA damage using our fluidic bioprocessor will be on the order of 90 min [21].

We propose a device design capable of measuring the unique electric signatures of dsDNA and the streptavidin labeled abasic sites to accomplish the fore mention assay for detection damage sites in dsDNA.

Figure 5.2 shows COMSOL simulations results for a nanofluidic device design with two nanopores. When the dsDNA with abasic sites passes through the nanopore it produces a signal two different electric readouts when the DNA passand each of the streptavidin labeled DNA passes through the pore. Currently, we are fabricating the devices to achieve nanopore dimensions less than 50 nm × 50 nm to incorporate it abasic site detections.

Table 5.1 Projected performance comparison between DNA fiber imaging, fluidic bio-processor, and Next Gen Sequencing approaches for reading AP sites in damaged DNA.

	Method	Genomic Region Analyzed	Number of Cells Needed	DNA Analyzed per Cell (Mb)[3]	% of Genome Analyzed	Genomic Coverage (fold)	Accuracy of Analysis[4]	Cost per Genome
Sequencing	Next Gen[7]	Specific	~15,000	7	70 to 80	30	90 to 95%	$10,000
DNA Damage	Fiber	Global/ Specific[1,5]	4 to 6[6]	25 to 50	2 to 4	<2	93%	$2000
	Bio-Processor	Global/ Specific[2,5]	4 to 100[5]	6,000 to 8,000	80 to 90	30	90 to 95%	$200

[1] Method has potential to analyze specific regions of genome if one uses FISH.[2] Method has potential to analyze specific regions of genome if one uses Bar Coding with PNA probes.[3] Mb equals megabases; size of 1 diploid genome is 12,000 Mb. [4]From our paper [20]. [5]Predicted. [6]Based on power calculations.[7]Data derived from [20].

5.2.2 Single Dye Molecule Imaging and Electrophoresis though Nanochannels

Detection of the single nucleotide bases (dNMPs) with high base call accuracy will depend on the electrophoretic resolution for each dNMP; the resolution will produce a base call accuracy >98%. The proposed single molecule identification scheme is dependent on realizing highly efficient electrophoretic separations in ms time scales using nanometer flight tubes that can

maximize resolution by minimizing dispersion effects and maximizing selectivity. To accomplish this we will investigate dispersion effects potentially arising from surface roughness, non-specific adsorption and surface charge heterogeneity, which are unique to our thermoplastic

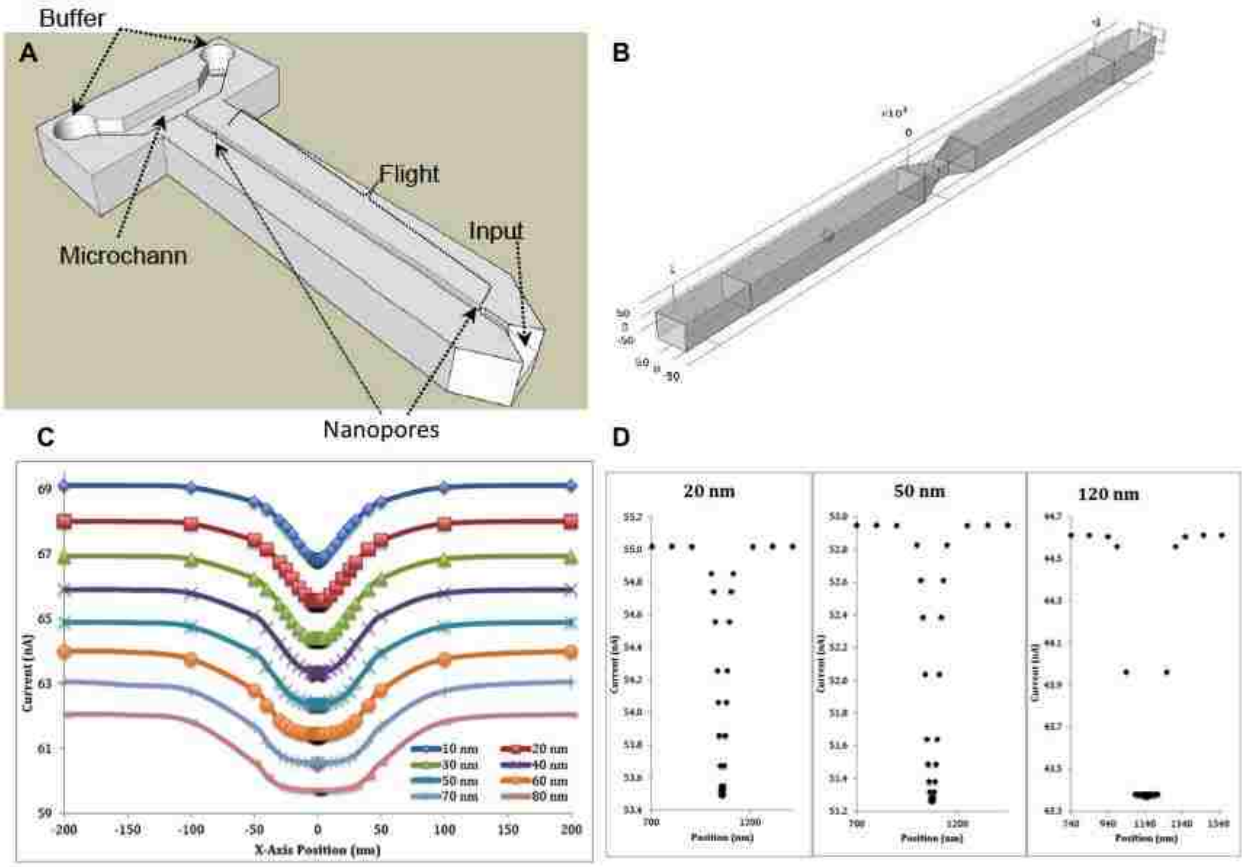

Figure 5.2 A) Computer assisted design image of the basic sensor geometry with important structures labeled B) Model for nanopore length simulations in which finer meshes were used to further understand the behavior of the particles and their signals as they passed through the pore. C) Simulation (COMSOL) results showing the effects of pore length on the current response generated. A pore with a cross section of 50 nm × 50 nm was varied in length from 10 nm to 80 nm. For each length a polystyrene bead with a diameter of 40 nm was stepped through positions inside of the pore, the resultant drop in current was recorded. D) Blockage current traces for simulations with 20, 50, ad 120 nm detection pore lengths. The 20 nm pore recorded a current change of 1.52 nA, the 50 nm pore recorded 1.67 nA, and the 120 nm pore recorded 1.23 nA.

nanochannel flight tubes. Our proposed thermoplastic materials are somewhat hydrophobic, which may require activation to produce hydrophilic surfaces to mitigate non-specific adsorption issues. The process of activation of thermoplastic materials results in increased surface

roughness and heterogeneous surface charge density. We will utilize novel tools, such a super-resolution microscopy, to probe the degree of surface charge density heterogeneity as well as classical tools such as COMSOL to determine how these parameters contribute to fluid flow in plastic nanometer tubes and ultimately contribute to dispersion of single dNMP flight times. Furthermore, high-resolution microscopy techniques will be used to study transverse electromigration properties of the dNMPs within nanochannels to assess these effects on dispersion. This will allow for the first ever 3-D tracking of single molecules within nanochannels. Any factors increasing dispersion beyond diffusion can be addressed through thermoplastic surface modifications following their activation. We have the capability to tailor polymers and activation protocols to minimize contributions of the aforementioned parameters, thus resulting in reduced dispersion that enhances resolution.

We also need to maximize resolution by optimizing the selectivity between nucleotides. Nanoelectrophoresis introduces many unique conditions allowing for enhanced separations and has been demonstrated in the literature as a useful tool for the separation of various biological molecules. Previous research in our group has demonstrated the successful separation of nucleotide monophosphates within conventional silica capillaries with the addition of buffer modifiers.[22] Our research here aims to demonstrate nanoelectrophoresis of the dNMPs without the addition of buffer additives due to the unique properties specific to nanodimensions, such as partial electrical double layer overlap and increased surface area-to-volume ratios. Figure 5.3 shows the microscopy setup we currently developed for single molecular imaging. It consists of a NS:YVO_4 (λ_{ex} = 532 nm; P= 0.01 – 5.00 W) laser to facilitate the excitation of dye molecules such as ATTO 532 (λ_{ex} = 532 nm; λ_{em} = 556 nm). The field of view expands up to 50 μm which

is adequate to cover the nanochannel imaging area and an EMCCD camera capable of recording 512 × 512 videos are integrated to the system.

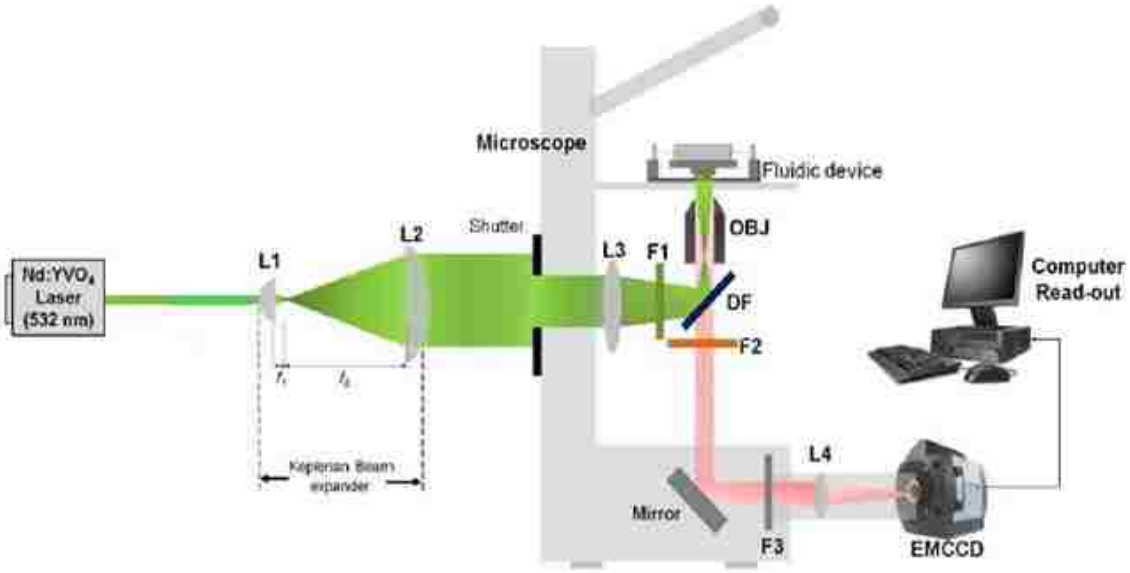

Figure 5.3 Optical set-up of the imaging system. The Gaussian beam from the Laser (Nd:VYAG (λex = 532 nm; P = 0.01-5W; 2.2 mm beam diameter) was initially passed through a Neutral density filter (NDF) then expanded 10 times with a Kaplerian beam expander (focal lengths are 20mm and 200mm for L1 and L2 plano-convex lenses, respectively) and the wings knocked out with a shutter that ensures uniform laser intensity in the field of view and complete back-filling of the objective (OBJ). The beam was focused through an iris into the back end of a 100x oil immersion objective lens (OBJ) using lens (L3) through a 532nm laser line filter (F1) and the reflection from a dichroic filter (DF). A collimated laser beam is impinged upon the polymer nanofluidic device. The fluorescence signal generated from the single molecule was collected by this same objective, passed through the DF and spectrally selected using a long pass filter (F2). A mirror was used to steer the fluorescence signal onto an EMCCD after through a band-pass filter (F3) and focused using lens (L4).

5.2.3 Single Nanopillar Translocation of DNA

To investigate the trapping of single DNA molecules in the entropic trap and the translocation through the single pillar geometry we designed a nanofluidic device with single entropic trap and an offset single pillar. The entropic trap size is 400 nm and the spacing between the entropic trap and the pillar is 30 μm (see Figure 5.4). The preliminary results from this device (see Figure 5.4) has shown that when the DNA in the entropic trap and when it is moving out of

the trap it stretches followed by relaxation in the nanochannel. The extension of λ-DNA was 30% assuming the length was 20 μm when stretching out of entropic trap. When it approached the nanopillar the extension was 17%.

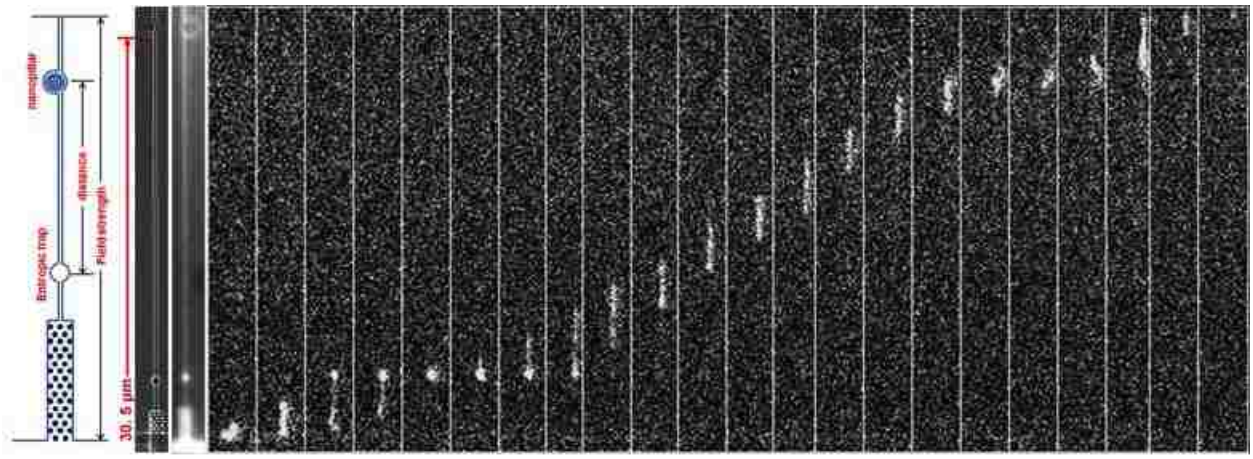

Figure 5.4 Representative series of frames showing the transport of λ-DNA that has been fluorescently stained in a 5:1 ratio and electrokinetically driven though an irregular nanochannel with a 30 μm trap to pillar spacing and contains an entropic trap of 400 nm.

Taking account of the collected results, device design was modified as shown in (a) of Figure 5.5. The single pillar can be translated to a resister to shape DNA while the entropic trap acts as a capacitor ((b) and (c) of Figure 5.5) to store DNA. Figure 5.5 (d) shows the translocation event of λ-DNA through the device at a bias voltage of 0.1 V. The complete translocation take about 650 ms while it stays in the entropic trap for ~15 ms before exit the trap and travel towards the pillar. Figure 5.5 (e) and (f) shows the histograms for resident time in the entropic trap and the tranlocation time of the events, respectively from the data collected so far. We are currently investigating the size effects of the trap and the effects nanochannel length. Subsequently, the nanopillars will be used to tether exonuclease enzyme to clip and feed single nucleotides from the captures dsDNA to the nanochannels.

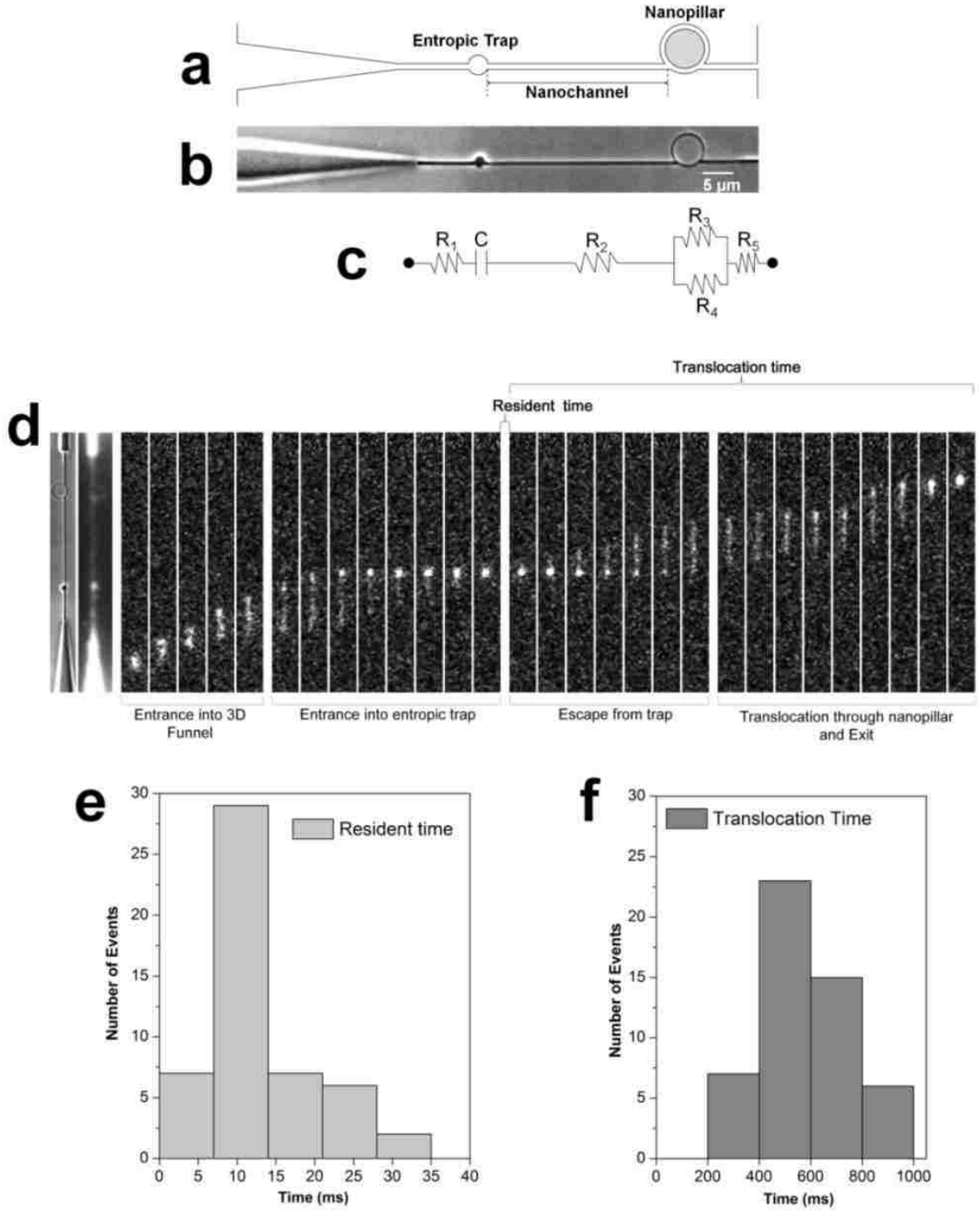

Figure 5.5 (a) Illustration, (b) SEM image and (c) Equivalent circuit of the multi-structured 3D Funnel/Entropic trap/Nanopillar device. Nanochannels are represented as resistors and the entropic trap is represented as a capacitor. (d) Frames showing the translocation of lambda DNA through the device. (e) and (f) shows the histograms of the resident time and translocation time of the migrating DNA, respectively under a 0.1 V driving voltage.

5.3 Future Directions

5.3.1 Fabrication of Transverse Electrodes for Single Molecular Detection

In our nanofluidic sensor device for single molecular detection, we proposed the need of two pairs of transvers electrodes to dictate the entrance of the single molecule in to the nanochannel and the exit of molecule, which indicates its ToF transduction modality. Figure 5.6 shows the preliminary results obtained from fabrication of the electrodes in the silica devices. The two

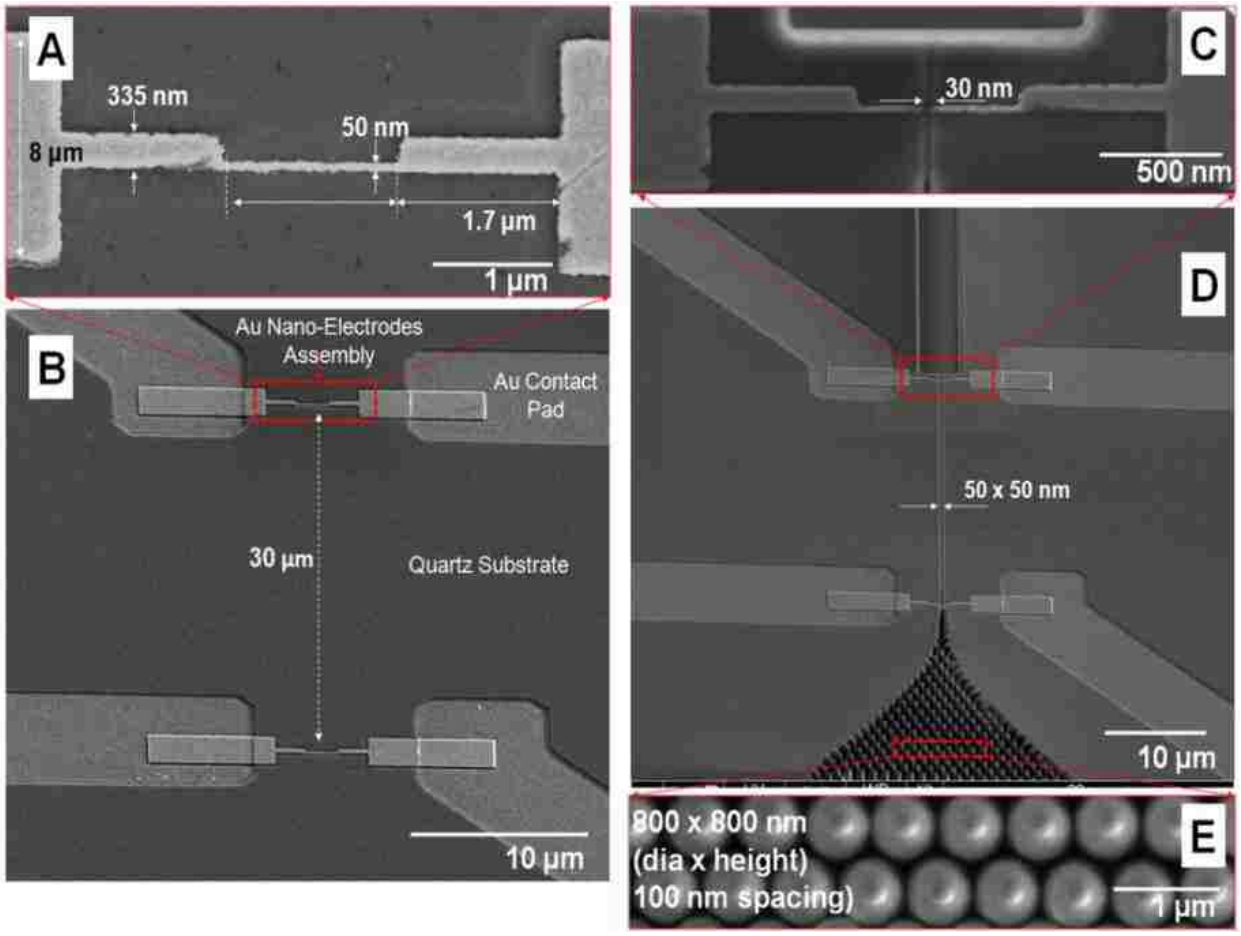

Figure 5.6 SEMs of the molecular nanosensor made in glass via a combination of optical lithography, EBL and FIB. (A) and (B) show the device before FIB milling while (C) and (D) show the device following FIB milling. (A) High resolution SEM of the nanoelectrode that is 50 nm wide with a depth of 50 nm. The electrode is buried into the glass substrate using EBL and ICP-RIE to make trenches to accommodate the electrodes. Also shown are the Au microcontacts. (B) Low resolution SEM showing the location of the 30 µm length nanochannel. (C) High resolution SEM showing the 30 nm gap between electrodes. (D) Low resolution SEM showing the entire device. (E) SEM of the pillars populating the input funnel.

electrodes will be places orthogonally to the nanochannel and they will be positioned such that the nanogap between the electrodes are equal or less than the nanochannel width. The fabrication process for producing this device involved four major steps; (i) Optical lithography to make micro-contact pads and the micro-scale fluidic channels; (ii) electron beam lithography and liftoff to make the nanoelectrodes; (iii) FIB milling of the substrate to build the nanofluidic network and produce the gap in the electrodes; and (iv) cover plate bonding to form the fluidic network. The nanoelectrode sizes are around 50 nm x 45 nm and 1.7 μm in length (A of Figure 5.6) and the distance between two entrance and exit nanoelectrodes are 30 μm (B of Figure 5.6). It was critical to ensure that the nanochannel width and the electrode gap had dimension below the reported persistence length of dsDNAs (50 nm), thus, fabricated width and depth for both nanogaps were ~30 nm and 50 nm, respectively (C of Figure 5.6).

Figure 5.7 shows a new fabrication scheme proposed for nanoelectrodes in fused silica that may be extended to polymer devices as well. Fabrication will be initiated with spin coating followed by lift-off resist and UV-resisnt on the cleaned substrate. The nanotrenches will be fabricated in to substrate via UV-NIL using Surlyn or PDMS stamp. This substrate will then undergo reactive ion etching to remove the UV resist and oxygen plasma treatment to remove lift-off resist. It will then undergo mercaptosilane treatment by vapor deposition, which will deposit an adhesion layer on tranches. Finally, after removing the lift-off resists, AuNPs will be deposited on the trenches by electron beam evaporation.

5.4 Conclusions

Proposed nanosenor device capable of sequencing based on the unique ToF measurement of the single monomer nuclotides is under progress. It will be capable of sequencing DNA, RNA and proteins to identify their genomic structure. Choice of enzyme can be changed depending on

the molecule of interest. ToF measurements will provide unique molecular signature via its interaction with the channels walls, thus modifying the surface of the channel walls appropriately may increase the resolution of separation.

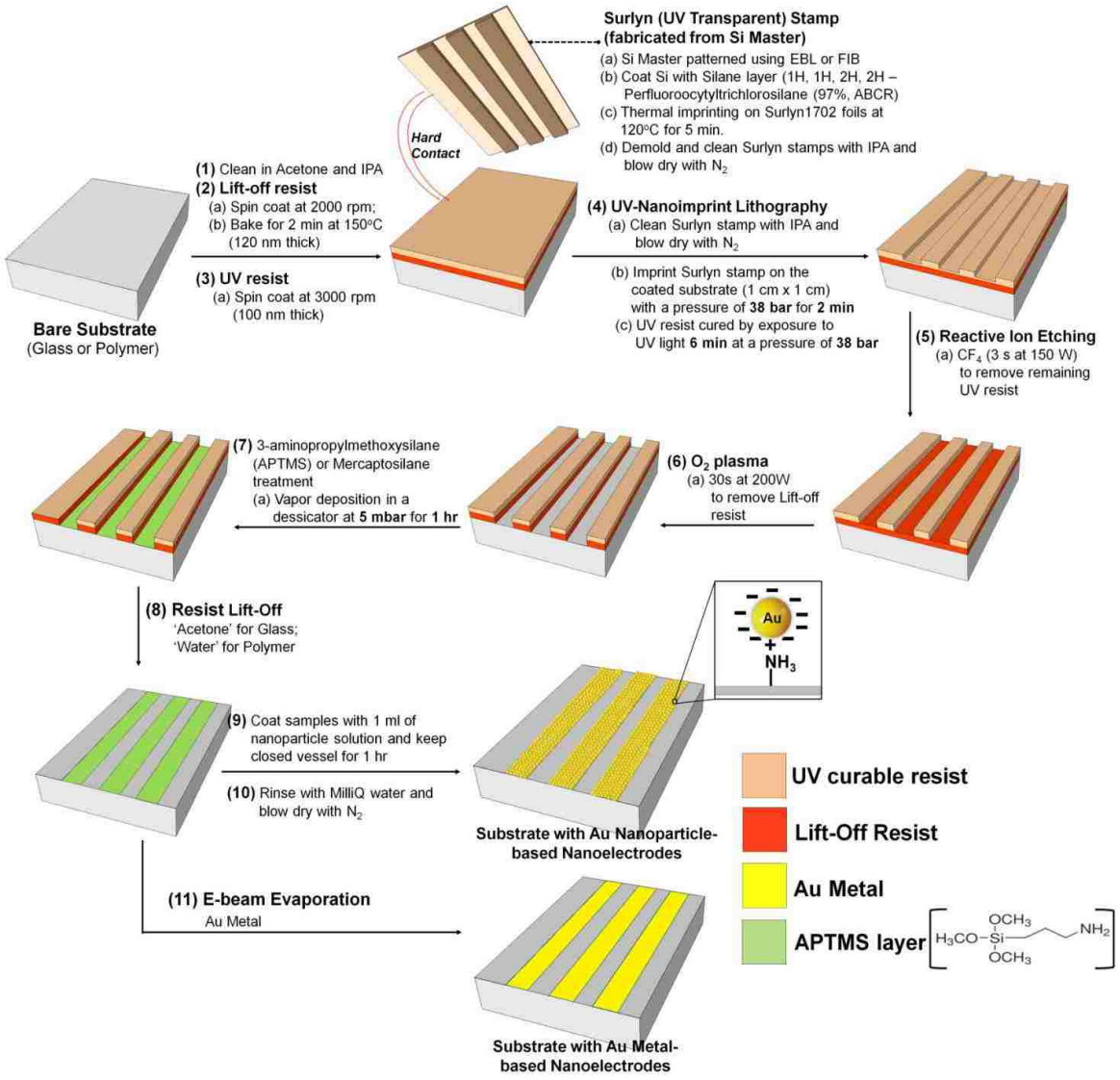

Figure 5.7 Full description of the newly proposed scheme for the fabrication of Au nanoparticle or Au metal-based nanoscale electrode in a glass or Polymer substrate. (Reproduced from Uba dissertation)

5.5 References

1. Werner, J. H.; Cai, H.; Keller, R. A.; Goodwin, P. M., Exonuclease I hydrolyzes DNA with a distribution of rates. *Biophysical journal* 2005, *88* (2), 1403-1412.

2. Novak, B. R.; Moldovan, D.; Nikitopoulos, D. E.; Soper, S. A., Distinguishing Single DNA Nucleotides Based on Their Times of Flight Through Nanoslits: A Molecular Dynamics Simulation Study. *Journal of Physical Chemistry B* 2013, *117* (12), 3271-3279.

3. Uba, F. I.; Pullagurla, S. R.; Sirasunthorn, N.; Wu, J.; Park, S.; Chantiwas, R.; Cho, Y.-K.; Shin, H.; Soper, S. A., Surface charge, electroosmotic flow and DNA extension in chemically modified thermoplastic nanoslits and nanochannels. *Analyst* 2015, *140* (1), 113-126.

4. Uba, F. I.; Hu, B.; Weerakoon-Ratnayake, K.; Oliver-Calixte, N.; Soper, S. A., High process yield rates of thermoplastic nanofluidic devices using a hybrid thermal assembly technique. *Lab on a Chip* 2015, *15* (4), 1038-1049.

5. Cerf, A.; Cipriany, B. R.; Benítez, J. J.; Craighead, H. G., Single DNA Molecule Patterning for High-Throughput Epigenetic Mapping. *Analytical Chemistry* 2011, *83*, 8073-8077.

6. Mirsaidov, U.; Timp, W.; Zou, X.; Dimitrov, V.; Schulten, K.; Feinberg, A. P.; Timp, G., Nanoelectromechanics of Methylated DNA in a Synthetic Nanopore. *BioPhysical Journal: Biophysical Letters* 2008, *12*, L32-L34.

7. Lim, S. F.; Karpusenko, A.; Sakon, J. J.; Hook, J. A.; Lamar, T. A.; Riehn, R., DNA methylation profiling in nanochannels. *Biomicrofluidics* 2011, *5*, 034106.

8. An, N.; Fleming, A. M.; White, H. S.; Burrows, C. J., Crown ether–electrolyte interactions permit nanopore detection of individual DNA abasic sites in single molecules. *Proceedings of the National Academy of Sciences of the United States of America* 2012, *109*, 11504-11509.

9. Kim, Y.; Kim, K. S.; Kounovsky, K. L.; Chang, R.; Jung, G. Y.; dePablo, J. J.; Jo, K.; Schwartz, D. C., Nanochannel confinement: DNA stretch approaching full contour length. *Lab on a Chip* 2011, *11* (10), 1721-1729.

10. Mannion, J. T.; Reccius, C. H.; Cross, J. D.; Craighead, H. G., Conformational analysis of single DNA molecules undergoing entropically induced motion in nanochannels. *Biophysical Journal* 2006, *90* (12), 4538-4545.

11. Reccius, C. H.; Stavis, S. M.; Mannion, J. T.; Walker, L. P.; Craighead, H. G., Conformation, length, and speed measurements of electrodynamically stretched DNA in nanochannels. *Biophysical Journal* 2008, *95* (1), 273-286.

12. Abad, E.; Juarros, A.; Retolaza, A.; Merino, S.; Marie, R.; Kristensen, A., DNA analysis by single molecule stretching in nanofluidic biochips. *Microelectronic Engineering* 2011, *88* (3), 300-304.

13. Cao, H.; Tegenfeldt, J. O.; Austin, R. H.; Chou, S. Y., Gradient nanostructures for interfacing microfluidics and nanofluidics. *Applied Physics Letters* 2002, *81* (16), 3058-3060.

14. Cho, Y. H.; Lee, S. W.; Fuji, T.; Kim, B. J., Fabrication of silicon dioxide nanochannel arrays without nanolithography for manipulation of DNA molecule. *Microelectronic Engineering* 2008, *85* (5-6), 1275-1277.

15. Kim, S. K.; Cho, H.; Park, H. K.; Kim, J. H.; Chung, B. H., Fabrication of Nanochannels by Anisotropic Wet Etching on Silicon-on-Insulator Wafers and Their Application to DNA Stretch. *Journal of Nanoscience and Nanotechnology* 2010, *10* (1), 637-642.

16. Liang, X. G.; Morton, K. J.; Austin, R. H.; Chou, S. Y., Single sub-20 nm wide, centimeter-long nanofluidic channel fabricated by novel nanoimprint Mold fabrication and direct imprinting. *Nano Letters* 2007, *7* (12), 3774-3780.

17. Mannion, J. T.; Craighead, H. G., Nanofluidic structures for single biomolecule fluorescent detection. *Biopolymers* 2007, *85* (2), 131-143.

18. Chantiwas, R.; Park, S.; Soper, S. A.; Kim, B. C.; Takayama, S.; Sunkara, V.; Hwang, H.; Cho, Y. K., Flexible fabrication and applications of polymer nanochannels and nanoslits. *Chemical Society Reviews* 2011, *40* (7), 3677-3702.

19. Wu, J. H.; Chantiwas, R.; Amirsadeghi, A.; Soper, S. A.; Park, S., Complete plastic nanofluidic devices for DNA analysis via direct imprinting with polymer stamps. *Lab on a Chip* 2011, *11* (17), 2984-2989.

20. Chastain II, P., Nakamura, J, Rao, S, Chu, H., Ibrahim, JG, Swenberg, JA, and Kaufman, DG, Abasic sites preferentially form at regions undergoing DNA replication. *FASEB J* 2010, *24*, 3674-3680.

21. Kamande, J. W.; Hupert, M. L.; Witek, M. A.; Wang, H.; Torphy, R. J.; Dharmasiri, U.; Njoroge, S. K.; Jackson, J. M.; Aufforth, R. D.; Snavely, A.; Yeh, J. J.; Soper, S. A., Modular Microsystem for the Isolation, Enumeration, and Phenotyping of Circulating Tumor Cells in Patients with Pancreatic Cancer. *Analytical Chemistry* 2013, *85*, 9092-9100.

22. Okagbare, P. I.; Soper, S. A., High throughput single molecule detection for monitoring biochemical reactions. *Analyst* 2009, *134* (1), 97-106.

VITA

Kumuditha Madusanka Weerakoon Ratnayake was born to Mr. Jayathilake Weerakoon Ratnayake and Mrs. Daya Wimalagunaratne at Colombo, Srilanka. He did his primary education at Wesley College- Colombo 09 from 1989-1999. He received his secondary education from Royal College- Colombo 07. During his school time he was an honor roll student in many aspects. After successfully completing of the high school, he was selected to attend University of Colombo to study Physical Sciences in 2004. Subsequently, he managed to get in to the Computational Chemistry special degree program which he successfully completed with Second class Upper honors in 2008. Together he completed his coursework for the Bachelor of Information Technology degree at University of Colombo in 2008, which broadened his carrier in to inter disciplinary pathway. The internship at IFS, which is a software development company, improved his programming skills to the most up to date technology.

As his determination Kumuditha received an assistantship to pursue his doctoral studies in Chemistry at Louisiana State University in 2009. In the spring 2010 he joined Prof. Steven A. Soper research group at Louisiana State University. He started his research carrier at LSU contributing to the project of next-generation DNA sequencing in nanofluidic sensor devices. He was also assigned to work with the computational component of the project in collaboration with the Dr. Dorel Moldovan's research group in mechanical engineering department at LSU. He moved to University of North Carolina at Chapel Hill for continuation of the experimental component of his research study in 2012. During his PhD carrier, he participated in several conferences such as Pittconn, ACS National Meeting, Gordon Research Conference etc. presenting his research to the community. Kumuditha was awarded 3rd place JACS Poster

Presentation in June 2014 at Gordon Research Conference. He also received Honorable Mention Award at 128th NC ACS meeting in November 2014.

Apart from studies, Kumuditha was an active member in different sports clubs. He was a junior athlete participated in inter-school athletic competitions. Also, he served to the Wesley College U-13 and U-15 cricket teams as an all-rounder. He was also participated in cricket and rowing clubs at the University of Colombo. Currently, he is an active player/ member at the UNC Cricket Club. Social work was also one of his main interests. He participated in many volunteering opportunities in Sri Lanka as well in USA.